On the Dynamics of Rigid Multi-Body Systems in Orbit

PhD candidate:

Daniele Pagnozzi
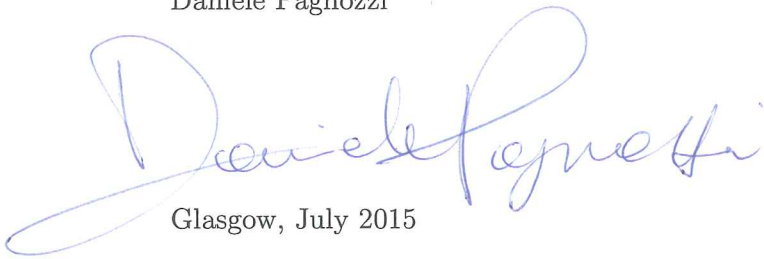
Department of Mechanical and Aerospace Engineering
University of Strathclyde

A.Y. 2014 - 2015

Daniele Pagnozzi

Glasgow, July 2015

Supervisors

First supervisor:

    Dr. James D. Biggs

    Advanced Space Concepts Laboratory

    Department of Mechanical and Aerospace Engineering, University of Strathclyde

    Glasgow, United Kingdom

Second supervisor:

    Professor Massimiliano Vasile

    Department of Mechanical and Aerospace Engineering, University of Strathclyde

    Glasgow, United Kingdom

Examiners

External examiner: Professor Matthew Cartmell

    Department of Mechanical Engineering, The University of Sheffield

    Sheffield, United Kingdom

Internal examiner: Dr Malcolm Macdonald

    Department of Mechanical and Aerospace Engineering, University of Strathclyde

    Glasgow, United Kingdom

Acknowledgments

The credit for this work belongs to the many people who helped and supported me. Firstly I would like to thank my supervisor, Dr. James Biggs, for his invaluable technical guidance, for his huge inspiration and, last but not least, his great human support during the whole PhD. He showed me the beauty of making research and taught me a lot, powering my professional growth and always believing in me. My thanks also go to Professor Massimiliano Vasile, my second supervisor, without his research group the Mechanical & Aerospace department would be a much more boring place, and to Dr Malcolm Macdonald, who gave me the opportunity to send a red nose to space (technically to the mid stratosphere) ! Thanks as well to Professor Colin McInnes who fired the spark which triggered all the events that took me here in Glasgow.

In my PhD I had the honour to develop part of my work together with some friends and I really want to thank them. Dr. Craig Maclean, from the University of Strathclyde, and I investigated the attitude dynamics of single rigid bodies and the results of our research are contained in the third chapter of this thesis. Together with Andrea Pisculli, Dr. Leonard Felicetti and Dr. Marco Sabatini, from the University of Rome La Sapienza, we addressed the dynamical coupling problem of space manipulators and the results of our research are shown in the sixth chapter of this thesis.

Once more, I have to give a special thanks to Professor Paolo Gasbarri and Professor Giovanni Battista Palmerini, from the University of Rome La Sapienza, who disclosed the world of space multi-body systems to me, encouraged me to undertake the journey to Scotland and who always had something more than just a friendly word for me.

Living in Glasgow has not been always easy for me, however what this city gave me is priceless and, as part of it, an incredible number of true Friends. Each of them left me with something unique and without them this work would have not been possible. I really hope the future will give us much more time to spend together.

Finally, two words for my whole family (meant in the broadest sense of the word): Grazie Mario !

Abstract

A critical factor for the success of space missions is the implementation of an appropriate spacecraft attitude control system. For multi-body space systems, the mechanical couplings have significant effects on the attitude dynamics. These effects, added to the high performance requirements and the number of strict constraints that, in general, space systems have to satisfy, make mission design very challenging. This calls for research to address these challenges. Dynamical systems analysis benefits system and control design by providing a quantity of information on the systems' natural behaviour. This thesis investigates the natural attitude dynamics of multi-rigid-body space systems and gains an insight into the nonlinear dynamics in order to develop efficient control techniques that exploit them. In addition this thesis aims to investigate the usefulness of dynamical systems tools in this area of application. To this end, the dynamics of the free single asymmetric rigid spacecraft, the two-body spacecraft in orbit, the three-body spacecraft in orbit and the generic N-body spacecraft are studied. Integrability of the single rigid body problem is used to derive a form of the well-known solution different from the classical and more suitable for aerospace applications. Hamiltonian and Lagrangian formalisms are used in the few-body problems where equilibria are identified and their nonlinear stability is addressed. Furthermore, the behaviour both in the neighborhood and far from the equilibria is examined, gaining an insight into the global nonlinear dynamics. Finally, the Newton-Euler formulation is employed to describe an N-body system and the problem of the dynamical coupling reduction, relevant for space manipulators, is addressed and a feedback controller is designed.

Contents

List of Figures

List of Tables

Introduction

1.1 Orbiting Multi-Body Systems

1.1.1 Outline

According to the definition by Shabana in [1], a multi-body system is defined to be:

> "a collection of subsystems, called bodies, kinematically constrained which
> may undergo large translations and rotational displacements".

This definition captures a wide class of systems which have applications in a diverse number of areas such as industrial robots, terrestrial vehicles, underwater vehicles, flying systems, bio-engineering systems and many others. Each of these systems can be differentiated by their working environment, which consequently defines their dynamics. This thesis focusses on multi-body systems in a space environment.

In general, space systems have extremely demanding and very strict requirements which have to be satisfied, for example: lightness, stiffness and reliability. Due to large time-delays in radio communications, autonomy is highly desired and, in addition, manoeuvreing control efficiency is a critical factor as energy resources are limited. In particular, orbiting multi-body systems differ from other multi-body systems in that they operate in microgravity conditions, thus subject to a gravity force which is not uniform[1] and that may vary in time, depending on the orbit. Additionally, as they are flying systems, they do not have an anchorage pivot and consequently the motion of each body affects the motion of all the other bodies of the system causing rotations

---

[1]Constant in direction and magnitude along the system.

and translations around the overall centre of mass, and, possibly, displacements of the center of mass itself, if external forces, e.g. air drag, or orbit and attitude control, are present. This does not generally hold for multi-body Earth systems, such as robotic arms, where at least one of the bodies is supported by the ground, exchanging reaction forces and momenta with it.

The overall dynamics of space multi-body systems are highly nonlinear and are generally non-integrable. The research area of space multi-body systems has roots in several fields including rigid-body mechanics, structural mechanics, mechanical engineering and attitude dynamics. In particular, the attitude dynamics is interdependent with the orbital dynamics. Notably, the term orbiting multi-body systems addresses a large number of different spacecraft. The following two sections provide a brief overview, starting from the first multi-body satellites to the current state of the art, to motivate this study.

1.1.2   An Historic Overview

Figure 1.1 outlines the historical evolution of space flight through a selection of landmark events and a selection of remarkable multi-body spacecraft missions.

Radio Astronomy Explorers

Multi-body systems were first introduced to model spacecraft with large appendages. Among these, the Radio Astronomy Explorer satellites (RAE-A Explorer38 and RAE-B Explorer49) launched in 1968 and 1973, conceived to monitor low-frequency cosmic radio noise (Explorer38), to measure the intensity of radio signal from celestial sources and to provide data on lunar gravity (Explorer49), [2] and [3]. In particular, the RAE-B spacecraft's experiment antennas consisted of four 229-m traveling wave antennas forming an X configuration, a 37-m dipole antenna and a 129-m boron libration damper boom system used to damp out any spacecraft oscillations about the equilibrium position.

Canadarm 1

A broader class of space multi-body systems emerged as in 1969 in the USA and Canada planned to cooperate in the development of the Space Shuttle program. In particular, the Canadian National Research Council (NRC) supervised the development of a manipulator to be hosted in the cargo bay of the Shuttle. In the following ten years the Canadian research program designed and realised the first space manipulator system: the Shuttle Remote Manipulator System (SRMS), also known as Canadarm1, which first flew on November 13th 1981 within the STS-2 mission. Recognition of the
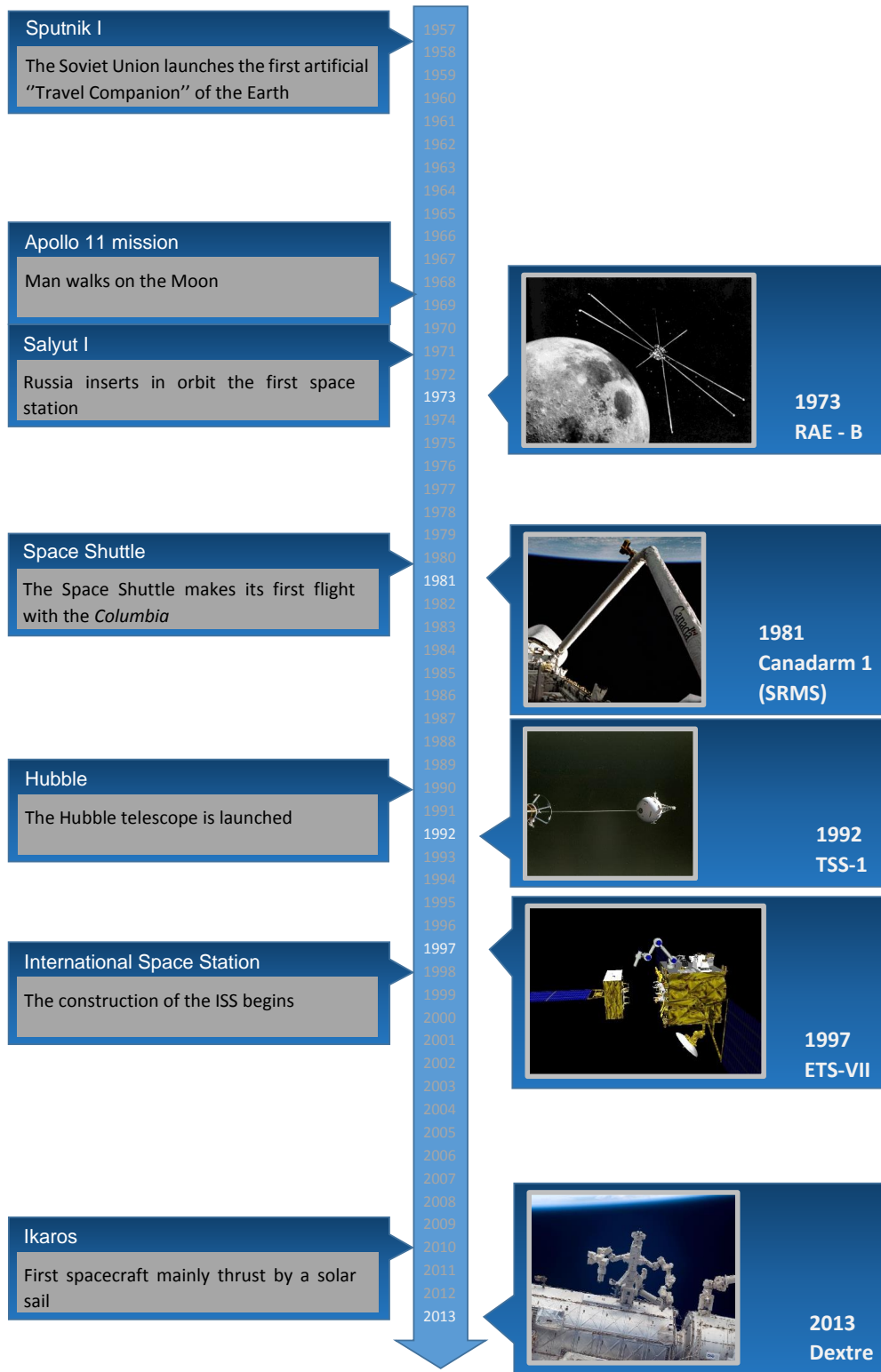
Figure 1.1: Space flight timeline. On the left hand, a selection of milestones of the space flight history. On the right hand, a selection of multi-body spacecraft missions.

advantages of employing robotic systems in space was immediate, [4, 5, 6], and continues through a number of space operations as, for instance, the Hubble maintenance missions -the first in 1993- and the retrieval of the Space Flyer Unit - in 1996.

In summary the use of space-multi body systems can be listed as

1. they can aid astronauts in their tasks enhancing safety

2. they can increase the tasks efficiency, the complexity of the operations and the maximum work loads

3. they can substitute astronauts avoiding Extra Vehicular Activity (EVA) time, lowering the overall human risk in space flight.

Robotic Spacecraft and Tethered Systems

In the 1980s, two completely different kind of concepts started to be discussed: autonomous space-flying robot and tethered spacecraft. The former was thought initially for rescuing and servicing malfunctioning satellites [7]. The latter was mainly addressed at that time for scientific purposes, even though several other applications had been advanced, e.g. using tethered systems for gravity gradient stabilisation.

In the following decade both system concepts were realised. In 1992 and 1996 the shuttle missions STS-46 and STS-75 were dedicated to the Tethered Satellite System (TSS) project, proposed by NASA and ASI, the Italian space agency Agenzia Spaziale Italiana. The aims were to verify the feasibility of tethered spacecraft and to research high atmosphere physics and plasma electrodynamics. In 1993 the Robot Technology Experiment, ROTEX, developed by the German Aerospace Center (DLR), flew within the STS-55 mission and in 1997 the Engineering Test Satellite VII (ETS-VII) was launched by the National Space Development Agency of Japan (NASDA). The Japanese mission, in particular, was made by a pair of satellites, a larger chaser, which carried a 2m robot arm, and a smaller target satellite for rendezvous and docking experiments, including rendezvous, docking, manipulation, berthing, orbital replacement unit exchange, fuel transfer and structure assembling.

Over the last twenty years both existing concepts have been developed and other new ones emerged.

1.1.3   Current Projects

Electrodynamic tether systems

Currently, an interesting example of a tethered spacecraft project is the Microsatellite Propellantless Electrodynamic Tether (PET) Propulsion System, [8]. This propulsion

system creates thrust exploiting the Lorentz-force produced by the interaction of an electrodynamic tether with the Earth's magnetic field. Electrodynamic tether systems are said to be able to dramatically reduce the cost of many space missions by eliminating the need to launch large quantities of propellant into orbit. A promising application of the PET Propulsion System is spacecraft de-orbiting, [9].

Dextre

The youngest member of the Canadarm family is the Special Purpose Dexterous Manipulator or Dextre, Fig. 1.2, [10, 11]. This system is the last module added to the Canada's Mobile Servicing System and, roughly speaking, it can be described as an ultra-sophisticated end-effector, endowed with two arms, each having a total of 21 degrees of freedom. Dextre is not an autonomous system and is remotely controlled by either the crew of the International Space Station (ISS) or the ground flight control center. Its mission goals are performing maintenance operations of the ISS, assisting the ISS crew when appropriate and testing space robotic operations, [10]. Each terminal segment of the arms can grasp and actuate payloads, tools and bolts, and provide power, data and video. In January 2013, Dextre proved the capability of on-orbit refueling in the Robotic Refueling Mission.

Figure 1.2: The Special Purpose Dexterous Manipulator, the last module added to the Canada's Mobile Servicing System. Image Credit: NASA

Robotic Spacecraft

As Yoshida and Wilcox write in [12], space robots are now considered to be spacecraft than can *facilitate manipulation, assembling, or servicing functions in orbit as assis-*

tants to astronauts, or to extend the areas and abilities of exploration on remote planets as surrogates for human explorers. It appears that robotic spacecraft will have a key role in the future of space flight. Recently, the recognition of the Earth's orbital debris mitigation as a critical factor for feasible exploitation of space in the future, called for new applications of multi-body space systems. For instance, the debris removal demonstration mission planned by the German Aerospace Centre DLR: the Deutsche Orbitale Servicing Mission (DEOS), [13, 14]. DEOS will be carried out by a semi-autonomous satellite endowed with a robotic arm, Fig. 1.3. Its job will be to berth, secure and de-orbit malfunctioned satellites from low Earth orbit. This kind of mission poses a high number of challenges, e.g. to rendezvous and to capture a tumbling non-cooperative object, to stabilise it and to de-orbit it. The manipulator will be applied to capture the client satellite, to stabilise the grappled compound and to move the client from the capture position to the unified berthing and docking port mechanism. Once both spacecraft are rigidly coupled the manipulator can be released from the satellite in order to be free for other maintenance tasks or it will be folded away and remain in its parking position. According to the DLR, the launch is planned between the end of 2017 and the beginning of 2018.

Modular spacecraft

Accessibility to space through low-cost and through micro and nano scale spacecraft has led to a novel multi-body mission concept: fractionated spacecraft. Launch constraints pose serious limitations to the size of a space system. To overcome this aspect, the mission concept proposed is to have an autonomous cluster of single elements which, when docked together, forms the major system. An example of such system is the Caltech - Surrey Space Centre joint project AAReST, [15], a technology demonstration mission for a large telescope in-space assembly. In particular, the AAReST mission involves seven nano-satellites, each housing a mirror element. One of the key-features of the system is the capability of autonomous reconfiguration in order to have different optical resolutions.

An additional notable system is the one proposed by Shoer, [16], who suggests to connect clusters modules with magnetic flux pins which, in practice, behave like variable stiffness revolution joints and to apply multi-body dynamics analysis to study efficient system reconfigurations. Figure 1.4, from [16], illustrates the mission concept using two cubesats. The flux-pinned interface can be used passively as a revolution joint as well as actively to change its inertia and reconfigure the modular components' relative positions. Station keeping and reconfiguration manoeuvres are indicated as ideal applications for this type of non-contracting architecture.

A modular architecture for space systems has several advantages, for instance [17, 18]:

1. enhanced mission and in-orbit robustness: it allows easy replacement of degraded or failed subsystems and eventually reduces launch failure damages

2. flexibility: it allows easy and progressive system upgrade

3. lowered mission recovery costs

4. rapid response

5. potential for mass production.

Multi-body theory is used to study the dynamical behaviour in the mission's phases where the spacecraft are physically connected to one another, i.e. once an assembly is formed. In general, the primary aim is to aid and inform control design, e.g. achieve of a desired system configuration or system attitude stabilisation.
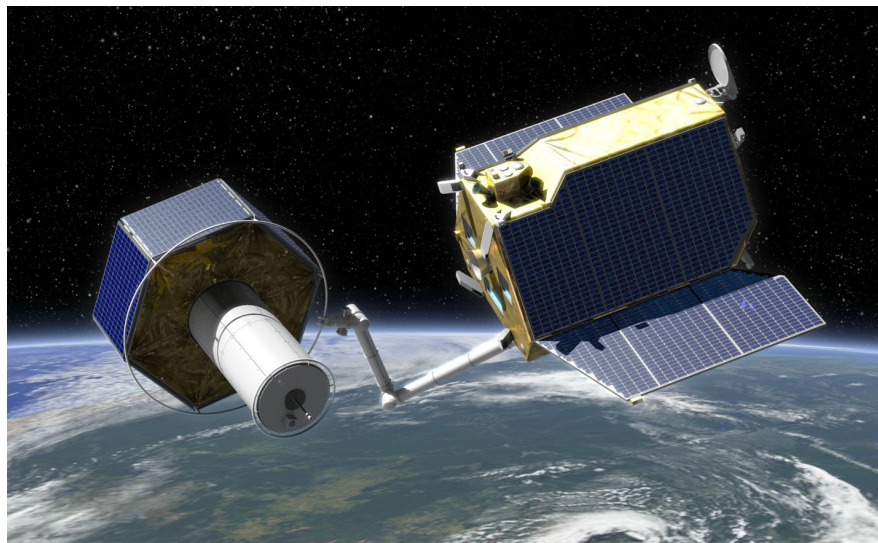
Figure 1.3: Artist impression of the Deutsche Orbitale Servicing Mission (DEOS), designed by DLR. Image Credit: German Aerospace Center - Deutsches Zentrum für Luft- und Raumfahrt e. V. (DLR).

All the examples presented belong to a wide class of multi-body space systems. Their dynamics have common features which are unique to this class. However, each kind of system differs from the rest, e.g. they can have different length scales and mission time scales, which can involve the use of different models for their physical description.

1.2 Thesis Motivation

A critical factor for the success of every mission is developing and implementing an appropriate spacecraft attitude control system. This, for instance, directly affects the accurate pointing of on-board instruments as well as the precise manoeuvering of a space manipulator end-effector. As remarked by Professor Hughes in [19], *no modern space*
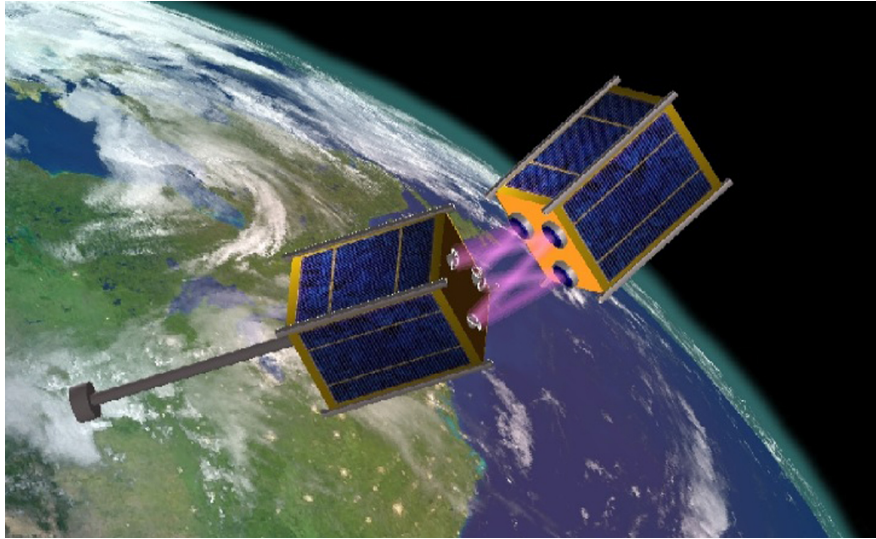
Figure 1.4: Modular Spacecraft where two cubesats are joined via a fluxed-pinned interface. Image courtesy of Joseph Paul Shoer, Cornell University.

vehicle, whether a low-orbit resources satellite, a geostationary communications plat-form, an interplanetary probe, or any other man-made space apparatus, can accomplish its mission objectives without a properly functioning attitude stabilization and control system. For multi-body space systems, the mechanical couplings have significant effects on the attitude dynamics. These effects, added to the high performance requirements and the number of strict constraints[2] that, in general, space systems have to satisfy, make mission design challenging. According to these motivations, this thesis is based on the fundamental concept that the investigation of the dynamics, benefits system and control design by providing a quantity of information on the systems' nature and its be-haviour. In general, problems of multi-body attitude mechanics are characterised by: a nonholonomic nature, a non-linearisable form of the differential equations, chaotic behaviour, a continuous exchange of energy among the bodies through the joints, a continuous exchange of angular momentum, coupling between attitude and orbital dy-namics and the presence of forces which depend on the system configuration. Few-body problems include - but are not limited to - tethered systems, debris removal missions and modular spacecraft. For these kinds of missions, it is fundamental to realise atti-tude manoeuvres which allow the desired reconfiguration and pointing while keeping consumption costs limited. Maintenance of the desired attitude is generally required for long periods of time, regardless of the presence of disturbances. Furthermore, very limited resources pose strict mission constraints as, commonly, this kind of missions in-volves micro-scale and nano-scale spacecraft powered by modest on-board solar arrays and controlled by particularly small actuators. Due to the time scale of the problems and, most of all, thanks to the reduced dimension of the configuration space, common research trends involve:

---

[2]as, for instance, energy consumption, control computational loads and components' weight.

- The study of the uncontrolled dynamics equilibria and their stability (see [20], [21] or [22])

- Linear control design (see [23])

- Parametric stability of the uncontrolled dynamics ([24])

- Investigation of the nonlinear uncontrolled dynamics of rigid-body systems (see [25])

Many-body problems commonly fall within space robotics, i.e. spacecraft endowed with robotic arms or space manipulators. In this field, great attention is driven towards debris removal missions, on-orbit servicing missions, maintenance missions and EVA activity aid. These types of operations involve interactions between different space systems thus call for high demands in the motion planning and control. In the design requirements of robotic devices, it is crucial for the end-effector to be capable of following precisely a desired path, avoiding obstacles and, at the same time, minimising the attitude disturbances on the main platform (thus, the required attitude control to take the main platform to the desired state). Current research trends mainly include:

- Motion planning and control design with a particular regard to:

    - Elimination or limitation of the dynamic coupling between robotic system and spacecraft bus (see [26])

    - Suppression or dumping of induced vibrations (see [7])

- Study of the interaction with passive objects on-orbit (e.g. uncooperative spacecraft) (see [27], [28] or [29])

Because of the nature of the problems considered, a number of approaches are used. In general, typical methods of engineering are used to study many-body systems, e.g. numerical optimisation or dynamic linearisation about the equilibria, while typical methods of mathematical physics are used to study few-body systems, e.g. non-linear dynamical systems analysis or geometric control. The highly complex nature of the problem has led most of the literature, in recent years, to focus on the control design and less on the analytical investigation of the dynamics, in particular for high dimensional systems. On the other hand, the behaviour of orbiting multi-body systems is far from being completely understood. As stated by Guerman, [20], analytical studies are extremely useful in creation of project concepts. Moreover, Dubowsky and Papadopoulos, who studied extensively free-flying and free-floating robotic systems, claim that understanding their fundamental dynamic behavior will improve system design, [30], it will lead to design systems working with reduced attitude control, [31], and that it will aid the development of solutions to problems of planning and control, [31] [6]. These factors are critical in a highly demanding working environment like space, where small enhancements in each subsystem can potentially lead to significant improvement

of the overall spacecraft performance[3].

In addition, it is well known that understanding the underlying dynamics of the system can aid system and control design. This holds for any dynamical system, as stated by a number of authors, Marsden[4] Bloch[5]. In orbital dynamics, for instance, the structure of the gravitational field is studied in order to efficiently move through the field, hence saving propellant mass by exploiting the full dynamics of the n-body models, see for instance [34], [35] or [36]. Concerning orbiting multi-body systems, an important example is the work of Sanyal, see for instance [23], dedicated to the investigation of the coupling effects of attitude and orbital dynamics demonstrating that, when time is not an important factor, these actions can be profitably used to make changes in spacecraft position and orientation. Moreover, another way the dynamical investigation can feasibly support system control design is providing information about natural motions. Similar to the orbital dynamics, investigation and understanding of the natural dynamics of the system offers the possibility to use natural motions to design reduced control manoeuvres. Flakamp, [37], for instance, constructs energy-efficient reconfiguration manoeuvres of a double pendulum through a sequence of free dynamics[6] arcs that guide the system from its initial state to the desired final. Such trajectories move on stable manifold trajectories that originate from the natural dynamics of the problem. Unfortunately, multi-body spacecraft are non-integrable systems that are highly non-trivial because of dynamic coupling between the various degrees of freedom. In order to deal with this complexity, often, the dynamical analysis is simplified, i.e. considering a limited number of bodies, assuming the bodies as point masses, as rigid, or reducing the number of external forces.

In general, assuming space systems as made of rigid bodies provides an acceptable degree of approximation for a significant number of applications without necessarily affecting the utility of the analysis and the significance of its results. Naturally, different levels of approximation of rigid-body models have both advantages and disadvantages, i.e. easing of study to the detriment of detailing the real system. The main disadvantage is that flexional behaviour is neglected together with all the related aspects, e.g. vibrations, deformations, dynamical loads. However, in most of the cases, orbital and attitude dynamics are represented with enough precision. Furthermore, it provides a higher level of detail than considering systems of point masses rigidly joined, thus realising a good trade-off between accuracy of description and simplification of the dynamics. This latter is certainly the most important advantage, as the dynamics equations result in a simple form and in a relatively reduced number of variables.

---

[3]Consider as a further example that reductions in fuel and power usage directly influence the useful operative life of the spacecraft, its weight and thus launch and mission costs.

[4]In [32] Marsden wrote that mechanics plays *a crucial role in control theory.*

[5] In [33], Bloch wrote that *there is a particularly rich connection between mechanics and nonlinear control theory.*

[6]Uncontrolled dynamics arc.

This facilitates the overall dynamical investigation both in the case of analytical and numerical studies.

In particular, it has to be considered that when the dimensions of the configuration manifold make it possible, rigid-body models benefit from a very rich mathematical structure which can be investigated using methods of classical mechanics and analysis in order to gain a deep insight into the dynamics, see for example Sanyal and Bloch, [22]. These are the cases of few-body systems like the single rigid-body system, which can be used to address attitude problems of either a single spacecraft or a rigidly joined multi-spacecraft system, or modular spacecraft, when bodies are mechanically connected, e.g. the DLR DEOS mission[7], [13]. During the mission phases where satellites are mechanically linked together, the system can be effectively modeled using a single-asymmetric rigid-body or, depending on the mechanical properties of the connection[8], using a two rigid-body system. The importance of this kind of analysis to multi-body dynamics has been highlighted by Rekleitis and Papadopoulos, [38], who reported a lack of studies concerning the dynamics and control of the motion of an already grasped body in multi-spacecraft missions. When many-body models are considered an exhaustive and global description of the behaviour of the system is extremely hard to obtain. Furthermore, in practice, the research target changes from modular spacecraft into space robotic systems. In this case, the focus moves to path-planning and control analysis, and the advantages of using rigid-body mechanics is that it provides a simplified dynamics to control and process. In particular, rigid-body models provide a valuable solution which can lower computational requirements bringing important time and power savings, which are critical factors during real time operations or automated on-board operations.

A rich literature is dedicated to the study of multi-body spacecraft dynamics, however, in general, bodies are not modeled as rigid and with a finite shape, i.e. a mass distributed over a finite volume. Conversely, systems of point masses linked by ideal massless joints or rods are preferred for low-dimensional systems, such as for tethered systems. While, on the other hand, finite shape flexible bodies are preferred for robotic systems as more accurate models are desired for the simulation of robotic spacecraft. Nevertheless, the application of rigid-body mechanics to orbiting multi-body spacecraft involves many advantages and it is identified as a promising field of research, which can provide an insight into their global dynamics, enhance the existing understanding on their behaviour, and provide novel control methods, e.g. based on natural motions. With respect to point mass systems, using finite-shape rigid bodies enriches the description as the effects due to the presence of a distributed mass in orbit are taken into

---

[7]In detail, operations involve: berthing the Client by the manipulator; using the manipulator to capture the client satellite, to stabilise the grappled compound and to move the client from the capture position to the mechanical linking mechanism; and finally releasing of the manipulator once both spacecraft are rigidly coupled.

[8]e.g. stiffness, size, joints used etc...

account; for instance, effects of the momenta of inertia and the different actions of the external forces, e.g. gravity gradient torque. With respect to more detailed physical models, it provides the possibility to design controllers based on a simplified dynamics, therefore, they are computationally light, without necessarily involving a loss in efficiency.

1.3   Objectives

The primary objectives of this thesis were understanding the natural motions of multi-link rigid body space systems, evaluating the usefulness of mathematical tools to inform system design and control design in this application area and, finally, the development of control techniques based on the natural motions. The main purpose of this work is defined as the investigation of the attitude dynamics of spacecraft modelled as rigid multi-body systems. More specifically, the following research objectives are defined:

- Investigate the natural dynamics of rigid-body systems in space searching for useful information for system and control design;

- Evaluate the usefulness of dynamical systems tools in the context of space multi-body systems, e.g. Poincaré maps;

- Investigate novel methods of control for multi-body systems based on rigid-body dynamics.

Each rigid body considered will be assumed to have a constant and uniform density and to be joined by ideal hinges.

1.4   Contributions to the Research

The thesis is composed of three sections. To the achievement of the thesis objectives, the complexity of the systems addressed increases chronologically, both in terms of the number of bodies considered and in terms of external forces taken into account acting on the spacecraft. In the first section the free single asymmetric rigid-body problem is addressed and its solution revisited. Results provide a set of closed-form expressions describing the kinematics of the body suitable for attitude engineering applications. Their employment for the generation of reference tracks based on natural motions is shown. In the second section, the two-body problem and the three-body problem are studied. Previous work often limits the dynamical analysis to the identification of the relative equilibria and to the study of their stability using a linearised set of equations of motion. In this thesis, equilibria are identified and their nonlinear stability is addressed. Furthermore, the behaviour both in the neighborhood and far from the equilibria is

examined, gaining an insight into the global nonlinear dynamics. As novelty in this field, tools typical of system dynamics are used to investigate the few-body systems. Finally, in the last section, an N-body system is considered and a relevant problem typical of articulated space systems, such as space manipulators, is addressed and a solution proposed. The investigation of the dynamics is used to design a novel controller capable of limiting the dynamic coupling between one of the bodies and the rest of the system.

The novel contribution of each section is discussed in detail below.

Single Asymmetric Rigid-Body

The problem of a single rigid-body either in a force-free environment and in space has been largely investigated. The second case provides, in general, an accurate description of a spacecraft in Earth orbit, the free case provides a good description in deep space. Additionally, the free single rigid-body problem is integrable and an analytic solution can be derived and used for attitude motion planning and control. The solution for the general three-dimensional asymmetric case is well known and classically solved using Euler angles in terms of Jacobi elliptic functions and theta functions [39], [40], [41], [42], [43]. However, this representation may not be the best choice for engineering applications were discontinuities in the analytic functions are not desired and low computational requirements are demanded to compute them. In this work, kinematics and dynamics are investigated adopting an approach based on geometric control theory. In particular, applying a Hamiltonian formulation and using a particular representation to describe the motion on its configuration space, i.e. the Special Unitary group $SU(2)$ - the the Lie group of 2×2 unitary matrices with determinant 1 -, the kinematic solution is obtained in a convenient quaternion representation, commonly used in space engineering. This form leads to an elegant, useful and compact attitude representation which is not Euler-angle-like, as the quaternions are not constructed using inverse trigonometric functions of the Euler angles, thus enhancing its applicability, e.g. to attitude motion design. Moreover, the solution is expressed in terms of an elliptic integral and Jacobian elliptic functions which can be evaluated using theta functions as well as many other alternative methods [44, 45]. In this respect when implementing the analytic solutions in software the user has the flexibility to choose the most appropriate method to evaluate the elliptic integral whether it be via theta functions or otherwise. In this chapter the analytical solution is used to design large slew manoeuvres using a very simple open-loop control, particularly suitable for micro and nano-spacecraft applications. Furthermore, the kinematic analytical solution derived can be used to aid analytical attitude motion planning, see [46] for instance, to generate reference tracks for space attitude manoeuvres or as an initial guess in numerical optimisation software. In particular, exploiting natural motions for attitude control has been undertaken for

the symmetric case, [47] and [48], in order to minimise torque requirement.

Two-Body and Three-Body Systems

Although a rich literature on rigid-body mechanics and space multi-body systems exists, to the best of the author's knowledge, no work has addressed the investigation of the global natural dynamics of a generic two-body system or three-body system, considering the bodies as having finite shape rather than being modeled as point masses and, at the same time, including the presence of a gravitational field. The investigation of these models is the main novelty of this section. In particular, the dynamics of a multi-body space system consisting of two rigid bodies joined by an ideal rotational hinge, subject to a central gravitational force is studied. The characteristic dimensions of the bodies are assumed to be negligible relative to the central body, as a spacecraft orbits a much larger celestial body. No other external forces are included. Moreover, the problem is restricted to the planar dynamics and the bodies are assumed to be one-dimensional. The latter two assumptions simplify the system's dynamics without qualitatively affecting the results of the analysis. Further novelty of this work is in the different methods of analysis used to study a multi-body problem, in order to provide new descriptions of their natural dynamics. This has been undertaken by providing a Poincaré map of the dynamics for a given energy level which shows regions of regular, quasi-regular and chaotic motion. Furthermore, a Lyapunov Characteristic Exponent (LCE) map is used. This technique has been used in celestial mechanics and fluid dynamics, but applied here to a space multi-body system for the first time. LCE maps are shown to be an extremely useful global visualisation tool for this particular multi-body planar system, reducing the order of the problem and condensing quantities of information into a lower-dimensional image. Finally, the practical implications of the analysis on a real spacecraft multi-body system in terms of control and system design are discussed. The study is, then, extended to a planar three-body system. Hinges are assumed to be ideal and the action of an ideal central gravitational field is taken into account. The central field of force lets the system' s motion to evolve on a plane, when all the initial conditions lie on a plane, [22]. The problem is, therefore, restricted to the planar case. As in the two-body, the characteristic dimensions of the bodies are assumed to be negligible relative to the central body, as a spacecraft orbits a much larger celestial body. No other external forces are included. As well as in the two-body problem, methods of systems analysis are applied to investigate the global behaviour of the system, in order to have a more accurate and novel description of the system.

The Hamiltonian dynamics are derived and used to assess the nonlinear stability of the equilibria. Hence a numerical investigation of the behaviour far from the equilibria is provided using tools from dynamical systems theory such as energy methods, phase portraits and Poincarè maps. Results reveal the existence of unstable equilibria as

well as nonlinearly stable equilibria. The nonlinearly stable equilibria appear to be
surrounded by very narrow regions of regular and quasi-regular motions. Trajectories
evolve chaotically in the rest of the domain. Results are discussed and the three-body
system is compared with the two-body problem.

N-Body System

The few-body problems addressed previously can describe a range of multi-spacecraft
missions. For n-bodies a Newton-Euler set of equations are used in the modelling and
control design as they can be expressed simply in a convenient matrix form, in contrast
to the Hamiltonian or the Lagrangian formulation. Operations of a typical robotic
mission terminate in minutes, significantly less than the order of magnitude of the
orbital dynamics time scale. Therefore, there is no interest in the long term behaviour
of the system, whether it be regular or chaotic. This section addresses the problem of
the dynamic coupling of a spacecraft bus and the manipulator hosted on the bus itself,
due to the reaction forces acting at the anchorage point.

In particular, concerning the use of space manipulators, it is common practice for
the spacecraft to be free-floating during the arm operation, by switching the attitude
control off. In order to reduce the deviations from the spacecraft reference configuration,
very low dynamical coupling between spacecraft and manipulator is desired. Standard
control techniques, either do not take into account the effects of the reaction forces
at the spacecraft' structure, require excessive computational effort, cannot guarantee
global optimal solutions or reduce the workspace.

This section investigates the highly non-linear 3D dynamics of multi-body space systems
in order to design a control method, named Minimum Reaction (MR) control, for space
manipulators which minimises the dynamic coupling with the spacecraft' structure to
which it is anchored but without reducing the initial workspace. The minimisation of
the reactions also minimise the induced vibrations on the flexible components of the
spacecraft, e.g. antennas and solar panels, limiting additional disturbances.

1.5   Related Publications

The research developed in the thesis has been published in the following journal and
conference papers:

Journal Papers

- Pagnozzi, D., Biggs, J.D., *The Dynamics of a 2-Link rigid-body System in Orbit*,
  submitted to the Aerospace Science and Technology journal, July 2015

- Pagnozzi, D., Pisculli, A., Felicetti, L., Sabatini, M., *A minimum reaction control to extend the reaction-null controller workspace*, submitted to the Official Journal of the Council of European Aerospace Societies, CEAS Space Journal, June 2015

- Maclean, C. D., Pagnozzi, D., Biggs, J.D., *Planning natural repointing manoeuvres for nano-spacecraft*, IEEE Transactions on Aerospace and Electronic Systems, 2014, Vol. 50, No. 3, 07.2014, p. 2129-2145

Refereed Conference Proceedings

- Pagnozzi, D., Maclean, C., Biggs, J. D., *A new approach to the solution of free rigid-body motion for attitude maneuvers*, European Control Conference 2013, July 2013, pp.664-669

- Pagnozzi, D. and Biggs, J. D., *Lyapunov characteristic exponent maps for multibody space systems analysis*, AIAA SciTech 2014, January 2014

Abstract-Refereed Conference Proceedings

- Pagnozzi, D. and Biggs, J.D., *Analysis of an Orbiting Three-Rigid-Body Systems Dynamics*, ICNPAA 2014 World Congress: 10th International Conference on Mathematical Problems in Engineering, Aerospace and Sciences, July 2014

- Pagnozzi, D., Pisculli, A., Felicetti, L., Sabatini, M., *3D minimum reaction control for space manipulators*, 65th International Astronautical Congress, September 2014, IAC-14, C2,2.3

- Maclean, C. D., Pagnozzi, D., Biggs, J.D., *Computationally light attitude controls for resource limited nano-spacecraft*, 62nd International Astronautical Congress 2011, September 2011

1.6 Thesis Structure

In order to pursue the research objectives, the thesis will be structured in five sections as follows:

The second chapter provides the theoretical background on multi-body kinematics and dynamics. The reference frames necessary to the identification of a generic mass particle are introduced as well as the basic notation. Position, velocity and acceleration for the particle are derived. Constrained equations are then introduced to reduce the order of the problem and to find the minimum set of configuration variables. Kinetic and potential energy are constructed and integration is performed over the body volumes to obtain the Hamiltonian function. A comparison of the Hamiltonian approach against the Euler-Newton approach is included.

1st Section:
Kinematics and dynamics of orbiting rigid multi-body systems   Chapter 2

2nd Section:
The single rigid-body problem   Chapter 3

3rd Section:
The few rigid-body problem   Chapter 4 and Chapter 5

4th Section:
The N rigid-body problem   Chapter 6

5th Section:
Conclusions   Chapter 7

The third chapter covers the single asymmetric rigid-body problem. A Hamiltonian
   formulation of free rigid-body motion defined on the Special Unitary Group SU(2)
   is used to integrate the system to obtain a convenient quaternion representation
   for attitude engineering applications. Novel content of this chapter concerns ap-
   plying a novel approach, based on geometric control theory to obtain the kine-
   matic solution in an elegant and compact form. Moreover, this integration leads
   to an attitude representation which is not Euler-angle-like, thus enhancing its
   applicability, e.g. to attitude motion design.

The fourth chapter is dedicated to the study of the two-body problem. It presents
   a study of a two-rigid-body system under the action of a central gravitational
   field. The aim is to gain an insight into the natural nonlinear dynamics. First
   the Hamiltonian dynamics is derived and used to assess the nonlinear stability
   of the equilibria. A parametric study of the system is provided and bifurcation
   sets are identified. A nonlinear analysis is undertaken using tools from dynamical
   systems theory such as energy methods, phase portraits, Poincarè maps and Lya-
   punov characteristic exponents. Results reveal regions of regular, quasi-regular
   and chaotic motions. Finally, the practical implications of the analysis on a real
   spacecraft multi-body system in terms of control and system design are discussed.

The fifth chapter is dedicated to the study of the three-body problem. It presents a
   study of a two-spacecraft system joined by an rigid link which is modeled as a
   three-finite-shape rigid-body system under the action of an ideal central gravita-
   tional field. The aim is to gain an insight into the natural nonlinear dynamics.
   The Hamiltonian dynamics is derived and used to assess the nonlinear stability
   of the equilibria. Hence a numerical investigation of the behaviour far from the
   equilibria is provided using tools from dynamical systems theory such as energy
   methods, phase portraits and Poincarè maps.

The sixth chapter addresses the control problem of a generic 3D N-body space system.

A novel controller is designed to minimise the dynamic coupling between one of the bodies and the rest of the system, e.g. a spacecraft endowed with a robotic manipulator, without reducing the system configuration space, e.g. the manipulator workspace. This offers a possible solution to the limitations of standard control techniques. To this end, the non-linear 3D dynamics of a multi-body system is derived in matrix form. Then, a minimum reaction control problem is formulated and solved analytically using a quadratic cost function. The presented solution is applied to a typical mission scenario involving a robotic arm deployment. The test is repeated for the case where flexible appendages - such as a solar panel - are included, in order to test the effect of the controller, based on rigid-body dynamics, on the vibrational behaviour. Results are discussed.

The seventh and final chapter contains the conclusions of the work.

CHAPTER 2

Kinematics and Dynamics

This chapter provides the theoretical background required to describe kinematics and dynamics of rigid orbiting multi-body systems. In the literature several approaches have been used to describe the motion of a multi-body system, since the very first papers on the subject, Hooker, [49, 50], through to the most recent ones, see Pisculli and Gasbarri, [51]. The main reason *for using different modelling approaches depends on the type of analysis that is used to study the system. Moreover, certain formulations are more suitable for numerical simulation while others more suitable for qualitative analysis.* An exhaustive review of modelling techniques can be found in Papadopoulos, [6], or in Sicialiano, [12]. In general, dynamical systems analysis can be used to understand the qualitative global dynamical behaviour of the system, which, in turn, is fundamental to the control design. Numerical simulations are fundamental to the study of the dynamics as well as to the testing and development of control strategies and motion planning techniques, see [12]. In particular, multi-body spacecraft ground test-beds are practically impossible to set up due to the difficulties of reproducing microgravity conditions in three spacial dimensions, so numerical simulations are of fundamental importance. In this work, kinematical description follows from the work of Santini and Gasbarri, see for instance [52], although a number of works used the same approach, see [6], [21] or [53]. They use an Earth centered reference frame, assumed to be inertial, an orbital reference frame, attached to the system's center of mass, and as many body reference frames as the number of bodies. This approach has several advantages; firstly, it allows the orbital motion to be distinguished from the attitude motion, which are based on completely different length scales and usually evolve over different time scales. This, allows one to nondimensionalise the equations thus reducing the existence of numerical errors. Secondly, by using the orbital reference frame, the description of the system attitude is simplified. Third, this approach aids the intuitive understanding of

the physical evolution of the system. As main downside, this approach is not convenient when a direct description of the kinematical state of one of the bodies is required. For instance, in some cases, e.g. dealing with space manipulators, it may be desired to have a direct information on the attitude of one particular body, i.e. the main bus, and on the relative attitude of the other bodies with respect to it, e.g. the position of the manipulator with respect to the bus. In such cases, the orbital reference frame origin is located over the main body reference frame and the attitude of the others body reference frames are described relatively to the first one.

The dynamical modelling follows two different derivations: *the Lagrangian and Hamiltonian formulations* and the *Newton-Euler formulation*. Each one has advantages and disadvantages and the preference of one rather than the other depends on the case considered. Their main differences are in the procedure of derivation of the equations of motions, in the variables used and in their number (Hamiltonian and Lagrangian formulations always use the minimum set of variables), and in the final form of the differential equations (e.g. Newton-Euler formulation can be conveniently expressed in a matrix form). In this dissertation both the formulations are used and described in detail in this chapter. A brief discussion comparing the two forms is included in the conclusions.

2.1   Assumptions

Assumptions that apply to all sections are listed here:

i. The multi-body system is made of N bodies connected as an open chain

ii. All bodies are rigid and have a finite shape

iii. Only spherical joints are considered

iv. All the joints are considered ideal (zero friction) and massless

v. When gravity is considered

    a. the gravitational field is assumed to be a pure central field of force

    b. the characteristic dimensions of the bodies are negligible relative to the celestial body the spacecraft is orbiting

    c. the gravitational potential is approximated using a second order Taylor series expansion.

vi. Gravity is the only conservative force considered in this work.

vii. All external perturbations will be excluded, except air drag. When air drag is considered, the force generated will be parallel to the orbital velocity vector and

in the opposite direction.

2.2   Reference Frames

In the kinematical description, the following reference frames are used:

- Inertial Reference Frame

- Orbital Reference Frame

- N Body Reference Frames

The Inertial Reference Frame, IRF, is assumed to be inertial and fixed in space. When gravity is considered, the origin of the IRF will be taken coincident with the origin of the gravity field. Axes form a right handed orthonormal frame. The fiducial direction of the IRF is not relevant to the ends of this work, without loosing any generality. The Orbital Reference Frame, ORF, is taken with origin over the center of mass of the whole multi-body system, CM. Its x-axis, X_{ORF}, is taken parallel with the vector going from the origin of the IRF to the origin of the ORF, with same direction; the Y_{ORF} axis is chosen perpendicular to the X_{ORF} axis and lying over the orbital plane. Again the z-axis, Z_{ORF}, is taken so that a right handed orthonormal frame is formed. Finally, each body will be associated with a reference frame, BRF, with origin over its center of mass and orientation set according to the body principal axes of inertia. To identify the bodies, these will be labelled with a number. The respective reference frames' names will have the body's number as subscript, i.e. BRF_i, with $i = 1, ..., N$.
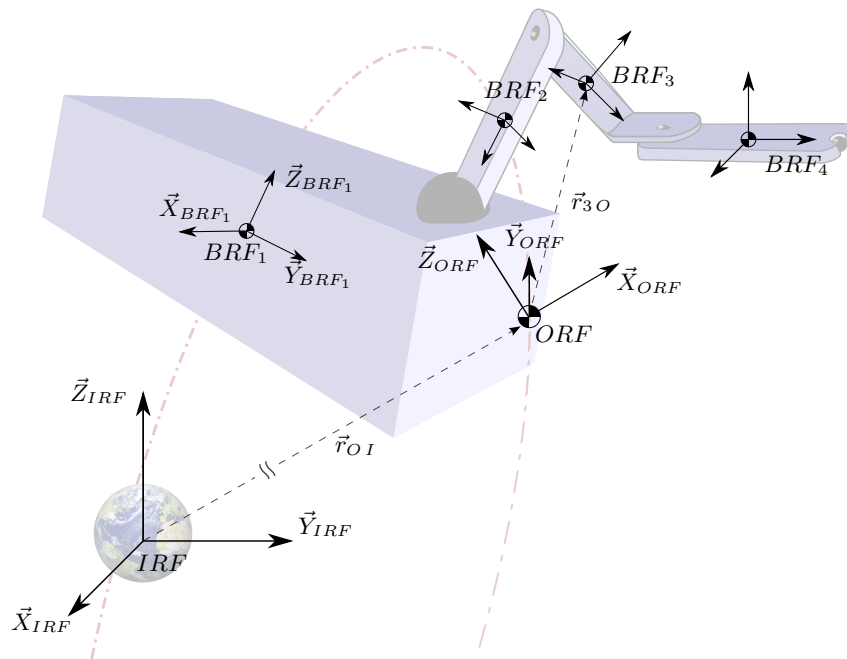
Figure 2.1: Kinematic description of a generic orbiting multi-body system. Note that not all position vectors are shown.

2.2.1 Notation

- If not explicitly stated, each vector is expressed in the IRF coordinates.

- Position, velocity and acceleration vectors of bodies and orbital reference frames will be identified by two subscripts. The first will indicate the element identified by the position vector; the second will indicate what the origin of the vector is. For example: $\vec{r}_{OI}$ is the position vector of the origin of the ORF with respect to the IRF; $\vec{r}_{iO}$ is the position vector of the BRF_i with respect to the ORF.

- Rotation matrices are identified by the symbol $\mathbf{T}$. Subscripts are added to describe the rotation: i.e. the matrix which transforms from reference frame A to B is named $\mathbf{T}_{AB}$.

- Differentiation in time with respect to IRF is written either with $\frac{d}{dt}(\cdot)$ or with $\dot{(\cdot)}$.

- Matrix transposition is indicated with the superscript T, e.g. $\mathbf{T}_{AB}^T$.

- Matrix inversion is indicated with the superscript -1, e.g. $\mathbf{T}_{AB}^{-1}$.

- Inner product between vectors is indicated as $< \cdot, \cdot >$.

- Given a generic vector $\vec{a} \in \mathbb{R}^3 : \vec{a} = \{a_x, a_y, a_z\}$, a skew-symmetric matrix operator is defined as $\hat{\vec{a}} = \begin{bmatrix} 0 & -a_z & a_y \\ a_z & 0 & -a_x \\ -a_y & a_x & 0 \end{bmatrix}$

- Likewise the joints are labelled with numbers, from 1 to $N - 1$. The $i - th$ joint is identified relatively to the two bodies which it connects as follows:

  $\vec{l}_{Li}$ is the vector from the BRF_i to the joint;

  $\vec{r}_{Li}$ is the vector from the joint to the BRF_{i+1}.

2.3 Kinematics

Each rigid body is kinematically identified by a position vector, $\vec{r}_{iI}$, and a rotation matrix, $\mathbf{T}_{iI}$ or either[1] $\mathbf{T}_{Ii} = \mathbf{T}_{iI}^T$. Furthermore, each system configuration in space can be described starting from position and orientation of the ORF relatively to the IRF, i.e. $\vec{r}_{iI} = \vec{r}_{iO} + \vec{r}_{OI}$ and $\mathbf{T}_{iI} = \mathbf{T}_{OI} \mathbf{T}_{iO}$.

Positions

---

[1] Rotation matrices have the property $\mathbf{T}_{AB}^T = \mathbf{T}_{AB}^{-1}$.

By definition, the weighted sum of the body position vectors determines the position of the ORF, described by the vector $\vec{r}_{OI}$:

$$\sum_{i=1}^{N} \vec{r}_{iI}\, m_i = \vec{r}_{OI}\, m \tag{2.1}$$

where m_i is the mass of the $i-th$ body and m is the total mass of the system.

A mass particle of the $i-th$ body is identified using the position of the ORF and that of the respective body reference frame as follows:

$$\vec{r}_{\delta m_i\, I} = \vec{r}_{OI} + \vec{r}_{iO} + \vec{r}_{\delta m_i\, i} \tag{2.2}$$

where $\vec{r}_{\delta m_i\, i} = \mathbf{T}_{iI}\, \vec{r}_{\delta m_i}$.

Constraints

By introducing the assumption that *only revolution joints are used*, the following $N-1$ kinematical constraint equations are defined:

$$\vec{r}_{iI} = \vec{r}_{OI} + \vec{r}_{1O} + \sum_{j=1}^{i-1} L_j \qquad \text{for} \quad 1 < i \leq N \tag{2.3}$$

with $L_j = l_{Lj} + r_{Lj}$.

Reduction of the system

Using the constraint equations together with Eq. (2.1), each BRF_i position can be formulated as a function of the joint vectors as :

$$\vec{r}_{iO} = \mathbf{T}_{OI} \left\{ \sum_{j=1}^{N} \left[\left(\mathbf{T}_{jO}\, \vec{l}_j + \mathbf{T}_{j+1O}\, \vec{r}_j \right) \Psi_{ij} \right] \right\} \tag{2.4}$$

with

$$\Psi_{ij} = \begin{cases} \sum_{k=1}^{j} \frac{m_k}{m} & \text{if } j < i \\ -\sum_{k=j+1}^{N} \frac{m_k}{m} & \text{if } j \geq i \end{cases}$$

Moreover, the vectors $\vec{l}_{Li}$ and $\vec{r}_{Li}$ have been described in each respective body reference frame as $\vec{l}_i$ and $\vec{r}_i$, i.e. $\vec{l}_{Li} = \mathbf{T}_{OI}\,\mathbf{T}_{iO}\,\vec{l}_i$ and $\vec{r}_{Li} = \mathbf{T}_{OI}\,\mathbf{T}_{i+1O}\,\vec{r}_i$. Mathematical details of Eq. (2.4) are reported in the appendix A.

Velocities

Linear velocities of the body position vectors are defined as $\vec{v}_{iI} = \dot{\vec{r}}_{iI}$, $\vec{v}_{OI} = \dot{\vec{r}}_{OI}$ and $\vec{v}_{iO} = \dot{\vec{r}}_{iO}$, with $\vec{v}_{iI} = \vec{v}_{OI} + \vec{v}_{iO}$. Vector $\vec{v}_{iO}$ is derived by differentiating Eq. (2.4) in time:

$$\vec{v}_{iO} = \Omega_{OI}\,\vec{r}_{iO} + \mathbf{T}_{OI}\left\{\sum_{j=1}^{N}\left[\left(\Omega_{jO}\,\mathbf{T}_{jO}\,\vec{l}_j + \Omega_{j+1O}\,\mathbf{T}_{j+1O}\,\vec{r}_j\right)\Psi_{ij}\right]\right\} \qquad (2.5)$$

Note that due to the assumption of rigid bodies $\dot{\vec{l}}_j = \dot{\vec{r}}_j = \vec{0}$. Furthermore, a property of rotation matrices is that $\dot{\mathbf{T}}_{AB} = \Omega_{AB}\mathbf{T}_{AB}$, with $\Omega_{AB} = \hat{\vec{\omega}}_{AB}$ and $\vec{\omega}_{AB}$ the instantaneous angular velocity vector.

By differentiating with respect to time Eq. (2.2), the velocity vector of a mass particle δm_i expressed in the IRF follows:

$$\vec{v}_{\delta m_i\, i} = \vec{v}_{OI} + \vec{v}_{iO} + \Omega_{iI}\mathbf{T}_{iI}\vec{r}_{\delta m_i} \qquad (2.6)$$

Orbital kinematics in spherical coordinates

The orbital position vector can, conveniently, be expressed using spherical coordinates so that $\vec{r}_{OI} = \mathbf{T}_{OI}\vec{r}_0$ with $\vec{r}_0 = \{r_0, 0, 0\}$. Therefore, its velocity is $\vec{v}_{OI} = \Omega_{OI}\mathbf{T}_{OI}\vec{r}_0 + \mathbf{T}_{OI}\dot{\vec{r}}_0$ with $\dot{\vec{r}}_0 = \{\dot{r}_0, 0, 0\}$.

2.4   Dynamics

All the approaches used for modelling the dynamics of multi-body systems in this dissertation are the: *Lagrangian and Hamiltonian formulations* and the *Newton-Euler formulation*. In this section both methods are briefly presented.

2.4.1   Lagrangian and Hamiltonian Formulation

Lagrangian mechanics and Hamiltonian mechanics are well known formulations which use different mathematical representations of the systems, which, ultimately provide two different "points of view" to the understanding of the dynamics and the underlying mathematical structure. Both the Lagrangian and the Hamiltonian functions are combinations of kinetic and potential energy of the problem and, in particular, the Hamiltonian formalism is derived from the Lagrangian function by the application of the Legendre transformation. The dynamic equations are derived from the Lagrangian function using the Euler-Lagrange differential equations or from the Hamiltonian function using Hamilton's equations. For multi-body systems, the total kinetic energy and the total potential energy are obtained by summing the energy contributions of each

body: $\mathcal{L} = \sum_{i=1}^{N} (\mathcal{T}_i - \mathcal{V}_i)$. This section shows the derivation of the kinetic and potential energy for a generic single body of the system. Therefore, the Lagrangian function of an orbiting N-body system is derived.

Kinetic Energy

By definition

$$\mathcal{T}_i = \frac{1}{2} \int_{\mathcal{B}_i} < \vec{v}_{\delta m_i\, I}\, , \, \vec{v}_{\delta m_i\, I} > \, dm_i \tag{2.7}$$

Considering that $\vec{v}_{\delta m_i\, I} = \vec{v}_{i\, I} + \vec{v}_{\delta m_i\, i} = \vec{v}_{i\, I} + \Omega_{i\, I} \vec{r}_{\delta m_i\, i}$, the kinetic energy is split in two terms

$$\mathcal{T}_i = \mathcal{T}_{i\natural} + \mathcal{T}_{i\sharp} \tag{2.8}$$

with

$$\mathcal{T}_{i\natural} = \frac{1}{2} m_i < \vec{v}_{i\, I}\, , \, \vec{v}_{i\, I} > \qquad \mathcal{T}_{i\sharp} = \frac{1}{2}\, \omega_{i\, I}^T \, \mathbf{T}_{i\, I} \, \mathbf{I}_i \, \mathbf{T}_{i\, I}^T \, \omega_{i\, I} \tag{2.9}$$

the inertia tensor $\mathbf{I}_i$ expressed in the BRF_i is:

$$\mathbf{I}_i = \begin{bmatrix} \int_{\mathcal{B}_i} (r_{\delta m_i\, y}^2 + r_{\delta m_i\, z}^2)\, dm_i & 0 & 0 \\ 0 & \int_{\mathcal{B}_i} (r_{\delta m_i\, x}^2 + r_{\delta m_i\, z}^2)\, dm_i & 0 \\ 0 & 0 & \int_{\mathcal{B}_i} (r_{\delta m_i\, x}^2 + r_{\delta m_i\, y}^2)\, dm_i \end{bmatrix}$$

with $\vec{r}_{\delta m_i} = \{ r_{\delta m_i\, x}, r_{\delta m_i\, y}, r_{\delta m_i\, z} \}$.

The mathematical derivation of the kinetic energy in its final form, starting from Eq. (2.7), are given in the appendix A.

Potential Energy

As reported in section 2.1, gravity is the only conservative force considered in this work. Its potential is derived through the following steps:

1. A Taylor series expansion of the gravitational potential for a generic single particle of mass δm_i is performed

2. The potential is integrated over the mass of each body

The series expansion of the gravity potential will be truncated to the second order, the minimum degree of approximation necessary to include gravity gradient torques, see for instance Bong Wie, [54], or Bogoyavlenskil, [55].

Taylor series expansion

For a particle δm_i, part of a body orbiting around the Earth, the gravitational potential is:

$$\delta \mathcal{U} = -\frac{G\,m_\oplus}{|\,\vec{r}_{\delta m_i\,I}\,|}\delta m_i = -\frac{\mu}{|\,\vec{r}_{\delta m_i\,i}\,|}\delta m_i \tag{2.10}$$

Where:

- G is the universal gravitational constant

- $m_\oplus$ is the mass of the Earth

- $\mu = G\,m_\oplus$

Such a potential can be expanded in series with respect to a convenient point in space. Here, the Taylor polynomial will be centered on the ORF position, having assumed that the magnitude orders of the vectors $\vec{r}_{O\,I}$ and $\vec{r}_{\delta m_i\,O}$ are significantly different, i.e. $\|\vec{r}_{O\,I}\| \gg \|\vec{r}_{\delta m_i\,O}\|$. For convenience of notation lets consider the description of the ORF in spherical coordinates, so that $r_0 = \|\vec{r}_{O\,I}\|$. Moreover, the orbital unit vector is defined as $\vec{\gamma}_0 = \frac{\vec{r}_{O\,I}}{r_0}$. The term $\frac{1}{|\vec{r}_{\delta m_i\,I}|}$ is hence approximated as:

$$
\begin{aligned}
\frac{1}{|\,\vec{r}_{\delta m_i\,I}\,|} \approx \frac{1}{r_0} &- \frac{1}{r_0^2}<\vec{\gamma}_0\,,\,\vec{r}_{\delta m_i\,O}> + \frac{1}{r_0^3}\left(\frac{3}{2}<\vec{\gamma}_0\,,\,\vec{r}_{\delta m_i\,O}>^2 + \right.\\
&\left. -\frac{1}{2}<\vec{r}_{\delta m_i\,O}\,,\,\vec{r}_{\delta m_i\,O}>\right) + o\left[\frac{1}{r_0^4}\right]
\end{aligned}
\tag{2.11}
$$

Introducing Eq. (2.11) into Eq. (2.10) and integrating over a single body mass, the $i-th$ body potential function follows as

$$
\begin{aligned}
\mathcal{U}_i = -\mu\frac{m_i}{r_0}&\left[1 - \frac{<\vec{\gamma}_0\,,\,\vec{r}_{iO}>}{r_0} + \frac{1}{2\,r_0^2}\left(3<\vec{\gamma}_0\,,\,\vec{r}_{iO}>^2 - <\vec{r}_{iO}\,,\,\vec{r}_{iO}>\right)\right] + \\
&+ \frac{\mu}{r_0^3}\left(-\int_{\mathcal{B}_i}\|\vec{r}_{\delta m_i}\|^2\,dm_i + \frac{3}{2}<\mathbf{I}_i\,\mathbf{T}_{iO}^T\,\vec{\gamma}\,,\,\mathbf{T}_{iO}^T\,\vec{\gamma}>\right)
\end{aligned}
\tag{2.12}
$$

The complete derivation is provided in appendix A.

Lagrangian Function

From previous results, each body contribution, $\mathcal{L}_i$, to the Lagrangian function, $\mathcal{L} = \sum_{i=1}^{N}\mathcal{L}_i$, is obtained as:

$$
\begin{aligned}
\mathcal{L}_i = &\frac{1}{2}m_i<\vec{v}_{i\,I}\,,\,\vec{v}_{i\,I}> + \frac{1}{2}\,\omega_{iI}^T\,\mathbf{T}_{iI}\,\mathbf{I}_i\,\mathbf{T}_{iI}^T\,\omega_{iI} + \\
&+ \mu\frac{m_i}{r_0}\left[1 - \frac{<\vec{\gamma}_0\,,\,\vec{r}_{iO}>}{r_0} + \frac{1}{2\,r_0^2}\left(3<\vec{\gamma}_0\,,\,\vec{r}_{iO}>^2 - <\vec{r}_{iO}\,,\,\vec{r}_{iO}>\right)\right] + \\
&+ \frac{\mu}{r_0^3}\left(\int_{\mathcal{B}_i}\|\vec{r}_{\delta m_i}\|^2\,dm_i - \frac{3}{2}<\mathbf{I}_i\,\mathbf{T}_{iO}^T\,\vec{\gamma}\,,\,\mathbf{T}_{iO}^T\,\vec{\gamma}>\right)
\end{aligned}
\tag{2.13}
$$

The system Lagrangian can be simplified by recalling that the origin of the ORF is the center of mass of the whole system, i.e. $\sum_{i=1}^{N} m_i \vec{r}_{iO} = \vec{0}$ and $\sum_{i=1}^{N} m_i \vec{v}_{iO} = \vec{0}$, with $\vec{0}$ the null vector. Additionally, it can be further transformed introducing the constraint equations to reduce the system.

This yields:

$$
\begin{aligned}
\mathcal{L} = &\frac{1}{2} m < \vec{v}_{O\,I} \,,\, \vec{v}_{O\,I} > + \sum_{i=1}^{N} \frac{1}{2} \bigg(m_i < \Omega_{O\,I}\, \vec{r}_{iO} \,,\, \Omega_{O\,I}\, \vec{r}_{iO} > + \\
&+ m_i < \vec{v}^{\,*}_{i\,O} \,,\, \vec{v}^{\,*}_{i\,O} > \ + \omega_{i\,I}^T \, \mathbf{T}_{i\,I}\, \mathbf{I}_i\, \mathbf{T}_{i\,I}^T\, \omega_{i\,I} \bigg) + \\
&+ \frac{\mu\, m}{r_0} + \sum_{i=1}^{N} \frac{\mu\, m_i}{2\, r_0^3} \bigg(3 < \vec{\gamma}_0 \,,\, \vec{r}_{iO} >^2 - < \vec{r}_{iO} \,,\, \vec{r}_{iO} > \bigg) + \\
&+ \sum_{i=1}^{N} \frac{\mu}{r_0^3} \left(\int_{\mathcal{B}_i} \|\vec{r}_{\delta m_i}\|^2\, dm_i \ - \frac{3}{2} < \mathbf{I}_i\, \mathbf{T}_{iO}^T\, \vec{\gamma} \,,\, \mathbf{T}_{iO}^T\, \vec{\gamma} > \right)
\end{aligned}
\tag{2.14}
$$

where

$$
\vec{v}^{\,*}_{i\,O} = \mathbf{T}_{O\,I} \left\{ \sum_{j=1}^{N} \left[\left(\Omega_{j\,O}\, \mathbf{T}_{j\,O}\, \vec{l}_j + \Omega_{j+1\,O}\, \mathbf{T}_{j+1\,O}\, \vec{r}_j \right) \Psi_{ij} \right] \right\}
$$

and where the explicit expression of $\vec{r}_{iO}$ is given by Eq. (2.4).

2.4.2 The Newton-Euler formulation

This formulation is based on the dynamic equations of classical mechanics, i.e. Newton's equation of motion and Euler's equations of a rigid body. This formulation can be developed in several different ways and a rich literature is dedicated to it. This section describes the Newton-Euler formulation used in this thesis which was originally used by Gasbarri and Santini, see for instance [52, 56], and recently by Pisculli and Gasbarri, [51].

The differential equation of the translational motion

The Newton equation of motion for the $i-th$ body can be written as:

$$
m_i\, \vec{a}_{i\,I} = \vec{f}_{g\,i} + \vec{f}_{ext\,i} + \vec{f}_{L\,i} - \vec{f}_{L\,i-1}
\tag{2.15}
$$

where: $\vec{a}_{i\,I}$ is the linear acceleration of the BRF_i, $\vec{f}_{g\,i}$ is total the gravity force applied at the body, $\vec{f}_{ext\,i}$ is the sum of all the external forces applied over the body (included the control forces), $\vec{f}_{L\,i}$ and $\vec{f}_{L\,i-1}$ are the reaction forces applied due to the link with

the neighbouring bodies.

From Eq. (2.1), the acceleration of the ORF follows as the sum of the N Newton equations:

$$\sum_{i=1}^{N} m_i \, \vec{a}_{i\,I} = m \, \vec{a}_{O\,I} = \sum_{i=1}^{N} \left(\vec{f}_{g\,i} + \vec{f}_{ext\,i} \right) \tag{2.16}$$

Note that $\sum_{i=1}^{N} \left(\vec{f}_{L\,i} - \vec{f}_{L\,i-1} \right) = 0$ as these are the system's internal forces. The use of Eq. (2.16) allows to distinguish the dynamics of the orbital motion of the system's CM from its translational motion of each BRF relatively to the ORF. These two coupled dynamics have significantly different magnitude orders both in length scale and time scale.

The differential equation of the attitude motion

The Euler's equations describe the body's rotational motion around the body's center of mass:

$$\mathbf{I}_i^I \, \dot{\vec{\omega}}_{i\,I} = -\vec{\omega}_{i\,I} \times \mathbf{I}_i \vec{\omega}_{i\,I} + \vec{t}_{g\,i} + \vec{t}_{ext\,i} + \vec{t}_{L\,i} - \vec{t}_{L\,i-1} \tag{2.17}$$

where: $\mathbf{I}_i^I$ is the inertia matrix expressed in the IRF, $\dot{\vec{\omega}}_{i\,I}$ is the angular acceleration of the BRF_i, $\vec{t}_{g\,i}$ is the gravity gradient torque, $\vec{t}_{ext\,i}$ is the sum of all the external torques applied over the body (included the control torques), $\vec{t}_{L\,i}$ and $\vec{t}_{L\,i-1}$ are torques produced by the reaction forces applied due to the link with the neighbouring bodies, i.e. $\vec{t}_{L\,i} = \vec{l}_{L\,i} \times \vec{f}_{L\,i} = \hat{\vec{l}}_{L\,i} \vec{f}_{L\,i}$ and $\vec{t}_{L\,i-1} = \vec{r}_{L\,i} \times \vec{f}_{L\,i-1} = \hat{\vec{r}}_{L\,i} \vec{f}_{L\,i-1}$. Note that the total angular velocity is the composition of rotational motion of ORF with respect to the IRF and the rotational motion of the body around its center of mass, i.e. $\vec{\omega}_{i\,I} = \vec{\omega}_{O\,I} + \vec{\omega}_{i\,O}$. Using the definition of angular velocity for a point mass, the first term is derived as $\vec{\omega}_{O\,I} = \frac{\vec{r}_{O\,I} \times \vec{v}_{O\,I}}{\|\vec{r}_{O\,I}\|^2}$.

The constraint equations

Constraint equations can be formulated in a new form as:

$$\vec{r}_{i\,O} + \vec{l}_{L\,i} = \vec{r}_{i+1\,O} + \vec{r}_{L\,i} \qquad \text{for} \quad i = 1, ..., N-1 \tag{2.18}$$

with $\vec{l}_{L\,i} = \mathbf{T}_{i\,I}\vec{l}_i$ and $\vec{r}_{L\,i} = \mathbf{T}_{i+1\,I}\vec{r}_i$.

Solving method

In order to integrate the Newton-Euler differential equations of motion, the reaction forces at the joints must be known at every time. To this end, the constraint equations can be used. Together with the definition of the ORF position, given by Eq. (2.1), these are a set of N vectorial equations. By differentiating the set twice in time, this becomes a set of N vectorial equations containing the accelerations, which can hence be introduced in the Newton-Euler differential equations in order to obtain the originally unknown reaction forces at the joints. Differentiating in time Eq. (2.18) gives:

$$\vec{a}_{iO} - \vec{a}_{i+1O} = \hat{\dot{l}}_{Li}\vec{\omega}_{iI} + \hat{\dot{r}}_{Li}\vec{\omega}_{i+1I} + \Omega^2_{i+1I}\vec{r}_{Li} - \Omega^2_{iI}\vec{l}_{Li} \qquad \text{for} \quad i = 1,...,N-1 \quad (2.19)$$

Matrix Form

Adopting a matrix form is convenient to derive the solution and at the same time to keep the notation compact and clear. By defining:

$$\vec{g} = \sum_{i=1}^{N} \vec{f}_{gi} \qquad \vec{g}_i = \vec{f}_{gi} - \vec{g}$$

$$\vec{e} = \sum_{i=1}^{N} \vec{f}_{exti} \qquad \vec{e}_i = \vec{f}_{exti} - \vec{e}$$

the set of Newton-Euler equations is written as:

$$\begin{cases} \mathbf{M}\vec{X} = \vec{G} + \vec{E} + \mathbf{F}\vec{L} \\ m\,\vec{a}_{OI} = \vec{g} + \vec{e} \end{cases} \qquad (2.20)$$

where

$$\vec{X} = \left(\vec{a}_{1O}, \vec{a}_{2O}, \cdots, \vec{a}_{NO}\,,\, \dot{\vec{\omega}}_{1I}, \dot{\vec{\omega}}_{2I}, \cdots, \dot{\vec{\omega}}_{NI} \right)$$
$$\vec{G} = \left(\vec{g}_1, \vec{g}_2, \cdots, \vec{g}_N\,,\, \vec{t}_{g1}, \vec{t}_{g2}, \cdots, \vec{t}_{gN} \right)$$
$$\vec{E} = \left(\vec{e}_1, \vec{e}_2, \cdots, \vec{e}_N\,,\, \vec{t}_{ext1}, \vec{t}_{ext2}, \cdots, \vec{t}_{extN} \right)$$
$$\vec{L} = \left(\vec{f}_{L1}, \vec{f}_{L2}, \cdots, \vec{f}_{LN-1} \right)$$

Note that, in this form, only the translational motion relative to the ORF is described in $\vec{X}$ and, in order to fully describe the problem, Eq. (2.16) has to be taken into account.

Constraints Equations

Constraint equations can be formulated in matrix form as:

$$\mathbf{A}\vec{X} = \vec{\Lambda} \tag{2.21}$$

with

$$\vec{\Lambda} = \left(\Omega_{2\,I}^2 \vec{r}_{L\,1} - \Omega_{1\,I}^2 \vec{l}_{L\,1}, \cdots, \Omega_{N\,I}^2 \vec{r}_{L\,N-1} - \Omega_{N-1\,I}^2 \vec{l}_{L\,N-1} \right)$$

Reaction Forces

Combining equations (2.20) and (2.21), reaction forces are solved as follows:

$$\vec{L} = \left(\mathbf{A}\,\mathbf{M}^{-1}\,\mathbf{F} \right)^{-1} \left[\vec{\Lambda} - \mathbf{A}\,\mathbf{M}^{-1} \left(\vec{G} + \vec{E} \right) \right] \tag{2.22}$$

The full set of the equations of motion

Eq. (2.22) is introduced back into Eq. (2.20) to obtain the set of the second order differential equations of the dynamics:

$$\begin{cases} \mathbf{M}\vec{X} = \vec{G} + \vec{E} + \mathbf{F} \left(\mathbf{A}\,\mathbf{M}^{-1}\,\mathbf{F} \right)^{-1} \left[\vec{\Lambda} - \mathbf{A}\,\mathbf{M}^{-1} \left(\vec{G} + \vec{E} \right) \right] \\ m\,\vec{a}_{O\,I} = \vec{g} + \vec{e} \end{cases} \tag{2.23}$$

This system can be further arranged including $\vec{a}_{O\,I}$ in $\vec{X}$ and manipulating the equation in order to obtain a simpler final form:

$$\tilde{\mathbf{M}}\vec{X} = \vec{G} + \vec{E} + \tilde{\vec{\Lambda}} \tag{2.24}$$

Further details and matrices definitions can be found in the appendix A.

Use of a minimum set of variables

As demonstrated in [57] and [51], the most convenient solution to the integration of orbiting multi-body systems is the use of an Eulerian approach based on the reduced set of configuration variables. This can be obtained introducing eq.s (2.4) and (2.5) into Eq. (2.24). As a result, the form of Eq. (2.24) does not change qualitatively, however the set's size reduces to $3(N + 1)$.

Furthermore, it is worth noting that, depending on the case, rotation matrices $\mathbf{T}_{i\,I}$ and

angular velocity vectors ω_{iI} can alternatively be described as:

$$\begin{cases} \mathbf{T}_{iI} = \mathbf{T}_{OI}\mathbf{T}_{iO} \\ \omega_{iI} = \omega_{OI} + \omega_{iO} \end{cases}$$

or

$$\begin{cases} \mathbf{T}_{1I} = \mathbf{T}_{OI}\mathbf{T}_{1O} \\ \mathbf{T}_{iI} = \mathbf{T}_{OI}\mathbf{T}_{1O}\prod_{j=2}^{i}\mathbf{T}_{j\,j-1} \quad \text{for} \quad i > 1 \end{cases}$$
$$\begin{cases} \omega_{1I} = \omega_{OI} + \omega_{1O} \\ \omega_{iI} = \omega_{OI} + \omega_{1O} + \sum_{j=2}^{i}\omega_{j\,j-1} \quad \text{for} \quad i > 1 \end{cases}$$

The second solution is generally preferred when manipulator systems are considered. In these cases, a convenient configuration variable set is formed by the position vector of the ORF, the position vector of the spacecraft bus and the manipulator's joint angles.

The method conceived by Gasbarri and Santini includes a non-dimensionalisation of the quantities involved in order to contain numerical errors due to the different length scales of the orbital and attitude dynamics.

2.5 Conclusions

The choice of using either the Lagrangian approach or the Newton-Euler depends on the application and on the type of analysis that will be undertaken to study the motion. In general, the first approach is preferred when the qualitative nature of the problem is under investigation or when the dynamical study is focussed on the control design. This formulation allows one to gain a deep insight into the nonlinear behaviour of the system, and, to reveal the structure of the system's dynamics. Furthermore, it is quite convenient to use the Lagrangian approach for problems with a limited number of configuration variables and with a fixed architecture, e.g. problems where no bodies are added or removed during the manoeuvre considered. On the contrary, the Newton-Euler approach is particularly appropriate for numerical simulations and for the physical understanding of the problems. Moreover, it is a convenient choice when the computation of reaction forces and torques is desired and when manoeuvres with a variable number of bodies are considered, e.g. when objects are grasped by a space manipulator. For multi-body systems in general, according to Siciliano, [12], the Lagrangian formulation has the advantage of being a *systematic* methodology and of *immediate comprehension*, describing the problem in an *analytical form*. On the other hand, the Newton-Euler formulation is synthetically described as a *recursive method*

that is computationally efficient. Santini and Gasbarri compared the two formulations specifically for orbiting multi-body systems in [57]. They concluded that, although the Lagrangian formulation is *conceptually very simple*, its derivation is extremely heavy, thus prone to programming errors and not flexible from a computational point of view[2]. Moreover, they state that the differential equations of the Eulerian approach *describe equivalent motions* to the Lagrangian but these equations are *more clear from a physical point of view* and *algebraically not too heavy.* Table 2.1 provides a summarised comparison of the two methodologies:

Lagrangian	Newton-Euler
Analytical Formulation	Compact Matrix Formulation
Convenient for the investigation of the mathematical structure of the dynamics	Convenient for numerical simulations
Convenient for control design	Better physical understanding of the problem provided
Based on a minimal set of configuration variables	Reaction forces and torques provided
Dynamics relatively easy to derive for low-dimensional systems	Dynamics relatively easy to derive

Table 2.1: A schematic overview of the advantages of the Lagrangian formulation and of the Newton-Euler formulation.

---

[2]When the configuration variable set is changed, e.g. due to a grasped object, the dynamics has to be completely derived again.

The Single Asymmetric Rigid Body

When all the joints of an orbiting multi-body system are locked, this behaves like an asymmetric rigid body, i.e. $N = 1$. A spacecraft in orbit around the Earth is subject to external forces such as gravity gradient torque, air drag, solar radiation pressure and electro-magnetic forces. For the attitude dynamics, the weakness of the corresponding torques means that the force-free case provides a good approximation of the dynamical behaviour in the short to medium term, i.e. over seconds or minutes depending on the orbit. Under these assumptions the problem is integrable, as mechanical energy and angular momentum are conserved quantities. Furthermore, a closed form analytical solution can be derived. The analytical solutions are shown to be useful for planning and designing large slew manoeuvres. The equations of the attitude dynamics of a rigid body were first formulated by Euler in *Memoires de Berlin, Annee* 1758 and the solution, in terms of angular velocities, first suggested by Rueb (Utrecht, 1834) and later completed by Jacobi in *Journal fur Math, xxxix* (1849), p. 293., [41]. The complete solution was obtained using Jacobi elliptic functions and theta functions [40] - [43]. However, its final form is too complex to be used for on-board applications as implies the calculation of a number of complex infinite series, see [44]. In [39] the solution was derived in terms of Euler angles, which unfortunately do not provide a complete coverage of the rotation matrixes' space, SO(3) (the Lie group of Special Orthogonal matrixes[1]), as it suffers from singularities originated by the use of inverse trigonometric functions. This problem of classical mechanics has been revisited in this thesis to reformulate the well-known solution in a form different from existing ones,

---

[1]An element of SO(3) is a 3×3 matrix with determinant equal to 1 which multiplied by its transposed return the identity matrix.

which would be more appropriate for aerospace applications as they are derived in quaternion form or in rotation matrix form.

In particular, the chapter derives the analytical solution equations in quaternions and rotation matrix form using the general Lax Pair integration for Hamiltonian systems on the Lie group SO(3) [58] adapted to SU(2), i.e. the Special Unitary group SU(2) - the the Lie group of 2×2 unitary matrices with determinant 1 -, and specialised to the equations of the Hamiltonian of the asymmetric rigid body. Additionally, it remarks implementation issues throughout the sections to make this work accessible to practical applications as, for instance, for reference trajectory generation. To this end, a large spacecraft repointing demonstrative manoeuvre is provided.
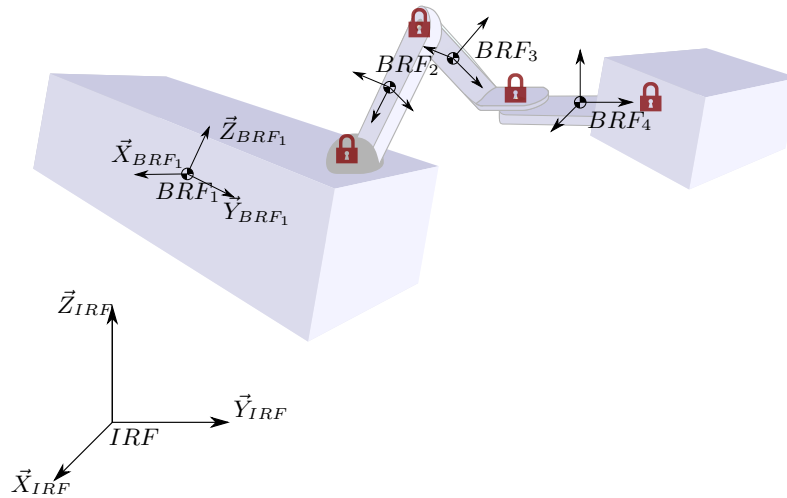
Figure 3.1: A multi-body system, with locked joints, is modeled as a single asymmetric rigid body.

Part of the results of this chapter have been published together with Dr. Craig Maclean[2] in:

- Maclean, C. D., Pagnozzi, D., Biggs, J.D., *Planning natural repointing manoeuvres for nano-spacecraft*, IEEE Transactions on Aerospace and Electronic Systems, 2014, Vol. 50, No. 3, 07.2014, p. 2129-2145

- Maclean, C. D., Pagnozzi, D., Biggs, J.D., *Computationally light attitude controls for resource limited nano-spacecraft*, 62nd International Astronautical Congress 2011, September 2011

In particular, the contribution of the author of this thesis was in the derivation of the closed-form solution for the asymmetric rigid body, both in quaternions and in rotation matrix forms and in the implementation of the solution in the software used[3].

---

[2]Department of Mechanical and Aerospace Engineering, University of Strathclyde, Glasgow
[3]Wolfram Mathematica and MathWorks Matlab

In addition, the work presented in the cited papers was extended to include the analysis of the singularities contained in the quaternions solution and an open-loop control strategy for a spacecraft in low-Earth orbit.

3.1   Mathematical representation of free rigid body motions in SU(2)

In order to study the motion of a rigid body, it is first necessary to choose an appropriate way to describe it. In particular, there are many possible manners to represent the attitude position around the center of mass, and, each one has advantages and drawbacks. Table 3.1, from [59], shows attitude representations and their properties. Often sets of three or four parameters are used, e.g. Euler angles or quaternions. However, none of these parametrisations is both unique and global. For instance, Euler angles suffer from gimbal lock as singularities occur in their time derivatives; quaternions are not unique as an attitude position can be described by two antipodal sets. According to Chaturvedi et al., [59], these representations *"fail"* as they lie in spaces which are not the same of a rigid-body attitude motion, e.g. Euclidean $\mathbb{R}^3$ for Euler angles and the three-sphere $\mathbb{S}^3$ for the quaternions. It is possible to refer to [54, 60, 61, 62] for more details. Referring to Table 3.1, in order to obtain an attitude kinematical description both global and unique, a rotation matrix $\mathbf{R}(t)$, element of the Special Orthogonal Group SO(3), [63, 64], has to be used. Novel spacecraft attitude controls are based on rotation matrixes, see [59], however, despite their limitations, quaternions are typically used in aerospace as they provide a global representation with a minimum set of parameters, have no inherent geometrical singularity, successive rotations follow the quaternion multiplication rules and, finally, are well suited for on-board real-time computation since only products and no trigonometric relations exist in the quaternion equations, [65].

Attitude Representation	Global	Unique
Euler angles	No	No
Rodrigues parameters	No	No
Modified Rodrigues paramters	No	No
Quaternions - SU(2)	Yes	No
Axis-angle	Yes	No
Rotation matrix - SO(3)	Yes	Yes

Table 3.1: Attitude Representations and their properties, from Chaturvedi et al..

As quaternions are isomorphic to the Special Unitary Group[4] SU(2), [32], it is conve-

---

[4]SU(2) $\subset$ U(n) $\subset$ GL(n). GL(n) is the group of all invertible matrixes.

nient to describe the attitude motion using

$$R(t) = \begin{pmatrix} z_1 & z_2 \\ -\bar{z}_2 & \bar{z}_1 \end{pmatrix} \qquad \text{with} \quad R(t) \in \text{SU}(2) \tag{3.1}$$

with $z_1, z_2 \in \mathbb{C}$ and $\bar{z}_1, \bar{z}_2$ their complex conjugates such that $|z_1|^2 + |z_2|^2 = 1$. The main reason to consider SU(2) as the configuration space, is that it is possible to express the equations of motion in a convenient Lax pair form, whose general solution is known. The mapping F from SU(2) to the unit quaternions $\mathbf{Q}$ is a simple one: $F : SU(2) \leftrightarrow \mathbf{Q}$:

$$F : \begin{pmatrix} z_1 & z_2 \\ -\bar{z}_2 & \bar{z}_1 \end{pmatrix} \leftrightarrow z_1 + z_2\mathbf{j} = q_0\mathbf{e} + q_1\mathbf{i} + q_2\mathbf{j} + q_3\mathbf{k} \tag{3.2}$$

where the complex numbers $z_1 = q_0 + i\,q_1$, $z_2 = q_2 + i\,q_3$ are regarded in their quaternion form $z_1 = q_0\mathbf{e} + q_1\mathbf{i}$, $z_2 = q_2\mathbf{e} + q_3\mathbf{i}$.

It seems that it was Klein [66] who discovered that for the symmetric Lagrange and toy top (a symmetric rigid body in a constant gravitational field) simpler solutions can be obtained when SU(2) is used as configuration space rather than SO(3). Furthermore, a integration of the toy top which uses the setting of Lagrangian mechanics on the Lie group SU(2) was used to find the solution in terms of hyperelliptic functions, [67].

3.2 The equations of motion

3.2.1 Kinematics

Kinematic equations are expressed in the special unitary group, [68], as:

$$\frac{dR(t)}{dt} = R(t)(\omega_1 A_1 + \omega_2 A_2 + \omega_3 A_3) \tag{3.3}$$

where $\vec{\omega} = (\omega_1, \omega_2, \omega_3)$ is the angular velocity vector in body fixed coordinates and A_1, A_2, A_3 describe the infinitesimal motion of the spacecraft in the roll, pitch and yaw directions respectively. In other terms, they form a basis for the Lie algebra $\mathfrak{su}(2)$ of the Lie group SU(2):

$$A_1 = \frac{1}{2}\begin{pmatrix} i & 0 \\ 0 & -i \end{pmatrix}, A_2 = \frac{1}{2}\begin{pmatrix} 0 & 1 \\ -1 & 0 \end{pmatrix}, A_3 = \frac{1}{2}\begin{pmatrix} 0 & i \\ i & 0 \end{pmatrix}. \tag{3.4}$$

with its commutator defined by $[X, Y] = XY - YX$ called the Lie bracket such that $[A_1, A_2] = A_3$, $[A_2, A_3] = A_1$ and $[A_1, A_3] = -A_2$. Note the $\frac{1}{2}$ in the basis is introduced so that the commutative relation of the Lie bracket corresponds to the cross product in $\mathbb{R}^3$.

3.2.2   Dynamics

The attitude dynamics of a free rigid spacecraft is described by the Euler equations:

$$\mathbf{I}\dot{\vec{\omega}}(t) = \mathbf{I}\vec{\omega} \times \vec{\omega} \tag{3.5}$$

with $\mathbf{I}$ the inertia tensor expressed in the BRF:

$$\mathbf{I} = \begin{bmatrix} \mathbf{I}_1 & 0 & 0 \\ 0 & \mathbf{I}_2 & 0 \\ 0 & 0 & \mathbf{I}_3 \end{bmatrix}$$

It is easily shown that the kinetic energy of the system and the magnitude of the total angular momentum are conserved quantities:

$$\begin{aligned}
\mathcal{T} &= \frac{1}{2} \left[\, \mathbf{I}_1\,\omega_1^2(t) + \mathbf{I}_2\,\omega_2^2(t) + \mathbf{I}_3\,\omega_3^2(t) \,\right] \\
\mathbf{L}^2 &= \mathbf{I}_1^2\,\omega_1^2(t) + \mathbf{I}_2^2\,\omega_2^2(t) + \mathbf{I}_3^2\,\omega_3^2(t)
\end{aligned} \tag{3.6}$$

with $\mathbf{L} = \|\vec{L}\| \,:\, \vec{L} = \mathbf{I}\,\vec{\omega}(t)$. In $\mathfrak{su}(2)$, angular momentum vector and angular velocity vector are defined as:

$$\begin{aligned}
L(t) &= \mathbf{I}_1\,\omega_1(t)A_1 + \mathbf{I}_2\,\omega_2(t)A_2 + \mathbf{I}_3\,\omega_3(t)A_3 \\
\Omega(t) &= \omega_1(t)A_1 + \omega_2(t)A_2 + \omega_3(t)A_3
\end{aligned} \tag{3.7}$$

The variation in time of $L(t)$ can be derived in two equivalent ways. First as:

$$\frac{dL(t)}{dt} = \mathbf{I}_1\,\dot{\omega}_1(t)A_1 + \mathbf{I}_2\,\dot{\omega}_2(t)A_2 + \mathbf{I}_3\,\dot{\omega}_3(t)A_3$$

where the the angular velocity variations in time are calculated by means of the Euler equation (3.5). Alternatively, in $\mathfrak{su}(2)$, by using the Lie brackets:

$$\frac{dL(t)}{dt} = [L(t), \Omega(t)] \tag{3.8}$$

In particular, the latter form, Eq. (3.8), is convenient as it is known as a Lax's equation. In consequence, $L(t)$ and $\Omega(t)$ constitute a Lax Pair on SU(2), [58, 69, 70]. As the angular momentum vector is constant in magnitude and in direction, in an inertial reference frame, the eigenvalues of $L(t)$ are independent of t. Holding this condition, a solution of Eq. (3.8) exists, see [71], and it was first formulated by Lax in 1968 during the study of the Kortewegde Vries equation of waves. Furthermore, in its general form,

the solution is:

$$L(t) = U(t) \, L(t_0) \, U(t)^{-1} \tag{3.9}$$

where $L(t_0)$ is the value of $L(t)$ for a desired time instant and $U(t)$ is a family of unitary operators that satisfies the following identity:

$$\frac{dU(t)}{dt} = U(t) \, \Omega(t) \tag{3.10}$$

As Eq. (3.10) is equivalent to Eq. (3.3), and, rotation matrices form a unitary operator, it is chosen $U(t) = R(t)$. Therefore, the final solution of the Lax's equation of the angular momentum is

$$L(t) = R(t)^{-1} \, L(t_0) \, R(t) \tag{3.11}$$

Regarding this specific case, the physical meaning of the Lax equation's solution can be stated, roughly speaking, in these words: as the angular momentum vector is constant in direction and magnitude in the IRF, the instantaneous rotation matrix, solution of the equations of motion, is the one that transforms the actual angular momentum vector, in body coordinates, to the one in inertial coordinates, defined at desired time instant.

3.3   Angular velocities' solution

The solution of the Euler equations of the free asymmetric rigid-body is known. Excluding single axis rotations, where it is trivial, a closed form expression is analytically derived by means of Jacobi elliptic functions, see [32] and [72]:

Lemma 1 *When the initial angular velocity vector has at most one null component, the angular velocities ω_i, for a free asymmetric rigid body, i.e. $I_i \neq I_j \neq I_k$, can be expressed in the analytic form:*

$$\omega_i(t) = \zeta_i \, sn \left(\xi_i \, t + \gamma_i \, , \, \mu_i \right) \tag{3.12}$$

All parameters depend on the body's mass properties and on the initial angular velocities. Constants are defined as follows:

$$
\begin{aligned}
\zeta_i &= \frac{\sqrt{s_i}}{\mathbf{I}_i}; \\
\xi_i &= \pm \sqrt{\alpha_i \, s_j}; \\
\gamma_i &= sn^{-1} \left(\frac{\mathbf{I}_i \, \omega_i(0)}{\sqrt{s_i}}, \mu_i \right); \\
\mu_i &= \frac{s_i}{s_j};
\end{aligned}
\tag{3.13}
$$

where

$$\alpha_i = -\frac{(\mathbf{I}_i - \mathbf{I}_j)(\mathbf{I}_i - \mathbf{I}_k)}{\mathbf{I}_j\,\mathbf{I}_k}$$

$$\beta_i = \frac{4\,\mathbf{I}_j\,\mathbf{I}_k\,\mathcal{T} - 2\mathbf{I}_i\,(\mathbf{I}_j + \mathbf{I}_k)\,\mathcal{T} + 2\mathbf{I}_i\,\mathbf{L}^2 - (\mathbf{I}_j + \mathbf{I}_k)\,\mathbf{L}^2}{\mathbf{I}_i\,\mathbf{I}_j\,\mathbf{I}_k}$$

$$\chi_i = -\frac{\left(2\mathbf{I}_j\,\mathcal{T} - \mathbf{L}^2\right)\left(2\mathbf{I}_k\,\mathcal{T} - \mathbf{L}^2\right)}{\mathbf{I}_i^2\,\mathbf{I}_j\,\mathbf{I}_k} \qquad (3.14)$$

$$s_i = \frac{-\beta_i + \sqrt{\beta_i^2 - 4\alpha_i\,\chi_i}}{2\alpha_i}$$

$$s_j = \frac{-\beta_i - \sqrt{\beta_i^2 - 4\alpha_i\,\chi_i}}{2\alpha_i}$$

Indexes do not represent a sum; conversely i, j and k follow a "circular notation", which means they appear in a consecutive recursion (e.g. i=2,j=3,k=1). Conserved quantities $\mathcal{T}$ and $\mathbf{L}$ are defined by the initial conditions:

$$\mathcal{T} = \frac{1}{2}\left(\mathbf{I}_1\omega_1^2(0) + \mathbf{I}_2\omega_2^2(0) + \mathbf{I}_3\omega_3^2(0)\right)$$

$$\mathbf{L}^2 = \mathbf{I}_1^2\omega_1^2(0) + \mathbf{I}_2^2\omega_2^2(0) + \mathbf{I}_3^2\omega_3^2(0) \qquad (3.15)$$

Proof can be found in [63].

Lemma 2 *When two components of the angular velocity vector are null in the initial conditions, the former expression is singular and the kinematical solution reduces to the trivial case:*

$$\begin{cases} \omega_i(0) = 0 \\ \omega_j(0) = 0 \\ \omega_k(0) = \omega_0 \end{cases} \Rightarrow \begin{cases} \omega_i(t) = 0 \\ \omega_j(t) = 0 \\ \omega_k(t) = \omega_0 \end{cases}$$

Remark 1 $sn(z\,,\,m) = \sin\left(am(z\,,\,m)\right)$ *is the Jacobi elliptic sine function, which is defined over the complex domain[5]: $\{z,m\} \in \mathbb{C}^2$. Furthermore, note that the domain of an inverse elliptic function is $\mathbb{C}^2$ as well. Refer to [44] for further details.*

Remark 2 *The sign of ξ_i in Eq. (3.13) is dependent on the initial conditions. In particular, it has to be set by comparing the first derivative of $\omega_i(t)$ from Eq. (3.12) with the first derivative at the initial time from the Euler equations, Eq. (3.5):*

$$\frac{d}{dt}\omega_i(0) = \xi_i\zeta_i\,dn\left(\gamma_i\,,\,\mu_i\right)cn\left(\gamma_i\,,\,\mu_i\right)$$

$$\frac{d}{dt}\omega_i(0) = \delta_i\,\omega_l(0)\,\omega_k(0) \qquad (3.16)$$

---

[5]The modulus m should be defined over a limited real domain $m \in (0,1)$, however there exist a number of transformations which can be applied to extend the domain. For instance, if $\|m\| > 1$ the following identity can be used $\sqrt{m}\,sn(z,m) = sn(\sqrt{m}\,z, m^{-1})$

with $\delta_1 = \frac{\mathbf{I}_2 - \mathbf{I}_3}{\mathbf{I}_1}$, $\delta_2 = \frac{\mathbf{I}_3 - \mathbf{I}_1}{\mathbf{I}_2}$, $\delta_3 = \frac{\mathbf{I}_1 - \mathbf{I}_2}{\mathbf{I}_3}$. It results:

$$sign(\xi_i) = \frac{\sqrt{\alpha_i \, s_j} \; \zeta_i \, dn \, (\gamma_i \, , \, \mu_i) \, cn \, (\gamma_i \, , \, \mu_i)}{\delta_i \, \omega_l(0) \, \omega_k(0)} \tag{3.17}$$

Remark 3 *In order to avoid singularities, the following conditions have to be satisfied:*

$$\begin{aligned} \alpha_i \neq 0 \quad &\Leftrightarrow \quad & \mathbf{I}_i \neq \mathbf{I}_j \neq \mathbf{I}_k \\ s_i \neq 0 \quad &\Leftrightarrow \quad & \omega_i(0) \neq 0 \wedge \omega_j(0) \neq 0 \\ s_j \neq 0 \quad &\Leftrightarrow \quad & \omega_i(0) \neq 0 \wedge \omega_k(0) \neq 0 \end{aligned} \tag{3.18}$$

In particular, the first condition is not satisfied when symmetric bodies are considered. For the solution of the symmetric case refer to [48]. The last two conditions are not satisfied in the trivial case of single axis rotation.

3.4 Solution in quaternion form

The main novel content of this chapter is the closed-form solution of the free motion of an asymmetric rigid body, expressed in quaternion form and rotation matrix form, and, additionally, without the use of any inverse trigonometric function or theta function. Results are stated as a theorem:

Theorem 1 *Given a quaternion set $\vec{q}(t) = \{q_0(t)\,, q_1(t)\,, q_2(t)\,, q_3(t)\}^T$, natural motions of a free asymmetric rigid body, with $\mathbf{I}_3 > \mathbf{I}_2 > \mathbf{I}_1$, can be described as:*

$$\vec{q}(t) = \tilde{Q}_0 \, \vec{\tilde{q}}(t) \tag{3.19}$$

By definition, see [54], the rotation matrix, element of SO(3), relative to $\vec{q}(t)$ is:

$$\mathbf{R}(t) = \begin{bmatrix} 1 - 2(q_2^2 + q_3^2) & 2(q_1 \, q_2 + q_3 \, q_0) & 2(q_1 \, q_3 - q_2 \, q_0) \\ 2(q_1 \, q_2 - q_3 \, q_0) & 1 - 2(q_1^2 + q_3^2) & 2(q_3 \, q_2 + q_1 \, q_0) \\ 2(q_3 \, q_1 + q_2 \, q_0) & 2(q_3 \, q_2 - q_1 \, q_0) & 1 - 2(q_1^2 + q_2^2) \end{bmatrix} \tag{3.20}$$

where the dependency on time of the quaternions has been omitted for clarity. In detail, excluding single axis rotations:

$$\vec{\tilde{q}}(t) = \{\tilde{q}_0(t)\,,\, \tilde{q}_1(t)\,,\, \tilde{q}_2(t)\,,\, \tilde{q}_3(t)\}^T$$

$$\tilde{q}_0(t) = \mathcal{F}_1(t)\, \left[\cos(\frac{\varphi_1(t)}{2})\,\mathcal{F}_3(t) - \sin(\frac{\varphi_1(t)}{2})\,\mathcal{F}_4(t)\right]$$

$$\tilde{q}_1(t) = \mathcal{F}_1(t)\, \left[\sin(\frac{\varphi_1(t)}{2})\,\mathcal{F}_3(t) + \cos(\frac{\varphi_1(t)}{2})\,\mathcal{F}_4(t)\right] \tag{3.21}$$

$$\tilde{q}_2(t) = \mathcal{F}_2(t)\, \left[\cos(\frac{\varphi_1(t)}{2})\,\mathcal{F}_3(t) + \sin(\frac{\varphi_1(t)}{2})\,\mathcal{F}_4(t)\right]$$

$$\tilde{q}_3(t) = \mathcal{F}_2(t)\, \left[\sin(\frac{\varphi_1(t)}{2})\,\mathcal{F}_3(t) - \cos(\frac{\varphi_1(t)}{2})\,\mathcal{F}_4(t)\right]$$

and

$$\tilde{Q}_0 = \begin{bmatrix} \tilde{q}_0(0) & \tilde{q}_1(0) & \tilde{q}_2(0) & \tilde{q}_3(0) \\ -\tilde{q}_1(0) & \tilde{q}_0(0) & \tilde{q}_3(0) & -\tilde{q}_2(0) \\ -\tilde{q}_2(0) & -\tilde{q}_3(0) & \tilde{q}_0(0) & \tilde{q}_1(0) \\ -\tilde{q}_3(0) & \tilde{q}_2(0) & -\tilde{q}_1(0) & \tilde{q}_0(0) \end{bmatrix} \tag{3.22}$$

The angle $\varphi_1(t)$ is defined as:

$$n = \left(\frac{\mathbf{I}_1\zeta_1}{L}\right)^2\,;$$

$$\theta = am\,(\xi_1\,t + \gamma_1, \mu_1)\,; \tag{3.23}$$

$$\varphi_1(t) = \frac{L}{\mathbf{I}_1}t - \frac{(L^2 - 2\mathbf{I}_1T)}{L\,\mathbf{I}_1\,\xi_1}\Pi\,(n, \theta, \mu_1) + \varphi_0\,;$$

where φ_0 is the integration constant and all the other quantities are defined in Lemma 1. Functions $\mathcal{F}_1(t)$ and $\mathcal{F}_2(t)$ are defined as follows:

$$x(t) = \frac{\mathbf{I}_1}{L}\,\omega_1(t)$$

$$\mathcal{F}_1(t) = \mathcal{S}_1\sqrt{\frac{1 + x(t)}{2}} \tag{3.24}$$

$$\mathcal{F}_2(t) = \mathcal{S}_2\sqrt{\frac{1 - x(t)}{2}}$$

Functions $\mathcal{F}_3(t)$ and $\mathcal{F}_4(t)$ are defined in two equivalent formulations:

$$y_1(t) = \frac{\mathbf{I}_2\omega_2(t)}{\mathbf{I}_3\omega_3(t) + \sqrt{L^2 - \mathbf{I}_1^2\omega_1(t)^2}}$$

$$\mathcal{F}_3(t) = \mathcal{S}_3\frac{1}{\sqrt{1 + y_1(t)^2}}$$

$$\mathcal{F}_4(t) = \mathcal{S}_4\frac{y_1(t)}{\sqrt{1 + y_1(t)^2}}$$

or (3.25)

$$y_2(t) = \frac{1}{y_1(t)}$$

$$\mathcal{F}_3(t) = \mathcal{S}_3\frac{y_2(t)}{\sqrt{1 + y_2(t)^2}}$$

$$\mathcal{F}_4(t) = \mathcal{S}_4\frac{1}{\sqrt{1 + y_2(t)^2}}$$

where the $\mathcal{S}_i$ functions are sign functions: $\mathcal{S}_i = \pm1$.

Remark 4 *These $\mathcal{S}_i$ functions do not depend on time and, to implement the equations, signs are set by direct comparison with the first derivative of the quaternions at the initial time, known by the initial conditions. Furthermore, excluding all qualitatively equivalent combinations, it is enough to consider only two of them. By choosing $\mathcal{S}_1 = 1$, $\mathcal{S}_4 = 1$, when the first formulation of $\mathcal{F}_3(t)$ and $\mathcal{F}_4(t)$ is used, it results in:*

$$\mathcal{S}_3 = \begin{cases} \frac{(1+y_1(0)^2)\,(\omega_1(0)-x(0)\,\dot{\varphi}_1(0))}{2\,\dot{y}_1(0)} & If \quad \|\omega_1(0)\| > 0 \\[2em] \frac{2\,\ddot{y}_1(0)\,L^4}{(1+y_1(0)^2)\,(L^2-2\,\mathbf{I}_1\,T)\,L^2\,\ddot{\omega}_1(0)} & Otherwise \end{cases}$$

(3.26)

$$\mathcal{S}_2 = \frac{\omega_3(0)\,\sqrt{1 - x(0)^2}\,(1 + y_1(0)^2)}{2\,\mathcal{S}_3\,\dot{x}(0)\,y_1(0) + (x(0)^2 - 1)\,(y_1(0)^2 - 1)\,\dot{\varphi}_1(0)}$$

In the other case:

$$
\mathcal{S}_3 = \begin{cases} -\dfrac{2\,\dot{y}_2(0)}{(\,\omega_1(0)-x(0)\dot{\varphi}_1(0)\,)\,(\,1+y_2(0)^2\,)} & \text{If} \quad \|\omega_1(0)\| > 0 \\[4mm] -\dfrac{2\,L^2\,\ddot{y}_2(0)}{(L^2 - 2\,\mathbf{I}_1\,T)\,\omega_2(0)\,\omega_3(0)\,(\,1+y_2(0)^2\,)\delta_1} & \text{Otherwise} \end{cases}
\tag{3.27}
$$

$$
\mathcal{S}_2 = -\frac{\omega_2(0)\,\sqrt{1-x(0)^2}\,(\,1+y_2(0)^2\,)}{\dot{x}(0)\,(\,-1+y_2(0)^2\,) + 2\,\mathcal{S}_3\,(\,-1+x(0)^2\,)\,y_2(0)\,\dot{\varphi}_1(0)}
$$

Remark 5 *An attitude configuration is described by two antipodal sets of quaternions, which are totally equivalent. In general, the solution proposed here describes the motion by means of both these sets, depending on the kinematic state. This implies that, at specific time instants, jump discontinuities will arise in the motion described in the quaternions'space. Note that such discontinuities only exist in this space and do not exist in the rotation matrixes' space. Jump discontinuities of the quaternion solution are caused by singularities in the $\mathcal{F}(t)$ functions, which will take places at zero crossings of either ω_2 or ω_3. The occurrence of these events can be foreseen by the initial conditions, therefore, a condition on the formulation to be preferred, i.e. if using $y_1(t)$ or $y_2(t)$ in eq.(3.25), can be derived. In particular, by denoting*

$$
\begin{cases} \lambda = \dfrac{2\,\mathbf{I}_3\,T - L^2}{\mathbf{I}_3 - \mathbf{I}_1} \\[4mm] \rho = \dfrac{L^2 - 2\,\mathbf{I}_2\,T}{\mathbf{I}_2 - \mathbf{I}_1} \end{cases}
\tag{3.28}
$$

the first formulation of $\mathcal{F}_3(t)$ and $\mathcal{F}_4(t)$ should be preferred when initial conditions determine

$$
\lambda > \rho > 0 \quad \vee \quad (\rho > \lambda > 0 \quad \wedge \quad \omega_3(0) > 0)
\tag{3.29}
$$

The second formulation should be preferred at

$$
\rho > \lambda > 0 \quad \wedge \quad \omega_3(0) < 0
\tag{3.30}
$$

Remark 6 *As resulting from equations (3.19 - 3.27), $\mathbf{R}(t)$ is a smooth and continuous function of time for all possible initial conditions. Conversely, because of the dual nature of quaternions[6], $\vec{q}(t)$ can not be a continuous function for all cases. In particular, when $\lambda < 0$ or $\rho < 0$, both the antipodal equivalent sets of quaternions are part of the solution and, therefore, jump discontinuities appear. Figure 3.2 is an example of the closed form solution when such conditions are satisfied.*

Remark 7 *The assumption made on the body's mass properties, $\mathbf{I}_3 > \mathbf{I}_2 > \mathbf{I}_1$, does*

---

[6]i.e. an attitude position is described by a unique rotation matrix or by two equivalent set of quaternions.
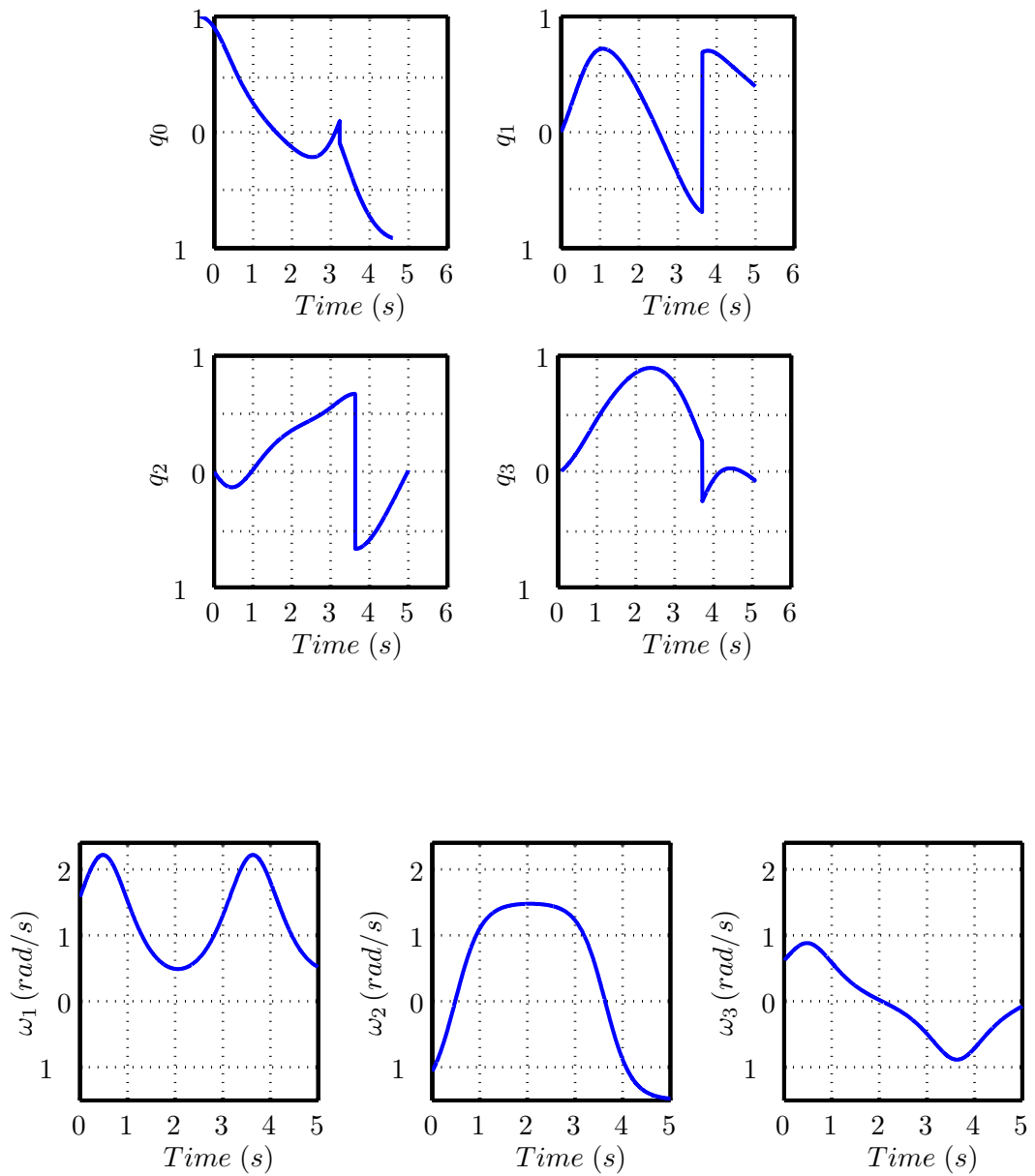
Figure 3.2: Example of closed form solution. The case shown is for $\lambda < 0$. Only when $\lambda < 0$ or $\rho < 0$, the analytical solution in quaternions form includes jump discontinuities. For all the other cases quaternions are continuous functions. Conversely, the elements of the relative rotation matrix are *always* continuous functions.

not imply a loss of generality.

Remark 8 $\Pi(n, \theta, \mu_1)$ *is the incomplete elliptic integral of the third kind, which is defined over* $\mathbb{C}^3$. *Refer to [44] for further details.*

Remark 9 *The solution of the trivial case* $\omega_i(t) = 0$, $\omega_j(t) = 0$, $\omega_k(t) = \omega_0$ *is well known:*

$$q_0 = \cos(\tfrac{\varphi_k(t)}{2})$$
$$q_i = 0$$
$$q_j = 0 \qquad\qquad with \qquad \varphi_k(t) = \omega_0 \, t$$
$$q_k = \sin(\tfrac{\varphi_k(t)}{2})$$

Figure 3.3 illustrates the method used for the integration of the kinematics.
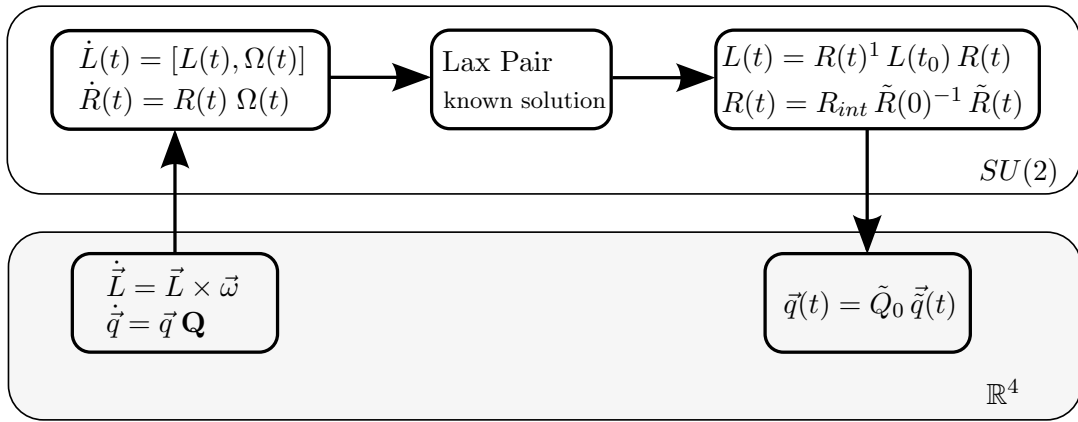
Figure 3.3: Integration scheme describing how the kinematical solution has been obtained.

Proof of Theorem 1.

From equation (3.11):

$$R(t)L(t)R(t)^{-1} = L(0) \tag{3.31}$$

where $L(0)$ is a matrix of constant entries and $R(t)L(t)R(t)^{-1}$ describes the conjugacy class of $L(t)$. Therefore a particular solution $\tilde{R}(t)$ can be conveniently chosen such that at the initial time $\tilde{R}(0)L(t)\tilde{R}(0)^{-1} = \mathbf{L}A_1$. Therefore, it suffices to integrate the particular solution:

$$L(t) = \mathbf{L}\tilde{R}(t)^{-1} A_1 \, \tilde{R}(t) \tag{3.32}$$

where $\mathbf{L}$ is the constant defined in (3.6). Furthermore, as $\exp(\varphi_1(t)A_1)$ is a stabiliser of A_1, and, $\exp(\varphi_2(t)A_2)$ a stabiliser of A_2, it is convenient to introduce the coordinate form [58]:

$$\tilde{R}(t) = \exp(\varphi_1(t)A_1) \, \exp(\varphi_2(t)A_2) \, \exp(\varphi_3(t)A_1) \tag{3.33}$$

By direct comparison with Eq. (3.1), quaternions of $\tilde{R}(t)$ can be derived as:

$$\tilde{q}_0(t) = \cos\left(\frac{\varphi_1}{2}\right)\cos\left(\frac{\varphi_2}{2}\right)\cos\left(\frac{\varphi_3}{2}\right) - \cos\left(\frac{\varphi_2}{2}\right)\sin\left(\frac{\varphi_1}{2}\right)\sin\left(\frac{\varphi_3}{2}\right)$$
$$\tilde{q}_1(t) = \cos\left(\frac{\varphi_2}{2}\right)\cos\left(\frac{\varphi_3}{2}\right)\sin\left(\frac{\varphi_1}{2}\right) + \cos\left(\frac{\varphi_1}{2}\right)\cos\left(\frac{\varphi_2}{2}\right)\sin\left(\frac{\varphi_3}{2}\right)$$
$$\tilde{q}_2(t) = \cos\left(\frac{\varphi_1}{2}\right)\cos\left(\frac{\varphi_3}{2}\right)\sin\left(\frac{\varphi_2}{2}\right) + \sin\left(\frac{\varphi_1}{2}\right)\sin\left(\frac{\varphi_2}{2}\right)\sin\left(\frac{\varphi_3}{2}\right)$$
$$\tilde{q}_3(t) = \cos\left(\frac{\varphi_3}{2}\right)\sin\left(\frac{\varphi_1}{2}\right)\sin\left(\frac{\varphi_2}{2}\right) - \cos\left(\frac{\varphi_1}{2}\right)\sin\left(\frac{\varphi_2}{2}\right)\sin\left(\frac{\varphi_3}{2}\right)$$

$$(3.34)$$

Substituting Eq. (3.33) into (3.32) yields:

$$L(t) = \frac{i\,\mathbf{L}}{2}\begin{pmatrix} \cos\varphi_2(t) & e^{-i\,\varphi_3(t)}\sin\varphi_2(t) \\ e^{i\,\varphi_3(t)}\sin\varphi_2(t) & -\cos\varphi_2(t) \end{pmatrix} \tag{3.35}$$

then equating (3.35) with $L(t)$ in (3.7)

$$L(t) = \begin{pmatrix} \frac{i\,I_1\omega_1}{2} & \frac{I_2\omega_2}{2} + \frac{i\,I_3\omega_3}{2} \\ -\frac{I_2\omega_2}{2} + \frac{i\,I_3\omega_3}{2} & -\frac{i\,I_1\omega_1}{2} \end{pmatrix}$$

yields:

$$\mathbf{I}_1\omega_1(t) = \mathbf{L}\cos\varphi_2(t) \tag{3.36}$$

which gives $\cos\varphi_2(t)$ and

$$\begin{cases} \mathbf{I}_2\omega_2(t) + i\,I_3\omega_3(t) = i\mathbf{L}\,e^{-i\,\varphi_3(t)}\sin\varphi_2(t) \\ -\mathbf{I}_2\omega_2(t) + i\,I_3\omega_3(t) = i\mathbf{L}\,e^{i\,\varphi_3(t)}\sin\varphi_2(t) \end{cases} \tag{3.37}$$

which gives $\tan\varphi_3(t)$:

$$\tan\varphi_3(t) = \frac{\mathbf{I}_2\omega_2(t)}{\mathbf{I}_3\omega_3(t)} \tag{3.38}$$

Let $x(t) = \cos\varphi_2(t)$ and $y(t) = \tan\varphi_3(t)$, then yields:

$$\cos\left(\frac{\varphi_2}{2}\right) = \mathcal{S}_1\sqrt{\frac{1+x(t)}{2}}$$
$$\sin\left(\frac{\varphi_2}{2}\right) = \mathcal{S}_2\sqrt{\frac{1-x(t)}{2}}$$
$$\tan\left(\frac{\varphi_3}{2}\right) = \frac{y(t)}{1+\sqrt{1+y(t)^2}}$$

$$(3.39)$$

By denoting $y_1(t) = \tan\left(\frac{\varphi_3}{2}\right)$, it follows:

$$\cos\left(\frac{\varphi_3}{2}\right) = \mathcal{S}_3\frac{1}{\sqrt{1+y_1(t)^2}}$$
$$\sin\left(\frac{\varphi_3}{2}\right) = \mathcal{S}_4\frac{y_1(t)}{\sqrt{1+y_1(t)^2}}$$

$$(3.40)$$

or equivalently

$$\cos\left(\frac{\varphi_3}{2}\right) = \mathcal{S}_3 \frac{y_2(t)}{\sqrt{1 + y_2(t)^2}}$$

$$\sin\left(\frac{\varphi_3}{2}\right) = \mathcal{S}_4 \frac{1}{\sqrt{1 + y_2^{-1}(t)^2}}$$

(3.41)

with $y_2 = y_1^{-1} = cotan\left(\frac{\varphi_3}{2}\right)$ and $\mathcal{S}_i = \pm 1$. It remains to solve for $\varphi_1(t)$. Using the coordinate representation of $\tilde{R}(t)$, Eq. (3.33), yields:

$$\frac{d\tilde{R}(t)}{dt} = \frac{d}{dt}\left[\exp(\varphi_1(t)A_1)\right] \exp(\varphi_2(t)A_2) \exp(\varphi_3(t)A_1) +$$

$$+ \exp(\varphi_1(t)A_1)\frac{d}{dt}\left[\exp(\varphi_2(t)A_2)\right] \exp(\varphi_3(t)A_1) +$$

$$+ \exp(\varphi_1(t)A_1) \exp(\varphi_2(t)A_2)\frac{d}{dt}\left[\exp(\varphi_3(t)A_1)\right]$$

(3.42)

As the single terms $\tilde{R}(t)$ are stabilisers, it follows that:

$$\frac{d}{dt}\left[\exp(\varphi_1(t)A_1)\right] = \exp(\varphi_1(t)A_1)\,\dot{\varphi}_1(t)\,A_1$$

$$\frac{d}{dt}\left[\exp(\varphi_2(t)A_2)\right] = \exp(\varphi_2(t)A_2)\,\dot{\varphi}_2(t)\,A_2$$

$$\frac{d}{dt}\left[\exp(\varphi_3(t)A_1)\right] = \exp(\varphi_3(t)A_1)\,\dot{\varphi}_3(t)\,A_1$$

(3.43)

Therefore:

$$\frac{d\tilde{R}(t)}{dt} = \tilde{R}(t)\left[\Xi_{23}\,\dot{\varphi}_1(t)\,A_1\,\exp(\varphi_2(t)A_2)\,\exp(\varphi_3(t)A_1) + \right.$$

$$\left. + \Xi_3\,\dot{\varphi}_2(t)\,A_2\,\exp(\varphi_3(t)A_1) + \dot{\varphi}_3(t)\,A_1\right]$$

(3.44)

where $\Xi_{23} = \left[\exp(\varphi_2(t)A_2)\exp(\varphi_3(t)A_1)\right]^{-1}$ and $\Xi_3 = \left[\exp(\varphi_3(t)A_1)\right]^{-1}$.

$$\tilde{R}(t)^{-1}\frac{d\tilde{R}(t)}{dt} = \frac{\dot{\varphi}_1(t)}{2}\left(\begin{array}{cc} i\cos\varphi_2(t) & ie^{-i\varphi_3(t)}\sin\varphi_2(t) \\ ie^{i\varphi_3(t)}\sin\varphi_2(t) & -i\cos\varphi_2(t) \end{array}\right) +$$

$$+ \frac{\dot{\varphi}_2(t)}{2}\left(\begin{array}{cc} 0 & e^{-i\varphi_3(t)} \\ -e^{i\varphi_3(t)} & 0 \end{array}\right) + \frac{\dot{\varphi}_3(t)}{2}\left(\begin{array}{cc} i & 0 \\ 0 & -i \end{array}\right)$$

(3.45)

then equating (3.45) to (3.3) yields:

$$\left\{\begin{array}{l} \omega_2(t) + i\omega_3(t) = \dot{\varphi}_1(t)ie^{-i\varphi_3(t)}\sin\varphi_2(t) + \dot{\varphi}_2(t)e^{-i\varphi_3(t)} \\ -\omega_2(t) + i\omega_3(t) = \dot{\varphi}_1(t)ie^{i\varphi_3(t)}\sin\varphi_2(t) - \dot{\varphi}_2(t)e^{i\varphi_3(t)} \end{array}\right.$$

(3.46)

the two equations in (3.46) can be rearranged to give:

$$\begin{cases} \frac{\omega_2(t)}{e^{-i\varphi_3(t)}} + \frac{i\omega_3(t)}{e^{-i\varphi_3(t)}} = \dot{\varphi}_1(t)i\sin\varphi_2(t) + \dot{\varphi}_2(t) \\ -\frac{\omega_2(t)}{e^{i\varphi_3}} + \frac{i\omega_3(t)}{e^{i\varphi_3}} = \dot{\varphi}_1(t)i\sin\varphi_2(t) - \dot{\varphi}_2(t) \end{cases} \qquad (3.47)$$

then adding the two equations in (3.47) and using the expressions in (3.37) and simplifying gives:

$$\dot{\varphi}_1(t) = \mathbf{L}\left(\frac{\omega_2^2(t)\mathbf{I}_2 + \mathbf{I}_3\omega_3^2(t)}{(\mathbf{I}_2\omega_2(t))^2 + (\mathbf{I}_3\omega_3(t))^2}\right) \qquad (3.48)$$

Finally, using the conserved quantities (3.6) can be expressed as:

$$\varphi_1(t) = \int \mathbf{L}\left(\frac{2\mathcal{T} - \mathbf{I}_1\omega_1^2(t)}{\mathbf{L}^2 - (\mathbf{I}_1\omega_1(t))^2}\right) dt \qquad (3.49)$$

Similarly, as shown in [39], such an expression can be taken to a known form after algebraic manipulation and a proper change of variable. By taking into account the expression of the angular velocity and the definition of the elliptic sine function:

$$\omega_1(t) = \zeta_1 sn(\xi_1 t + \gamma_1 , \mu_1) = \zeta_1 \sin(\theta)$$

with $\theta = am(\xi_1 t + \gamma_1 , \mu_1)$, it yields:

$$\mathbf{L}\left(\frac{2\mathcal{T} - \mathbf{I}_1\omega_1^2(t)}{\mathbf{L}^2 - (\mathbf{I}_1\omega_1(t))^2}\right) = \frac{\mathbf{L}}{\mathbf{I}_1} + \frac{2\mathcal{T}\mathbf{I}_1 - \mathbf{L}^2}{\mathbf{L}\mathbf{I}_1} \frac{1}{1 - (\frac{\mathbf{I}_1\zeta_1}{\mathbf{L}})^2 \sin^2(\theta)} \qquad (3.50)$$

The integration of the first term is trivial, while for the integration of the second term the following change of variable is considered:

$$d\vartheta = \xi_1 \sqrt{1 - \mu_1^2 sn^2(\xi_1 t + \gamma_1, \mu_1)}\, dt \qquad (3.51)$$

This step, takes the integral to the form

$$\varphi_1(t) = \int \frac{\mathbf{L}}{\mathbf{I}_1} dt + \frac{\mathbf{L}^2 - 2\mathbf{I}_1 T}{\mathbf{I}_1 \mathbf{L} \xi_1} \int \frac{1}{1 - (\frac{\mathbf{I}_1\zeta_1}{\mathbf{L}})^2 \sin^2(\theta)} \frac{1}{\sqrt{1 - \mu^2 \sin^2(\theta)}} d\vartheta \qquad (3.52)$$

whose solution is a linear term plus an indefinite elliptic integral of the third kind, [39] [44], and an integration constant, as stated in *Theorem* 1:

$$\varphi_1(t) = \frac{L}{\mathbf{I}_1}\left[t - \frac{\mathbf{L}^2 - 2\mathbf{I}_1 T}{\mathbf{L}^2 \xi_1}\Pi\left(\frac{\mathbf{I}_1^2 \zeta_1^2}{\mathbf{L}^2} , am(\xi_1 t + \gamma_1, \mu_1) , \mu_1\right)\right] \qquad (3.53)$$

At this point, the isomorphism (3.2) is used to map $\tilde{R}(t)$ onto the quaternions $\vec{\tilde{q}}$ in (3.21). To obtain the initial state through the origin R_{int}, $R(t)$ has to be calculated by

pulling $\tilde{R}(t)$ in (3.33) back to the identity via:

$$R(t) = R_{int}\tilde{R}(0)^{-1}\tilde{R}(t) \tag{3.54}$$

and again, to obtain the final expression, the isomorphism (3.2) has to be used to map onto the quaternions. The final result is then

$$\vec{q}(t) = \tilde{Q}_0\,\vec{\tilde{q}}(t) \tag{3.55}$$

Solution of the sign functions $\mathcal{S}_i$

The general solution of the sign functions should take into account the value of the angles $\varphi_2(t)$ and $\varphi_3(t)$. However, due to the dual nature of quaternions, it can be demonstrated that it is not possible to define the angles over the whole real domain. Therefore, for convenience, it is assumed here that

$$\begin{aligned} \varphi_2 &\in (-\pi\,,\,\pi) \\ \varphi_3 &\in (0\,,\,2\pi) \end{aligned} \tag{3.56}$$

These assumptions do not imply any loss of generality and, additionally, involve $\mathcal{S}_1 = \mathcal{S}_4 = 1$. It remains to solve for $\mathcal{S}_2$ and $\mathcal{S}_3$. Trigonometric identities can be used to identify a relation between $\mathcal{F}_3(t)$ and $\mathcal{F}_4(t)$:

$$\frac{d}{dt}\mathcal{F}_4(t) = \frac{1}{2}\,\dot{\varphi}_3(t)\,\mathcal{F}_3(t) \tag{3.57}$$

Equating (3.45) to (3.3) and, then, using Eq. (3.36) and Eq. (3.53), yields:

$$\dot{\varphi}_3(t) = \frac{\omega_1}{L^2 - \mathbf{I}_1^2\,\omega_1^2}\,\left(L^2 - 2\,\mathbf{I}_1\,T\right) \tag{3.58}$$

The same procedure cannot be repeated for the angle $\varphi_2(t)$, as at most its square, $\varphi_2(t)^2$, can be obtained by the sets of the differential equations of kinematics and dynamics. Introducing Eq. (3.58) into Eq. (3.57), at the initial time, gives:

$$\mathcal{S}_3 = \frac{(\,1 + y_1(0)^2\,)\,(\,\omega_1(0) - x(0)\,\dot{\varphi}_1(0)\,)}{2\,\dot{y}_1(0)} \tag{3.59}$$

However, the function $\dot{y}_1(t)$

$$\dot{y}_1(t) = \frac{\mathbf{I}_2\,\mathbf{I}_3\,\omega_1(t)\,\left(-\delta_3\omega_2(t)^2 + \delta_2\omega_3(t)^2\right)}{\mathbf{I}_2^2\omega_2(t)^2 + \mathbf{I}_3\omega_3(t)\left(\mathbf{I}_3\,\omega_3(t) + \sqrt{L^2 - \mathbf{I}_1^2\,\omega_1(t)^2}\right)} \tag{3.60}$$

is null for $\omega_1(t) = 0$. Therefore, in case $\dot{y}_1(0) = 0$, the sign $\mathcal{S}_3$ can be derived from the second derivative of $\mathcal{F}_4(t)$:

$$\frac{d^2}{dt^2}\mathcal{F}_4(t) = \frac{1}{2}\left(\ddot{\varphi}_3(t)\,\mathcal{F}_3(t) - \frac{1}{2}\,\dot{\varphi}_4(t)\,\mathcal{F}_3(t)\right) \tag{3.61}$$

which gives:

$$\mathcal{S}_3 = \frac{2\,\ddot{y}_1(0)\,L^4}{(1 + y_1(0)^2)\,(L^2 - 2\,\mathbf{I}_1\,T)\,L^2\,\dot{\omega}_1(0)} \tag{3.62}$$

By the initial conditions, the first derivative in time of quaternions is known:

$$\vec{\dot{q}}(0) = Q_d(0)\,\vec{\omega}(0) \tag{3.63}$$

with

$$Q_d(0) = 1/2 \begin{bmatrix} -q_1(0) & -q_2(0) & -q_3(0) \\ q_0(0) & -q_3(0) & q_2(0) \\ q_3(0) & q_0(0) & -q_1(0) \\ -q_2(0) & q_1(0) & q_0(0) \end{bmatrix} \tag{3.64}$$

From Eq. (3.19), Eq. (3.63) can be equated with:

$$\vec{\dot{q}}(0) = \tilde{Q}_0\,\frac{d}{dt}\vec{q}(0) \tag{3.65}$$

Note that, in the most general case, due to the dual nature of the quaternions it is not possible to solve the system (3.65) for all the sign variables. Solving the system made by Eq. (3.63) and Eq. (3.65), taking into account Eq. (3.59) and remembering the choice made $\mathcal{S}_1 = \mathcal{S}_4 = 1$, it follows:

$$\mathcal{S}_2 = \frac{\omega_3(0)\,\sqrt{1 - x(0)^2}\,(1 + y_1(0)^2)}{2\,\mathcal{S}_3\,\dot{x}(0)\,y_1(0) + (x(0)^2 - 1)\,(y_1(0)^2 - 1)\,\dot{\varphi}_1(0)} \tag{3.66}$$

The same procedure can be repeated for the equivalent formulation adopting $y_2(t)$ rather than $y_1(t)$, obtaining the results included in the theorem.

Remark 10 *The function $y_1(t)$ is an indeterminate form at $\omega_2(t) = 0 \wedge \omega_3(t) < 0$:*

$$\lim_{\omega_2(t)\to 0} y_1(t)\bigg|_{\omega_3(t)<0} = \frac{0}{\mathbf{I}_3\omega_3(t) + \|\mathbf{I}_3\omega_3(t)\|}\bigg|_{\omega_3(t)<0} = \frac{0}{0}$$

Studying the function at the point, by applying L'Hôpital's rule, it results:

$$
\lim_{\omega_2(t)\to 0} y_1(t)\Big|_{\omega_3(t)<0} =
$$

$$
\lim_{\omega_2(t)\to 0} \frac{\mathbf{I}_2\dot{\omega}_2(t)}{\mathbf{I}_3\dot{\omega}_3(t) - (\ \mathbf{I}_1^2\,\omega_1(t)\,\dot{\omega}_1(t)\ )(\ L^2 - \mathbf{I}_1^2\omega_1(t)^2\ )^{-1/2}}\Big|_{\omega_3(t)<0} = \tag{3.67}
$$

$$
\frac{\mathbf{I}_2\,\delta_2\,\omega_1(t)\,\omega_3(t)}{0} = \pm\infty
$$

Therefore, at this condition it is convenient to formulate $\mathcal{F}_3(t)$ and $\mathcal{F}_4(t)$ as function of $y_2(t)$, whose limit, at the same point, is zero. The behaviour of $y_1(t)$ and $y_2(t)$ will, hence, be:

$$
\lim_{\omega_2(t)\to 0} y_1(t)\Big|_{\omega_3(t)<0} = \pm\infty
$$

$$
\lim_{\omega_2(t)\to 0} y_1(t)\Big|_{\omega_3(t)>0} = 0
$$

$$
\lim_{\omega_2(t)\to 0} y_2(t)\Big|_{\omega_3(t)<0} = 0 \tag{3.68}
$$

$$
\lim_{\omega_2(t)\to 0} y_2(t)\Big|_{\omega_3(t)>0} = \pm\infty
$$

It is possible to foresee when discontinuities will occur by the initial conditions. In particular, formulating $\omega_2(t)$ and $\omega_3(t)$ as function of $\omega_1(t)$ using the conserved quantities, it follows:

$$
\omega_2(t)^2 = \frac{L^2 - 2\,\mathbf{I}_3\,T + \mathbf{I}_1(\mathbf{I}_3 - \mathbf{I}_1)\,\omega_1(t)^2}{\mathbf{I}_2\,(\mathbf{I}_2 - \mathbf{I}_3)}
$$

$$
\omega_3(t)^2 = \frac{-L^2 + 2\,\mathbf{I}_2\,T + \mathbf{I}_1(\mathbf{I}_1 - \mathbf{I}_2)\,\omega_1(t)^2}{\mathbf{I}_3\,(\mathbf{I}_2 - \mathbf{I}_3)} \tag{3.69}
$$

Assuming $\mathbf{I}_3 > \mathbf{I}_2 > \mathbf{I}_1$, conditions for a feasible solution are:

$$
\begin{cases} \omega_1(t)^2 \leq \frac{2\,\mathbf{I}_3\,T - L^2}{\mathbf{I}_1(\mathbf{I}_3 - \mathbf{I}_1)} \\ \omega_1(t)^2 \leq \frac{L^2 - 2\,\mathbf{I}_2\,T}{\mathbf{I}_1(\mathbf{I}_2 - \mathbf{I}_1)} \end{cases} \tag{3.70}
$$

By defining

$$
\left\{ \lambda = \frac{2\,\mathbf{I}_3\,T - L^2}{\mathbf{I}_3 - \mathbf{I}_1} \quad , \quad \rho = \frac{L^2 - 2\,\mathbf{I}_2\,T}{\mathbf{I}_2 - \mathbf{I}_1} \right\}
$$

the former conditions can be reformulated as:

$$\begin{cases} \omega_1(t)^2 \leq \frac{\lambda}{\mathbf{I}_1} \\ \omega_1(t)^2 \leq \frac{\rho}{\mathbf{I}_1} \end{cases} \tag{3.71}$$

follows that if $\lambda > \rho > 0$, $\omega_2(t)^2$ can never be zero. Conversely, if $\rho > \lambda > 0$, it is $\omega_3(t)^2$ that can never be zero[7]. Based on these considerations, the guide lines expressed in Remark 5 are formulated.

3.5   Use of the closed-form solution for a large repointing manoeuvre

For those cases where the environmental conditions make the free-rigid body dynamics an acceptable approximation of the system's uncontrolled dynamics, the solution derived can be used as a reference track for large reconfiguration manoeuvres. As the reference is a force-free motion, from a dynamical point of view, the main drawback of this method is that variations of angular momentum or kinetic energy are not included. Conversely, the main advantage is that, when prescribed boundary conditions are matched, no control action is needed to accomplish the manoeuvre. In the following subsection, a procedure to generate reference tracks is suggested, then, a test case manoeuvre is shown.

3.5.1   Reference Track via Parametric Optimisation

To describe a free rigid-body motion around its center of mass, given some initial conditions $\bar{q}_i$ and $\vec{\omega}_i$, equations (3.21 to 3.27) and (3.54) have to be used. In order to design a reference trajectory which takes to a desired final configuration $\bar{q}_f$, the natural motion from $\bar{q}_i$ to $\bar{q}_f$ has to be identified. To this end, as $\tilde{R}(t)$ in Eq. (3.54) depends on the angular velocity vector $\vec{\omega}(t)$, a boundary condition problem on the initial angular velocity vector $\vec{\omega}_i$ is posed. *Due to the high complexity of the closed form solution, it is not possible to directly and analytically derive the required $\vec{\omega}_i$.* Therefore, the problem can be solved via a parametric optimisation. In detail, the procedure is as follows:

1. Set the initial position $\vec{q}_i$

2. Select a target position $\vec{q}_f$

---

[7]When $\lambda \leq 0$ or $\rho \leq 0$, remembering the physical meaning of eq.(3.69), eq.(3.70) assumes the form

$$\begin{cases} \omega_1(t)^2 \geq -\frac{\lambda}{\mathbf{I}_1} \\ \omega_1(t)^2 \geq -\frac{\rho}{\mathbf{I}_1} \end{cases}$$

3. Select a desired manoeuvre time t_f

4. Choose a $\vec{\omega}_i$ vector.

5. Calculate $\vec{\omega}(t)$

6. Calculate the quaternions evolution $\vec{q}(t)$ using Eq. (3.21) and (3.54)

7. If $\vec{q}(t_f) = \vec{q}_f$, the desired natural motion is found. Otherwise, go back to point 4.

3.5.2 Example Manoeuvre

Considering spacecraft large repointing manoeuvres, the derived closed form solution has some benefits. Firstly, if properly implemented on the on-board computer, it offers a low computational solution as no integration is required and, additionally, the reference track calculation is straightforward once the three components of the angular velocity are set. Secondly, the equations provided are the exact solution to the complete nonlinear problem, without any linearisation or truncation. Therefore, it can be applied globally, over the entire attitude configuration domain. Thirdly, although it is not possible to state that the reference track generated by the motion planner is optimal, e.g. time or fuel optimal, it could be realised with a reduced control strategy. From an ideal point of view, an instantaneous torque pulse would suffice to achieve instantaneously the desired angular velocity, thus matching the reference kinematical profile. In effect, however the precision of the manoeuvre will be affected by many parameters as, for instance, by the effect of disturbances, i.e. external torques, by the mass properties, uncertainties or by the divergence of the angular velocity track from the reference. In order to have an approximate idea of the magnitude of the error on the manoeuvre, in this section, given a reasonable scenario, see [54] for reference, an open loop test case manoeuvre is provided for a $3.4kg$ nano-satellite in a circular orbit at $300km$ altitude. The orbit, whose details are reported in Table 3.2, has been chosen such that the most general case is addressed. The perigee altitude is one of the lowest possible for a LEO orbit, where the air drag effects are significant and the eccentricity is non-zero so that the effects of gravity are time dependent. Orbit inclination is set as the same of the International Space Station.

	Value	Unit
Perigee Altitude	300	km
Eccentricity	0.2	
Inclination	51.65	deg

Table 3.2: A schematic overview of the orbit considered.

Air drag effects and gravity gradient effects are included while the actions of solar radiation pressure and magnetic interactions are neglected [8]. The spacecraft is endowed with reaction wheels and a nominal manoeuvre time $t_f = 30$ seconds is chosen for a large rest-to-rest manoeuvre. Properties of the spacecraft are listed in Table 3.3.

Spacecraft Net Mass	Kg
m	3.4

Spacecraft Dimensions	m
l_1	0.9
l_2	0.2
l_3	0.1

Spacecraft Momenta of Inertia	$Kg\,m^2$
$\mathbf{I}_1$	0.01083
$\mathbf{I}_2$	0.13917
$\mathbf{I}_3$	0.14417

Table 3.3: Spacecraft mass properties - the reaction wheels' mass is included.

The reaction wheels' properties are shown in Table 3.4. For the manoeuvre, the fol-

	Value	Unit
Max Wheel Speed	6000	rpm
Max Torque	20	mNm
Wheel Inertia	0.001	$Kg\,m^2$

Table 3.4: A schematic overview of each reaction wheel's characteristics.

lowing initial and target configurations are given in terms of relative position between BRF and ORF and are expressed in quaternion form:

$$\begin{cases} \vec{q}_i = \{1, 0, 0, 0\} \\ \vec{q}_f = \{0\,,\,0.26726\,,\,0.53452\,,\,0.80178\} \end{cases}$$

The Wolfram Mathematica `NMinimize` optimisation algorithm has been used to find the desired initial conditions leading the trajectory to $\vec{q}_f$ in $30s$ such that

$$\vec{\omega}_i \quad : \quad |\vec{q}_f - \vec{q}(t_f)| \quad \leq \quad 10^{-8} \tag{3.72}$$

Resulting optimal trajectories from the motion planner is shown in the quaternion space

---

[8]In a region between $300km$ and $600km$ of altitude, for a CubeSat, aerodynamic and gravitational torques are comparable, while solar torques could be neglected, [73].

in Figure 3.4 and in the angular velocity space in Figure 3.5 by dashed lines.
The equations of motion used for the simulation are derived from the result of the previous chapter. A detailed description of the physical model used, including external torques, actuators's dynamics and controller design is included in appendix B.

The controller is designed in order to follow an open loop strategy during the nominal duration of the manoeuvre, and a velocity feedback strategy in the final seconds of the manoeuver to drive the residual angular velocity to zero. Tracking of the reference involves a fast change of velocity at t_0 and t_f time instants. To this end, spacecraft actuators are used to spin it to the initial reference slew rate and then stop it to rest after $t_f - t_0$ seconds. From a purely theoretical point of view, only two torque pulses would be enough to instantaneously reach the reference angular velocity and, later, to halt the motion. However, in practice, uncertainties, finite-time pulses and disturbances will produce a deviation from the reference, therefore, after the second torque pulse there is a residual non-null spinning rate, which can be cancelled by a feedback control.

Results are shown in Figures 3.4, 3.5, where the trajectory is shown in the quaternions space and in the angular velocity space by solid lines. Figure 3.6 shows the control torque applied and Figure 3.7 shows the acceleration and deceleration phases. Note that torque pulses have been designed as rectangular functions during the open loop control manoeuvre's phase.
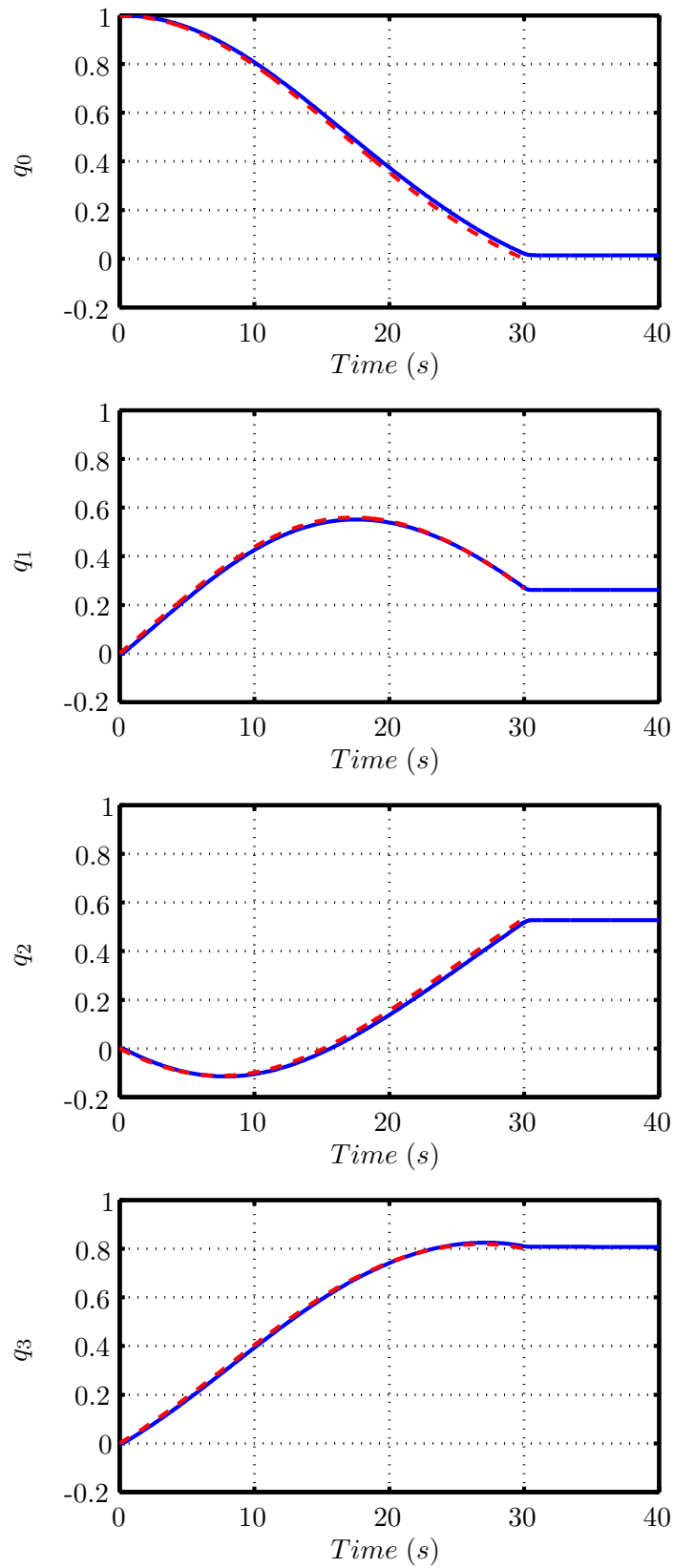
Figure 3.4: Quaternions evolution in time. The solid line is the realised trajectory while the dashed line is the ideal free motion from the motion planner.
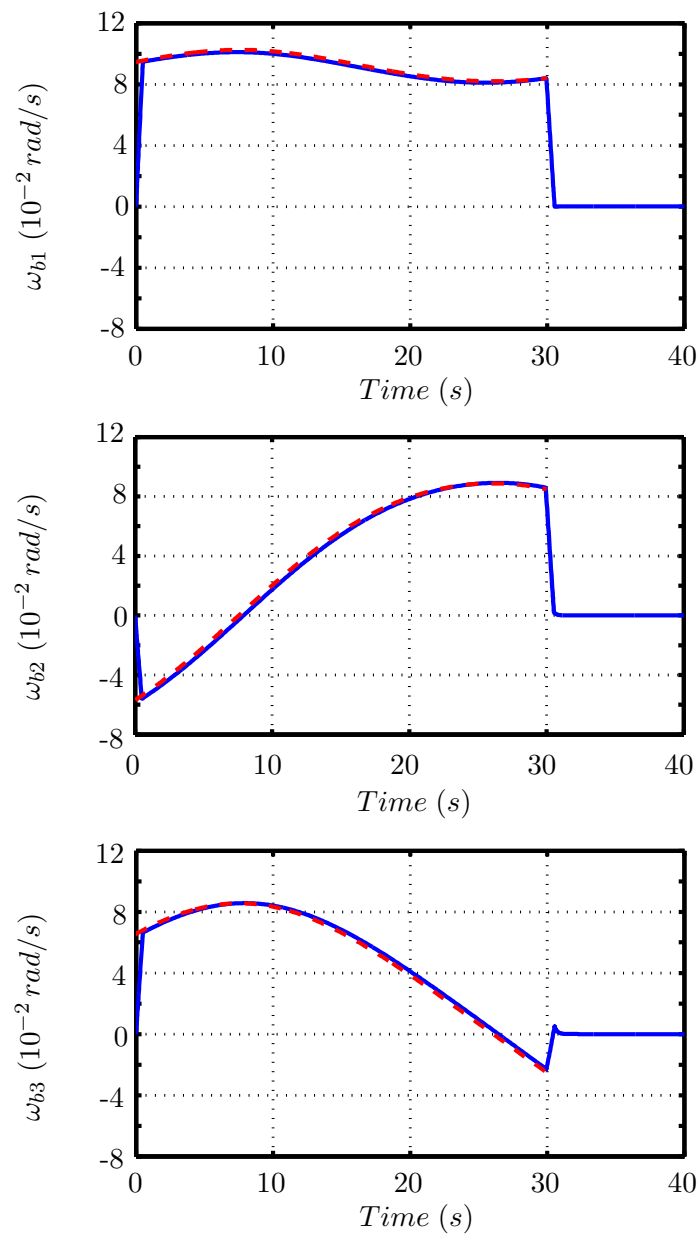
Figure 3.5: Angular velocity of the body with respect to the orbital reference frame. The solid line is the realised trajectory while the dashed line is the ideal free motion from the motion planner.
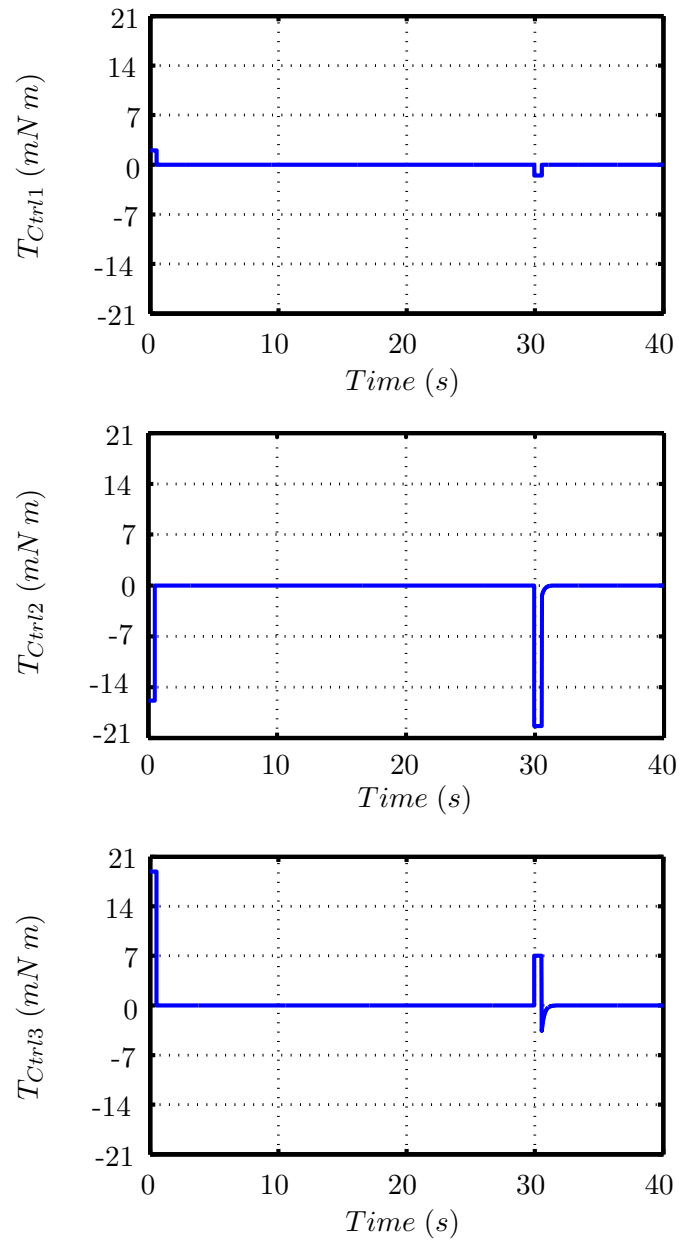
Figure 3.6: Control torques vs time. The open loop control phase ends at the time $t = 30.6\,s$. Details can be found in the appendix B.
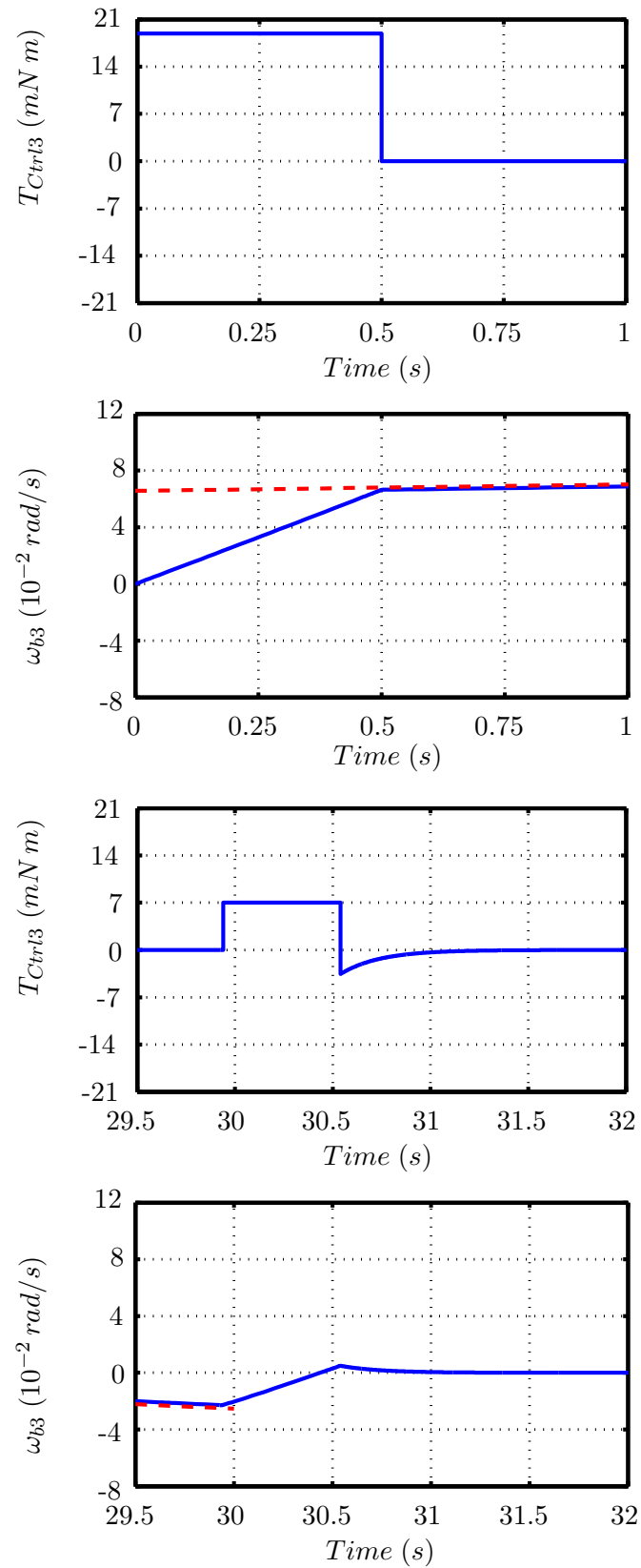
Figure 3.7: Details of the third component of the control torque function and of the body angular velocity for the first and last time instants of the manoeuvre.

Manoeuvre's results are gathered in Table 3.5.

Manoeuvre Results at $t = 40s$		
Angular Velocity	$1.0119\,10^{-5}$	rad/s
Quaternion's Error	$\{-0.39\,,\,-0.20\,,\,1.55\,,\,-0.99\}$	10^{-2}
Norm of the Quaternion's Error	1.8869	10^{-2}
Angular Error on the spacecraft z-axis pointing	1.0746	deg

Table 3.5: Results of the test case manoeuvre.

Although not enough to satisfy high accuracy demands, results show that the method could be a feasible solution to get the spacecraft attitude to a close proximity of a target configuration. It should be considered that this result has been achieved for a non-equatorial elliptical low Earth orbit at its perigee where the effects of air drag and gravity gradient are more relevant. On the other hand, the spacecraft considered has a modest size, modest area-to-mass ratio and no external appendages. Moreover, actuators considered belong to a feasible technology level for the scenario treated, however no errors of any type on their action have been considered as well as on the spacecraft sensor' system. Additionally, in the controller no uncertainties have been introduced. Nevertheless, a pointing accuracy of roughly 1 degree has been obtained without any position feedback and with a relatively simple control strategy.

At the moment, the most critical aspect of the application suggested is the parametric optimisation of the closed form solution. Due to the use of complex Jacobi functions, the optimisation process is computationally demanding so may not be feasible on-board micro- and nano-spacecraft, which have very limited on-board resources and energy and power consumptions remain crucial factors.

In [48] natural motions of symmetric spacecraft were addressed for low-computational nano-satellites, where the natural motions are expressed as standard functions.

3.6 Summary

The chapter derives an analytic solution for the natural motions of a free asymmetric rigid body using a Lax pair integration on the Special Unitary Group SU(2). This integration method enables the solution to be expressed in a useful compact quaternion form. Furthermore, different to the classically stated solutions, see [41] [39] [42] or [43], this geometric approach leads to a form that involves neither theta functions

nor Euler angles defined by inverse trigonometric functions. Conversely, the proposed quaternions are expressed in terms of an elliptic integral and Jacobian elliptic functions which constitute a non-singular set of variables describing the attitude of a free rigid body, therefore, they are convenient for a variety of engineering applications (e.g. space attitude motion planning and control).

The main limitations are the use of both antipodal quaternions sets for a limited part of the initial conditions domain and the use of the incomplete elliptic integral of the third kind.

Due to the existence of two equivalent quaternions' sets for every attitude configuration, the problem cannot have a unique solution in quaternion form. In particular, for a defined sub-set of all possible initial angular velocities, the rigid body motion is described using a set of quaternions over a part of the time domain, and its dual quaternions set over the remaining part. Roughly speaking, the solution behaves similarly to a piecewise function and shows jump discontinuities in quaternions space. Furthermore, the presence of the indefinite Jacobi elliptic integral makes the evaluation of the analytical solution extremely difficult on low-performance processors. In such cases, a straightforward implementation of the equations is not feasible due to the introduction of large numerical errors and long computational times.

Nevertheless, when the use of both the antipodal sets of quaternions is problematic, the attitude configuration can be identified by the rotation matrix constructed using the closed-form quaternion solution. The derived rotation matrix will identify uniquely and globally any attitude configuration, without suffering from any singularity nor discontinuity. This will not affect the efficiency of the method nor its applicability. In fact, in aerospace applications, rotation matrices are used as well as quaternions due to their advantages, see Chaturvedi et al. [59] for instance.

Furthermore, issues caused by the evaluation of the elliptic integral might be tackled using advanced programming techniques. Series representations as well as many other alternative methods [44, 45] exist to evaluate or approximate the indefinite integral over a specific domain, therefore, the user has the flexibility to choose the most appropriate method.

In this work the use of the closed-form solution for spacecraft attitude control is presented. In particular the kinematical representation of the free rigid body motion was used to design large open loop slew manoeuvres avoiding numerical integration. An example manoeuvre has been provided and results show that for an asymmetric spacecraft in low-Earth orbit under the action of gravity gradient and air drag, an accuracy of the order of $1deg$ on the final configuration can be obtained.

The Dynamics of a 2-Link Rigid Body System in Orbit

This chapter presents a study of the nonlinear dynamics of two linked rigid bodies under the action of a central gravitational field. First the Hamiltonian dynamics are derived and used to assess the nonlinear stability of the equilibria. A bifurcation analysis is undertaken by studying the Hessian of the Hamiltonian. Global behaviour is studied by using energy methods, phase portraits, Poincarè maps and Lyapunov characteristic exponents. Results reveal regions of regular, quasi-regular and chaotic motions. Finally, the practical implications of the analysis on a real spacecraft multi-body system in terms of control and system design are considered and a tailored control solution is provided for an efficient large reconfiguration manoeuvre.

4.1   Introduction

Emerging mission concepts involve the use of multi-joint-satellite systems. In the introduction a brief overview of the main areas of application has been shown. Among them, many mission concepts, see [74, 75], require two main bodies connected via hinges, robotic arms or tethers, see the DLR mission (DEOS), [13, 14], and the Orbital Express Demonstration System (OEDS) flight test, [76, 77]. Such systems may be described using a two-link rigid body system.

The aim of this chapter is to study the dynamics of this physical model, subject to the gravitational force. An artist representation of the mission concept for a two linked 3-U Cubesat is illustrated in Figure 4.1. A number of related dynamical systems have been studied in the literature but with subtle differences. Sreenath, et. al., [21] and [25],
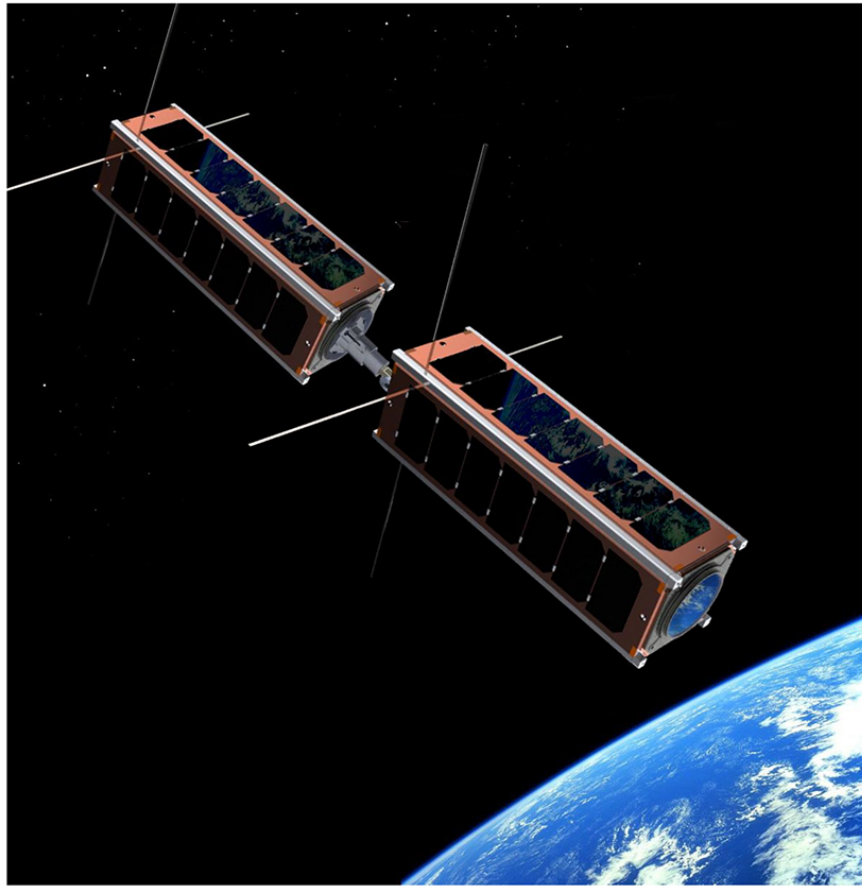
Figure 4.1: Mission concept of a multi 3-U Cubesats. Original image credit: Clyde Space Ltd.

and Patrick, [24], provide a study of the dynamics of coupled planar rigid bodies in the absence of any external force. Their work is based on the manipulation and analysis of the Hamiltonian structure in the reduced phase space and examines equilibria and their stability using the energy-Casimir method. It is notable that they illustrate that around homoclinic orbits, chaotic motion arises when the system is perturbed by the presence of a third body.

Bogoyavlenskil, [55] presented all the possible particular cases in which a multi-body system subject to a central gravity field is an integrable problem, identifying the necessary conditions such that angular momentum and energy for each individual body are conserved quantities. However, the integrable cases relate to restrictive assumptions on the positions of the joints which are not assumed in this chapter. Other approaches model space multi-body systems, rather than finite shape bodies as in this chapter, as chains of point masses, [78]. [78] addressed the problem of tethered satellites, consisting of point masses connected by light rods and spherical hinges, assuming the orbital dynamics as uncoupled with the attitude dynamics. Moreover, the system centers of mass are assumed to be moving along circular orbits in order to find all sets of equilibria

of a generic N-link chain. In [23], two-rigid-body systems under the action of a central potential force were studied however this force is assumed to be concentrated on the center of gravity only. Finally, in [22] geometric methods of analysis are applied on the Hamiltonian, where the cyclic coordinate is eliminated via Routh reduction. However, in [22] multi-body systems are modelled as rigid massless links connected by a hinge joint and with a point mass at one end. Therefore, [22] misses all the effects of the gravity gradients due to the presence of finite shape bodies. As it is demonstrated in this chapter, this significantly affects the overall dynamics and their equilibria.

In this chapter, the problem is restricted to the planar dynamics and the bodies are assumed to be one-dimensional, under the general assumptions listed in the introduction. This description of the multi-body system distinguish this work from previous ones in literature. Further novelty is in the different methods of analysis used to study the problem, in order to enrich existing analysis of the natural dynamics. This has been undertaken by providing a Poincaré map of the dynamics for a given energy level which shows regions of regular, quasi-regular and chaotic motion. Furthermore, a Lyapunov Characteristic Exponent (LCE) map is used. This technique has been used in celestial mechanics and fluid dynamics, but applied here to a space multi-body system for the first time. LCE maps are shown to be an extremely useful global visualisation tool for this particular multi-body planar system, reducing the order of the problem and condensing quantities of information into a lower-dimensional image.

The chapter is presented as follows:

- In Section 2 the assumptions and model used are presented. The corresponding Hamiltonian dynamics for the multi-body system in orbit around a large celestial body is derived.

- In Section 3 relative equilibria are identified and their nonlinear stability determined using Dirichlet's theorem. A bifurcation and the corresponding critical values of the system's parameters are identified.

- Section 4 shows density plots of the attitude mechanical energy of the system as function of the attitude angles to provide indications of the stability regions.

- In Section 5 the dynamics is investigated using numerical tools, such as phase portraits and a Poincaré map. The most representative and important graphs are shown. Furthermore, the analysis is extended by using Lyapunov Characteristic Exponents.

- In Section 6 results are discussed and their implications for future multi-body space system design and control are discussed.

- Finally, in Section 7, an example of application of the study developed is suggested
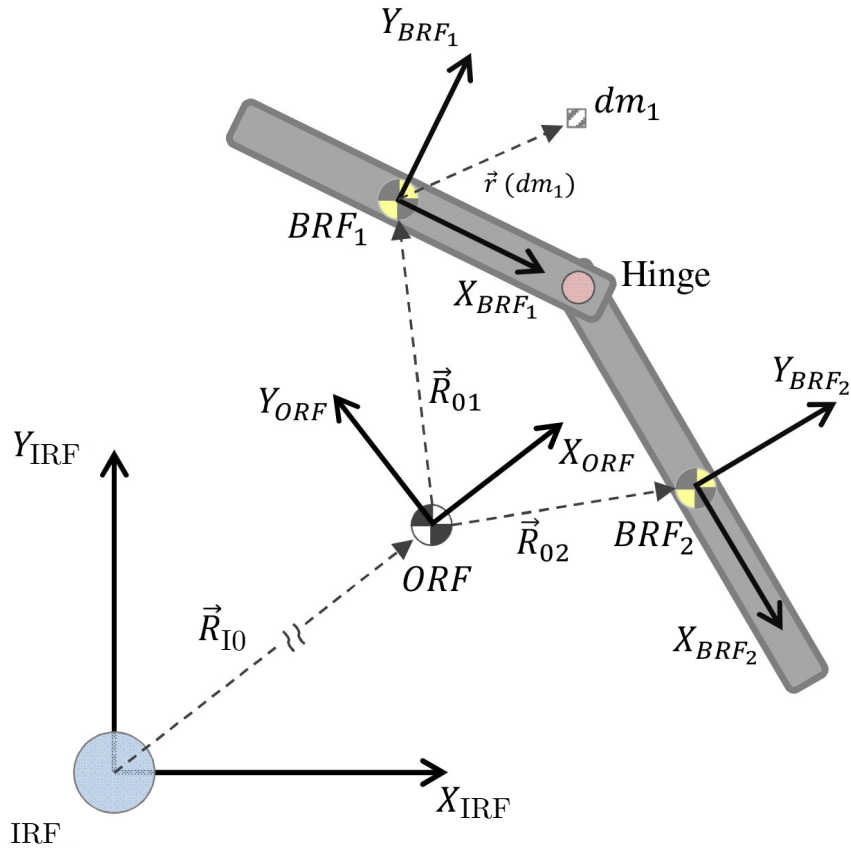
Figure 4.2: Illustration of the system and the reference frames used to describe it.

and a large reconfiguration mission design is proposed.

4.2   The physical model

As described in chapter 2, to the kinematical description the following reference frames
are used: i. Inertial Reference Frame, IRF, ii. Orbital Reference Frame, ORF, iii.
Body Reference Frame - one per body, BRF_i - where the subscript i is a number
identifying the body. The IRF is assumed to be inertial and fixed in space; its origin is
the origin of the gravity field. The $(X|_{IRF}, Y|_{IRF})$ plane contains the orbital plane and
the $Z|_{IRF}$ is parallel to the orbital angular momentum vector. The ORF has origin
over the instantaneous overall center of mass of the multi-body system with $X|_{ORF}$
parallel to the position vector of the origin with respect to the IRF, $Z|_{ORF}$ parallel
to the $Z|_{IRF}$ and with y-axis forming a right handed frame. On each body, a BRF_i
is attached with its origin on the center of mass and orientation set according to the
principal axes of inertia.

In the next sections, the Hamiltonian equations of motion are derived. This form is
convenient to analyse the equilibria and their non-linear stability through Dirichlet's

theorem.

4.2.1   System configuration variables

A mass particle of the $i - th$ body is kinematically described by Eq. (2.2). Note that $\mathbf{T}_{I0}$ depends on the orbital true anomaly ν only and $\mathbf{T}_{0i}$ depends on the attitude angle of the i-th body θ_i only, as the problem is set as 2-D. Constraint equations from Eq. (2.3) are:

$$m_1\vec{R}_{01} + m_2\vec{R}_{02} = \vec{0} \quad ; \quad \vec{R}_{01} + \vec{d}_{1\,H} = \vec{R}_{02} + \vec{d}_{2\,H} \tag{4.1}$$

Where $\vec{d}_{1\,H}$ and $\vec{d}_{2\,H}$ are the position vectors of the hinge with respect to the bodies centers of mass and $\vec{0}$ is the null vector. The first identity is satisfied because it has been set the overall center of mass of the system as origin of the ORF. The second identity describes that the bodies are joined at the hinge via a rotational joint.

Introducing the constraint equations into the kinematics of this problem, the system is reduced. In particular, from Eq. (2.4):

$$\vec{R}_{01} = \frac{-m_2}{m_1 + m_2}(\vec{d}_{1\,H} - \vec{d}_{2\,H}) \quad ; \quad \vec{R}_{02} = \frac{m_1}{m_1 + m_2}(\vec{d}_{1\,H} - \vec{d}_{2\,H}) \tag{4.2}$$

As the bodies are assumed to be rigid, the vectors $\vec{d}_{1\,H}$ and $\vec{d}_{2\,H}$ are fixed in their respective body reference frames:

$$\vec{d}_{1\,H} = \mathbf{T}_{M0}\mathbf{T}_{01}\{\vec{d}_{1\,H}\}_1 \quad ; \quad \vec{d}_{2\,H} = \mathbf{T}_{M0}\mathbf{T}_{02}\{\vec{d}_{2\,H}\}_2 \tag{4.3}$$

Also, let the position vector of the ORF be expressed in cylindrical coordinates, $\vec{R}_{I0} = \{R_0\cos(\nu), R_0\sin(\nu)\}$, so that the system is fully described by the following set of configuration variables:

$$\{R_0, \nu, \theta_1, \theta_2\} \quad ; \quad \left\{\dot{R}_0, \dot{\nu}, \dot{\theta}_1, \dot{\theta}_2\right\} \tag{4.4}$$

4.2.2   Kinetic Energy

From Equations (2.8) and (2.9), the kinetic energy of the system follows as:

$$\begin{aligned}\mathcal{K} = \frac{1}{2}&\left\{m\|\dot{\vec{R}}_{I0}\|^2 + \hat{I}_1(\omega_{M0} + \omega_{01})^2 + \hat{I}_2(\omega_{M0} + \omega_{02})^2+\right.\\ &\left.+2\epsilon < \vec{d}_{1\,H}, T_\theta\vec{d}_{2\,H} > \left[\omega_{01}\omega_{02} + \omega_{M0}^2 + \omega_{M0}(\omega_{01} + \omega_{02})\right]\right\}\end{aligned} \tag{4.5}$$

Where: m is the total mass of the multi-body system ; $m\|\dot{\vec{R}}_{I0}\|^2$ is the term related with the translational kinetic energy of the overall C.G. where $\|\dot{\vec{R}}_{I0}\|^2 = \dot{R}_0^2 + \dot{\nu}^2 R_0^2$; ϵ is the masses ratio $\epsilon = \frac{m_1 m_2}{m}$; I_i is the momentum of inertia of the i-th body with respect to its

center of mass ; $\hat{I}_i$ is the augmented inertia of the body $\hat{I}_i = I_i + \epsilon \|\vec{d}_{i\,H}\|^2$ for i = 1,2 ($\hat{I}_i$ can be considered as the moment of inertia of each body relative to the hinge); $\mathbf{T}_\theta$ is the rotation matrix which transforms from BRF_2 to BRF_1 : $\mathbf{T}_\theta = \mathbf{T}_{\theta_2 - \theta_1} = \mathbf{T}_{01}^{-1}\mathbf{T}_{02}$ which is dependent on the angle $\theta = \theta_2 - \theta_1$.

4.2.3 Potential Energy

The system's potential energy can be derived from Eq. (2.12). To this end, two assumptions are considered: the dimensions of the bodies allow their representation as *one dimensional* shapes ; the density is constant $\rho(\vec{x}) = \bar{\rho}$. It follows that: $\vec{r}_i(\delta m) = \{s, 0\}$ with s a generic coordinate along the body. Moreover, following the convention used by Marsden et al. [21], the position vectors of the hinge in their respective body frames will be taken as

$$\{\vec{d}_{H1}\}_1 = \{d_1, 0\} \quad ; \quad \{\vec{d}_{H2}\}_2 = \{-d_2, 0\} \qquad \text{with} \quad d_1, d_2 \in \mathbb{R}^+ \tag{4.6}$$

The two body problem potential function follows as:

$$\begin{aligned}
\mathcal{U} = \; &\mathcal{U}_1 + \mathcal{U}_2 = -\mu \left[\frac{m}{q} + \frac{3}{2}\frac{1}{q^3}\left(-2\epsilon d_2 d_1 \cos(\theta_1)\cos(\theta_2)+\right.\right. \\
&\left.\left. + \cos(\theta_1)^2 \hat{I}_1 + \cos(\theta_2)^2 \hat{I}_2\right) - \frac{1}{2}\left(\frac{\hat{I}_1 + \hat{I}_2 - 2\epsilon d_1 d_2 \cos(\theta)}{q^3}\right)\right]
\end{aligned} \tag{4.7}$$

4.2.4 Derivation of the Hamiltonian function

Let the name of the variables be changed to the following, in order to coincide with the general Lagrangian notation:

$$\{R_0, \nu, \theta_1, \theta_2\} \quad \equiv \quad \{q_1, q_2, q_3, q_4\} \tag{4.8}$$

The Lagrangian function of the system is:

$$\begin{aligned}
\mathcal{L} = \;&\mathcal{K} - \mathcal{U} = \frac{1}{2}\left\{m(\dot{q}_1^2 + \dot{q}_2^2 q_1^2) + \hat{I}_1(\dot{q}_2 + \dot{q}_3)^2 + \hat{I}_2(\dot{q}_2 + \dot{q}_4)^2+\right. \\
&\left. + \alpha c_\theta \left[\dot{q}_3\dot{q}_4 + \dot{q}_2^2 + \dot{q}_2(\dot{q}_3 + \dot{q}_4)\right]\right\} + \mu\left[\frac{m}{q_1} - \frac{1}{2}\frac{1}{q_1^3}\left(\hat{I}_1 + \hat{I}_2 + \alpha c_\theta\right)+\right. \\
&\left. \frac{3}{2}\frac{1}{q_1^3}\left(\alpha c_{q_3}c_{q_4} + c_{q_3}^2 \hat{I}_1 + c_{q_4}^2 \hat{I}_2\right)\right]
\end{aligned} \tag{4.9}$$

where

$$\theta = q_4 - q_3 \quad ; \quad \alpha = 2\,\epsilon\,d_1\,d_2 \tag{4.10}$$

and the trigonometric functions are expressed as: $\cos(\psi) = c_\psi$; $\sin(\psi) = s_\psi$; $\cos(\psi + \phi) = c_{(\psi+\phi)}$.

Note that the variable q_2 does not appear explicitly in the Lagrangian and is a cyclic variable. Its momentum is a conserved quantity of the system.

The Legendre transform is applied to the Lagrangian function to obtain the Hamiltonian function. The conjugate momenta, $\vec{p} = \{p_1, p_2, p_3, p_4\}$, are derived from Eq. (4.9) as:

$$
\begin{cases}
p_1 &= m\dot{q}_1 \\
p_2 &= mq_1^2\dot{q}_2 + \hat{I}_1(\dot{q}_2 + \dot{q}_3) + \hat{I}_2(\dot{q}_2 + \dot{q}_4) \\
      & \quad -\frac{\alpha}{2}(2\dot{q}_2 + \dot{q}_3 + \dot{q}_4)\, c_\theta \\
p_3 &= \hat{I}_1(\dot{q}_2 + \dot{q}_3) - \frac{\alpha}{2}(\dot{q}_2 + \dot{q}_4)\, c_\theta \\
p_4 &= \hat{I}_2(\dot{q}_2 + \dot{q}_4) - \frac{\alpha}{2}(\dot{q}_2 + \dot{q}_3)\, c_\theta
\end{cases}
\tag{4.11}
$$

the following notation is adopted :

$$\vec{p} = \mathbf{J}\,\vec{\dot{q}} \tag{4.12}$$

with

$$
\mathbf{J} =
\begin{bmatrix}
m & 0 & 0 & 0 \\
0 & mq_1^2 + \hat{I}_1 + \hat{I}_2 - \alpha\, c_\theta & \hat{I}_1 - \frac{\alpha}{2}\, c_\theta & \hat{I}_2 - \frac{\alpha}{2}\, c_\theta \\
0 & \hat{I}_1 - \frac{\alpha}{2}\, c_\theta & \hat{I}_1 & -\frac{\alpha}{2}\, c_\theta \\
0 & \hat{I}_2 - \frac{\alpha}{2}\, c_\theta & -\frac{\alpha}{2}\, c_\theta & \hat{I}_2
\end{bmatrix}
\tag{4.13}
$$

so that the Hamiltonian can be written as:

$$\mathcal{H} = \vec{p}^{Tr}\mathbf{J}^{-1}\vec{p} - \mathcal{K}(\vec{q}, \mathbf{J}^{-1}\vec{p}) + \mathcal{U}(\vec{q}) = \frac{1}{2}\vec{p}^{Tr}\mathbf{J}^{-1}\vec{p} + \mathcal{U}(\vec{q}) \tag{4.14}$$

4.2.5 Complete Dynamics

In this subsection the equations of motions are derived.

The Hamiltonian equations of motion follow with: $\frac{\partial\mathcal{H}}{\partial\vec{p}} = \vec{\mathbf{I}}^{Tr}\mathbf{J}^{-1}\vec{p}$ where $\vec{\mathbf{I}}^{Tr} = \{1,1,1,1\}$ and $\frac{\partial\mathcal{H}}{\partial\vec{q}} = \vec{p}^{Tr}\frac{\partial\mathbf{J}^{-1}}{\partial\vec{q}}\vec{p} + \frac{\partial\mathcal{U}(\vec{q})}{\partial\vec{q}}$ yield:

$$
\begin{cases}
\dot{q}_1 &= \frac{p_1}{m} \\
\dot{q}_2 &= \frac{p_2 - p_3 - p_4}{mq_1^2} \\
\dot{q}_3 &= \frac{-p_2 + p_3 + p_4}{mq_1^2} + \frac{p_3\,\hat{I}_2 + p_4\,\alpha/2\, c_\theta}{\Delta} \\
\dot{q}_4 &= \frac{-p_2 + p_3 + p_4}{mq_1^2} + \frac{p_4\,\hat{I}_1 + p_3\,\alpha/2\, c_\theta}{\Delta}
\end{cases}
\tag{4.15}
$$

$$\begin{cases} \dot{p}_1 = & -\frac{m\,\mu}{q_1^2} + \frac{(p_3+p_4-p_2)^2}{m q_1^3} + \\ & -\frac{3}{4}\frac{\mu}{q_1^4}\Big[\hat{I}_1(3\,c_{(2q_3)}+1) + \hat{I}_2(3\,c_{(2q_4)}+1) + \\ & +2\,\alpha(c_\theta - 3c_{q_4}\,c_{q_3})\Big] \\ \dot{p}_2 = & 0 \\ \dot{p}_3 = & \frac{-\alpha\,s_\theta}{2\Delta^2}\left(\hat{I}_1 p_4 + \frac{\alpha}{2}p_3\,c_\theta\right)\left(\frac{\alpha}{2}p_4\,c_\theta + \hat{I}_2 p_3\right) + \\ & -\frac{\mu}{q_1^3}\left(\frac{3}{2}\hat{I}_1\,s_{(2q_3)} - \frac{\alpha}{2}\,s_{(q_4+q_3)} - \frac{\alpha}{2}\,c_{q_4}\,s_{q_3}\right) \\ \dot{p}_4 = & \frac{\alpha\,s_\theta}{2\Delta^2}\left(\hat{I}_2 p_3 + \frac{\alpha}{2}p_4\,c_\theta\right)\left(\frac{\alpha}{2}p_3\,c_\theta + \hat{I}_1 p_4\right) + \\ & -\frac{\mu}{q_1^3}\left(\frac{3}{2}\hat{I}_2\,s_{(2q_4)} - \frac{\alpha}{2}\,s_{(q_4+q_3)} - \frac{\alpha}{2}\,c_{q_3}\,s_{q_4}\right) \end{cases}$$

where $\Delta = \hat{\mathbf{I}}_1\hat{\mathbf{I}}_2 - (\frac{\alpha}{2})^2\,c_\theta^2$. Some additional observations: the overall angular momentum is a conserved quantity of the problem; with respect to the free case, the sum of the momenta $p_3 + p_4$ is no longer constant (there is a continuous exchange of momentum between the orbital and the attitude dynamics).

4.3 The system's uncoupled dynamics and equilibria analysis

4.3.1 Relative Equilibria of the Complete Dynamics

Relative equilibria of the system (4.15) are of the form:

$$\{\dot{q}_1\,,\,\dot{q}_3\,,\,\dot{q}_4\,,\,\ddot{q}_1\,,\,\ddot{q}_2\,,\,\ddot{q}_3\,,\,\ddot{q}_4\} = \vec{0} \tag{4.16}$$

This condition is satisfied at the following two initial conditions:

$$\begin{aligned} q_3 = q_4 = \zeta &= \pm\kappa\frac{\pi}{2} \qquad \kappa \in \mathbb{Z} \\ \dot{q}_2 &= \sqrt{\frac{\mu}{q_1^3} + \frac{3\mu(\hat{I}_1 + \hat{I}_2 + \alpha)(1 + 3\cos(2\,\zeta))}{4\,m\,q_1^5}} \end{aligned} \tag{4.17}$$

$$\begin{aligned} q_3 = -q_4 = -\zeta &= \pm\kappa\frac{\pi}{2} \qquad \kappa \in \mathbb{Z} \\ \dot{q}_2 &= \sqrt{\frac{\mu}{q_1^3} + \frac{3\mu(\hat{I}_1 + \hat{I}_2 + 3\alpha + \left[3(\hat{I}_1 + \hat{I}_2) + \alpha\right]\cos(2\,\zeta))}{4\,m\,q_1^5}} \end{aligned} \tag{4.18}$$

Two classes of equilibria identified in Sanyal and Bloch, Equations (12) and (13) in [22], do not exist in this model as they do not consider bodies as a distributed mass, thus effects of gravity gradient are neglected.

4.3.2   Uncoupled Dynamics

The previous system of equations in Eq. (4.15) shows that the orbital dynamics and the attitude dynamics are coupled. However, an analysis of the magnitude order of the terms in the equations highlights a very small dependency of the orbital dynamics on the attitude, provided the length scale of the 2-body system holds.

For systems orbiting around the Earth:

$$o\{q_1\} \simeq o\{\mathcal{R}\} \ , \ o\{\dot{q}_2\} \simeq o\{\frac{1}{\mathcal{T}_{Orb}}\}$$

$$o\{\mu\} \simeq o\{2\pi \frac{\mathcal{R}^3}{\mathcal{T}_{Orb}^2}\}$$

$$o\{\hat{I}\} \simeq o\{m \, \ell^2\} \ , \ o\{\dot{q}_3\} \simeq o\{\dot{q}_4\} \simeq o\{\omega_{Spin}\} \qquad (4.19)$$

$$o\{p_3\} \simeq o\{p_4\} \simeq o\{m \, \ell^2 \left(\frac{1}{\mathcal{T}_{Orb}} + \omega_{Spin}\right)\}$$

$$o\{p_2\} \simeq o\{m \frac{\mathcal{R}^2}{\mathcal{T}_{Orb}} + m \, \ell^2 \left(\frac{1}{\mathcal{T}_{Orb}} + \omega_{Spin}\right)\}$$

with: $\mathcal{R}$ magnitude order of the semi-major axis of the orbit; $\mathcal{T}_{Orb}$ magnitude order of the orbital period; m magnitude order of the mass of the system; ℓ magnitude order of the length of the bodies; ω_{Spin} magnitude order of the angular velocities of the bodies.

Hence, when $o\{\frac{\mathcal{R}^2-\ell^2}{\mathcal{T}_{Orb}}\} \gg o\{\ell^2\omega_{Spin}\}$, the reduced orbital dynamics follows as:

$$\begin{cases} \dot{q}_1 = & \frac{p_1}{m} \\ \dot{q}_2 \simeq & \frac{p_2}{mq_1^2} \\ \dot{p}_1 \simeq & -\frac{m\,\mu}{q_1^2} + \frac{p_2^2}{mq_1^3} \\ \dot{p}_2 = & 0 \end{cases} \qquad (4.20)$$

Moreover, going back to the Hamiltonian of Eq. (4.14), two components can be recognised. The first is a constant term in the reduced dynamics and it will be addressed as $\mathcal{H}_{Orb}$. The second is time dependent and it is several magnitude orders smaller than the first. This latter will be referred as the attitude dynamics Hamiltonian and identified

with the term $\mathcal{H}_{Att}$.

$$
\begin{aligned}
\mathcal{H} ={}& \mathcal{H}_{Orb} + \mathcal{H}_{Att} \\
\mathcal{H}_{Orb} ={}& -\mu \left(\frac{m}{q_1} + \frac{\hat{I}_1 + \hat{I}_2}{4q_1^3} \right) + \frac{(-p_2 + p_3 + p_4)^2 + p_1^2 q_1^2}{2\, m\, q_1^2} \\
\mathcal{H}_{0\ Att} ={}& \frac{1}{2\,\Delta} \left(\hat{I}_2 p_3^2 + \hat{I}_1 p_4^2 + \alpha\, p_3\, p_4\, \cos(\theta) \right) \\
\mathcal{H}_{1\ Att} ={}& \frac{1}{2} \frac{\mu}{q_1^2} \left[-\frac{3}{2} \left(\hat{I}_1\, \cos(2q_3) + \hat{I}_2\, \cos(2q_4) \right) + 3\,\alpha\, \cos(q_3)\cos(q_4) - \alpha\, \cos(\theta) \right] \\
\mathcal{H}_{Att} ={}& \mathcal{H}_{0\ Att} + \frac{1}{q_1}\, \mathcal{H}_{1\ Att}
\end{aligned}
$$

$$(4.21)$$

The assumption that the orbital dynamics does not depend on the attitude dynamics allows us to focus on the attitude dynamics only.

4.3.3   Equilibria of the Attitude Dynamics

Equilibria of the attitude motions are of the form:

$$
\begin{cases}
q_3 = \bar{q}_3 = const & \dot{q}_3 = 0 \\
q_4 = \bar{q}_4 = const & \dot{q}_4 = 0
\end{cases}
\tag{4.22}
$$

The condition on the dynamical system in order to satisfy these equations is:

$$
\begin{cases}
\dot{q}_3 = 0 & \dot{p}_3 = 0 \\
\dot{q}_4 = 0 & \dot{p}_4 = 0
\end{cases}
\tag{4.23}
$$

In the system (4.15) the following set of solutions can be obtained:

$$
\begin{cases}
p_3 = \dfrac{\bar{p}_2(\hat{I}_1 - \frac{\alpha}{2} c_\theta)}{\hat{I}_1 + \hat{I}_2 + m q_1^2 - \alpha c_\theta} \\[2mm]
p_4 = \dfrac{\bar{p}_2(\hat{I}_2 - \frac{\alpha}{2} c_\theta)}{\hat{I}_1 + \hat{I}_2 + m q_1^2 - \alpha c_\theta} \\[2mm]
\theta = 0 + k\pi \\[1mm]
s_{q_3} \wedge s_{q_4} = 0 \ \vee \ c_{q_3} \wedge c_{q_4} = 0
\end{cases}
\tag{4.24}
$$

It is important to consider that in this set the value of the momenta depend on q_1. *This implies that for circular orbits the condition will hold, however for elliptic orbits, where q_1 depends on time, there cannot be a natural stable equilibrium configuration in this coordinate frame.* Note again that q_1 would never be exactly constant due to a continuous exchange of energy and momentum with the orbital dynamics. However, these particular effects are small enough to be considered negligible.

In particular, the system (4.24) has the following equilibrium configurations:

$$\left(\kappa\,\pi\,,\,\kappa'\,\pi\right) \qquad \text{and} \qquad \left(\tau\,\frac{\pi}{2}\,,\,\tau'\,\frac{\pi}{2}\right)$$

$$\text{with} \qquad \kappa\,,\,\kappa' \in \mathbb{Z} \qquad \tau\,,\,\tau' \in \mathbb{Z}_0$$

(4.25)

4.3.4 Nonlinear Stability Analysis

Using Dirichlet's Theorem[1], stable equilibria will be identified as critical points of the Hamiltonian. The Hessian of the Hamiltonian at the equilibria, limited to the reduced dynamic variables only, can be expressed as a block diagonal matrix of the form:

$$H_{\mathcal{H}}|_{Equilibria} = \begin{bmatrix} \mathbf{D}_1 & \mathbf{0} \\ \\ \mathbf{0} & \mathbf{D}_2 \end{bmatrix}$$

(4.26)

After some algebraic manipulations, specific conditions are defined in order for $H_{\mathcal{H}}$ to be either positive or negative definite with respect to its two sub-matrices. In particular, the matrix $\mathbf{D}_2$ does not change with the equilibrium point. Its eigenvalues are:

$$\lambda_{1,2} = \frac{a_2 \pm \sqrt{b_2}}{\Delta}$$

$$\lambda_1\,\lambda_2 = \frac{c_2}{\Delta} \quad : \; c_2 > 0 \;\; \text{always}$$

(4.27)

This implies that the eigenvalues will always have the same sign[2] at $\Delta > 0$. In Eq. (4.27) when $\Delta > 0$ $a_2 > 0$ as

$$a_2 = mq_1^2\left(\hat{I}_1 + \hat{I}_2\right) + 2\Delta$$

(4.28)

and consequently $\mathbf{D}_2$ is positive definite. Because of the assumptions taken on the shape of the bodies, in this specific case Δ cannot be negative, however, for more complex cases, when the inequality is not satisfied, the configuration cannot be nonlinearly stable.

The eigenvalues of the matrix $\mathbf{D}_1$ are of the form:

$$\lambda_{1,2} = \frac{a_1 \pm \sqrt{b_1}}{c_1}$$

$$c_1^2\lambda_1\,\lambda_2 = a_1^2 - b_1^2 = d_1^2\,e_1$$

(4.29)

Table 4.1 lists the conditions on the eigenvalues of the matrix $\mathbf{D}_1$:

---

[1]Where the Hamiltonian function is considered as a Lyapunov function, e.g. see [79]

[2]That is $\mathbf{D}_2$ is negative or positive definite.

Equilibrium Point	e_1	a_1
$(\kappa\pi, \kappa\pi)$	$e_1 > 0$ always	$a_1 > 0$ always
$(\kappa\pi, \kappa'\pi)$	$e_1 > 0$	$a_1 > 0$
	if $Term_1 > 0$	if $Term_2 > Term_3$
$(\kappa\frac{\pi}{2}, \kappa\frac{\pi}{2})$	$e_1 > 0$ always	$a_1 < 0$ always
$(\kappa\frac{\pi}{2}, \kappa'\frac{\pi}{2})$	$e_1 > 0$ not always	$a_1 < 0$ always

Table 4.1: Analysis of the $\mathbf{D}_1$ eigenvalues. $\kappa, \kappa' \in \mathbb{Z}$ and $\kappa \neq \kappa'$

with[3]:

$$
\begin{aligned}
Term_1 =& \frac{\alpha}{2} p_2^2 q_1^3 (-\hat{I}_1 - \hat{I}_2 + \alpha) + (\hat{I}_1 + \hat{I}_2 + mq_1^2 + \\
& - \alpha)^2 \left[3\hat{I}_1\hat{I}_2 - \alpha(\hat{I}_1 + \hat{I}_2) + (\frac{\alpha}{2})^2 \right] \mu \\
Term_2 =& \mu \left[3 \left(\hat{I}_1 + \hat{I}_2 \right) - 2\alpha \right] (\hat{I}_1 + \hat{I}_2 - \alpha + mq_1^2)^2 \\
Term_3 =& \alpha p_2^2 q_1^3
\end{aligned}
\tag{4.30}
$$

Table 4.1 shows that:

1. The two equilibria where the bodies are perpendicular to the orbital radius are always unstable

2. The equilibrium in which the bodies are aligned with the orbital radius and are fully extended is always nonlinearly stable

3. The equilibrium in which the bodies are aligned with the orbital radius and they are closed lying one over the other is conditionally nonlinearly stable depending on the physical parameters of the system.

---

[3]Note that $3 \left(\hat{I}_1 + \hat{I}_2 \right) - 2\alpha > 0$ always, as it may be written $3[I_1 + I_2 + \epsilon(d_1 - d_2)^2] + \alpha$
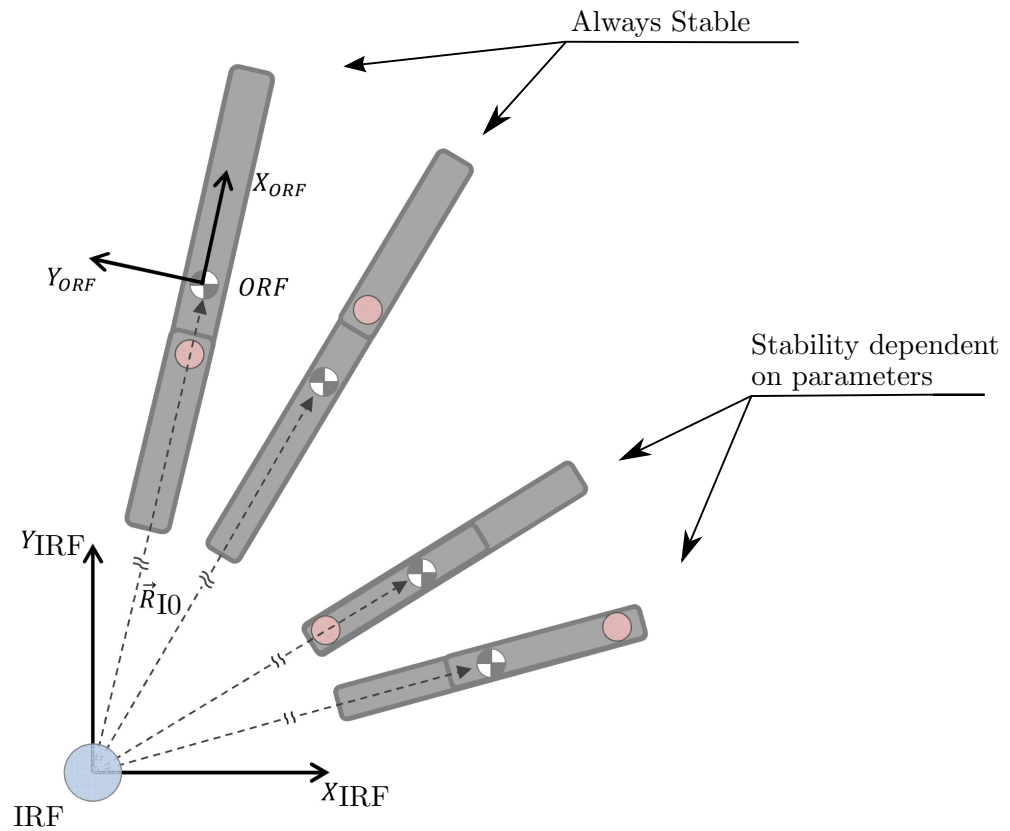
Figure 4.3: Illustration of the stable equilibrium configurations of the system. They apply only for circular orbits. Two unfolded cases in the upper part, two folded cases in the lower part.

4.4   The Zero-Velocity Energy Plot

As a consequence of the weak dependance of the orbital dynamics on the attitude dynamics, orbital trajectories of the system will be extremely close (a distance of magnitude order of centimeters[4]) to the orbital trajectories of the Keplerian two-body problem. Therefore, we focus the analysis on the attitude dynamics, which is described by the four configuration variables: q_3, q_4, p_3 and p_4.
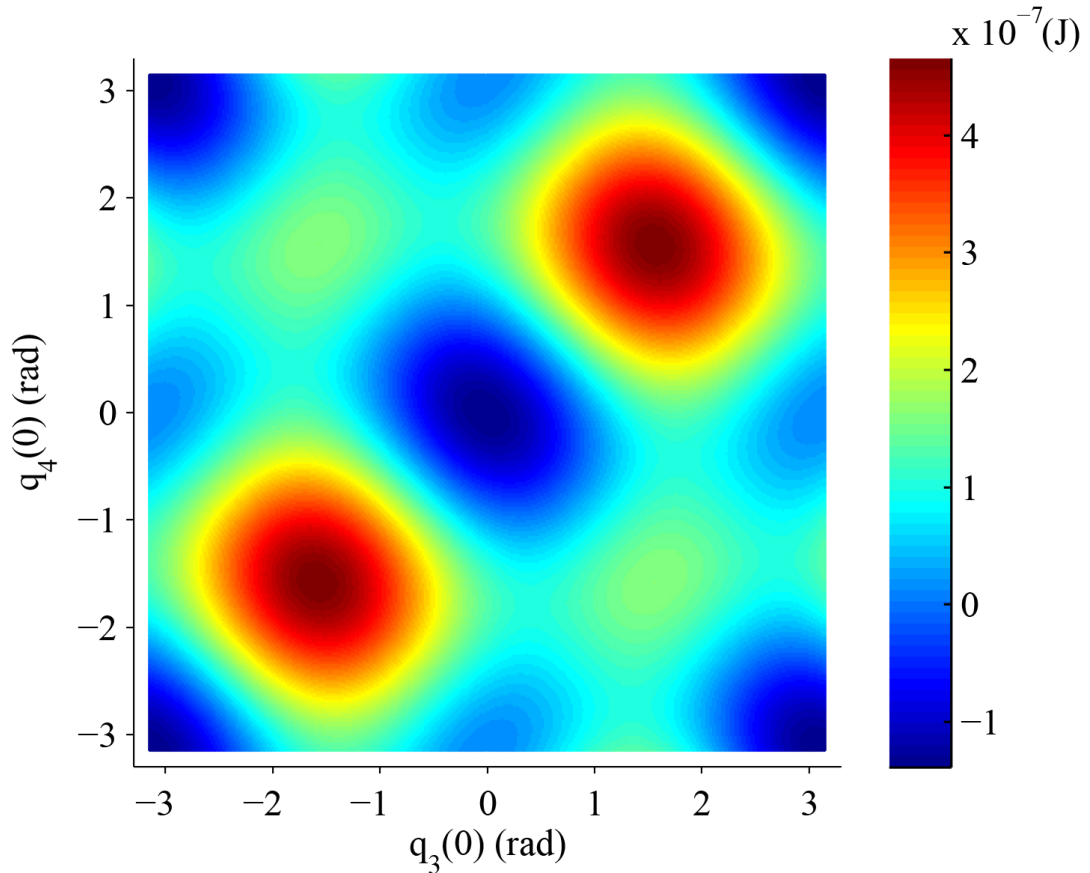
Figure 4.4: Density plot of the attitude mechanical energy of the system, $E_{Att\,0}$, as function of the attitude angles for a spacecraft in a circular orbit. Spacecraft details used are reported in Table 4.2.

Figure 4.4 shows a density plot of the total attitude mechanical energy $E_{Att\,0}$ for a circular orbit (the only case in which relative equilibria exist), with $E_{Att\,0} = \mathcal{H}_{Att} \mid \{\dot{q}_3 = 0 , \ \dot{q}_4 = 0\}$. For this particular case the data in Table 4.2 are used.

In Fig. 4.4, the Hamiltonian gradient is visible as variations in the colours. As the density plot uses darker colours for lower energy regions, where the lowest energy is

---

[4]It can be verified using Eq.s (4.15,4.20)

Variable	Value	Unit
l_1	50	cm
l_2	50	cm
d_1	25	cm
d_2	25	cm
m_1	1.5	kg
m_2	1.5	kg
$\mathbf{I}_1 = \frac{1}{12}m_1 l_1^2$	0.0078	$kg\ m^2$
$\mathbf{I}_2 = \frac{1}{12}m_2 l_2^2$	0.0078	$kg\ m^2$

Table 4.2: Data used for evaluating Fig.(4.4). Bodies are considered orbiting around the Earth on a nominal orbit circular at an altitude of 300km above the surface.

associated with the local minima, and brighter for the higher energy regions, where the highest energy is associated with the local maxima, all the equilibria are clearly shown by peaks and troughs of the potential. Hence, this analysis shows graphically the results derived in section 4.3. Furthermore, it gives a description of the distribution of $E_{Att\,0}$ in all the attitude angles' domain, providing indications of the dislocation and the size of the low-potential regions which contain stable equilibria and consequently periodic motions. Note that the equilibria of the class $(\kappa\pi, \kappa\pi)$ (refer to Table 4.1) correspond to a negative value of $E_{Att\,0}$; conversely those of the class $(\kappa\pi, \kappa'\pi)$ exist for a positive energy level.

As can be seen from equation (4.21), the total mechanical energy depends on the following physical parameters: relative positions of the hinges and the centers of mass; masses of the bodies; inertias of the bodies. The dependency of the motion on these parameters is shown using the zero-velocity energy maps. When the length of the second body is changed to $l_2 = 2\ m$ a bifurcation occurs and the conditionally stable equilibria are brought to instability. The new zero velocity map is shown in Figure 4.5.

The comparison between Figures 4.4 and 4.5 show that a variation in the parameters cause a variation in size of the highest potential region and the lowest potential region (i.e. those associated with the classes of equilibria: $(\kappa\frac{\pi}{2}, \kappa\frac{\pi}{2})$ and $(\kappa\pi, \kappa\pi)$). When the bifurcation occurs, the lowest potential region becomes large enough to include the mid-low potential region containing the conditionally stable equilibrium.

Figure 4.6 shows the limiting case where the size of one body is many magnitudes of order larger than the other. This behaviour is very close to the one of single rigid body problem, where the stability regions are only dependent on one attitude angle .
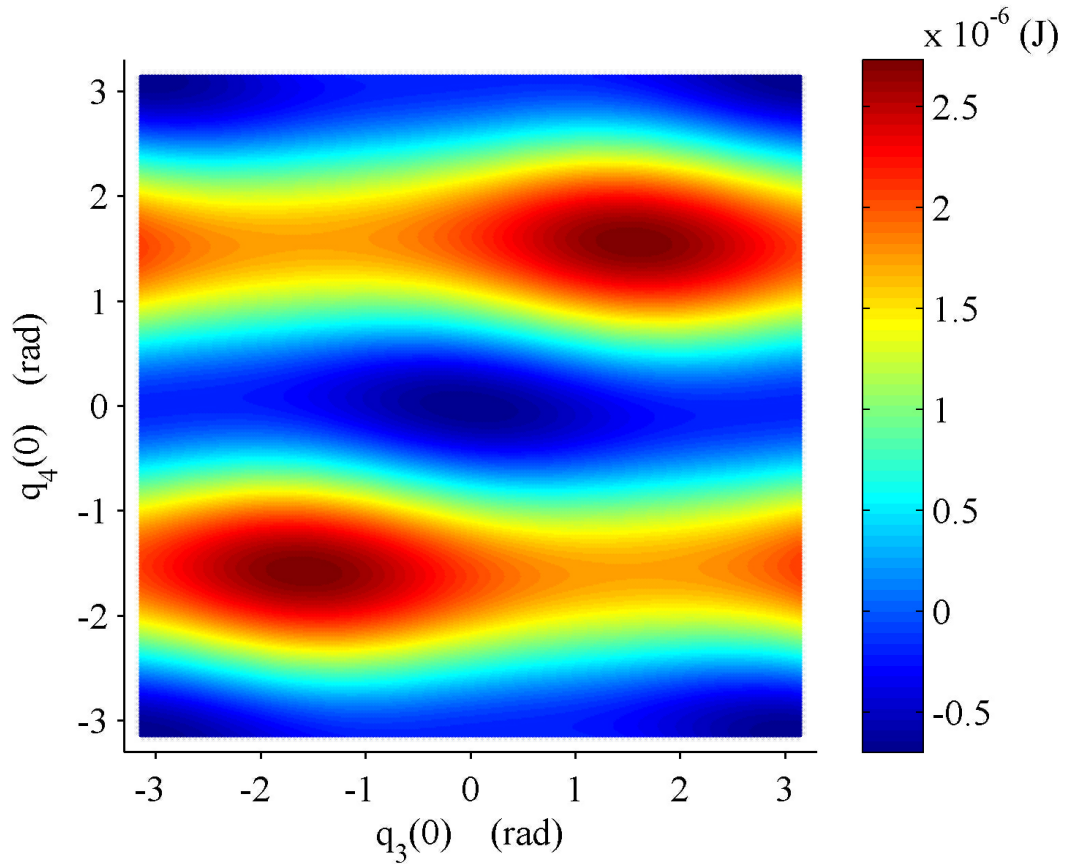
Figure 4.5: Density plot of the attitude mechanical energy of the system, $E_{Att\,0}$, as function of the attitude angles for a spacecraft in a circular orbit. The particular set of system parameters used in this case makes some of the former nonlinearly stable configurations unstable.

4.5   Dynamical systems analysis

In the previous sections of the chapter a model has been derived and analysed using the Hamiltonian function. In order to provide a global description of the system behaviour, different representations of the dynamics will be shown using various analysis tools. The dynamic equations (4.15) are integrated and the trajectories analysed. Inspired by common techniques of integration using symplectic integrators, Hamiltonian and total angular momentum are introduced in the differential equations set in order to keep control of the numerical errors and to drive the accuracy of the integration always below a maximum relative error of an order of $o(10^{-13})$ on the initial values of the
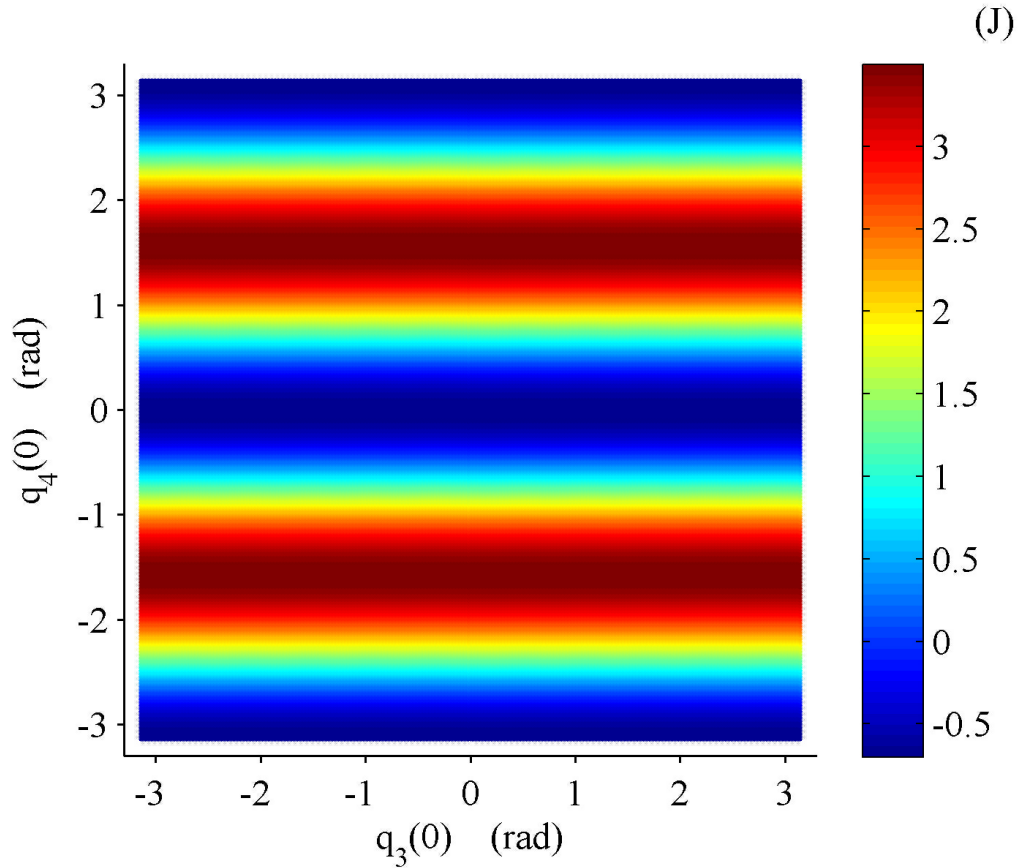
Figure 4.6: Density plot of the attitude mechanical energy of the system, $E_{Att\,0}$, as function of the attitude angles for a spacecraft in a circular orbit, in the limiting case where the size of a body is negligible with respect to the size of the other one.

conserved quantities[5]. The conditions in Table 4.2 are used in the next sections.

4.5.1 Phase Plots

The initial analysis of the system involves simple phase plots which capture the regular and chaotic motion. Figures 4.7a, 4.7b, 4.8a, 4.8b, 4.9a and 4.9b are the projections of the trajectories of the system in the $\{q_3, q_4\}$ plane and in the $\{q_3, \dot{q}_3\}$.
The trajectory in Figure 4.7a is generated by an initial condition "relatively close" to the stable equilibrium point. The trajectory in Figures 4.8a and 4.8b are generated by

---

[5]This solution has been preferred to the reduction of the system introducing into the equations the conserved quantities, in order to effectively have way of monitoring the magnitude order of the error.

an initial condition "relatively far" from both the stable and the unstable equilibrium points. This is identified as "quasi-periodic" as it evolves in a bounded region on almost periodic trajectories without ever exactly coming back on themselves.
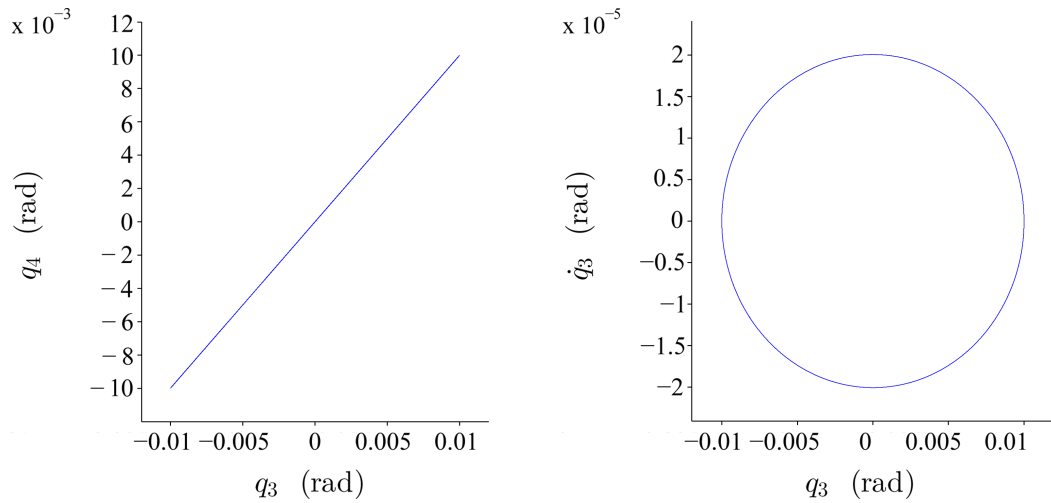
(a) Phase plot in the plane $\{q_3, q_4\}$. The motion repeats itself over a line moving from left to right then from right to left.

(b) Phase plot in the plane $\{q_3, \dot{q}_3\}$. The motion repeats itself over a circle from this perspective and it moves clockwise.

Figure 4.7: Case 1: periodic behaviour.
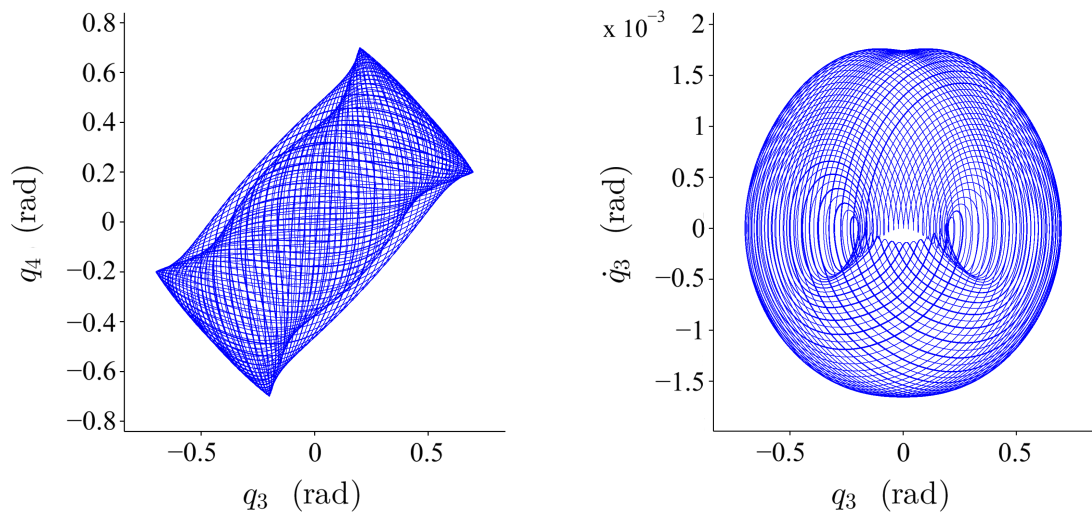
(a) Phase plot in the plane $\{q_3, q_4\}$.

(b) Phase plot in the plane $\{q_3, \dot{q}_3\}$.

Figure 4.8: Case 2: this plot shows a regular motion even though not periodic. This motion is classified as quasi-periodic.

Figure 4.8b suggests the presence of a chaotic attractor[6]. However, observing motions generated by initial conditions in the neighborhood of this particular case (Case 2), high sensitivity on the initial conditions has not been shown and qualitatively similar

---

[6]See for instance the typical phase plot of a Lorentz attractor.

trajectories have been observed [7]. This last elements agree with the identification of this behaviour as quasi-periodic. By this it is meant that the system regularly does not evolve on the same trajectory, but on a trajectory "close" to the previous one, thus showing irregular periodicity and remaining confined in a limited region of the phase space. Figures 4.9a and 4.9b are generated starting with an initial condition "relatively close" to the unstable equilibrium point. The motion becomes highly irregular and chaotic.

(a) Phase plot in the plane $\{q_3, q_4\}$.

(b) Phase plot in the plane $\{q_3, \dot{q}_3\}$.
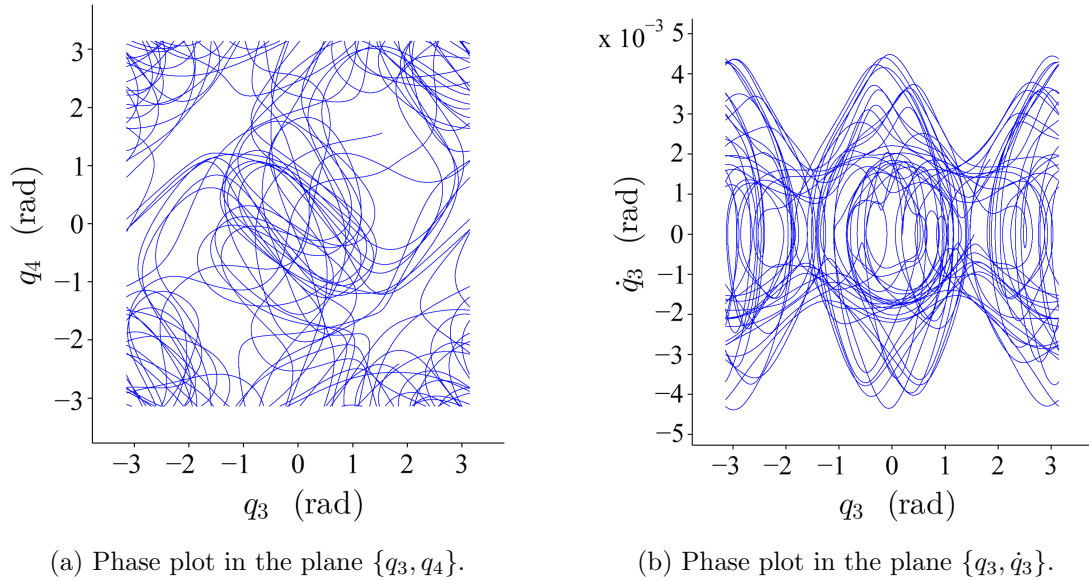
Figure 4.9: Case 3: the behaviour exhibited is clearly irregular and fully aperiodic. It is identified as chaotic.

4.5.2 Poincaré Map

In order to further investigate the same system's evolutions from another perspective, first Poincaré sections are used, hence, a Poincaré map is constructed. Poincaré sections are a standard technique to inspect complex systems. These are projections of phase spaces where a snap shot is taken whenever the trajectory intersects a prescribed plane in the phase space. The Poincaré mapping[8] is a collection of points sampled in a regular way from the phase portraits.

For this problem Poincaré sections are constructed sampling the state of the system when:

$$\{\theta_1 = 0, \omega_1 \geq 0\} \tag{4.31}$$

Figure 4.10 shows characteristic Poincaré sections of the problem, which are projections

---

[7]Presumably, this particular motion is characterized by irrational frequencies, typical element of quasi-periodicity.

[8]Also referred as a stroboscopic technique. For further details on Poincaré maps, see [80] or [81].

of the trajectory in the plane $\{q_4, \dot{q}_4\}$. The left plot, Fig. 4.10a, referres to the regular motion and the whole trajectory is described simply by two dots indicating a periodic orbit. The right plot, Fig. 4.10b, referes to Case 2. Here regularity is shown and the system's natural evolution is completely described by a set of aligned points. This feature is typical of quasi-periodic motions, for instance, see the Hénon-Heiles Poincaré section for $e = 0.08333$ in [82]. Figure 4.10c, refers to Case 3. This type of behaviour can be recognised in the Poincaré sections of many systems such as the double pendulum, the three body system or again in the Hénon-Heiles equations for $e = 0.12500$, see [82].
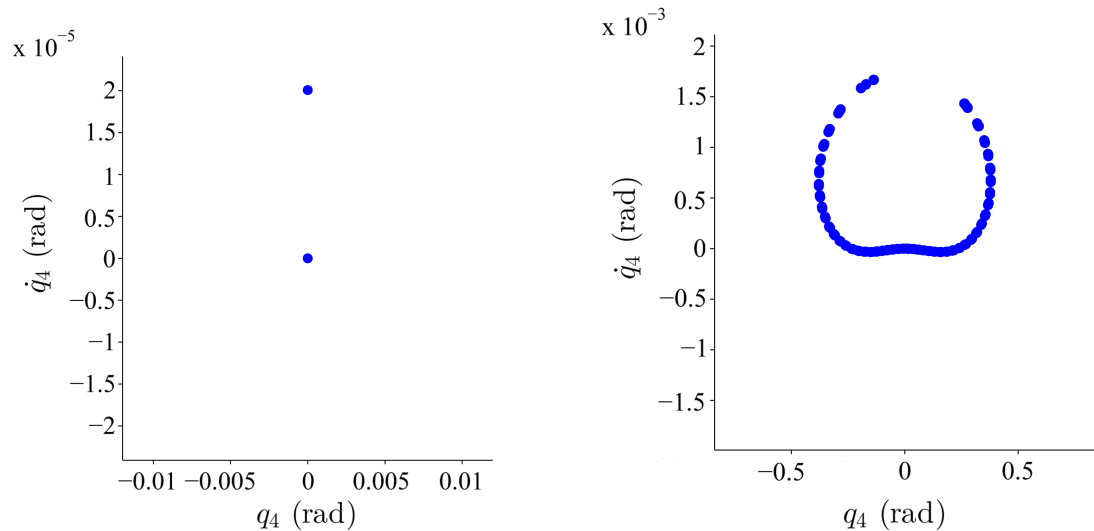
(a) Case 1: the whole motion is represented by two points only.

(b) Case 2: the motion is represented by a series of alligned points.
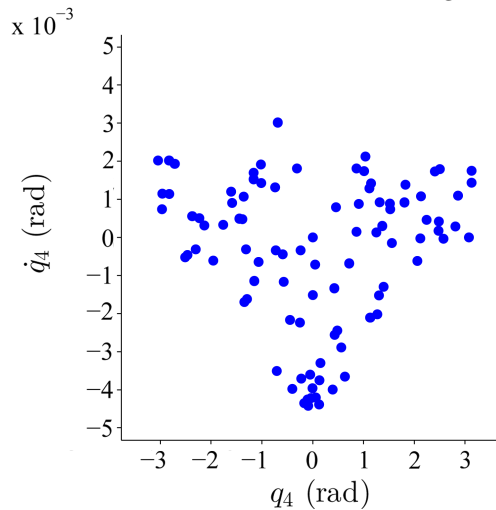
(c) Case 3: the motion is dense over an area.

Figure 4.10: Poincaré sections in the plane $\{q_4, \dot{q}_4\}$.

A Poincaré map is constructed collecting all the Poincaré sections generated from initial conditions belonging to $E_{Att\ 0} = 3 \times 10^{-8}$ J. This energy state is chosen as it shows a wide range of different qualitative behaviours. Fig. 4.11a shows the initial conditions belong to the indicated energy.
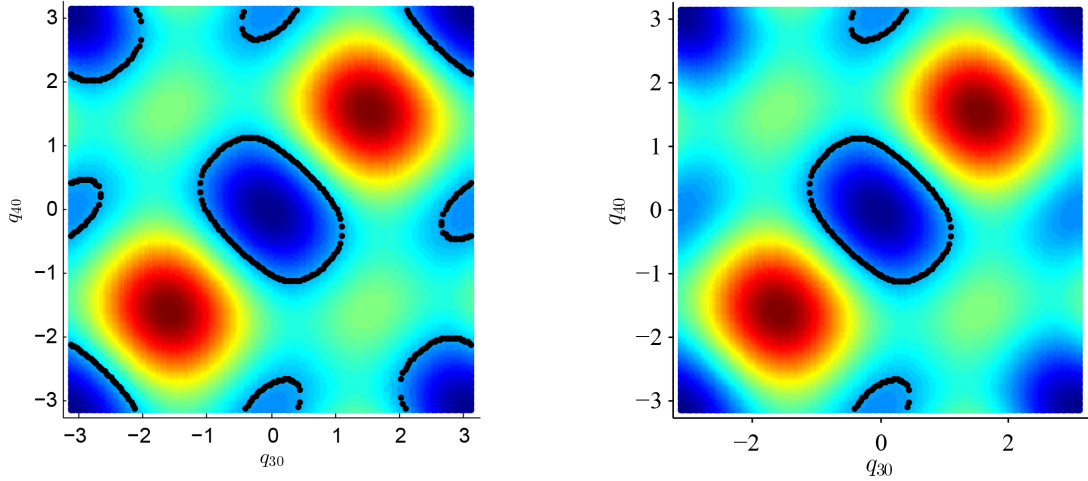
(a) Points in black provide an indication of all the initial conditions satisfying $E_{Att\ 0} = 3 \times 10^{-8}$ J.

(b) Points in black are in the sub-set generating the Poincaré map.

Figure 4.11: Zero-velocity energy map of the problem as resulting from the parameters shown in Table 4.2.

Each initial condition shown in Fig.4.11a has been integrated and the trajectory analysed. Only a subset generated a non-empty Poincaré section according to the rules defined in Eq. (4.31) and this subset is shown in Fig.4.11b. All the initial conditions excluded from the set shown in Fig.4.11a, produce trajectories which either do not cross $\theta_1 = 0$ or evolve with negative angular velocity $\omega_1 < 0$. The collection of all the Poincaré sections is shown in Fig. 4.12.

Chaotic motion can be seen where the region is dense on the set, as shown in subfigures 4.13 a) and d) show a formation of points in an appartent disordered and randomic disposition. Invariant Tori can be observed in the regions shown in subfigures b) and c). Both are characterised by a sequence of concentric discontinuous lines in a layout typical of quasi-periodic motions. In particular, the bottom left plot contains several closed-curve like formations of points, which stand out in Fig. 4.12 as well as "island-shaped" at the top of the plot. This kind of structure clearly suggests the presence of motions developing into invariant tori. Furthermore, the boundary between different qualitative behaviours is fuzzy. There are some particular cases where the quasi-periodicity is weak and the motion can be classified as either quasi-periodic or chaotic.
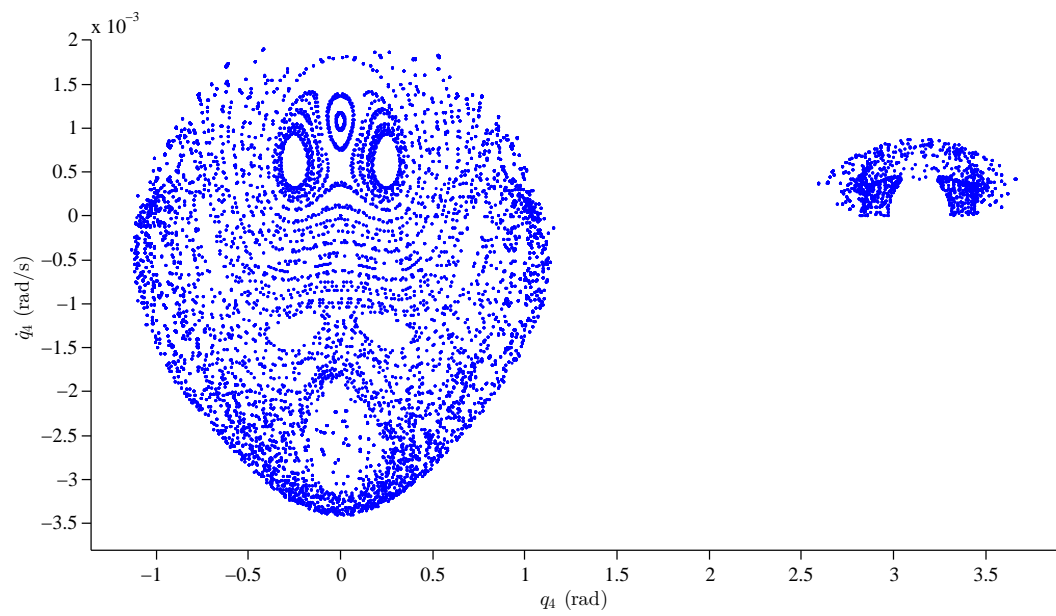
Figure 4.12: Poincaré map of the problem relative to $E_{Att\ 0} = 3 \times 10^{-8}$ J. The map is made of two distinct parts.
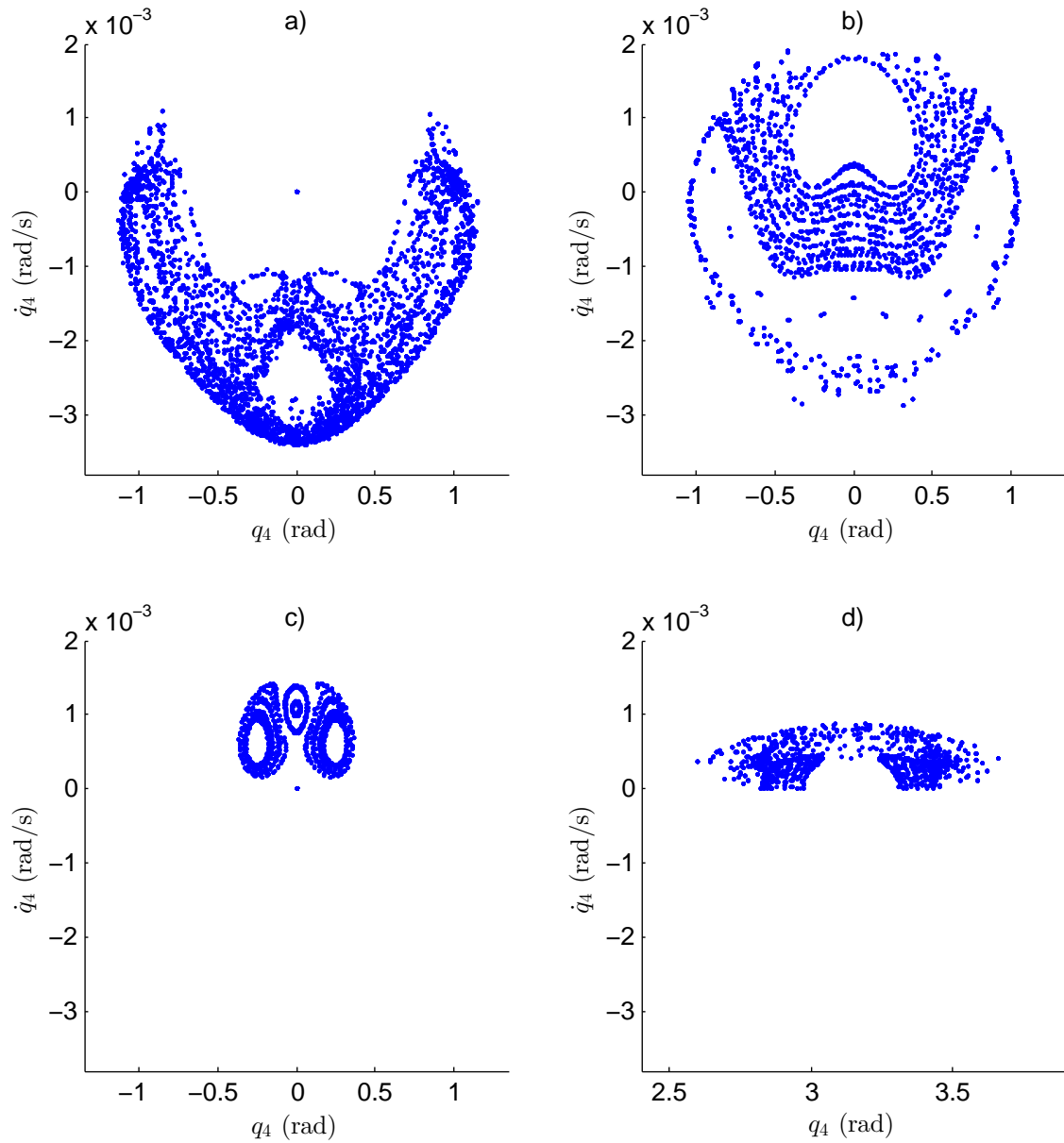
Figure 4.13: Sub-maps of the Poincaré map of Fig. 4.12. For the sake of clarity, the whole map has been broken down into 4 sub-maps drawn by isolating the relative initial conditions associated with each of them.

4.5.3 Lyapunov Characteristic Exponents

LCEs are a concept introduced by Lyapunov in the early 20th century but largely addressed by the academic community from the 1960 (refer to [83], [84], [85] and [86] for an overview). Roughly speaking they are a measure of the mean exponential rate of divergence of system's trajectories. A single LCE is calculated from a specific initial condition, thus it provides a local description of the behaviour of the system. This piece of information is contained in a real number and therefore a density map of the LCEs can be illustrated, collecting a quantity of information in an image. The calculation of a Lyapunov Exponent can rarely be done analytically, thus only with the introduction of modern computers the LCEs have become an effective tool in studying complex dynamical systems. This makes them a relatively new technique which, in particular, have found application in astrodynamics, [87, 88], and in fluid dynamics, [89, 90].

In this chapter we use the Gram-Schmidt orthonormalisation method, [91], to compute the LCE spectrum.

Given the flow along an orbit $x(t) = \phi^t(x_0)$, the evolution of a nearby orbit could be expressed as $x'(t) = \phi^t(x_0 + \delta x_0) = x(t) + u(t)$. Given $x'(0) = x_0 + u_0$, $u(t)$ can be defined using the tangent map $u(t) = M_{x_0}(t)u_0$, with the transition matrix $M_{x_0}(t) = \partial\phi^t(x_0)/\partial x_0$. The spectrum of the matrix $M_{x_0}^T(t)M_{x_0}(t)$ is real and positive and the generic eigenvalue can be defined as $\mu_k^2(t)$. Then, the Lyapunov Exponent associated with the initial condition x_0 can be defined as:

$$\lambda_k = \lim_{t \to +\infty} \frac{1}{t} \log \mu_k(t) \tag{4.32}$$

where $\lambda_k \in \mathbb{R}$. When the LCE associated to one of the configuration variables is positive, two very close initial conditions will evolve exponentially diverging along that direction. Similarly, a negative exponent represents converging motions and a zero exponent can be considered representative of invariant motions.

Figure 4.14 shows the evolution in time of LCEs associated to the variable q_3 in Case 1 (continuous line at the bottom) and Case 3 (dashed line at the top). By definition, LCEs are exact only for infinite time of integration, however, note that the LCE decreases exponentially to its value. Moreover, the right tail of the LCE curve is not flat but presents periodic oscillations. This attitude is maintained in all the cases calculated. In order to overcome these problems and to provide a reliable LCE value, two actions have been taken: first a minimum time integration of 200000 seconds is used; hence, only the last 10000 seconds are considered and over this range a mean value is calculated.

Following this procedure, LCEs are used as a further tool to investigate the dynamics of the system. Table 4.3 summarises the values obtained for Cases 1, 2 and 3:
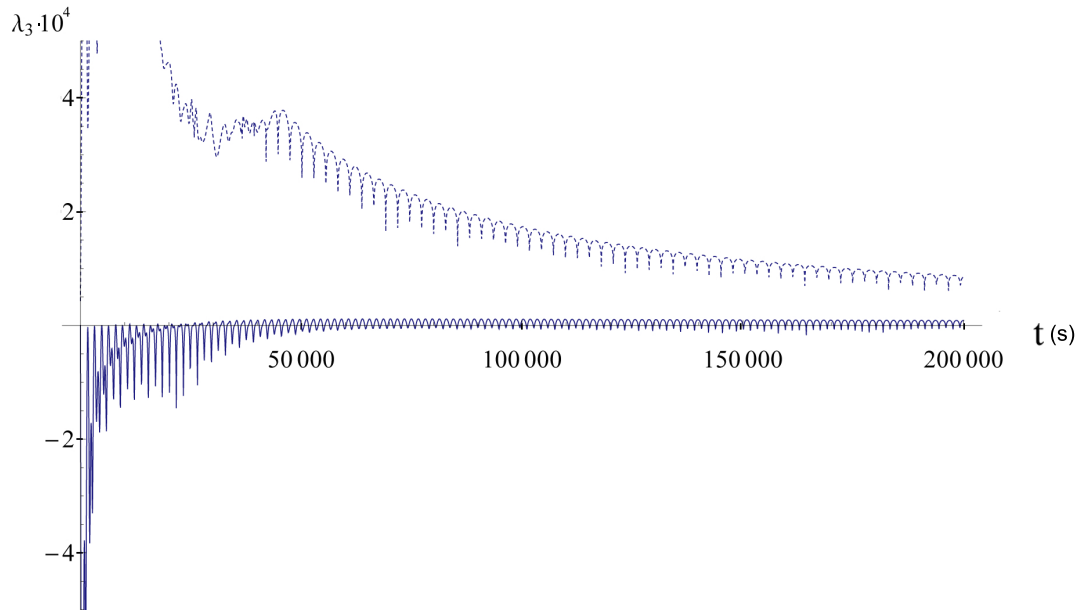
Figure 4.14: Evolution in time of the Lyapunov Characteristic Exponent λ_3 associated with the configuration variable q_3 during the system integration. The curve at the bottom refers to Case 1, the one at the top refers to Case 3. It is observed that the trend exhibited is qualitatively exponential. Thus, a minimum time of integration is required in order to let the LCE converge its value.

Once normalised with respect to the magnitude of the largest, the LCEs can be compared to one another, see tab. 4.4.

Note that the first case (periodic motion) shows one negative LCE and another one two orders of magnitude smaller than the ones of the 3rd case; the second case (identified as quasi-periodic) shows LCEs one magnitude order smaller than the ones of the 3rd case.

The presence of different orders of magnitudes in tables 4.3 and 4.4, together with the results of the phase portraits and the Poincaré sections prove that different kinds of motion are related to clearly distinct LCEs. This implies that different regions of motions will be shown in a density map: see Fig. 4.15. Every dot of the plot represents an initial condition $\{q_3(0), q_4(0), 0, 0\}$. Its color is associated with the value of the LCE calculated. Darker colors represent lower LCE values. Because the initial angular velocities are both null, nonlinearly stable equilibria appear explicitly in the map which can be taken as an equilibria stability analysis as well. The markers 1, 2 and 3 correspond to the initial conditions used to generate the three cases showed in the first part of the chapter. As verified from the Eq. (4.24), equilibria are located at the center of the darkest regions surrounded by a white ring. In practice, these white rings define the regular regions around the stable equilibrium points (analogous to separatrices in phase plots).

Shadowed areas surrounding the rings, in this particular problem, are associated with

Case	λ_3	λ_4
1st	0.55	-0.18
2nd	1.93	1.68
3rd	6.88	1.60

Table 4.3: LCEs values. Values are scaled by a factor 10^{-5}.

Case	λ_3	λ_4
1st	0.08	-0.02
2nd	0.28	0.22
3rd	1	0.23

Table 4.4: LCEs values normalised with respect to the larger calculated.

quasi-periodic regions. Far from those shadowed regions, the colour of the map becomes much brighter and chaotic regions arise. Cases 1, 2 and 3 belong, respectively, to the regular, the quasi-regular and the irregular region of motion. In Fig. 4.15, the initial conditions used to generate these specific cases are marked by the numbers 1, 2 and 3. It is interesting to note, comparing Fig. 4.15 with Fig. 4.4, that the characteristic elliptic form of the potential in the zero-velocity map has a different orientation with respect to the white rings at the centre of the LCE map. This indicates that regular motions are more likely to be found along the bisectrix of the first quadrant of the plane $(q_{30} = q_{40})$ while quasi-periodic and chaotic along the bisectrix of the fourth quadrant. This has been clearly observed in the construction of the Poincaré map. Finally, when Fig. 4.4 and Fig. 4.15 are compared it can be seen that the regular motions exist in the negative potential region associated with the nonlinearly stable equilibria. Furthermore, due to numerical errors, it can be observed that the regions surrounding the parameter dependent equilibria are not displayed in the LCE map.

The richness of information enclosed in the map has a significant value as it provides, in a single image, a quasi-global description of the system's behaviour. As each map is related to only two configuration variables, in order to obtain a global description of the system a collection of maps is required so to cover the entire phase space. Moreover, all this comes at the cost of a moderate numerical computational effort[9].

---

[9]The computation of the LCE map, using Wolfram Mathematica® on a Windows® platform, required two full days using a pc with a 3.10GHz quad-core processor and a RAM of 8 Gb.
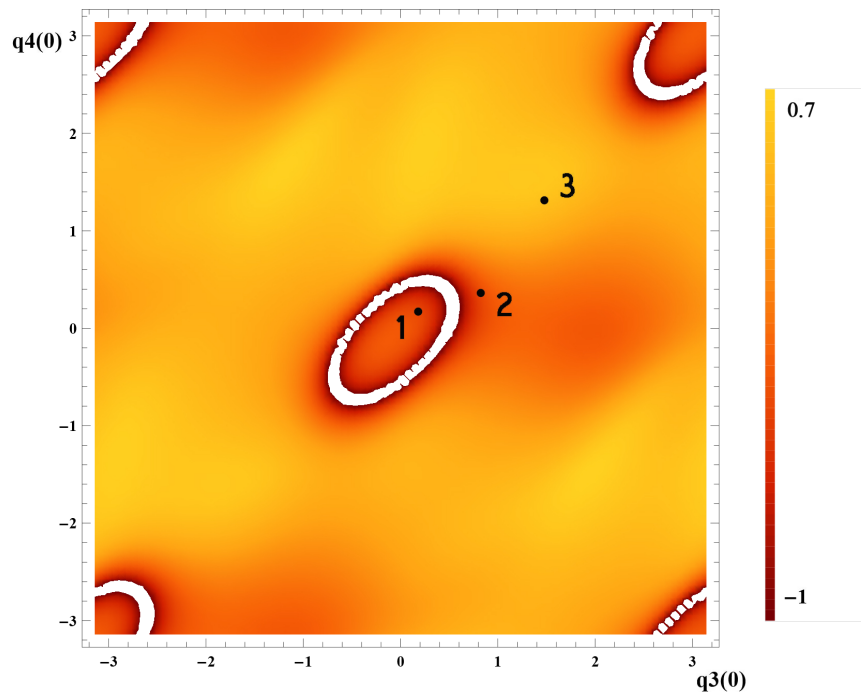
Figure 4.15: LCE density map of the planar gravitational two-body problem.

4.6   Large Reconfiguration Manoeuvre Design

In order to demonstrate how the identified natural dynamics can be used to develop efficient controls, this section designs a large reconfiguration manoeuvre by exploiting the system's natural motions. A couple of nano-satellites, endowed with reaction wheels, forms the dual spacecraft system detailed in tables 4.5 and 4.6. The two-body system is considered to be inserted on a nominal equatorial circular orbit around the Earth at an altitude of 600km above the surface. Initially the manoeuvre is designed assuming that only the gravity and control torques act on the system. Later, air drag is introduced and a comparison with a PD controller is made.

Quantity	Variable	Value	Unit
Body 1 Length	l_1	90	cm
Body 2 Length	l_2	90	cm
Hinge distance from BRF_1	d_1	45	cm
Hinge distance from BRF_2	d_2	45	cm
Body 1 mass	m_1	2	kg
Body 2 mass	m_2	2	kg

Table 4.5: Spacecraft characteristics

Quantity	Value	Unit
Max Wheel Speed	6000	rpm
Max Torque	20	mNm
Wheel Inertia	0.001	$Kg\,m^2$

Table 4.6: A schematic overview of each reaction wheel's characteristics.

4.6.1   Manoeuvering Strategy

Results of the dynamical investigation show that only a limited number of configurations can be in a steady state. Therefore, it is reasonable to design a manoeuvre from one of the equilibria to another and consider the following initial and final positions:

$$(q_3\,,\,q_4)_{t=0} = (\pi\,,\,0)\;(rad) \qquad ; \qquad (q_3\,,\,q_4)_{t=t_f} = (0\,,\,0)\;(rad)$$

In this case, the starting configuration is a parameter dependent stable equilibrium as bifurcation occurs depending on the spacecraft's parameters. This characteristic can possibly be used to drive the system out of its initial state with a very limited effort. The desired target configuration corresponds to a global minimum of the attitude mechanical energy. As a consequence, once a motion is started, it suffices to dissipate a quantity of attitude kinetic energy equal to the difference of attitude potential energy between initial and desired configurations and the system will converge toward the

target. This result can be obtained by the application of guidance control torques, $T_{ctrl\,1}$ and $T_{ctrl\,2}$. In order to introduce these torques in the dynamical system, the Euler-Lagrange equations of motion are considered:

$$\frac{d}{dt}\frac{\partial \mathcal{L}}{\partial \vec{\dot{q}}} - \frac{\partial \mathcal{L}}{\partial \vec{q}} = \vec{T} \tag{4.33}$$

with $\vec{T} = \{0\,,\,0\,,\,T_{ctrl\,1}\,,\,T_{ctrl\,2}\}$. It is immediate to verify that their presence causes a variation of the total system's mechanical energy, i.e. variation in time of the system's Hamiltonian, equal to:

$$\frac{d\mathcal{H}}{dt} = \dot{q}_3\,T_{ctrl\,1} + \dot{q}_4\,T_{ctrl\,2} \tag{4.34}$$

In order to guarantee a monotone decreasing of $\mathcal{H}$, the control can be designed as:

$$T_{ctrl\,1} = -k\,\dot{q}_3 \qquad T_{ctrl\,2} = -k\,\dot{q}_4 \qquad \text{with} \quad k \in \mathcal{R}^+ \tag{4.35}$$

Note that, at constant mechanical energy, highest spinning rates will takes place in the surroundings of the minimum attitude energy position. Based on all the considerations illustrated, a preliminary outline of the control strategy is proposed:

1. Change the system's parameters in order to make the initial stable configuration unstable

2. Destabilise the system by applying a small disturbances

3. Dissipate the energy excess by applying the designed control torques (Eq. (4.35), until the target configuration is reached.

This last phase of the control strategy ensures that the total mechanical energy of the system is gradually reduced until the minimum energy state is reached. This state is determined uniquely and is the nonlinearly stable equilibrium configuration. Figure 4.16 shows a bifurcation diagram of the system based on a variation of length and hinge position of the second spacecraft. In particular the function Ψ illustrated is a combination of the eigenvalues of the Hessian of the Hamiltonian[10].

$$\Psi(l_2, d_2) = \begin{cases} \frac{1}{\Lambda}\prod_{i=1}^{4}\lambda_i & \text{if} \quad \lambda_i \geq 0\ \forall i \quad \text{or} \quad \lambda_i \leq 0\ \forall i \\[2ex] -\frac{1}{\Lambda}\left|\prod_{i=1}^{4}\lambda_i\right| & \text{otherwise} \end{cases} \tag{4.36}$$

with λ_i eigenvalues of $H_{\mathcal{H}}|_{(\pi,0)}$, and $\Lambda = \max(|\Psi|)$ over the domain considered. Assuming that the spacecraft is able to vary the relative position of the hinge without significantly altering the position of its center of mass it can be observed that increasing d_2 to $0.78m$ instability is introduced. ZVMs for the two different system configurations

---

[10]Refer to Section 4.3.4
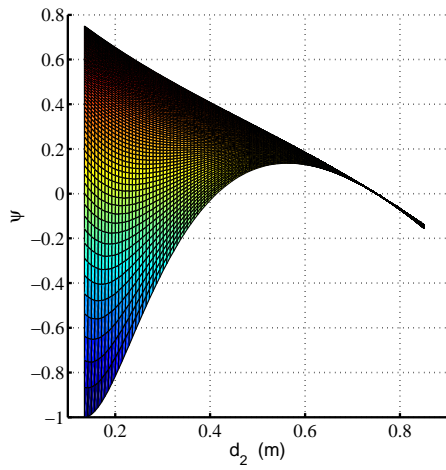
(a) Function $\Psi(l_2, d_2)$. Projection on the (d_2, Ψ) plane.
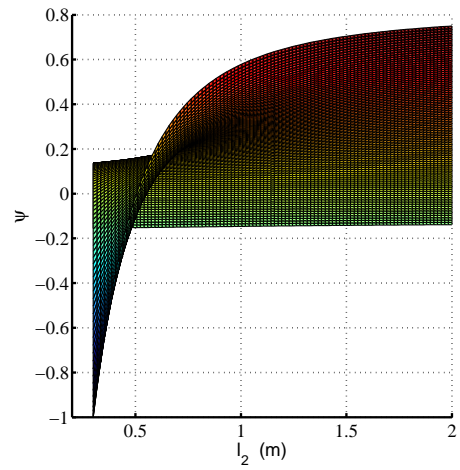
(b) Function $\Psi(l_2, d_2)$. Projection on the (l_2, Ψ) plane.
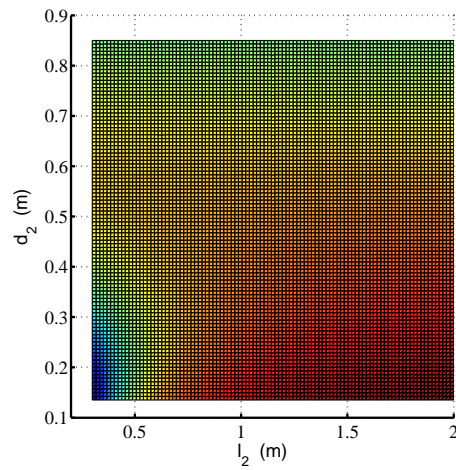
(c) Function $\Psi(l_2, d_2)$. Projection on the (l_2, d_2) plane.

Figure 4.16: Bifurcation diagram of the system based on the variation of length and hinge position of the second spacecraft.

are shown in Fig. 4.17. By comparing them, it can be observed that a "corridor" between initial and target configuration is created. As the motion is chaotic far from the equilibria, in Fig.4.17b, it is reasonable to expect that the natural motion passes in a neighborhood of the target. Nonetheless, at the same time, Fig.4.17a shows that the energy gap between initial and desired configuration is larger in the d_2 extended configuration than in the d_2 retracted configuration, Fig.4.17a. Consequently, once the
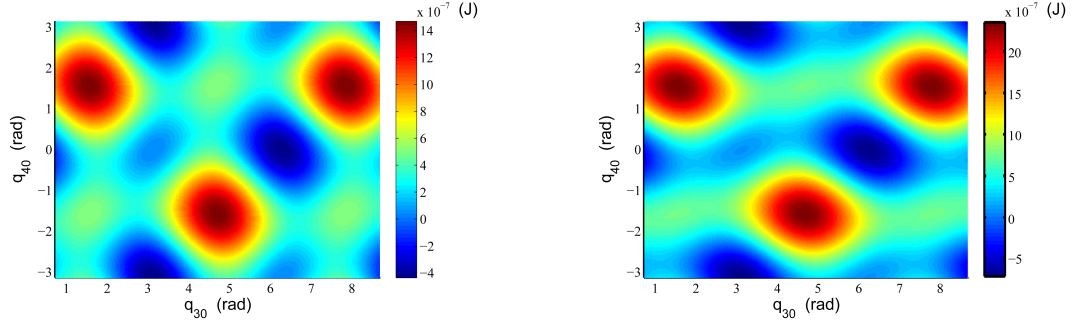
(a) System's zero velocity map for $d_2 = 0.45$ m.

(b) System's zero velocity map for $d_2 = 0.78$ m.

Figure 4.17: Zero velocity map for two values of d_2. Note that the colour scales are not the same. Furthermore, the case with d_2 extended presents higher maxima and lower minima.

motion is bounded around the target, reducing d_2 to its initial value will reduce the control effort required in the final phase. The design of the control strategy for the reconfiguration manoeuvre assumes, then, the following final form:

1. Increase the distance of the hinge from the center of mass of the secondary spacecraft, d_2, from $0.45m$ to $0.78m$

2. Destabilise the system by applying a small disturbance torque

3. Wait for the natural motion to be bounded in a desired neighborhood of the target configuration, ρ_d, to reduce the hinge distance to its original value

4. Wait for the natural motion to move into a desired neighborhood of the target configuration, ρ_{ctrl}, before applying the control in order to reduce the manoeuvre time, due to small spinning rates

5. Transfer the energy excess by applying the design control torques until the target configuration is reached

Note that the time required to accomplish the manoeuver depends both on the time scale of the natural evolution and on the intensity of the control action. If the control torques applied are too weak the system will converge slowly to the target due to a slow dissipation of the energy. On the contrary, if the control torques applied are too large, angular velocities will be kept very limited and the trajectory will evolve very slowly

anyway. In order to avoid an excessively long manoeuvre time, the control parameter ρ_{ctrl} is introduced, so that the control action takes place only over a limited region of the domain.

4.6.2 Results with gravity force only

A first manoeuver has been performed considering the gravity only. For this case, control gain, k, and radius of the controlled area, ρ_{ctrl}, have been chosen through a quick optimisation process aimed to minimise: final distance to the target, final bodies' tumbling rates and final reaction wheels' spinning rates. It has been arbitrarily decided to retract the hinge to its initial value once the trajectory falls within a pre-set distance of $1\,rad$ from the target.

Results show that the control effort required is extremely limited both in terms of torques magnitude and overall energy consumed (a consumption index has been defined as the integral of the absolute value of the torques over the time). Due to the slow dynamics, a minimum manoeuvering time of roughly 11 hours has been found in order to get sufficiently close to the target. Details are reported in Table 4.7:

Quantity	Variable	Value	Unit
Manoeuvre Time	t_f	11.11	hrs
Final distance to the target	q_n	$1.228\ 10^{-4}$	rad
Final bodies' spinning rate	$\dot{q}_n$	$1.971\ 10^{-7}$	rad/s
Final body 1 wheels' spinning rate	ws_1	0.1852	rad/s
Final body 2 wheels' spinning rate	ws_2	-0.1412	rad/s
Energy consumption index	E_{ctrl}	$7.7\ 10^{-4}$	$N\,m\,s$

Table 4.7: Results of the reconfiguration manoeuvre for the case where only gravity and control forces are considered.

where:

$$q_n = \sqrt{q_3(t_f)^2 + q_4(t_f)^2} \qquad \dot{q}_n = \sqrt{\dot{q}_3(t_f)^2 + \dot{q}_4(t_f)^2}$$

$$E_{ctrl} = \int_0^{t_f} (|T_{ctrl\,1}| + |T_{ctrl\,2}|)\,dt \tag{4.37}$$

The trajectory followed in the manoeuvre is shown in Figure 4.18 in the $\{q_3, q_4\}$ plane. A limited torque of order of magnitude of $10^{-6}\ Nm$ has been applied for 1 second as a disturbance to move the system out of the equilibrium. Then the system, unstable, moves uncontrolled toward the (q_3, q_4) plane's origin. As a result of the optimisation, once within a distance of approximately $\rho_{ctrl} = 0.4\,rad$ from the target, the control

torque is applied to halt the system, with $k = 2.56 \ 10^{-4}$. The attitude energy along
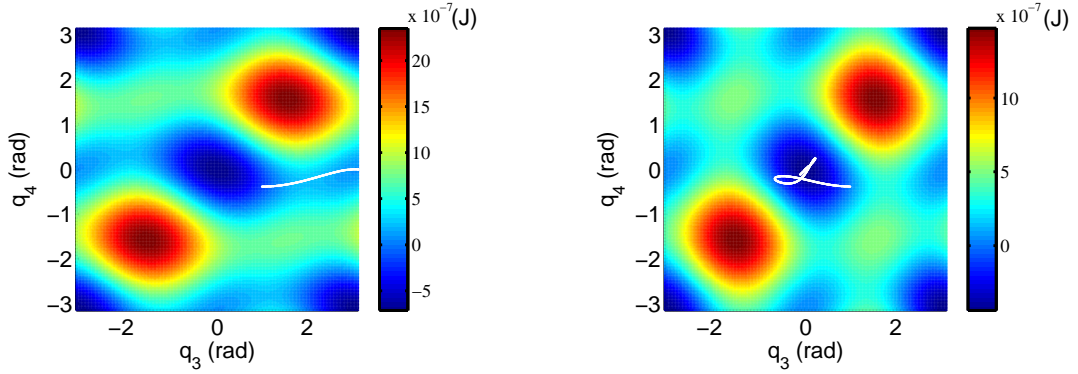
(a) Trajectory part with $d_2 = 0.78 \ m$.   (b) Trajectory part with $d_2 = 0.45 \ m$.

Figure 4.18: Shown by the white solid lines, the trajectory in the (q_3, q_4) domain divided in two phases. In (a) from the beginning to the retraction of the hinge in body 2. In (b) in the last part of the manoeuver when $d_2 = 0.45 \, m$. On the backgrounds, the zero velocity maps relative to the two system configurations.

the path is shown in Fig. 4.19b. It can be seen that effect of the hinge manoeuvering is to increase and then decrease the mean value of the energy. In particular, the hinge retraction takes place at $t_{d_2} = 19191 \ s$. Conversely, control activates $185 \ s$ after, at $t_{ctrl\,on} = 19376 \ s$, causing the final dumping of the energy to its minimum. Figure 4.20 shows that the control torques applied have the same order of magnitude, i.e. $10^{-6} Nm$, of the disturb torque applied initially, which can be observed on the far left-hand side of fig. 4.20b. As a remark, it shall be noted that the disturbance's intensity has influence on the manoeuver time; a very small disturbance will cause the system to diverge from its position very slowly. In this case the disturbance torque has been set as: $T_{ctrl\,1} = 0$, $T_{ctrl\,2} = (q_4 - q_3)\,10^{-6}$.
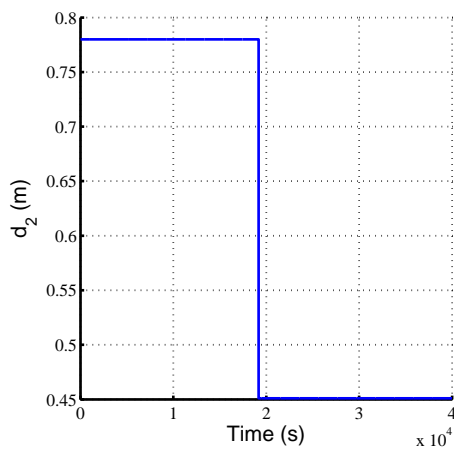
(a) Distance of the hinge from the body 2 center of mass as function of time.
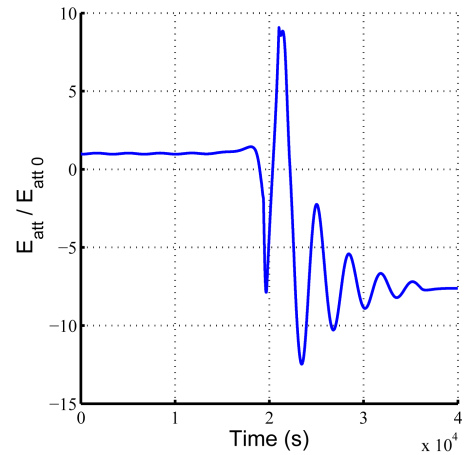
(b) Attitude energy as function of the manoeuver time. The quantity is normalised with respect its value at the initial time, i.e. $E_{att}(0)$

Figure 4.19: Description of the test case manoeuver: in (a) $d_2(t)$; in (b) $E_{att}(t)$.
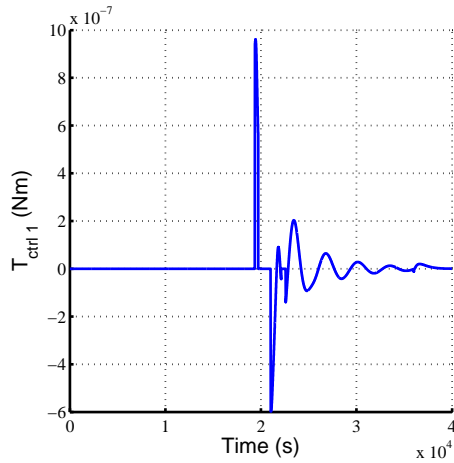
(a) Body 1 control torques.
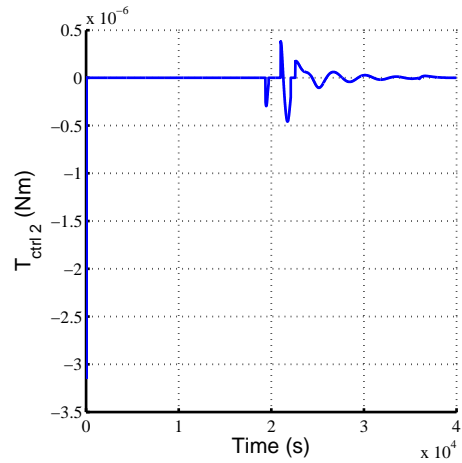
(b) Body 2 control torques.

Figure 4.20: Control torques actuated.

4.6.3 Air Drag

To consider a more realistic case air drag is introduced. The following model is adopted for the air drag torque, [73]:

$$ADT_1 = \frac{1}{2} l_{cm\,1} \rho_{air} v_{wind}^2 Cd_1 A_{wind\,1} \cos(q_3)$$
$$ADT_2 = \frac{1}{2} l_{cm\,2} \rho_{air} v_{wind}^2 Cd_2 A_{wind\,2} \cos(q_4)$$

(4.38)

where: $l_{cm\,i}$ is the displacement of the geometric centre from centre of mass for the i-th body; ρ_{air} density of the air at the orbit altitude; v_{wind} velocity of the wind; Cd_i the drag coefficient of the i-th body - both are taken as 2, which is a standard value for preliminary studies in cases equivalent to this considered, see [73] for instance; $A_{wind\,i} \cos(q_i)$ the area exposed to the wind for the i-th body - here it is considered the following approximation $A_{wind\,i} = l_i\, 0.1$, with l_i the length of the body. All the equilibria continue to exist, displaced, in case, to the position where air drag torques are balanced by the gravitational torques. It can be verified that, for each body, the configurations parallel to wind are not subject to any displacement. In particular, new displaced equilibria can be exactly obtained using the Euler-Lagrange equations, see Eq. (4.33) where both air drag and control torques are introduced in the dynamical system using the vector $\vec{T}$. By solving the system (4.33) for $\ddot{q}_3 = \ddot{q}_4 = 0$ the new equilibria are derived. For the case considered the following parameters are used:

$$l_{cm\,1} = 0.02\,m \qquad\qquad l_{cm\,2} = -0.02\,m$$
$$\rho_{air} = 1.5600\,10^{-13}\,Kg/m^3 \quad v_{wind} = \dot{q}_2\,q_1\,m/s$$
$$Cd_1 = Cd_2 = 2$$
$$A_{wind\,1} = A_{wind\,2} = 0.09\,m^2$$

Note that a very simple atmospheric model is used and the density of the air will be considered as constant. Figure 4.21 shows how the attitude angles of the bodies displace by varying d_2. Figure 4.22 provides a description of the intensity of the air drag action depending on the attitude configuration for this mission. In particular, the colour used for each point of the domain is dependent on the sum of the air drag torques acting on the bodies; blue dark colours indicate low torques regions while red bright colours indicate high torque regions. Nonlinear stability of the new equilibria can not be determined a priori and should be addressed in detail again, however, this is out of the scopes of this section. To the ends of manoeuvre design, only the linear stability of the initial and target configurations have been studied numerically and resulted to be, respectively, stable or unstable depending on parameters and always stable. In this case, no disturbance torque may be expected to be required as the displacement of the equilibria, due to the air drag, depends on the system's parameters and a variation of a system parameter, i.e. a variation of d_2 will destabilise the system and trigger a
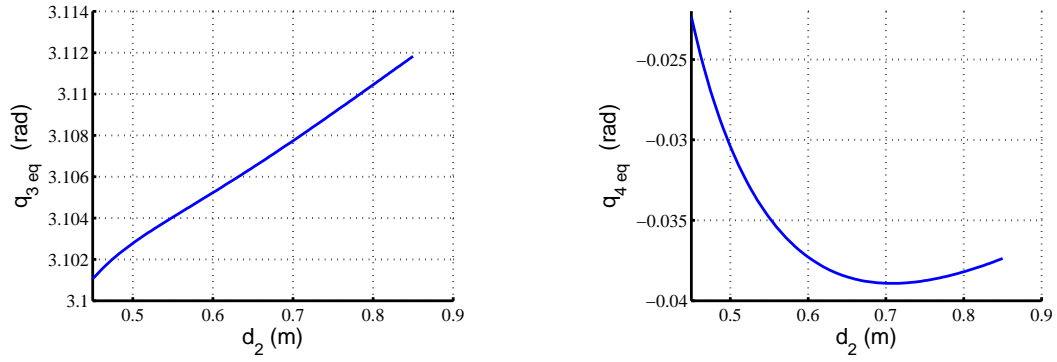
(a) Value of the Body 1 attitude angle at the equilibrium depending on d_2.

(b) Value of the Body 2 attitude angle at the equilibrium depending on d_2.

Figure 4.21: Displacement of the initial equilibrium point, caused by the presence of air drag, depending on d_2.
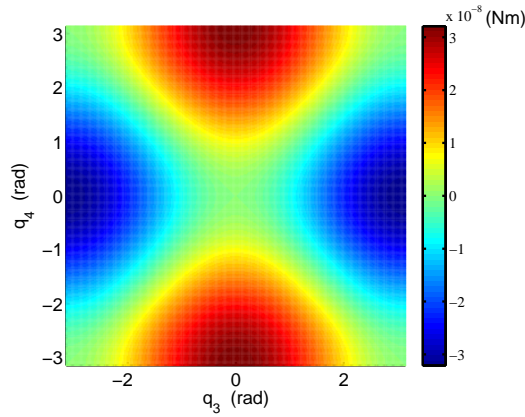
Figure 4.22: Intensity of the air drag effects as function of the system configuration. The effects are measured as the sum of the torques produced on each body.

natural motion.

The mission considered in this section will start from the new displaced position of the parameter-dependent stable equilibrium and the target is the new displaced configuration of the nonlinearly stable point:

$$(q_3, q_4)_{t=0} = (3.421, 0.87) \ (rad) \qquad ; \qquad (q_3, q_4)_{t=t_f} = (0.087, -0.087) \ (rad)$$

The same control strategy adopted previously will be used for this case, with the only difference that no disturbing action will be required once the system is destabilised. As in the previous case, an optimisation of the controller parameters has been run in order to minimise final distance to the target, final bodies' tumbling rates and final reaction wheels' spinning rates. However, in this case, the parameters optimised have been: k, ρ_d and ρ_{ctrl}. Results are detailed in Table 4.8. As it is evident, the air drag aids the manoeuver significantly reducing the manoeuvre time to roughly 2 hours. The

Quantity	Variable	Value	Unit
Manoeuvre Time	t_f	2.27	hrs
Final distance to the target	q_n	$1.4914\ 10^{-6}$	rad
Final bodies' spinning rate	$\dot{q}_n$	$1.6991\ 10^{-7}$	rad/s
Final body 1 wheels' spinning rate	ws_1	0.0475	rad/s
Final body 2 wheels' spinning rate	ws_2	-0.3790	rad/s
Energy consumption index	E_{ctrl}	$7.8\ 10^{-3}$	$N\,m\,s$

Table 4.8: Reconfiguration manoeuvre results using the designed manoeuvre strategy when gravity and air drag are considered.

trajectory followed, see Fig.4.23, is shorter than in the previous case. This element is evident in Fig.4.24a, where a direct approach to the target is shown. In the simulations extension rate and retraction rate of the hinge have an absolute value of 1 cm/s. Results show that the control effort required is extremely small both in terms of torques' magnitude and overall energy consumed (a consumption index has been defined as the integral of the absolute value of the torques over the time). Figure 4.25 shows that the control torques applied have the an order of magnitude of 10^{-6} Nm. It shall be noted that no control action is taken approximately for the first 5500 s, which is when the manoeuvre is uncontrolled for nearly 70% of its duration. Hinge extension and retraction are shown in Fig. 4.26a. The first takes place after 60 s of simulated time, there the system maintains its initial position, see the far left hand side of the plot. The retraction takes place after 5000 s from the beginning of the simulation and it is clearly visible in the central part of the plot. By comparing Figures 4.19b and 4.26b, a different response of the system can be observed through the attitude energy variation. While in Fig. 4.19b, there is a number of oscillations before, in Fig.4.26b the energy converges smoothly to the equilibrium and the only oscillation shown is due to the hinge contraction and the final control action.
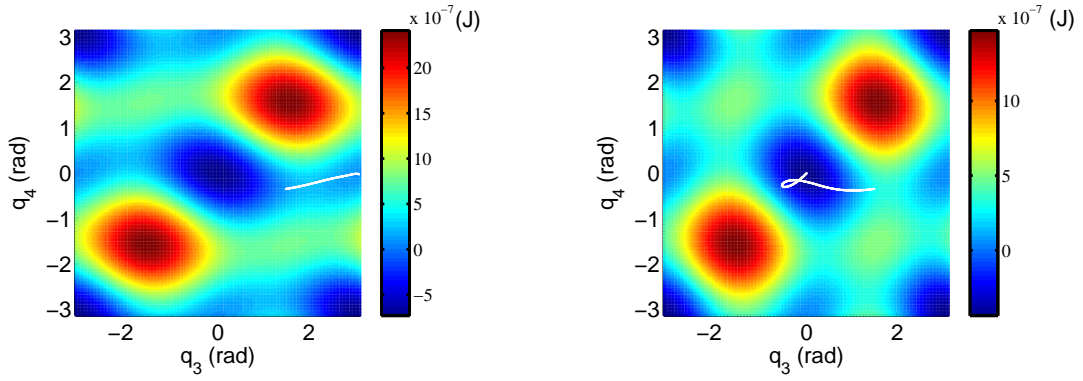
(a) Trajectory part with $d_2 = 0.78\,m$.

(b) Trajectory part with $d_2 = 0.45\,m$.

Figure 4.23: Shown by the white solid lines, the trajectory in the q_3, q_4 domain divided in two phases. In (a) from the beginning to the retraction of the hinge in body 2. In (b) the last part of the manoeuver when $d_2 = 0.45\,m$. On the backgrounds, the zero velocity maps relative to the two system configurations.
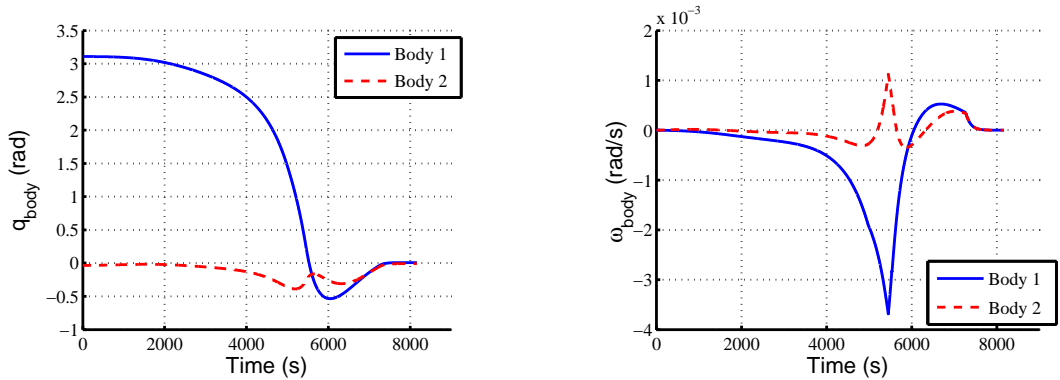
(a) Trajectory in the attitude angle space.

(b) Trajectory in the angular velocity space.

Figure 4.24: Description of the trajectory considering independently the bodies' attitudes and spinning rates.
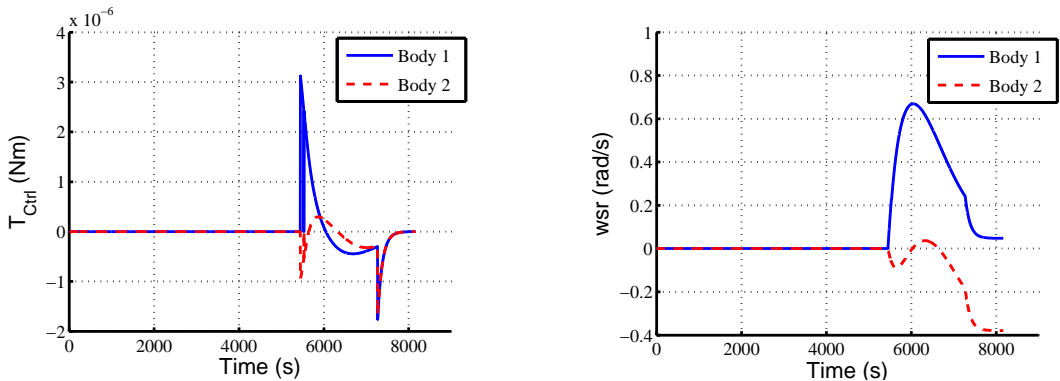
(a) Body 1 control torques.

(b) Body 2 control torques.

Figure 4.25: Control torques actuated by the attitude control system of the bodies.
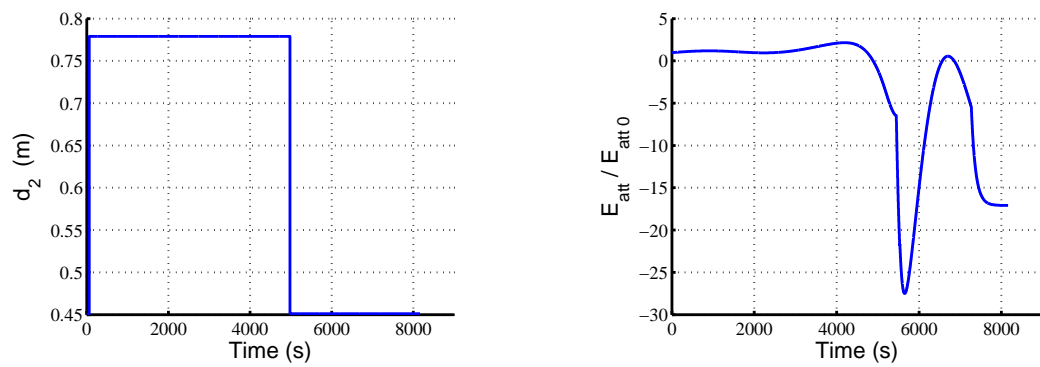
(a) Distance of the hinge from the body 2 center of mass as function of time.

(b) Attitude energy as function of the manoeuver time. The quantity is normalised with respect its value at the initial time, i.e. $E_{att}(0)$

Figure 4.26: Description of the test case manoeuver: in (a) $d_2(t)$; in (b) $E_{att}(t)$.

4.6.4   Comparison with a standard PD controller

For the purpose of comparison, the same objective as in section 4.6.2 is addressed using a simple PD controller. Although this may be considered an unfair comparison as, in this case, no variation of the system's parameters is introduced, PID controllers are considered a standard in engineering due to their simplicity and their efficacy and reliability in a wide range of applications (both with linear and nonlinear systems). Therefore the comparison puts in relation the tailored control with an engineering standard. This, additionally, allows an undirect, but immediate, correlation with any other control technique.

The maximum manoeuver time is taken from previous results and equal to $t_f = 2\,hrs\,16\,min\,12\,s$. The controller has the following form:

$$T_{ctrl\,1} = -k_p\,(q_3 - q_{3\,target}) - k_d\,\dot{q}_3 \quad T_{ctrl\,2} = -k_p\,(q_4 - q_{4\,target}) - k_d\,\dot{q}_4 \qquad (4.39)$$

Using again the same functional, control gains has been set via numerical optimisation, i.e. gains are chosen in order to have the minimum amount of wheels' accumulated angular momentum required to reach the final configuration satisfying the desired tolerance and within the time t_f.

$$k_p = 4.2289\,10^{-6} \quad k_d = 3.9326\,10^{-4} \qquad (4.40)$$

In this case, a control effort is required to drive the system out of the initial configuration, which remains a stable one. This effort is generated by the proportional terms of the controller. Furthermore, the same terms will force the system to move towards the target configuration, however, this action will introduce a certain amount of energy into the system that will have to be dissipated by the derivative terms. Therefore, a less efficient manoeuvre is expected. Results detailed in Table 4.9 have been obtained. As

Quantity	Variable	Value	Unit
Manoeuvre Time	t_f	2.27	hrs
Final distance to the target	q_n	$2.062\,10^{-5}$	rad
Final bodies' spinning rate	$\dot{q}_n$	$3.9745\,10^{-6}$	rad/s
Final body 1 wheels' spinning rate	ws_1	$0.5687\,10^{-3}$	rad/s
Final body 2 wheels' spinning rate	ws_2	$0.2176\,10^{-3}$	rad/s
Energy consumption index	E_{ctrl}	$4.92\,10^{-2}$	$N\,m\,s$

Table 4.9: Reconfiguration manoeuvre results using a PD controller - both gravity and air drag considered.

resulting from the optimisation, at an approximately equal manoeuvre precision, the

amount of stored angular momentum in the reaction wheels, with the PD controller, is almost negligible. In order to achieve this result, the trajectory followed in the config-uration space, Figures 4.27a, 4.27a and 4.28a, follows a number of oscillations around the target before settling on it. The manoeuvre is controlled during all its time and the control torques are one order of magnitude larger than in the previous case. The result is that the control energy consumption index is an order of magnitude higher than the former, as well. Note that the energy index provides an undirect measure of the work done by the actuators' torques in the manoeuvre and it should not be related to the energy consumed by the reaction wheels. In particular, different kinds of actuators may execute exactly the same manoeuvre, i.e. producing the same control torques in time, with different costs in terms of energy required to feed the devices. However, the work done by the control torques will always be the same. Therefore, having an index of the work done by the control torques allows to directly compare these cases with any other case, even with those where different kinds of actuators are used.   Note that saturation

(a) Trajectory part with $d_2 = 0.78\ m$.

(b) Trajectory part with $d_2 = 0.45\ m$.
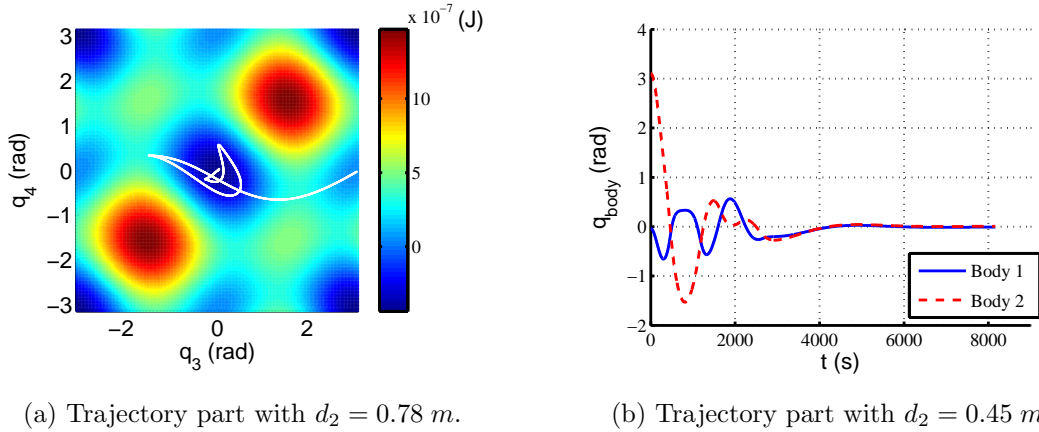
Figure 4.27: Evolution of the bodies' attitude angles described in the q_3, q_4 plane, (a), with the system's zero velocity map in the background, and against time (b).

of reaction wheels has been included in the simulations, therefore the amount of stored angular momentum can never be greater than the wheels capacity.
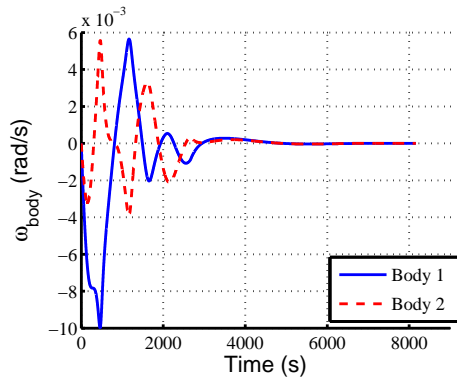
(a) Distance of the hinge from the body 2 center of mass as function of time.
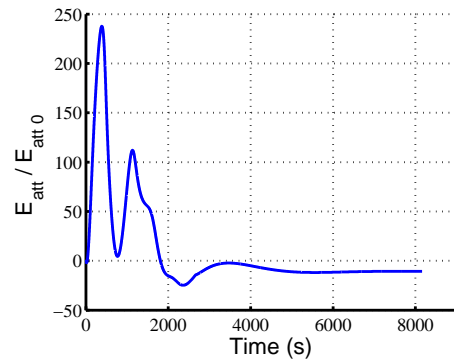
(b) Attitude energy as function of the manoeuver time. The quantity is normalised with respect its value at the initial time, i.e. $E_{att}(0)$

Figure 4.28: Description of the test case manoeuver: in (a) $d_2(t)$; in (b) $E_{att}(t)$.
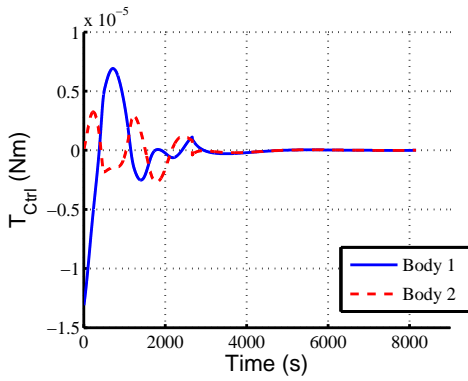
(a) Body 1 control torques.
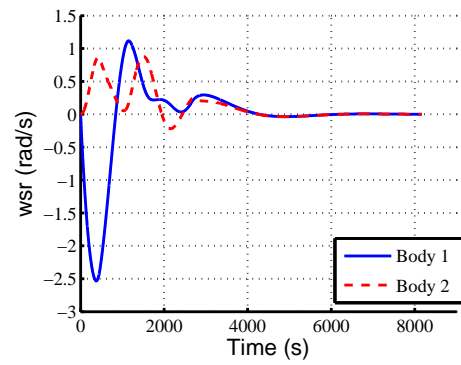
(b) Body 2 control torques.

Figure 4.29: Control torques actuated by the attitude control system of the bodies and relative reaction wheel spinning rates.

4.7 Summary of the dynamical investigation

The use of multi-body systems in space engineering presents new challenges for space mission design. In this work the nonlinear natural dynamics of a two-rigid-body system under an ideal central gravitational field is studied. The zero-velocity energy plots show that varying the parameter set causes an expansion or contraction of the size of the global maximum and minimum energy regions. At the bifurcation, connections are created between the minima. Consequently, the region of the conditionally stable equilibrium is surrounded by a lower energy region. Phase portraits and Poincaré sections highlight the existence of three different behaviours: regular, quasi-regular and chaotic. The stable equilibria are surrounded by regions of periodic motion. On the contrary, unstable equilibria are surrounded by regions of chaotic motion. In the remaining domain, quasi-periodic motions arise. The Poincaré map reveals that the transition from quasi-periodic behaviour to chaotic is not clearly defined as weakly chaotic motions are observed. Moreover, the map is evidence that there are energy levels where this wide variety of behaviours co-exist. LCEs are calculated over the domain when the initial angular velocities are set to zero, similarly to the zero-velocity maps. Once normalised with respect to the greatest value calculated, LCEs are plotted using a density map. Results show how the regular motion regions are almost clearly bordered by white rings which separate them from the other kinds of motion. Comparison between Fig. 4.4 and Fig. 4.15 shows that these rings lie within the lowest energy regions associated with the nonlinearly stable equilibria. Moreover, the orientation of the white rings indicates that regular motions exist in part of the bisectrix of the first and third quadrant of the (q_{30}, q_{40}) plane and in its neighbourhood.

The analysis provided here has several practical implications for real spacecraft multi-body systems. For example, the presence of both periodic and chaotic orbits suggests the possibility to use natural motions to achieve desired configurations saving fuel. Moreover, in terms of control, different strategies may be used depending on the qualitative behaviour of the system. In chaotic regions using a chaotic controller, see for instance the OGY method, [92], or a Pyragas continuous time-delay control (DFC), may be more efficient, [93]. Despite its very simple form, comparable to a standard PID controller, a DFC controller is based on the basic properties of chaotic systems[11] and hence are, in general, more efficient to stabilise the system on periodic motions.

In terms of system design, the fact that the nonlinear stability of one kind of equilibria depends on the design parameters, suggests that the system can be designed to directly affect the stability of certain configurations. For example, the length of a body of the spacecraft can be chosen to induce instability or stability as shown in section 4.

---

[11]i.e. a chaotic set, on which the trajectory of the chaotic process lives, has embedded within it a large number of unstable periodic orbits (UPOs) - as stated in [93].

4.7.1 Summary of the Manoeuvre Design

Extension of the practical implications of this work have been addressed. The time scale of the natural attitude dynamics is of the same order of magnitude of the orbital dynamics. It is, therefore, impossible to design a fast reconfiguration mission by exploiting the uncontrolled motions; results indicate a minimum duration of the order of magnitude of hours (2 hrs for the controlled test case shown). It has also been observed that the introduction of the air drag does not significantly alter the behaviour of the system. The time scale of the controlled test case under the action of gravity and air drag is shortened but does not change order of magnitude; the equilibria are displaced by tenths of radians but no new equilibria are created and the existing equilibria's stability are changed.

It was shown that a reconfiguration manoeuvre can be successfully accomplished by exploiting the natural motions, if long mission times are acceptable. This paves the way to a class of high efficiency manoeuvres where the system evolution is left uncontrolled for a significant amount of time. For the demonstrated example, the proposed strategy integrates a conventional active attitude control with the ability to vary the system's relative distance centre of mass-hinge to design efficient manoeuvres. In particular, a very simple derivative controller is designed for the on-board reaction wheel system, which is demonstrated to guarantee monotone convergence of the system to the global minimum. Additionally, manoeuvering efficiency is increased introducing the ability, to control the distance of its center of mass from the hinge. The designed strategy is proposed in two different environmental conditions and a comparison with a simple PD controller has been performed. The controllers show a radically different behaviour when compared with the PD controller. It is shown that the PD controller performs better in terms of stored angular momentum in the reaction wheel system. Nevertheless, the proposed manoeuvre strategy is more energy efficient, with both control torques and energy consumption index one order of magnitude smaller than the PD controller. The main implication of these two results is that the use of low-torque thrusters for attitude control, such as electric propulsion actuators (see [94]) becomes feasible.

For the class of spacecraft considered, a lower quantity of stored momentum in the reaction wheel systems would make the PD controller a better candidate for the demonstrated reconfiguration. Furthermore, the magnitude of torques and energy savings of the derivative controller are very limited and, in practical terms, may be considered negligible for a number of applications. However, the maximum absolute value of the control torque that exploits the natural motions is 80% smaller than the PD controller, $max(|T_{ctrl\ d}|) \approx \frac{1}{5} max(|T_{ctrl\ PD}|)$, and the energy consumption index approximately 84% smaller, $E_{ctrl\ d} \approx \frac{1}{6.3} E_{ctrl\ PD}$ than the PD one. As the employment of a number of different types of actuators is limited by fuel consumptions and maximum torques, exploiting the natural motions would allow the extension of their operational ranges

thus, increasing the number of attitude control solutions.

Note that the test case shown is only one of many possible solutions to exploit the quantity of information provided by the two-body system investigation. Also, note that although a planar two-body problem has been considered in this chapter, a 3-d system will follow the same behaviour when all the initial conditions will lie on the orbital plane and no disturbances act out of plane.

CHAPTER 5

The Dynamics of a 3-Link Rigid Body System in Orbit

5.1 Introduction

In this chapter, the physical model of the two-body system is enriched introducing a further body. A three-body system may be used, for instance, to model multi-spacecraft missions in the phases after grasping or docking, where two main bodies are connected together via a rigid link or for complex architecture spacecraft made of three main buses. The aim of this chapter is to extend the analysis of multi-rigid-body spacecraft started in previous chapter in order to gain a further insight into the natural dynamics. To the end of the analytical investigation, the system is assumed to be under the action of an ideal central gravity field only and the problem is restricted to the planar case.

The Hamiltonian dynamics is derived and used to identify relative attitude equilibria of the system with respect to the orbital reference frame. Then a numerical investigation of the behaviour far from the equilibria is provided using tools from dynamical systems theory such as energy methods, phase portraits and Poincarè maps. Results reveal a complex structure of the dynamics as well as the existence of connections between some of the equilibria. Stable equilibrium configurations appear to be surrounded by very narrow regions of regular and quasi-regular motions. Trajectories evolve on chaotic motions in the rest of the domain. A numerical simulation is presented for a reasonable mission scenario to verify if a standard feedback controller, namely a PD controller, is able to accomplish a basic but fundamental task such as station-keeping on one of the unstable equilibria. In the simulation, the action of the air drag is taken into account. The novelty of this work is in using finite-shape bodies to model the problem in order

to have a more accurate description of the system. Moreover, the methods of analysis applied to study a multi-spacecraft problem are relatively new in this field.

Based on the same logic of the 2-body system study, the content of this chapter is as follows:

- In Section 2 the three-body model is introduced. The corresponding Hamiltonian dynamics for the multi-body system in orbit around a large celestial body is derived.

- In Section 3 relative equilibria are identified, approximations are introduced to uncouple the orbital dynamics from the attitude dynamics and an analysis of the Hamiltonian of the attitude dynamics is addressed numerically via Hamiltonian plots.

- In Section 4 the behaviour far from the equilibria is investigated using numerical tools, such as phase portraits and a Poincaré map.

- In Section 5 results are discussed. They are compared with the ones from a two-rigid-body system and their implications for future multi-body space system design and control are discussed.

- The chapter is closed by Section 6, where the feasibility of using proportional-derivative controller for station-keeping purposes is verified.

5.2   The physical model

As done previously, the Hamiltonian equations of motion are derived and following reference frames are used to describe the system: IRF, ORF, BRF_i with $i = 1, 2, 3$.

5.2.1   System configuration variables

From Eq. (2.3), kinematical constraints follow as:

$$\begin{cases} m_1 \vec{R}_{01} + m_2 \vec{R}_{02} + m_3 \vec{R}_{03} = \vec{0} \\ \vec{R}_{01} + \vec{d}_{1\,H_1} + \vec{d}_{H_1\,2} = \vec{R}_{02} \\ \vec{R}_{02} + \vec{d}_{2\,H_2} + \vec{d}_{H_2\,3} = \vec{R}_{03} \end{cases} \qquad (5.1)$$

Where $\vec{d}_{1\,H_1}$, $\vec{d}_{H_1\,2}$, $\vec{d}_{2\,H_2}$ and $\vec{d}_{H_2\,3}$ are the position vectors of the hinges with respect to the bodies centers of mass and $\vec{0}$ is the null vector. As the bodies are assumed to be rigid, the vectors are fixed in their respective body reference frames. The first identity is satisfied because it has been set the overall center of mass of the system as origin of the ORF. The second and third identities describe that the bodies are joined at the
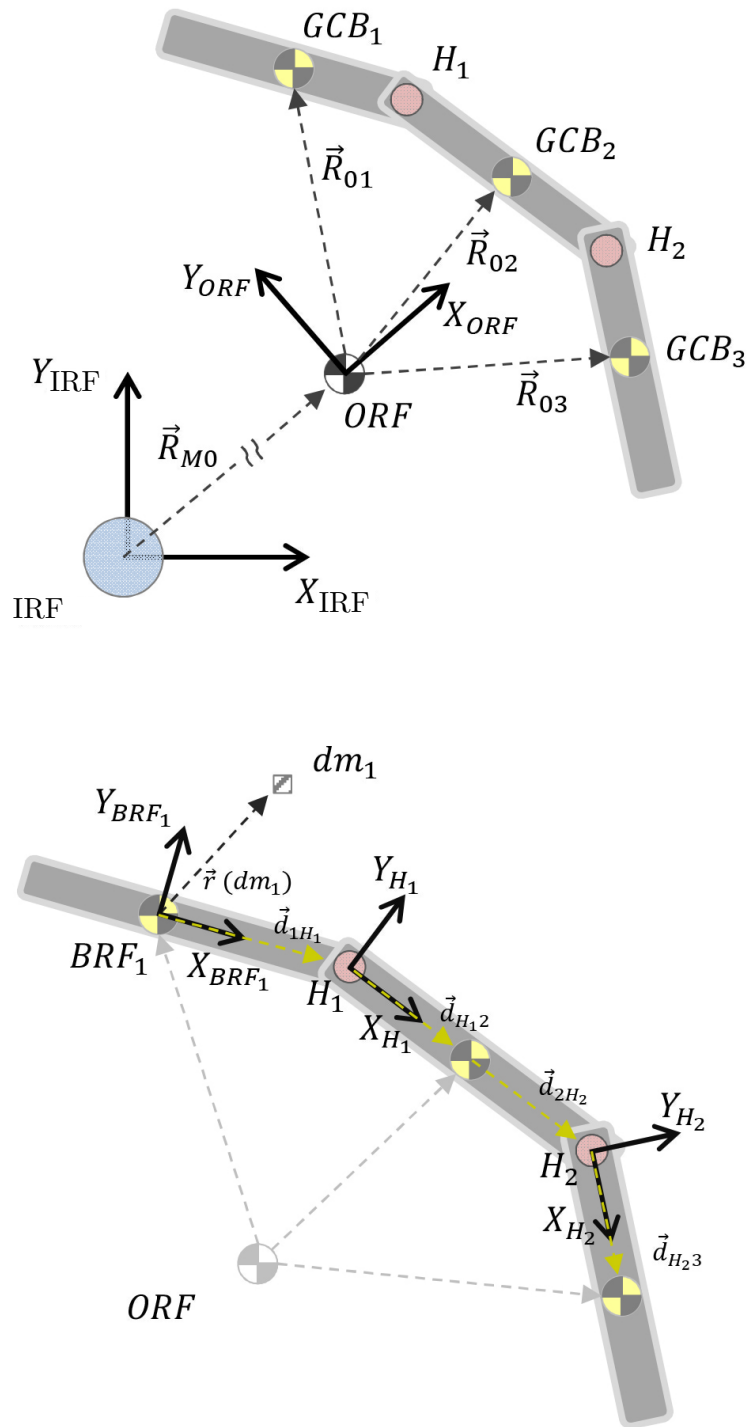
Figure 5.1: Illustrations of the system and of the vector set used to describe it

hinges via rotational joints. Using Eq. (2.4) to derive the reduced system, the following set of configuration variables is defined:

$$\{R_0, \nu, \theta_1, \theta_2, \theta_3\} \quad ; \quad \left\{\dot{R}_0, \dot{\nu}, \dot{\theta}_1, \dot{\theta}_2, \dot{\theta}_3\right\}$$

where R_0 is the modulus of the orbital vector; ν is the orbital anomaly angle; $\theta_1, \theta_2, \theta_3$ are the attitude angles of the bodies which describe the inclination of the $X|_{BRF_i}$ axis with respect to the $X|_{ORF}$ axis.

5.2.2   Kinetic Energy

From Equations (2.8) and (2.9), the kinetic energy of the system follows as:

$$
\begin{aligned}
\mathcal{K} = & \frac{m}{2}(\dot{R}^2 + R^2\omega_{M0}^2) + \lambda_{12}(\omega_{01} + \omega_{M0})(\omega_{02} + \omega_{M0})c_{\theta_1-\theta_2} + \\
& \lambda_{13}(\omega_{03} + \omega_{M0})(\omega_{01} + \omega_{M0})c_{\theta_1-\theta_3} + \lambda_{23}(\omega_{03} + \omega_{M0})(\omega_{02} + \omega_{M0})c_{\theta_2-\theta_3} + \quad (5.2) \\
& \frac{1}{2}\hat{I}_1(\omega_{01} + \omega_{M0})^2 + \frac{1}{2}\hat{I}_2(\omega_{02} + \omega_{M0})^2 + \frac{1}{2}\hat{I}_3(\omega_{03} + \omega_{M0})^2
\end{aligned}
$$

Where:

- $m = m_1 + m_2 + m_3$ total mass of the system;

- $\|\dot{\vec{R}}\|^2 = \dot{R}^2 + R^2\Omega_{M0}^2$ is the term related with the translational kinetic energy of the ORF ;

- $\epsilon_{ij} = (m_i m_j)/m$;

- $\lambda_{12} = d_{1\,H_1}\left[d_{2\,H_2}\epsilon_{13} + d_{H_1\,2}(\epsilon_{12} + \epsilon_{13})\right]$;

- $\lambda_{13} = d_1 d_{H_2\,3}\epsilon_{13}$;

- $\lambda_{23} = d_{H_2\,3}\left[d_{H_1\,2}\epsilon_{13} + d_{2\,H_2}(\epsilon_{13} + \epsilon_{23})\right]$;

- $\hat{I}_1 = I_1 + d_{1\,H_1}^2(\epsilon_{12} + \epsilon_{13})$;

- $\hat{I}_2 = I_2 + d_{H_1\,2}^2\epsilon_{12} + d_{2\,H_2}^2\epsilon_{23} + \epsilon_{13}(d_{H_1\,2} + d_{2\,H_2})^2$;

- $\hat{I}_3 = I_3 + d_3^2(\epsilon_{13} + \epsilon_{23})$;

- $c_{\theta_i-\theta_j} = cos(\theta_i - \theta_j)$.

Note that $\hat{I}_i$ is the augmented inertia of the body. Moreover it has been assumed that the bodies' centers of mass are aligned with the hinges and the generic position vector of the hinge takes the form $\{\vec{d}_{ij}\}_i = (d_{ij}, 0)$ in its body reference frame.

5.2.3 Potential Energy

Introducing the assumptions that bodies have a quasi 1-D shape and constant density, from Eq. (2.12), the the potential energy is derived as:

$$
\begin{aligned}
\mathcal{U} = &\mathcal{U}_1 + \mathcal{U}_2 + \mathcal{U}_3 = \\
&-\mu\frac{m}{R} + -mu\frac{1}{4R^3}\left\{\hat{I}_1 + \hat{I}_2 + \hat{I}_3 - \left[-3\hat{I}_1 c_{2\theta 3} - 3\hat{I}_2 c_{2\theta 4} - 3\hat{I}_3 c_{2\theta 5} + \right.\right. \\
&\left.\left. -8\lambda_{12}c_3 c_4 - 8(\lambda_{13}c_3 + \lambda_{23}c_4)c_5 + 4\lambda_{12}s_3 s_4 + 4(\lambda_{13}s_3 + \lambda_{23}s_4)s_5\right]\right\};
\end{aligned}
\tag{5.3}
$$

Trigonometric functions have been shortened using the notation: $cos(\phi) = c_\phi$ and $sin(\phi) = s_\phi$.

5.2.4 Derivation of the Hamiltonian function

Let the name of the variables be changed to the following, in order to coincide with the general Lagrangian notation:

$$
\{R_0, \nu, \theta_1, \theta_2, \theta_3\} \quad \equiv \quad \{q_1, q_2, q_3, q_4, q_5\}
$$

By constructing the Lagrangian function of the system $\mathcal{L} = \mathcal{K} - \mathcal{U}$ and applying the Legendre transform, momenta follow in the form:

$$
\vec{p} = \mathbf{J}\,\vec{q}
\tag{5.4}
$$

with

$$
\mathbf{J}(\vec{q}) = \begin{bmatrix}
m & 0 & 0 & 0 & 0 \\[4pt]
0 & \begin{matrix}q1^2 m + \hat{I}_1 + \hat{I}_2 + \hat{I}_3 + \\ 2(\lambda_{34}c_{34} + \lambda_{35}c_{35} + \lambda_{45}c_{45})\end{matrix} & \begin{matrix}\lambda_{34}c_{34} + \\ \lambda_{35}c_{35} + \hat{I}_1\end{matrix} & \begin{matrix}\lambda_{34}c_{34} + \\ \lambda_{45}c_{45} + \hat{I}_2\end{matrix} & \begin{matrix}\lambda_{35}c_{35} + \\ \lambda_{45}c_{45} + \hat{I}_3\end{matrix} \\[10pt]
0 & \lambda_{34}c_{34} + \lambda_{35}c_{35} + \hat{I}_1 & \hat{I}_1 & \lambda_{34}c_{34} & \lambda_{35}c_{35} \\[4pt]
0 & \lambda_{34}c_{34} + \lambda_{45}c_{45} + \hat{I}_2 & \lambda_{34}c_{34} & \hat{I}_2 & \lambda_{45}c_{45} \\[4pt]
0 & \lambda_{35}c_{35} + \lambda_{45}c_{45} + \hat{I}_3 & \lambda_{35}c_{35} & \lambda_{45}c_{45} & \hat{I}_3
\end{bmatrix}
$$

The Hamiltonian function follows as:

$$
\mathcal{H} = \mathcal{K}(\vec{q}, \vec{p}) + \mathcal{U}(\vec{q}) = \frac{1}{2}\vec{p}^{Tr}\mathbf{J}(\vec{q})^{-1}\vec{p} + \mathcal{U}(\vec{q})
\tag{5.5}
$$

Thereafter, the Hamilton's equations are:

$$
\frac{\partial \mathcal{H}}{\partial \vec{p}} = \mathbf{J}^{-1}\vec{p} \quad ; \quad \frac{\partial \mathcal{H}}{\partial \vec{q}} = \frac{1}{2}\vec{p}^{Tr}\frac{\partial \mathbf{J}^{-1}}{\partial \vec{q}}\vec{p} + \frac{\partial \mathcal{U}(\vec{q})}{\partial \vec{q}}
\tag{5.6}
$$

Because of the absence of dissipative forces, the total mechanical energy and total angular momentum are conserved (the variable q_2 is cyclic). However, a continuous exchange of energy and angular momentum between the two bodies and between orbital and attitude dynamics take place. Similarly to previous chapter, the Hamiltonian can be split in two contributions:

$$\mathcal{H} = \mathcal{H}_{Att} + \mathcal{H}_{Orb} \tag{5.7}$$

$\mathcal{H}_{Att}$ depends on all the variables but q_2; the $\mathcal{H}_{Orb}$ is function of the orbital elements only and their order of magnitude are significantly different: $o(\mathcal{H}_{Att}) \ll o(\mathcal{H}_{Orb})$. Furthermore, using the same considerations made in the previous chapter, the orbital dynamics can be uncoupled by the attitude dynamics introducing an approximation error between exact orbital motion and approximated one that can be proved to be of the order of centimeters for systems orbiting the Earth. This allows to focus on the attitude dynamics only.

5.3 System dynamics and analysis of the equilibria

Lagrangian dynamics is introduced in this section to derive the system's dynamics and to study its equilibria. The kinetic energy is displayed in the following form:

$$\mathcal{K} = \frac{1}{2}\vec{q}\,\Lambda\left(\vec{q}\right)\,\vec{q} \tag{5.8}$$

with $\Lambda\left(\vec{q}\right) = \mathbf{J}$. Using the form in Eq. (5.8), the Euler-Lagrange equations, including possible external torques, can be derived as:

$$\frac{\partial \mathcal{L}}{\partial \dot{\vec{q}}} = \Lambda\,\dot{\vec{q}} \quad ; \quad \frac{d}{t}\frac{\partial \mathcal{L}}{\partial \dot{\vec{q}}} = \left(\frac{\partial \Lambda}{\partial \vec{q}}\dot{\vec{q}}\right)\,\dot{\vec{q}} + \Lambda\,\ddot{\vec{q}}$$

$$\frac{\partial \mathcal{L}}{\partial \vec{q}} = \frac{1}{2}\dot{\vec{q}}^T\left(\frac{\partial \Lambda}{\partial \vec{q}}\right)\dot{\vec{q}} - \frac{\partial \mathcal{U}}{\partial \vec{q}} \tag{5.9}$$

with $\left(\frac{\partial \Lambda}{\partial \vec{q}}\dot{\vec{q}}\right)$ the square matrix equal to $\sum_{i=1}^{5}\frac{\partial \Lambda}{\partial q_i}\dot{q}_i$, and $\frac{1}{2}\dot{\vec{q}}^T\left(\frac{\partial \Lambda}{\partial \vec{q}}\right)\dot{\vec{q}}$ a vector whose components are $\frac{1}{2}\dot{\vec{q}}^T\left(\frac{\partial \Lambda}{\partial q_i}\right)\dot{\vec{q}}$. By the Euler-Lagrange equations, $\frac{d}{t}\frac{\partial \mathcal{L}}{\partial \dot{\vec{q}}} - \frac{\partial \mathcal{L}}{\partial \vec{q}} = \vec{T}$, it follows that

$$\ddot{\vec{q}} = \Lambda^{-1}\left[\vec{T} - \left(\frac{\partial \Lambda}{\partial \vec{q}}\dot{\vec{q}}\right)\,\dot{\vec{q}} + \frac{1}{2}\,\dot{\vec{q}}^T\left(\frac{\partial \Lambda}{\partial \vec{q}}\right)\dot{\vec{q}} - \frac{\partial \mathcal{U}}{\partial \vec{q}}\right] \tag{5.10}$$

5.3.1   Equilibria

Starting from the considerations contained in the previous chapter, the orbital dynamics
will be considered uncoupled from the attitude motions. This allows to focuss directly
on the relative equilibria of the attitude dynamics. These steady configurations of the
system with respect to the ORF are defined by: $\{\dot{q}_3 \,,\, \dot{q}_4 \,,\, \dot{q}_5 \,,\, \ddot{q}_3 \,,\, \ddot{q}_4 \,,\, \ddot{q}_5\} = \vec{0}$ together
with $\vec{T} = \vec{0}$. Applying these conditions to simplify Eq. (5.10), equilibria are derived by
defining the vector $\vec{\delta}$:

$$\vec{\delta} = \frac{1}{2}\,\vec{q}_O^T \left(\frac{\partial \Lambda}{\partial \vec{q}}_{(1:2,1:2)}\right)\vec{q}_O - \frac{\partial \mathcal{U}}{\partial \vec{q}} \tag{5.11}$$

so that $\vec{\ddot{q}} = \Lambda^{-1}\,\vec{\delta}$, and by imposing that all the components but the first[1] of $\vec{\delta}$ are null,
it reduces to:

$$\begin{cases} \frac{2\dot{q}_1\,\dot{q}_2}{q_1} = 0 \\ s_3\left(\lambda_{34}\,c_4 + \lambda_{35}\,c_5 + 3\hat{I}_1 c_3\right) + \lambda_{34}\,s_{3+4} + \lambda_{35}\,s_{3+5} = 0 \\ s_4\left(\lambda_{34}\,c_3 + \lambda_{45}\,c_5 + 3\hat{I}_2 c_4\right) + \lambda_{34}\,s_{3+4} + \lambda_{45}\,s_{4+5} = 0 \\ s_5\left(\lambda_{45}\,c_4 + \lambda_{35}\,c_3 + 3\hat{I}_3 c_5\right) + \lambda_{45}\,s_{4+5} + \lambda_{35}\,s_{3+5} = 0 \end{cases} \tag{5.12}$$

which can be further reduced to

$$\begin{cases} \dot{q}_1 = 0 \\ s_3 = s_4 = s_5 = 0 \quad \wedge \quad s_{3+4} = s_{3+5} = s_{4+5} = 0 \\ c_3 = c_4 = c_5 = 0 \quad \wedge \quad s_{3+4} = s_{3+5} = s_{4+5} = 0 \end{cases} \tag{5.13}$$

This set of equations has a solution for circular orbits only and at the following config-
urations:

$$(q_3 \,,\, q_4,\, q_5) = \left(\kappa\,\pi \,,\, \kappa'\,\pi,\, \kappa''\,\pi\right) \quad \text{and} \quad (q_3 \,,\, q_4,\, q_5) = \left(\tau\,\frac{\pi}{2} \,,\, \tau'\,\frac{\pi}{2}, \tau''\,\frac{\pi}{2}\right)$$

$$\text{with} \quad \kappa\,,\, \kappa'\,,\, \kappa'' \in \mathbb{Z} \quad \tau\,,\, \tau'\,,\, \tau'' \in 2\,\mathbb{Z}_0 + 1$$

This defines a number of 35 equilibria[2] over the domain $S \times S \times S$, which can be grouped
in six different classes depending on the symmetries of the configurations and the energy
level associated to them. This will be shown in detailed in the next sections.

---

[1]The first column of Λ^{-1} has only the first element non null.

[2]To calculate the number of equilibria defined in both the cases it suffices to calculate the number
of ordered dispositions. Defining the domain $[-\pi, \pi]$ for each angle, the $(\kappa\,\pi \,,\, \kappa'\,\pi,\, \kappa''\,\pi)$ defines a
number of configurations equal to 3^3, while $(q_3 \,,\, q_4,\, q_5) = \left(\tau\,\frac{\pi}{2} \,,\, \tau'\,\frac{\pi}{2}, \tau''\,\frac{\pi}{2}\right)$ defines a number of 2^3
configurations. The overall number is given by the sum of the number of dispositions (there is no
intersection between the sets of equilibria).

5.3.2   Orbital conditions at the equilibria

For completeness' purposes, the conditions which realise $\ddot{q}_1$ are derived from Eq. (5.10). At the equilibria, the orbital radial acceleration reduces to:

$$\ddot{q}_1 = q_1(\dot{q}_2^2 - \mu_p) + \frac{-3\,\mu_p}{4mq_1}\left\{\hat{I}_1 + \hat{I}_2 + \hat{I}_3 + 3\hat{I}_1 c_{2\,q_3} + 3\hat{I}_2\, c_{2\,q_4} + 3\hat{I}_3\, c_{2\,q_5} + \right.$$
$$4\Big[\lambda_{45}(2\,c_{q_4}\,cq_5 - s_{q_4}\,s_{q_5}) + \lambda_{34}(2\,c_{q_3}\,c_{q_4} - s_{q_3}\,s_{q_4}) + \tag{5.14}$$
$$\left.\lambda_{35}(2\,c_{q_3}\,c_{q_5} - s_{q_3}\,s_{q_5})\Big]\right\}$$

with $\mu_p = \frac{\mu}{q_1^3}$.   Depending on the equilibrium considered, the exact initial orbital conditions will be slightly different from the ones of the keplerian two body problem. The following table lists some of them:

Equilibrium Point $\{q_3, q_4, q_5\}$ (rad)	Orbital Angular Velocity $\dot{q}_2 = \omega_{orbital}$ (rad/s)
$\{0,0,0\}$	$\sqrt{\frac{3\mu_p}{mq_1^2}(\hat{I}_1 + \hat{I}_2 + \hat{I}_3 + 2\lambda_{34} + 2\lambda_{35} + 2\lambda_{45}) + \mu_p}$
$\{\pi,0,0\}$	$\sqrt{\frac{3\mu_p}{mq_1^2}(\hat{I}_1 + \hat{I}_2 + \hat{I}_3 - 2\lambda_{34} - 2\lambda_{35} + 2\lambda_{45}) + \mu_p}$
$\{\frac{\pi}{2}, \frac{\pi}{2}, \frac{\pi}{2}\}$	$\sqrt{-\frac{3\mu_p}{2mq_1^2}(\hat{I}_1 + \hat{I}_2 + \hat{I}_3 + 2\lambda_{34} + 2\lambda_{35} + 2\lambda_{45}) + \mu_p}$

Table 5.1: Example of solutions of Eq. (5.14). The table contains the exact orbital angular velocity depending on the equilibrium configuration.

5.3.3   Stability Analysis of the Equilibria

The stability analysis is used again the Dirichlet's theorem. The Hessian of the Hamiltonian is so obtained:

$$\frac{\partial^2 \mathcal{H}}{\partial \vec{p}^2} = \mathbf{J}^{-1}$$
$$\frac{\partial^2 \mathcal{H}}{\partial \vec{q}\partial \vec{p}} = \frac{\partial^2 \mathcal{H}}{\partial \vec{q}\partial \vec{p}} = \left(\frac{\partial \mathbf{J}^{-1}}{\partial \vec{q}}\right)\vec{p} \tag{5.15}$$
$$\frac{\partial^2 \mathcal{H}}{\partial \vec{q}^2} = \frac{1}{2}\vec{p}^{Tr}\frac{\partial^2 \mathbf{J}^{-1}}{\partial \vec{q}^2}\vec{p} + \frac{\partial^2 \mathcal{U}(\vec{q})}{\partial \vec{q}^2}$$

Because of the complexity of the expressions of the Hessian and of its eigenvalues, a numerical stability analysis has been preferred. In particular, the parameters relative to the bodies at the extremals will be fixed. Conversely, mass and length of the central

body will be varied within a reasonable range. Tables 5.2 and 5.3 show the details of the numerical analysis. Note that the hinge distances and bodies' inertia are calculated dependently of l_2 and m_2 as $d_{2a} = d_{2b} = \frac{l_2}{2}$ and $\mathbf{I}_2 = \frac{1}{12} m_2 l_2^2$.

Variable	Value	Unit
l_1	0.9	m
l_3	0.9	m
d_1	0.45	m
d_3	0.45	m
m_1	2	kg
m_3	2	kg
$\mathbf{I}_1$	0.135	$kg\ m^2$
$\mathbf{I}_3$	0.135	$kg\ m^2$

Table 5.2: Data used for the Hessian numerical analysis. Bodies are considered orbiting around the Earth on a nominal orbit circular at an altitude of 600km above the surface.

Variable	Range	Unit
l_2	$[0.1\ ;\ 10]$	m
m_2	$[0.1\ ;\ 10]$	kg

Table 5.3: Data used for the Hessian numerical analysis.

The eigenvalues of the Hessian of the Hamiltonian have been studied numerically and Table 5.4 reports the results obtained. Symmetric configurations have not been reported. Figures 5.2, 5.3 and 5.4 show the bifurcation diagrams for three configuration's

Stable	Conditionally Stable	Unstable
$\{q_3, q_4, q_5\}\ (rad)$	$\{q_3, q_4, q_5\}\ (rad)$	$\{q_3, q_4, q_5\}\ (rad)$
$\{0,\ 0,\ 0\}$	$\{\pi,\ 0,\ 0\}$	$\{\frac{\pi}{2},\ \frac{\pi}{2},\ \frac{\pi}{2}\}$
	$\{0,\ \pi,\ 0\}$	$\{-\frac{\pi}{2},\ \frac{\pi}{2},\ \frac{\pi}{2}\}$
	$\{0,\ 0,\ \pi\}$	$\{\frac{\pi}{2},\ -\frac{\pi}{2},\ \frac{\pi}{2}\}$
	$\{\pi,\ \pi,\ 0\}$	$\{\frac{\pi}{2},\ \frac{\pi}{2},\ -\frac{\pi}{2}\}$
	$\{0,\ \pi,\ \pi\}$	$\{-\frac{\pi}{2},\ -\frac{\pi}{2},\ \frac{\pi}{2}\}$
	$\{\pi,\ 0,\ \pi\}$	$\{-\frac{\pi}{2},\ \frac{\pi}{2},\ -\frac{\pi}{2}\}$
	$\{0,\ -\pi,\ 0\}$	$\{\frac{\pi}{2},\ -\frac{\pi}{2},\ -\frac{\pi}{2}\}$
	$\{0,\ -\pi,\ \pi\}$	
	$\{\pi,\ -\pi,\ 0\}$	

Table 5.4: Numerical study of the equilibria' stability. Geometrically equivalent configurations, due to symmetries, have been excluded for the sake of clarity.

exempla. On the basis of these numerical evidences and the analytical results of the previous chapter, it is reasonable to conclude that:

- Equilibria of the form $\{k\pi,\ k\pi,\ k\pi\}$ are stable in all conditions;

- Equilibria of the form $\left(\tau\,\frac{\pi}{2},\ \tau'\,\frac{\pi}{2}, \tau''\,\frac{\pi}{2}\right)$ are unstable in all conditions;

- All other equilibria are conditionally stable depending on the system's parameters, e.g. l_2 or d_1.
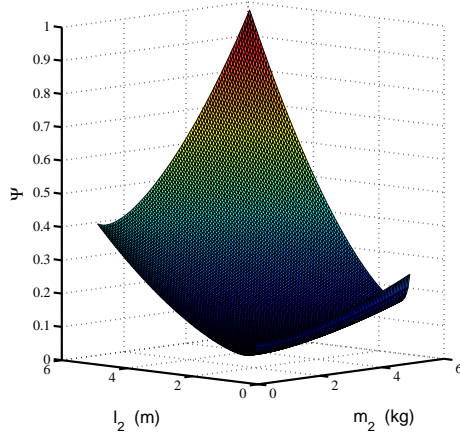
(a) Generic view of the bifurcation function
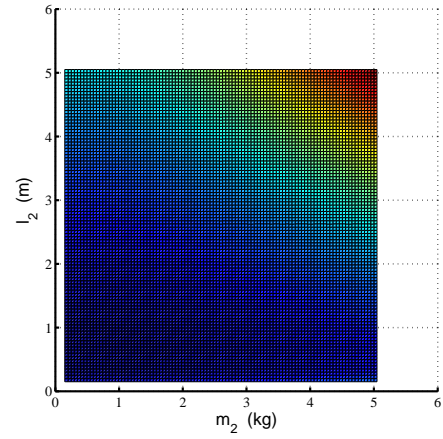
(b) Projection of the bifurcation function on the (m_2, l_2) plane

(c) Projection of the bifurcation function on the (m_2, Ψ) plane

(d) Projection of the bifurcation function on the (l_2, Ψ) plane

Figure 5.2: Ψ function's plot for the stable equilibrium configuration $\{0, 0, 0\}$

5.4 Hamiltonian Maps

Let the attitude Hamiltonian, for given initial conditions, be defined by:

$$\mathcal{H}_{Att\,0} = \mathcal{H}_{Att} : \{\vec{q}_0, \vec{p}_0\} \equiv \left\{ \vec{q}_0, \mathbf{J}(\vec{q}_0)\, \vec{\dot{q}}_0 \right\}$$

$$\text{with} \quad \vec{q}_0 = \{q_{10}, ..., q_{50}\} \; ; \; \vec{\dot{q}}_0 = \{\dot{q}_{10}, ..., \dot{q}_{50}\}$$
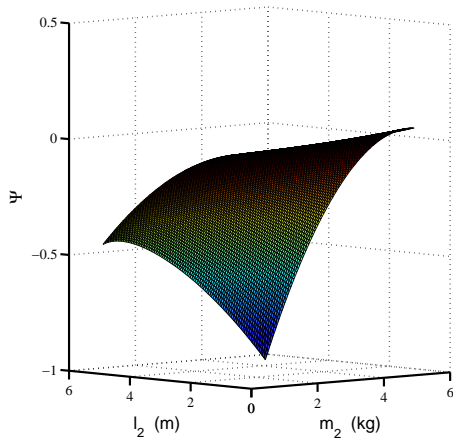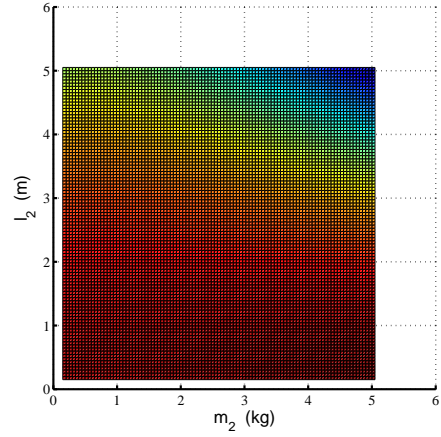
(5.16)

(a) Generic view of the bifurcation function

(b) Projection of the bifurcation function on the $(m_2 \,, l_2)$ plane
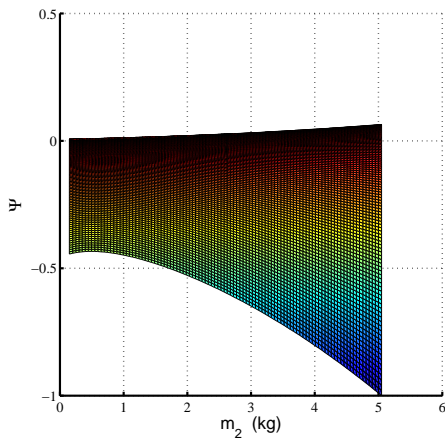
(c) Projection of the bifurcation function on the $(m_2 \,, \Psi)$ plane
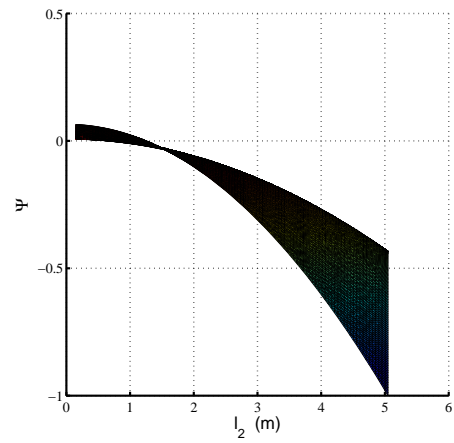
(d) Projection of the bifurcation function on the $(l_2 \,, \Psi)$ plane

Figure 5.3: Bifurcation diagram for the conditionally stable equilibrium configuration $\{\pi \,, 0 \,, 0\}$

(a) Generic view of the bifurcation function

(b) Projection of the bifurcation function on the (m_2, l_2) plane

(c) Projection of the bifurcation function on the (m_2, Ψ) plane

(d) Projection of the bifurcation function on the (l_2, Ψ) plane

Figure 5.4: Ψ function's plot for the unstable equilibrium configuration $\left\{ \frac{\pi}{2}, \frac{\pi}{2}, \frac{\pi}{2} \right\}$

Parameter	Value	Units
Total Body Length l_i	50	cm
$|d_i|$	25	cm
m_i	1.5	kg
$\mathbf{I}_i = \frac{1}{12}m_i l_i^2$	0.0078	$kg\ m^2$

Table 5.5: Data used for evaluating $\tilde{\mathcal{H}}_{Att\,0}$. Bodies are considered orbiting around the Earth on a nominal orbit circular at an altitude of 300km above the surface.

Then, let the following functions of the bodies'attitude angles be defined:

$$\tilde{\mathcal{H}}_{Att}(q_3, q_4, q_5) = \mathcal{H}_{Att} \; : \; \{\dot{q}_3, \dot{q}_4, \dot{q}_5\} = \vec{0} \qquad \text{with} \quad (q_3, q_4, q_5) \in S \times S \times S$$
$$\tilde{\mathcal{H}}_{Att\,0} = \tilde{\mathcal{H}}_{Att}(q_{30}, q_{40}, q_{50}) \tag{5.17}$$

This function will provide the energy state associated with each motion starting from the point (q_{30}, q_{40}, q_{50}) with zero bodies' initial spinning rates. For *circular orbits* (where relative attitude equilibria exist):

$$q_1 \approx const\,,\; p_1 \approx const\,,\; p_2 \approx const \Rightarrow \quad \mathcal{H} = \mathcal{H}(q_3, q_4, q_5, p_3, p_4, p_5)$$
$$\text{or equivalently} \qquad \mathcal{H} = \mathcal{H}(q_3, q_4, q_5, \dot{q}_3, \dot{q}_4, \dot{q}_5)$$

Hence, it follows that[3]

$$\tilde{\mathcal{H}}_{Att} \leq \tilde{\mathcal{H}}_{Att\,0} \tag{5.18}$$

as a consequence that for null spinning rates the value of the kinetic energy is at its minimum and the total mechanical energy must be constant.

A representation of the function $\tilde{\mathcal{H}}_{Att\,0}$ is provided for a system on a circular orbit with a nominal altitude of 300 km above the Earth in the case of three equal bodies with the parameters listed in Table 5.5. This set of parameters has been chosen according to the work in previous chapters, where symmetry was noted to help highlighting characteristic properties of the dynamics. With these conditions, the values of the $\tilde{\mathcal{H}}_{Att\,0}$ at the equilibria, $\tilde{\mathcal{H}}_{Att\,Eq.\,i}$ with $i = 1, .., 6$, are shown in Fig. 5.5.

To provide a description of $\tilde{\mathcal{H}}_{Att}$ over the three-dimensional domain, a sequence of iso-energy surfaces are shown in Fig.5.6. In particular, here only the energy levels associated with the equilibria, $\tilde{\mathcal{H}}_{Att\,Eq.\,i}$, have been plotted. In Figure 5.6, the value of $\tilde{\mathcal{H}}_{Att}$ at the point determines the colour of the point itself. As the value increases from the minimum value to the maximum, the colour varies from dark blue to bright red, as it can be seen in the colour bars. The Hamiltonian map shows graphically the position of the equilibria, as identified in the previous section. Moreover, the stable equilibria are shown by small and isolated ellipsoids of low-energy colour. These surfaces are surrounded by higher energy manifolds which confine the motion on the equilibrium

---

[3]when a motion starts with null spinning rates
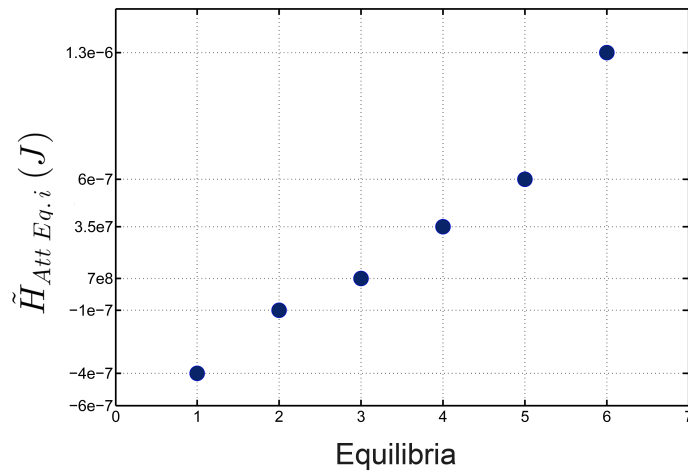
Figure 5.5: $\tilde{\mathcal{H}}_{Att}$ at the equilibria

itself. On the contrary, unstable equilibria can be recognised as they are part of large manifolds which are surrounded by lower energy surfaces. A motion starting in the neighborhoods of these points can evolve on a large part of the domain or even in the whole domain. Finally, the map gives a description of the distribution of $\tilde{\mathcal{H}}_{Att}$ in all the attitude angles' domain, revealing a very complex structure of the underlying dynamics of the problem. Equilibria are surrounded by ellipsoidal surfaces and some of them are connected by a "pipe-like" structure. These connections between equilibria can potentially be used in the manoeuvre design by exploiting the system's natural motions for reconfigurations manoeuvres. It is worth noting the importance of the role of the physical parameters which might be changed in the design stage of the system to introduce new connections between equilibria or "close" existing connections.

(a) Iso-energy surfaces at $\tilde{\mathcal{H}}_{Att\ Eq.\,1}$, the lowest value of $\tilde{\mathcal{H}}_{Att}$

(b) Iso-energy surfaces at $\tilde{\mathcal{H}}_{Att\ Eq.\,2}$

(c) Iso-energy surfaces at $\tilde{\mathcal{H}}_{Att\ Eq.\,3}$

(d) Iso-energy surfaces at $\tilde{\mathcal{H}}_{Att\ Eq.\,4}$

(e) Iso-energy surfaces at $\tilde{\mathcal{H}}_{Att\ Eq.\,5}$

(f) Iso-energy surfaces at $\tilde{\mathcal{H}}_{Att\ Eq.\,6}$
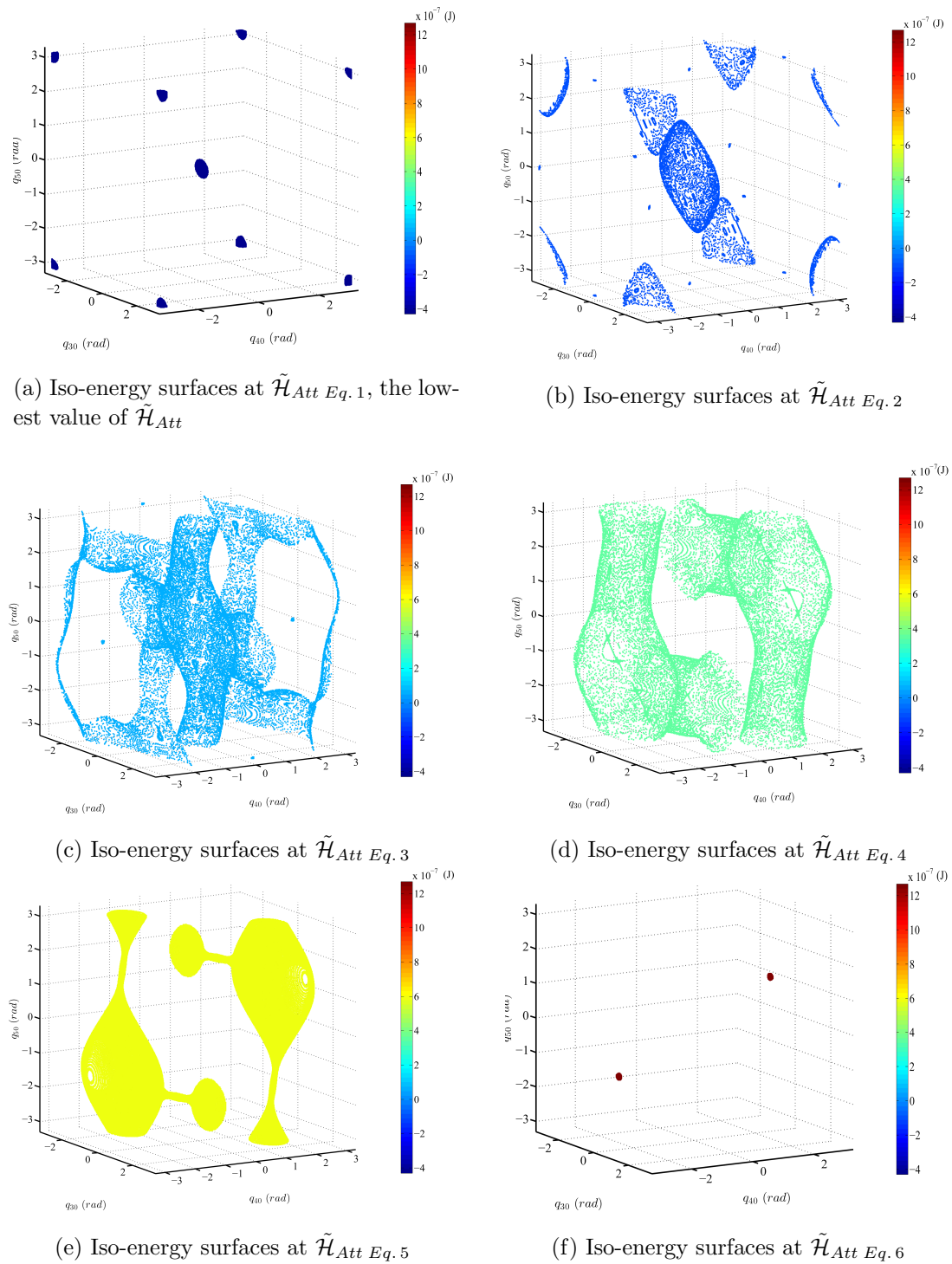
Figure 5.6: Illustration of $\tilde{\mathcal{H}}_{Att}$ over its three-dimensional domain through a series of iso-energy surfaces. The elements of each manifold have the same value of $\tilde{\mathcal{H}}_{Att}$

5.5 System Behaviour Far from Equilibria

In order to provide a global description of the system behaviour, different representations of the dynamics will be shown using various analysis tools. The dynamic equations (5.6) are integrated and the trajectories analysed. Inspired by common techniques of integration using symplectic integrators, Hamiltonian and total angular momentum are introduced in the differential equations set in order to keep control of the numerical errors and to drive the accuracy of the integration always below a maximum relative error of an order of $o(10^{-13})$ on the initial values of the conserved quantities[4]. Parameters in Table 5.5 are used in the following sections.

5.5.1 Phase Plots and Poincaré sections

Phase plots capture three different kinds of qualitative behaviours. Figure 5.7 shows projections of the trajectories of the system onto the $\{q_4, q_5\}$, $\{q_4, \dot{q}_4\}$ and $\{q_5, \dot{q}_5\}$ planes. Poincaré sections are a standard technique to inspect complex systems and are used here to analyse the dynamics of this system. These are projections of phase spaces where a snap shot is taken whenever the trajectory intersects a prescribed plane in the phase space. Consequently, the Poincaré mapping[5] is a collection of points sampled in a regular way from the phase portraits. For this problem Poincaré sections are constructed sampling the state of the system when the following condition is met: $\{\theta_1 = 0, \omega_1 \geq 0\}$. Here, the sections are provided in the same planes of phase plots[6].

In Figure 5.7a regular behaviour is observed[7]. The motion is periodic and its projections evolve over a line in the plane $\{q_4, q_5\}$ and over circles (clockwise) in the planes $\{q_4, \dot{q}_4\}$ and $\{q_5, \dot{q}_5\}$. Trajectories topologically equivalent to the one shown here have been observed for initial conditions in a relatively small[8] neighborhood of the stable equilibrium point.

Figure 5.7b shows a regular behaviour which is identified as "quasi-periodic" as it evolves in a bounded region on almost periodic trajectories without ever exactly coming back on themselves. In the Poincaré sections, the system's natural evolution is completely described by a set of points which appears to be aligned on a closed curve, even though not totally drawn. This feature is typical of quasi-periodic motions, for instance, see the Hénon-Heiles Poincaré section for $e = 0.08333$ in [82].

Finally, in Figure 5.7c any sort of regularity disappears and the points cover an apparently random shaped area rather than being ordered along a curve. This kind of

---

[4]This solution has been preferred to the reduction of the system introducing into the equations the conserved quantities, in order to effectively have way of monitoring the magnitude order of the error.

[5]Also referred as a stroboscopic technique

[6]For further details on Poincaré maps, see [80] or [81].

[7]It should be noted that no dissipative forces have been included in the model.

[8]Note the magnitude orders of the x and y axis scales in Fig.5.7a are particularly small.

behaviour can be recognised in the Poincaré sections of many systems such as the double pendulum, the three body system or again in the Hénon-Heiles equations for $e = 0.12500$, see [82].

5.5.2   Poincaré Map

A Poincaré map is constructed collecting all the Poincaré sections generated from initial conditions which have $\tilde{\mathcal{H}}_{Att} = -3.96 \times 10^{-7}$ J. This energy state is chosen as it shows a wide range of different behaviours. Fig. 5.8a shows, which initial conditions belong to the indicated energy. Each initial condition shown in Fig.5.8a has been integrated and the trajectory analysed. The resulting Poincaré map is shown from three different projections in Fig. 5.8. Chaotic motion can be seen where the region is dense on the set, as shown in Figures 5.8b, 5.8c and 5.8d. Invariant tori can be recognised in the regions at the center-bottom of 5.8b, the center of 5.8c and in center-top of 5.8d. In these areas, ordered sequences of concentric discontinuous lines in a layout typical of quasi-periodic motions can be found. This kind of structure clearly suggests the presence of motions developing into invariant tori. Furthermore, the boundary between different qualitative behaviours is fuzzy. There are some particular cases where the quasi-periodicity is weak and the motion can be classified as either quasi-periodic or chaotic.
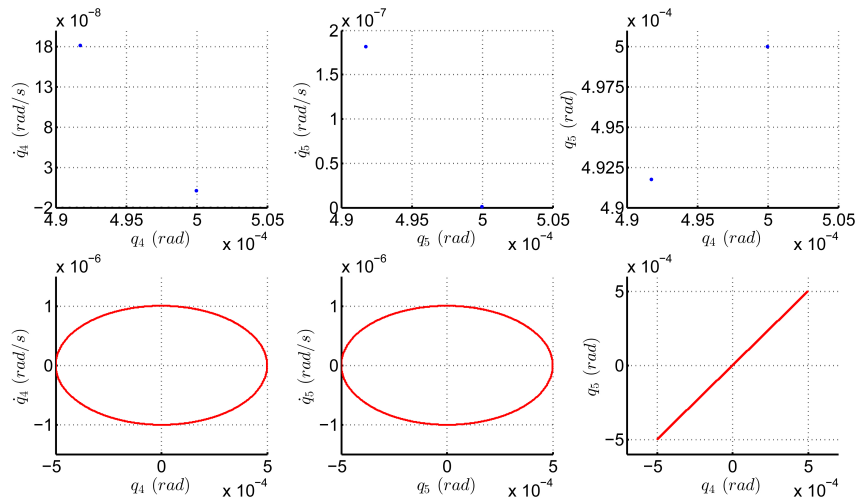
(a) Example of periodic behaviour of the system
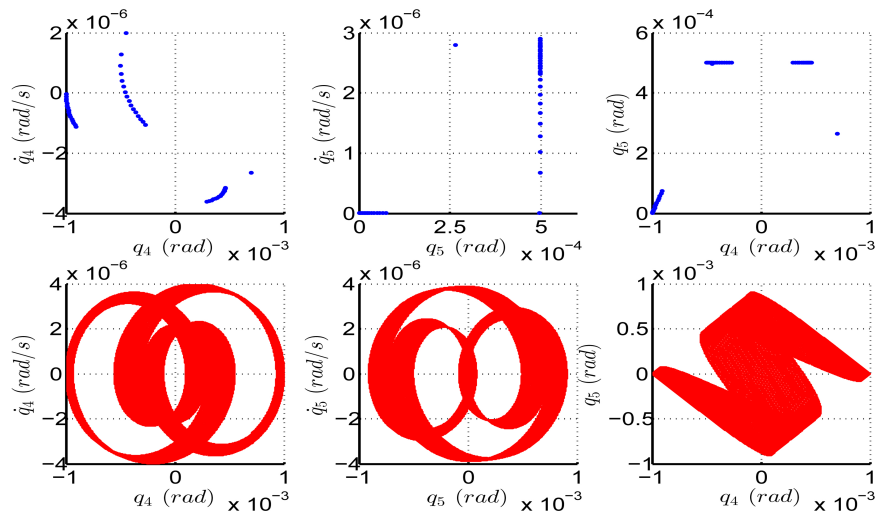
(b) Example of quasi-periodic behaviour of the system
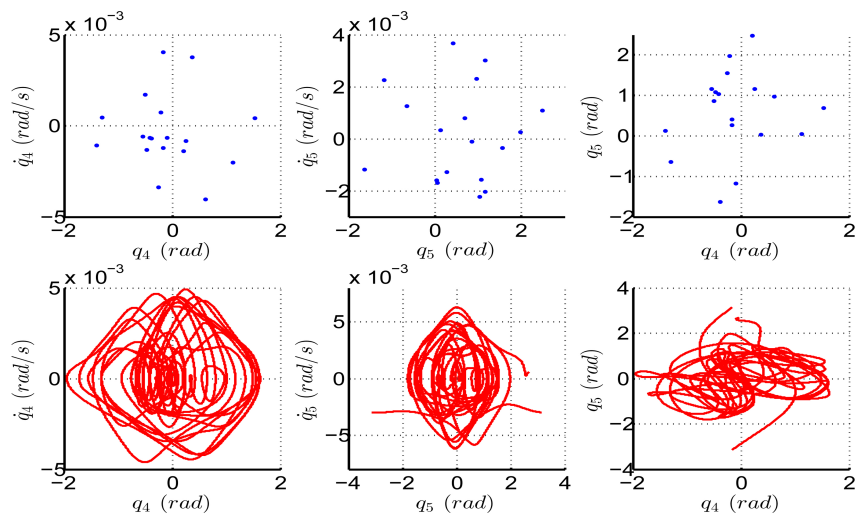
(c) Example of chaotic behaviour of the system

Figure 5.7: Illustration of three different behaviours of the system using phase plots and Poincaré sections.
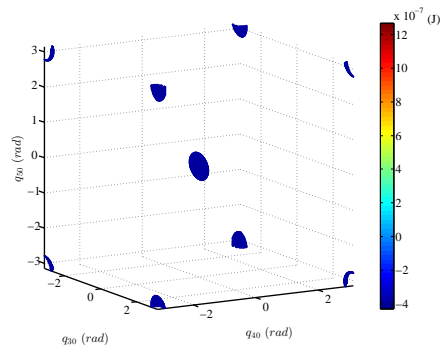
(a) Iso-energy surfaces at $\tilde{\mathcal{H}}_{Att\ Eq.\,0}$
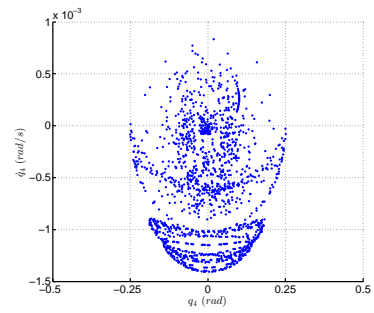
(b) Poincaré Map from $\tilde{\mathcal{H}}_{Att\ Eq.\,0}$ in the plane $(q_4, \dot{q}_4)$
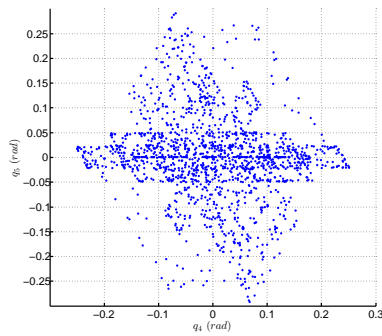
(c) Poincaré Map from $\tilde{\mathcal{H}}_{Att\ Eq.\,0}$ in the plane (q_4, q_5)
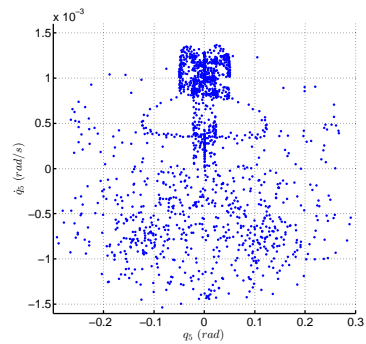
(d) Poincaré Map from $\tilde{\mathcal{H}}_{Att\ Eq.\,0}$ in the plane $(q_5, \dot{q}_5)$

Figure 5.8: A Poincaré Map of the problem

5.6   Test Manoeuvre: validation of a PD controller for attitude maintenance

As evident from the dynamical investigation the number of stable equilibria is only 2. Therefore, due to the nature of the system, in most of the practical cases it may be necessary to maintain an unstable equilibrium configuration. To this end, a controller is required and, by using a numerical simulation, it is shown that a simple PD controller is an operational and practical solution. As it will be shown in the next chapter, a number of control strategies for space manipulators are based on this controller's architecture. For instance, a well-known technique for space manipulators is called the Jacobian Transposed control which is often used as a reference standard. The controller will be designed on the base of the linearised equations of the dynamics and it will then be applied using the full nonlinear system in simulations. The mission scenario considers a micro-spacecraft[9] connected by a short and light link to an uncooperative object (U.O.) of the same weight and size. Attitude control is realised by means of: the spacecraft attitude control system (reaction wheels are adopted) and two motors at the joints. The mission goal is to stabilise the system on the equilibrium $\{\frac{\pi}{2}, \frac{\pi}{2}, \frac{\pi}{2}\}$, which is meant as the original initial state from which the system has been perturbed. Table 5.6 reports details of the multi-spacecraft considered and Table 5.7 reports details of the actuators.

Quantity	Variable	Value	Unit
Spacecraft Length	l_1	90	cm
Link Length	l_2	90	cm
U.O. Length	l_3	60	cm
Spacecraft mass	m_1	2	kg
Link mass	m_2	0.3	kg
U.O. mass	m_3	2	kg

Table 5.6: Spacecraft characteristics. Hinges are assumed at each body's extremals.

Quantity	Value	Unit
Max Wheel Speed	6000	rpm
Max Torque	20	mNm
Wheel Inertia	0.001	$Kg\,m^2$
Motors Maximum Torque	5	$N\,m$
Motors Maximum Speed	0.1	rad/s

Table 5.7: Actuators characteristics.

Note that the first spacecraft attitude control torque may be model, in first approximation[10], as external; however, the remaining two motor torques are internal. Further-

---

[9]of the same kind considered in the previous chapters.
[10]Neglecting an accurate model of the inertial wheels.

more, air drag will be included as external force and modeled similarly to the previous chapter. Table 5.8 provides details of the initial conditions.

Quantity	Variable	Value	Unit
Orbit height	R	600	km
Orbit eccentricity	e	0	
Spacecraft initial attitude	q_{30}	$\frac{\pi}{2} + 0.3$	rad
Link initial attitude	q_{40}	$\frac{\pi}{2} + 0.1$	rad
U.O initial attitude	q_{50}	$\frac{\pi}{2} - 0.2$	rad
Spacecraft initial spinning rate	$\dot{q}_{30}$	1/60	rad/s
Link initial spinning rate	$\dot{q}_{40}$	1/60	rad/s
U.O. initial spinning rate	$\dot{q}_{50}$	1/60	rad/s

Table 5.8: Mission initial conditions. Bodies' attitudes are displaced from the equilibrium and have a non-null spinning rate.

5.6.1   Controller design

Define the status vector of the attitude dynamics $\vec{x} = \{q_3\,,\,q_4\,,\,q_5\,,\,\dot{q}_3\,,\,\dot{q}_4\,,\,\dot{q}_5\}$ and its value at the equilibrium $\vec{x}_{eq} = \{q_{3\,eq}\,,\,q_{4\,eq}\,,\,q_{5\,eq}\,,\,\dot{q}_{3\,eq}\,,\,\dot{q}_{4\,eq}\,,\,\dot{q}_{5\,eq}\}$. The system's equations linearised can be expressed as:

$$\dot{\delta \vec{x}} = \mathbf{A}|_{\vec{x}_{eq}}\,\delta \vec{x} \tag{5.19}$$

with $\delta \vec{x} = \vec{x} - \vec{x}_{eq}$ and $\mathbf{A}$ is a 6×6 square matrix, namely:

$$\mathbf{A}|_{\vec{x}_{eq}} = \left[\begin{array}{cc} \mathbf{0} & \mathbf{I} \\ \mathbf{A}_{21} & \mathbf{A}_{22} \end{array} \right]$$

where the blocks $\mathbf{0}$ and $\mathbf{I}$ have size 3×3 and are the null matrix and the identity matrix. Moreover, the square sub-matrixes $\mathbf{A}_{21}$ and $\mathbf{A}_{22}$ are obtained by differentiating the attitude dynamics equations, from Eq. (5.10), with respect to $\delta \vec{x}$. Note that the air drag effects are included as well. To the controller design, matrix $\mathbf{A}$ is calculated taking: $\vec{x}_{eq} = \{\frac{\pi}{2}\,,\,\frac{\pi}{2}\,,\,\frac{\pi}{2}\,,\,0\,,\,0\,,\,0\}$. At the above conditions, the system is naturally unstable and the eigenvalues of the matrix $\mathbf{A}$ are shown in Fig.5.9

A feedback controller is hence introduced as follows:

$$\begin{aligned} \dot{\delta \vec{x}} &= \mathbf{A}\,\delta \vec{x} + \mathbf{B}\,\vec{u} \\ \vec{u} &= -\mathbf{F}\,\delta \vec{x} \end{aligned} \tag{5.20}$$

with: $\vec{u} \in \mathbf{R}^3$ control vector and $\mathbf{B}$ a 6×3 matrix. Based on the assumption introduced,
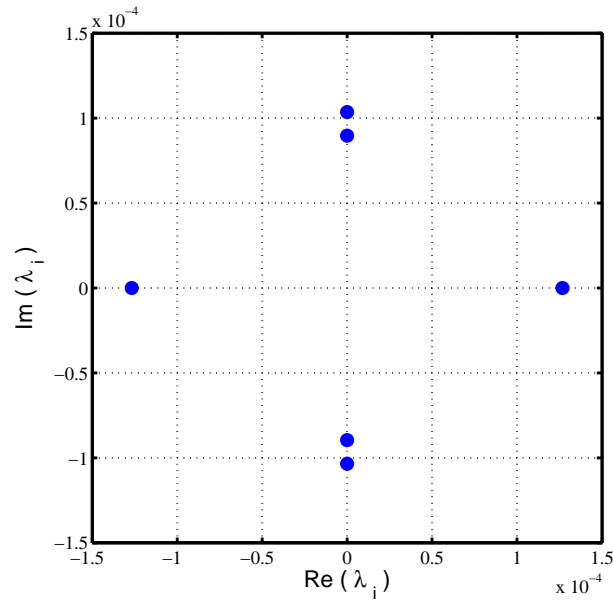
Figure 5.9: Eigenvalues of the linearised system shown in the complex plane. System is linearised around the equilibrium $\{\frac{\pi}{2}, \frac{\pi}{2}, \frac{\pi}{2}\}$; air drag torque is considered.

B is:

$$
\mathbf{B} = \begin{bmatrix}
0 & 0 & 0 \\
0 & 0 & 0 \\
0 & 0 & 0 \\
1 & 1 & 0 \\
0 & -1 & 1 \\
0 & 0 & -1
\end{bmatrix}
$$

In order to stabilise the system while guaranteeing an adequate stability margin on the linearised system, control gains are chosen so that the eigenvalues of the closed loop state feedback system matrix, $\mathbf{A} - \mathbf{B} \ \mathbf{F}$, have all negative real part with an adequate phase. These conditions are introduced as constraints into an optimisation algorithm used for the tuning in order to minimise the gains values. Fig. 5.10 shows the eigenvalues of the controlled system as resulting from the optimisation both in the complex plane, $(Im(\lambda_i), Re(\lambda_i))$ and in their phase, $\phi_i = \arctan(\frac{Im(\lambda_i)}{Re(\lambda_i)})$.

As it is possible to see, for some of the eigenvalues it has been possible to obtain a critical damped behaviour. The designed controller is then applied to the full non-linear system.
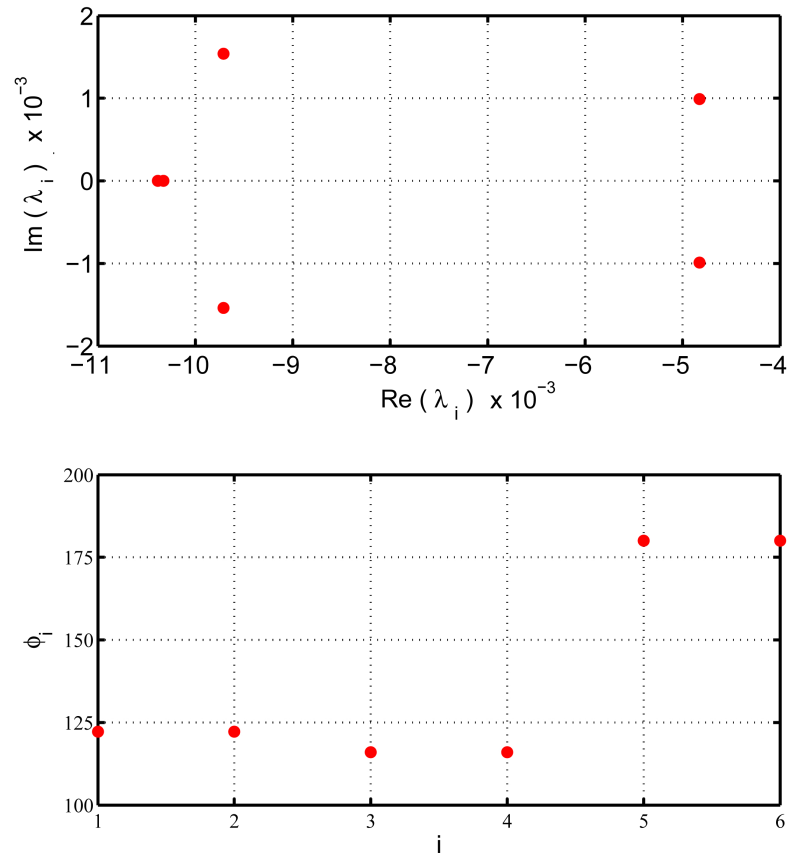
Figure 5.10: Eigenvalues of the linearised controlled system shown in the complex plane, (a), and in their phase, ϕ_i, (b).

5.6.2   Validation results

The trajectory described using the attitude angles of the bodies is depicted in Figures 5.11 and 5.12, while, the spinning rates are shown in Fig. 5.13. Controller tuning has been done using the transfer matrix of the linearised system and there has been no need for further adjustment once applied to the nonlinear dynamics. Furthermore, as it can be seen, the behaviour is very close to that of critically damped system, which should have been expected in the linear system. Initial conditions have been intentionally taken not too close to the equilibrium in order to test the behaviour of the PD controller and, as a result, the controller works very well even in this case. Fig. 5.14 shows the actuators' torques which are quite limited. Their order of magnitude is of one tenth of $m\,Nm$, which is well within the range of manoeuvre' s feasibility.
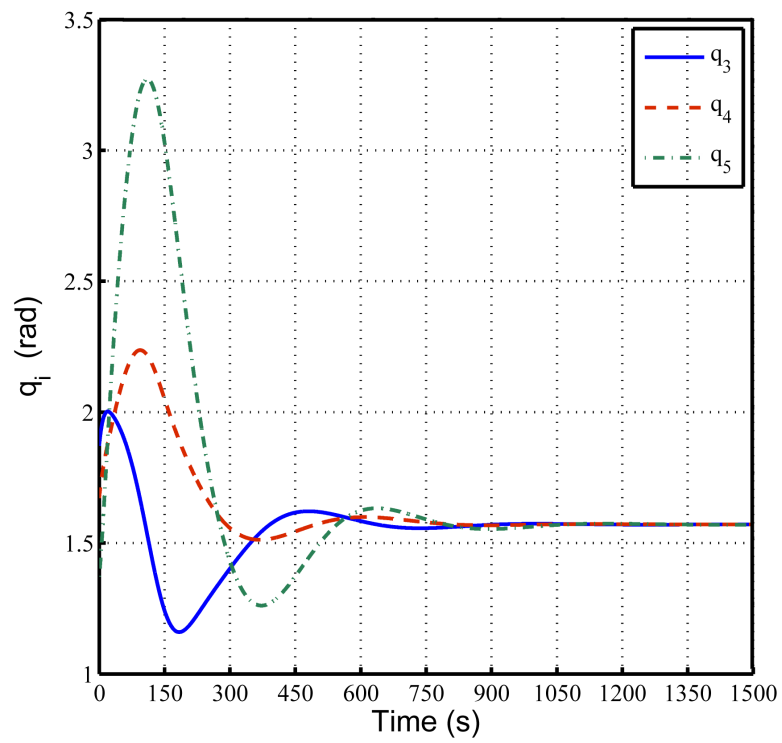
Figure 5.11: Evolution of the bodies' attitude angles in time.
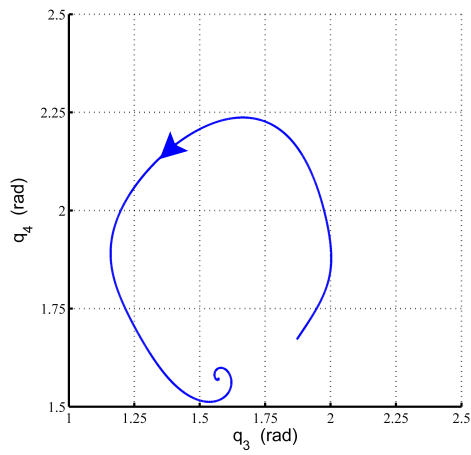
(a) Projection on the $\{q_3, q_4\}$ plane.
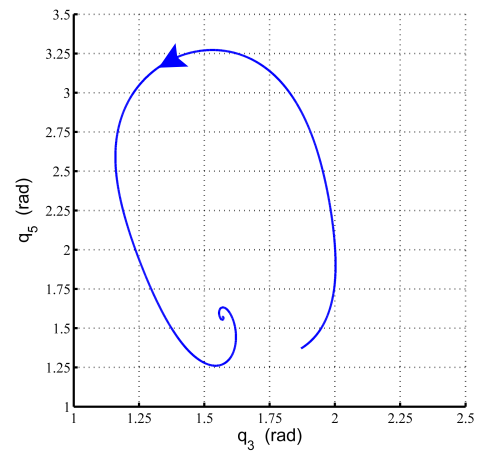
(b) Projection on the $\{q_3, q_5\}$ plane.
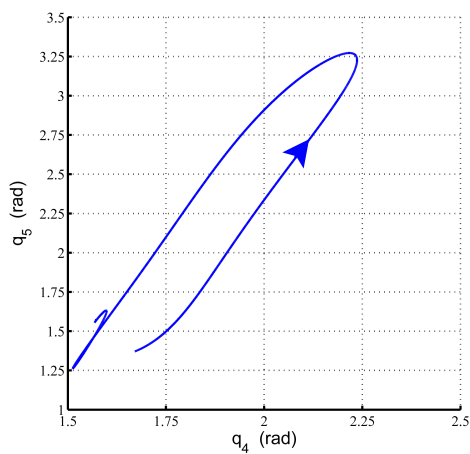
(c) Projection on the $\{q_4, q_5\}$ plane.
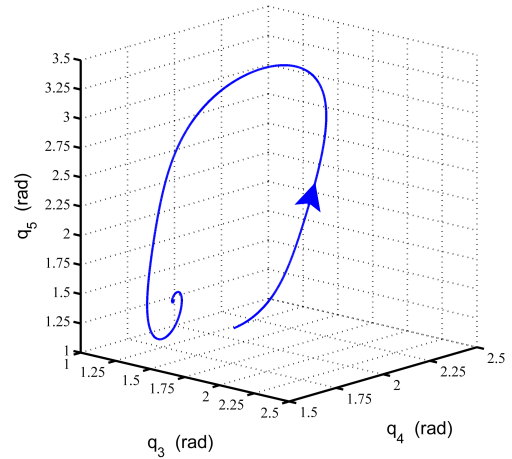
(d) 3-d view of the trajectory.

Figure 5.12: Trajectory projection in the 3-d space $\{q_3, q_4, q_5\}$.
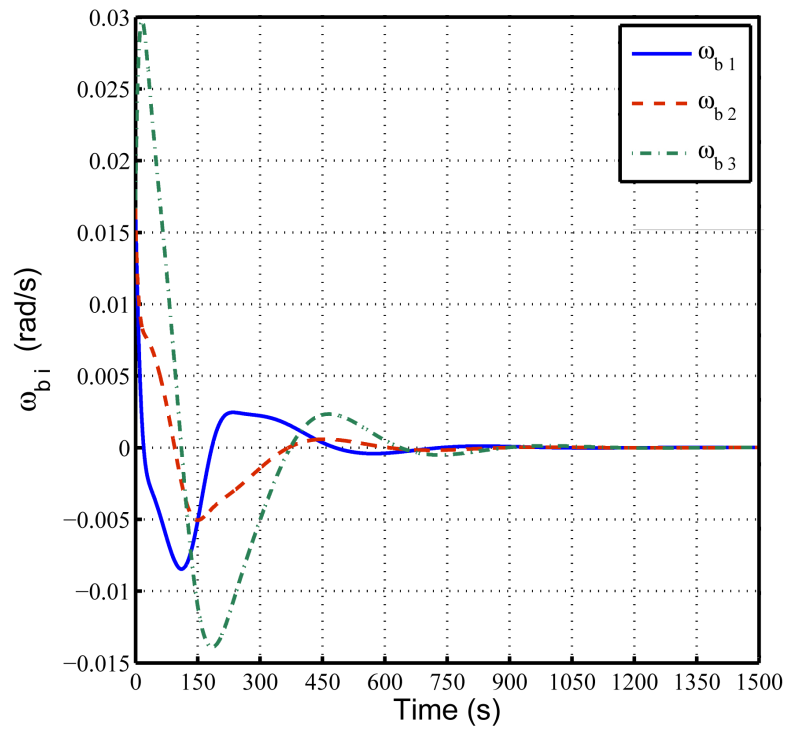
Figure 5.13: Evolution of the bodies' angular velocities in time.
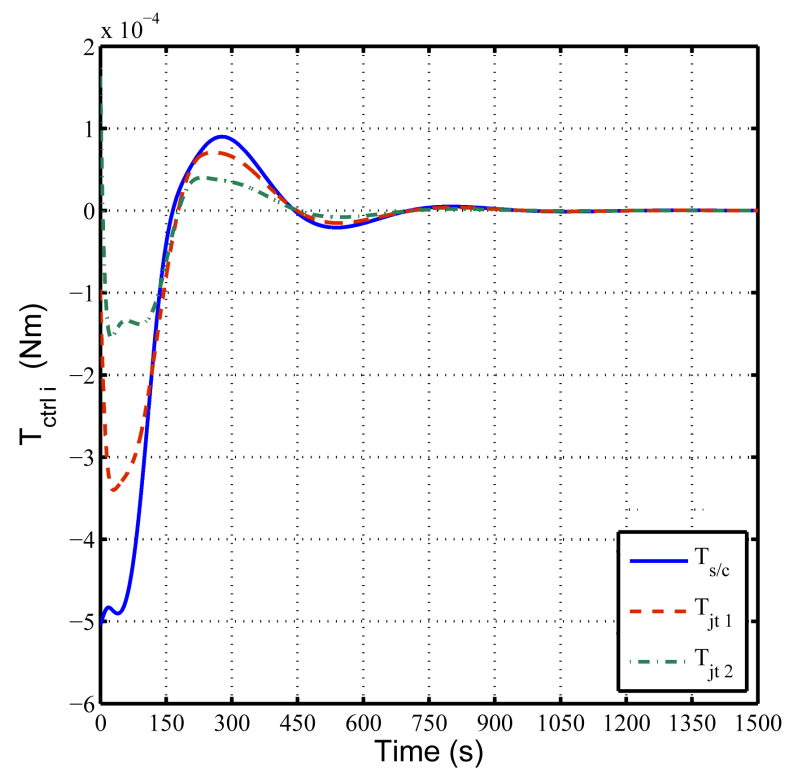
Figure 5.14: Control torques exerted by the actuators.

5.7   Conclusions of the dynamical investigation

A three finite-shape rigid-body system has been studied. The problem is restricted to the planar case and under the effect of an ideal gravitational field only. A Hamiltonian approach has been used to highlight conserved quantities of the problem and derive the dynamics. With the introduction of a negligible approximation error the orbital dynamics is taken as uncoupled from the attitude dynamics and the analysis of the problem restricted to the attitude dynamics behaviour only. This reveals six classes of relative equilibria for a total number of 35 equilibria. For every class each body is either aligned with the $X|_{ORF}$ or with the $Y|_{ORF}$, that is, parallel or perpendicular to the position vector of the overall center of mass with respect to the main inertial reference frame. A numerical stability analysis of the equilibria by the application of the Dirichlet's theorem, supported by results obtained in previous chapters, has led to conclude that all the equilibria where the bodies are perpendicular to $X|_{ORF}$ are unstable; furthermore all the configurations where the bodies' chain is fully open and bodies are aligned with $X|_{ORF}$ are stable while all the others are conditionally stable. Additionally, bifurcation diagrams have been shown. A further numerical investigation of the problem in the case of three equal bodies has been undertaken. First, the Hamiltonian has been studied graphically revealing a very complex structure of the underlying natural dynamics. Connections between equilibria are observed. The analysis of the behaviour far from the equilibria has been undertaken using phase plots and Poincaré sections. Three different kinds of motions have been found: periodic, quasi-periodic and chaotic. Fully regular motions are observed only in a relatively small neighborhood of the stable equilibria. A Poincaré map for a given energy level of the initial conditions is provided. The map shows the presence of invariant tori as well as chaotic manifolds. In conclusion, the three-body-problem shows very complex dynamics mostly driven by a chaotic behaviour and a high number of equilibria, of which the stable are surrounded by relatively small regular motion regions. The presence of many connections between equilibria is identified as a potential element to design large reconfiguration manoeuvres using natural motions. Moreover, like the two-body problem, the choice of parameters may influence the stability of some of the equilibria and has been identified as a critical design factor.

5.8   Conclusions of the PD controller validation

Results show that a three-body system can be efficiently and practically controlled around every equilibrium using a simple feedback controller. Nevertheless, in other circumstances such simple architecture controllers may not satisfy stricter requirements. This may be the case when fuel/energy efficient manoeuvres are required (for example when many large reconfigurations are needed or larger masses are involved), or either

when large and long-term periodic motions are required (for instance one of the bodies has to continuously point at the same direction while orbiting). For such cases, the dynamical analysis provided suggests that tailored control strategies may be a valid alternative, as, for instance, the exploitation of natural motions or the stabilisation of unstable orbits using chaotic controllers.

This chapter outlines some important characteristics of orbiting multi-body systems. At first, while increasing the number of bodies composing the system, the mathematical form of the dynamics is preserved. However, this brings an increase in complexity of the set of differential equations in terms of number, parameters involved and non-linearity. In addition, the number of bodies, the number of equilibria increases. The relative size of the regular motions domain decreases and the dynamics becomes more and more chaotic. For the analysis of the spacecraft systems shown in previous chapter, Hamiltonian and Lagrangian formalisms have been used and problems have been limited to the planar cases. By considering all these elements, a radically different approach is introduced to extend the study to more complex multi-body systems, and, methods more typically used in space engineering are used. The next chapter will focus on the study of a generic N-body problem. To this end, Hamiltonian or Lagrangian formalisms are left and systems dynamics is studied in its matrix form. Furthermore, due to the nature of typical space systems which can be modeled by N rigid bodies, e.g. space manipulators, the analysis will focus on the short term behaviour rather than on long time scales motions, considering different applications, e.g. target grasping.

N-body systems: 3D control for minimum dynamical coupling

Previous chapters outlined the very complex nature of space multi-body systems. The main results revealed different types of behaviour, with chaotic motion occurring in most of the domain, and characterised by a strong dynamical coupling between the bodies of the system which exchange kinetic energy and angular momentum. Furthermore, the time scale of the attitude natural motions emerged to be of the same order of magnitude of the orbital motions around the planet (e.g. the Earth), even in presence of air drag[1]. The Hamiltonian and Lagrangian formalisms in the previous sections are particularly useful to gain an insight into the complex dynamical structure by exploiting the conserved quantities. However, as the number of bodies increases the derivations become very complex.

In this section a general N-body system is studied. In particular, the focus is placed on the reduction of the dynamic coupling between a specific body and the rest of the system, for instance, the spacecraft's bus and the robotic arm attached to it. The dynamical investigation will be subject to deviations with respect to the previous chapters. Due to the fact that a task executed by a space articulated system has a typical duration of minutes, a time much smaller than the natural attitude dynamics. For the study of "short-term" behaviours, spacecraft can be assumed to be in free space and the actions of gravity gradient torques and air drag torques even neglected (as they produce significative effects in a much longer time scale - typically hours). Consequently, attention is not placed on the understanding the natural motions, but, rather, on the

---

[1] high area-to-mass ratio spacecraft have been excluded from dissertation

study of motions which cancel, or at least minimise, reaction forces and torques on the main body. This, typically, results in a motion planning problem or in a control design problem. The Newton-Euler approach is used to derive the n-body equations of motion in a compact matrix form rather than the Hamiltonian approach of the previous chapters.

This chapter presents a novel controller for a generic 3D multibody space system designed to minimize the dynamic coupling between one of the bodies and the rest of the system. The case of a spacecraft endowed with a robotic manipulator is considered. Standard control techniques suffer from some limitations. For instance, the Jacobian Transposed (JT) control, [95, 96], does not explicitly address the reduction of the reaction forces over the main body. Or else, the so-called "Reaction Null" (RN) technique, [97, 98, 28], has a limited workspace due to the strictness of the constraint of zero reactions over the spacecraft. A new closed-loop controller, called Minimum Reaction (MR) control, combines the RN and JT approaches, limiting the dynamic coupling between base platform and manipulator without reducing the manipulators workspace. To this end, the non-linear 3D dynamics of a multibody system is derived in matrix form. Then, a minimum reaction control problem is formulated and solved analytically using a quadratic cost function. The presented novel solution is applied to a typical mission scenario involving a robotic arm deployment, both in the case of a rigid multibody system and in the case in which a flexible appendage (such as a solar panel) is included. In order to evaluate the performance of the designed controller, the test case manoeuvre is executed using the JT, the RN and the MR controllers. It is shown that MR controller is particularly suitable for the reduction of vibrations of the flexible panels during the manipulator motion.

Results of this chapter can be found in:

- Pagnozzi, D., Pisculli, A., Felicetti, L., Sabatini, M., *A minimum reaction control to extend the reaction-null controller workspace*, submitted to the Official Journal of the Council of European Aerospace Societies, CEAS Space Journal, June 2015

- Pagnozzi, D., Pisculli, A., Felicetti, L., Sabatini, M., *3D minimum reaction control for space manipulators*, 65th International Astronautical Congress, September 2014, IAC-14, C2,2.3

The cited publications were in collaboration with Andrea Pisculli, Dr. Leonard Felicetti and Dr. Marco Sabatini from the University of Rome La Sapienza[2]. In particular, the contribution of the author of this thesis was in the design of the minimum reaction controller by defining the minimum problem functional, deriving the general controller form and, then, by designing the reference input.

---

[2]Andrea Pisculli: Dipartimento di Ingegneria Meccanica e Aerospaziale. Leonard Felicetti, Marco Sabatini: Dipartimento di Ingegneria Astronautica, Elettrica ed Energetica

6.1 Introduction

The ongoing studies on debris removal strategies and on-orbit operations often call for the use of space manipulators, in order to grasp and handle specific targets (e.g. uncooperative spacecraft), [74, 99, 100]. One of the main issues of the operations concerning the use of space manipulators is the interaction of the arm motion with the attitude control of the spacecraft platform. If the resulting spacecraft motion is not limited, the system performance could be seriously degraded. In some cases this motion is actively controlled using the attitude control reaction jets, requiring substantial amounts of propellant and limiting the useful on-orbit life of the system, or using reaction wheels, with limitations due to the saturation of these devices [101, 102]. The main risk of this strategy is to lead the spacecraft into over-controlled regimes, caused by unstable feedback behavior, which can compromise the mission. In order to avoid this contingency, the spacecraft is usually left free-floating during the arm operation, by switching the attitude control off. As a consequence, very low reaction forces and momenta exchanged between the arm and its base are desired, in order to reduce the deviations from the reference attitude configuration.

Standard control techniques, like the "*Jacobian Transposed*" method, (JT), can be simple and efficient in most of the practical cases, but they do not generally take into account the effects of the reaction forces at the spacecraft structure, [95, 96]. This issue can be only tackled as a secondary task via optimal gain tuning [103, 104]. On the other hand, a well-known technique, largely investigated in the past years [97, 98, 28], is the "*Reaction Null space*", (RN), that completely cancels the dynamic coupling between manipulator and spacecraft. Its advantage is that the base body remains in its initial state during the whole manipulators maneuvering. The drawback is that the manipulators workspace is drastically reduced, see [105] for instance. Due to the limitations of the two aforementioned techniques, different solutions have been considered for precisely controlling the end-effector without causing undesired spacecraft motion. In this sense, the reaction-null constraint can be relaxed and some dynamic coupling has to be accepted.

Most of the literature addresses this issue as a path-planning problem. A number of works, facing a kinematical constrained optimization problem, characterizes the degrees of freedom (d.o.f.) as redundant and non-redundant, in order to reduce the number of variables [106, 107, 108]. This distinction can be avoided by identifying directions of minimum disturbances in the full joints space, [109]. Part of the literature focuses directly on the equations of the dynamics and formulates an optimization problem on the instantaneous reaction forces and torques, [110, 111]. Finally, the introduction of the "*Virtual Manipulator*" method, [31, 112], allows the application of methods typical

of ground manipulators to space ones. The main advantages of formulating the minimum disturbance problem as a motion planning one are that: it can be solved off-line; it potentially reduces the on-board computational load, as only the optimal reference trajectory has to be considered; it may potentially offer global optimal solution, as in general no constraints on the computational power are directly involved. However, as a main drawback, the reduction of the dynamic coupling may not be guaranteed during the maneuver, when the system can be driven out of the nominal trajectory by unforeseen disturbances. Moreover, autonomous systems will suffer from reduced operational capability since they will depend on external inputs, especially when a long time is required to solve the trajectory-planning problem off-line. To overcome such issues, the dynamic coupling minimization can be addressed in terms of a control problem, where the reduction of the disturbances is engaged at any time instant. This approach is rather unusual with respect to the path planning approach, and it has been faced for example in [113, 114, 115].

In this work a control method for space manipulators, named Minimum Reaction (MR) controller, is designed to minimize the dynamic coupling with the spacecraft structure without reducing the initial workspace. To this end, the control torque is analytically derived by minimizing a quadratic cost function of the tracking error and of the accelerations applied to the spacecraft. The main characteristics of the proposed controller are that the minimum reaction condition is realized without any off-line constrained optimization; in fact, the task is achieved by relying on the distance at each time step of the end-effector with respect to a desired target position. Additionally, although most of the literature considers planar test cases, in this work the complexity of a three-dimensional asymmetric spacecraft is taken into account, since it is fundamental to move to practical and realistic cases. The chapter is structured as follows: the equations of motion of a fully three-dimensional multibody system are derived and a brief overview of the theoretic background is presented in Section 6.2, then a minimum reaction control problem is formulated and analytically solved (Section 6.3). The controller is applied to a typical mission scenario involving the robotic arm deployment for on-orbit servicing (Section 6.4). Section 6.5 completes the analysis by including the flexible behavior of a solar panel in the system dynamics, and by studying the effects of the elastic oscillations on the performance of the proposed controller.

6.2   Theoretical Background

This section presents a description of the dynamics of space multibody systems and a description of two commonly used control strategies for robotic space manipulators: the Jacobian Transposed (JT) control and the Reaction Null (RN) control. This brief background recalls some concepts which will be used to design the MR controller and

necessary for a critical comparison of the control techniques.

6.2.1   System's Dynamics

Let us consider a space multibody system composed by a main set of bodies (i.e. the base platform, denoted as b) and a space manipulator system (denoted as m), anchored to b, as showed in Fig. 6.1. In the system dynamics all the bodies are considered as rigid and the manipulator joints as ideal. This dynamics will be used to design the controller. In Section 6.5 the possibility to include elastic appendages in the subsystem b will be considered, yet the form of the controller will not be changed and the flexibility will be treated as an input disturbance to the system. Two of the leading approaches

Figure 6.1: Space multibody system composed by the spacecraft platform (bus and solar panel) and the manipulator.

for describing the multibody dynamics are NewtonEuler (NE) and EulerLagrange (EL) approach, [116, 117]. The NE approach considers a complete set of equations of motion for each single body belonging to the system, including the reactions that allow the respect of the joints constraint; the results is a set of differential (from the dynamics) and algebraic (from the constraints) equations. The EL approach derives the equations of motion starting from the kinetic and potential functionals for the applications of the Hamiltons principle. A third approach can be obtained by employing the NE formulation for assembling the equations of motion and then by describing the ODE governing equations by a minimum set of variables as suggested by Kane in [118, 119]. A similar method has been outlined for the case of space multibody systems in [117, 116], and it will be adopted also in the present chapter; the complete details can be found in the referenced papers, while here only the fundamental definitions are reported. The vector of the system state space can be written as follows:

$$Q = \begin{bmatrix} Q_b{}^T & Q_m^T \end{bmatrix}^T \tag{6.1}$$

In Eq.(1), the variables representing the position and the attitude of the main platform are included in Q_b ; specifically it is called $Q_{b,ang}$ and $Q_{b,pos}$ the platform attitude and position, respectively. In the same way the joints' angles of the manipulator are represented by a vector Q_m. The equations of motion are partitioned as follows:

$$\begin{bmatrix} \mathbf{H}_b & \mathbf{H}_{b\,m} \\ \mathbf{H}_{m\,b} & \mathbf{H}_m \end{bmatrix} \begin{pmatrix} \ddot{Q}_b \\ \ddot{Q}_m \end{pmatrix} + \begin{pmatrix} \Sigma_b \\ \Sigma_m \end{pmatrix} = \begin{pmatrix} F_b \\ F_m \end{pmatrix} + \begin{pmatrix} \tau_b \\ \tau_m \end{pmatrix} \qquad (6.2)$$

where $\mathbf{H}_b$ and $\mathbf{H}_m$ are sub-matrices of the mass matrix representing the spacecraft inertia terms and the inertias of the manipulator's links along the joints' directions respectively. The off-diagonal sub-matrices $\mathbf{H}_{b\,m}$ and $\mathbf{H}_{m\,b}$ represent the coupling terms between the spacecraft and the manipulator ($\mathbf{H}_{b\,m} = \mathbf{H}_{m\,b}^T$). The Σ_b and Σ_m contain the Coriolis and centrifugal terms applied to the platform and to the manipulator respectively. The external forces and torques applied to the platform and to the multibody links are represented by the vectors F_b and F_m respectively. In general, these terms would include gravitational forces and torques. However, due to the brevity of the maneuvers considered in this work, these effects will be neglected. Finally, the control forces and torques applied to the platform and to the joints are represented by τ_b and τ_m . An inertial reference frame is defined as in Fig.6.2, with origin O coincident with the initial position of the main platform body reference frame.

6.2.2   Jacobian Transposed Control

Let us consider the multibody system represented in Fig. 6.2, where the position of the end-effector with respect to the main platform, projected in the inertial reference frame, is identified by the vector $\vec{r}_{ee}$ and the desired end-effector position is represented by the vector $\vec{r}_{ee}^d$. According to the JT control, the torques to be supplied by the motors of the manipulator in order to move the end effector from its actual position $\vec{r}_{ee}$ to the desired one $\vec{r}_{ee}^d$, can be computed with the following expression [120, 121]:

$$\tau_m|_{JT} = -\mathbf{J}_{ee}^T\,\mathbf{K}_p^{ee}\left(\vec{r}_{ee} - \vec{r}_{ee}^d\right) - \mathbf{K}_d^m\,\dot{Q}_m \qquad (6.3)$$

where $\mathbf{K}_p^{ee}$, $\mathbf{K}_d^m$ are the gain matrices for the end-effector position error and for the joint velocities respectively. The Jacobian matrix $\mathbf{J}_{ee}$ links the relative velocity of the end-effector with respect to the main platform to the joint angular velocities of the manipulator:

$$\dot{\vec{r}}_{ee}^{\,b} = \mathbf{J}_{ee}\,\dot{Q}_m \qquad (6.4)$$

The JT control scheme in Fig. 6.3 shows the logic steps which characterize this kind of controller. The state vector and the respective time derivatives are used for the computation of the Jacobian matrix $\mathbf{J}_{ee}$ as well as for the end-effector position. The control torques, evaluated taking the difference between the reference and actual end-
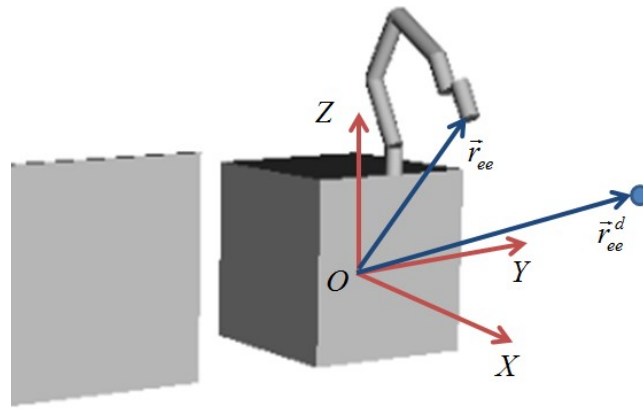
Figure 6.2: End-effector and target position vectors in the main spacecraft frame.

effector position into account, are then sent as a feedback to the dynamics block.
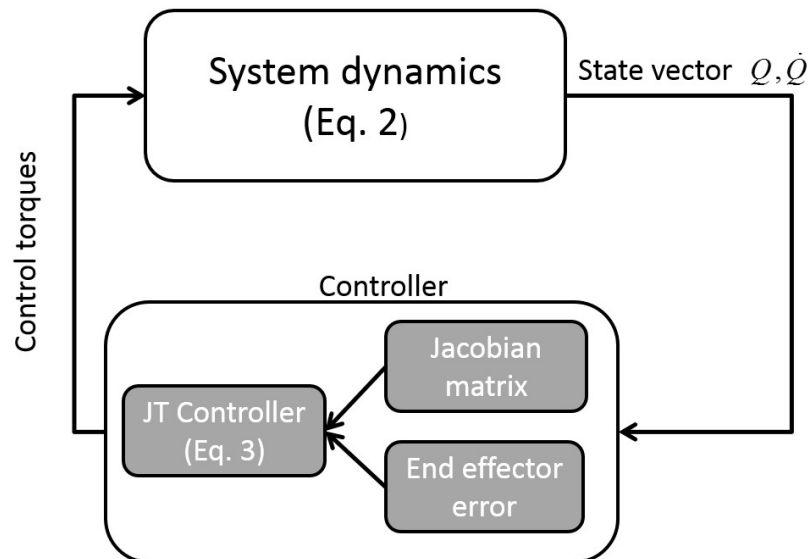
Figure 6.3: Control scheme of the JT controller.

6.2.3 Reaction Null Control

The reaction null approach can be developed either in terms of a path-planning problem, [95], or in terms of direct evaluation of the control torques during the maneuver, [122]. In the first case, the task of searching for the end-effector motion, which does not cause attitude variations of the base platform, is addressed. This can be accomplished by identifying different sub-matrices in the multibody mass matrix, relevant to the linear (subscript ν) and angular velocities (subscript ω), and to the coupling terms (subscript

$\nu\,\omega$):

$$\mathbf{H}_b = \begin{bmatrix} \mathbf{H}_{b,\nu} & \mathbf{H}_{b,\nu\,\omega} \\ \mathbf{H}_{b,\nu\,\omega}^T & \mathbf{H}_{b,\omega} \end{bmatrix} \; ; \; \mathbf{H}_{bm} = \begin{bmatrix} \mathbf{H}_{bm,\nu} \\ \mathbf{H}_{bm,\omega} \end{bmatrix} \tag{6.5}$$

By imposing that the linear and angular momenta are constant, under the constraint that the base angular velocity is constantly zero, it is possible to write

$$\left(-\mathbf{H}_{b,\nu\,\omega}^T\,\mathbf{H}_{b,\nu}^{-1}\,\mathbf{H}_{bm,\nu} \; + \; \mathbf{H}_{bm,\omega}\right)\dot{Q}_m = \mathbf{0} \tag{6.6}$$

Referring back to Eq. (6.4), it is possible to write Eq. (6.6) as a function of the velocities (linear and angular) of the end-effector with respect to the manipulator base $\dot{\vec{r}}_{ee}$:

$$\left(-\mathbf{H}_{b,\nu\,\omega}^T\,\mathbf{H}_{b,\nu}^{-1}\,\mathbf{H}_{bm,\nu} \; + \; \mathbf{H}_{bm,\omega}\right)\mathbf{J}_{ee}^{-1}\,\dot{\vec{r}}_{ee} = \mathbf{B}_{RN}\,\dot{\vec{r}}_{ee} = \mathbf{0} \tag{6.7}$$

where $\mathbf{J}_{ee}^{-1}$ could actually stand for a pseudo-inverse operation, according to the dimensions of the Jacobian matrix. The difference in the number of columns and rows of matrix $\mathbf{B}_{RN}$ represents the degree of redundancy of the manipulator in the reaction null workspace. In other words, if $m > n$ it is possible to choose $m - n$ components of the $\dot{\vec{r}}_{ee}$ vector (let us call them $\dot{\vec{r}}_{ee}^{\,ind}$ since they can be selected independently), while the remaining components $\dot{\vec{r}}_{ee}^{\,dep}$ must be evaluated solving Eq. (6.7). Defining two new sub-matrices of $\mathbf{B}_{RN}$, it is possible to write:

$$\begin{bmatrix} \mathbf{B}_{RN}^{ind} & \mathbf{B}_{RN}^{dep} \end{bmatrix} \begin{bmatrix} \dot{\vec{r}}_{ee}^{\,ind} \\ \dot{\vec{r}}_{ee}^{\,dep} \end{bmatrix} = \mathbf{0} \tag{6.8}$$

hence:

$$\dot{\vec{r}}_{ee}^{\,dep} = -(\mathbf{B}_{RN}^{dep})^{-1}\,\mathbf{B}_{RN}^{ind}\,\dot{\vec{r}}_{ee}^{\,ind} \tag{6.9}$$

It is now clear that it is possible to evaluate the dependent variables for achieving the desired end effector motion under the constraint of zero angular motion of the base only if matrix $\mathbf{B}_{RN}^{dep}$ is not singular. If it is singular, then the reaction null path of the end effector cannot be resolved. It is thus demonstrated that the application of the reaction null constraint introduces singularities that are not relevant to the pure multibody dynamics, limiting in this way the manipulator original workspace. For the sake of clarity, Fig.6.5 reports some of the singular configurations obtained for the simple case of a 2D manipulator, made of one base and three links. In this case the degree of redundancy is equal to 2, thus it is possible to choose 2 components of the end-effector velocity (in this example, the components relevant to the linear velocity), while the remaining components (the end-effector angular velocity) is evaluated solving Eq. (6.9). The configurations reported in Fig.6.5 are some of the configurations for which $\mathbf{B}_{RN}^{dep}$ (a scalar in this case) is zero. A further insight of the RN problem can be achieved by considering it as a constrained optimization problem, which requires the
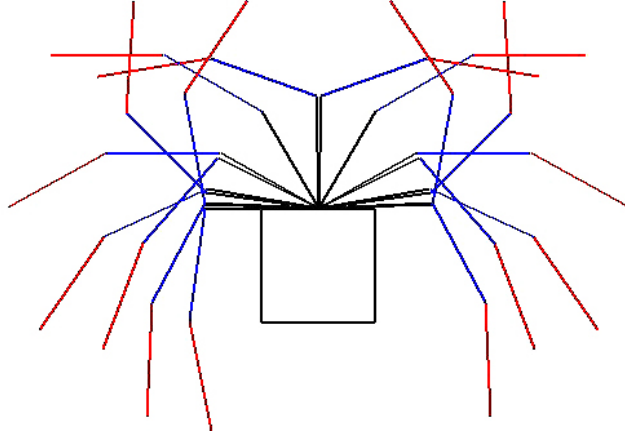
Figure 6.4: Some of the configurations that are singular for the reaction null case.

minimization of the following Hamiltonian function:

$$\mathcal{H}\left(\dot{Q}_m, \lambda_b\right) = \frac{1}{2}\left(\dot{Q}_m - \dot{\chi}_m\right)^T \left(\dot{Q}_m - \dot{\chi}_m\right) + \lambda_b^{\ T}\left(\mathbf{H}_{bm}\ \dot{Q}_m\right) \qquad (6.10)$$

where $\chi(t)$ is the vector containing the desired reference joints' trajectories. The cost function contains both a quadratic form expression, which takes the error between the actual and desired joints velocities into account, and a hard constraint, which decouples the dynamics of the manipulator and the platform. As shown in [116], the multiplication of the term $\mathbf{B}_{bm}\dot{Q}_m$ by the Lagrange multipliers $\lambda_b^{\ T}$ guarantees that the linear and angular momenta of the platform do not change when the robotic arm moves. In the case that only angular variations of the base are constrained, then the hard constraint in Eq. (6.10) is equivalent to Eq. (6.8). This approach, differently from the path planning previously explained, leads to the direct computation of the RN joints control torques, by minimizing the Eq. (6.10):

$$\tau_m|_{RN} = \mathbf{H}_m\ \mathbf{N}_s\ \ddot{\chi}_m - \mathbf{H}_m\ \mathbf{H}_{bm}^*\ \Sigma_b^* + \Sigma_m^* \qquad (6.11)$$

where $\mathbf{N}_s = \mathbf{E} - \mathbf{H}_{bm}^*\mathbf{H}_{bm}$ and $\mathbf{H}_{bm}^* = \mathbf{H}_{bm}^T\left(\mathbf{H}_{bm}\ \mathbf{H}_{bm}^T\right)^{-1}$ are the null space and pseudo-inverse of the sub-matrix $\mathbf{H}_{bm}$ respectively; $\mathbf{E}$ is the identity matrix and the terms Σ_b^* and Σ_m^* are defined as follows: $\Sigma_b^* = \Sigma_b - F_b$; $\Sigma_m^* = \Sigma_m - F_m$. The final form of the controller depends on the reference acceleration vector $\ddot{\chi}_m$. In reference [116], $\ddot{\chi}_m$ has been designed using a JT controller torque as input, i.e.:

$$\ddot{\chi}_m = -\mathbf{J}_{ee}^T\ \mathbf{K}_p^{ee}\left(\vec{r}_{ee} - \vec{r}_{ee}^{\ d}\right) - \mathbf{K}_d^m\ \dot{Q}_m \qquad (6.12)$$

and it is also the form adopted in the present chapter, since it allows to introduce a contribution of the end-effector error to the RN control at each time step. It is possible to see in Fig. 6.4 that part of the control scheme is identical to the JT control, but the resulting JT torque is not directly send as a feedback. Instead it enters the RN

block as reference acceleration to be tracked. In this sense, the RN acts as a sort of filter for the JT output. The application of this control guarantees that the condition of zero-reaction on the base platform b is satisfied at every time. However, it does not cancel the risk of not reaching the target due to the reduction of the manipulators workspace.
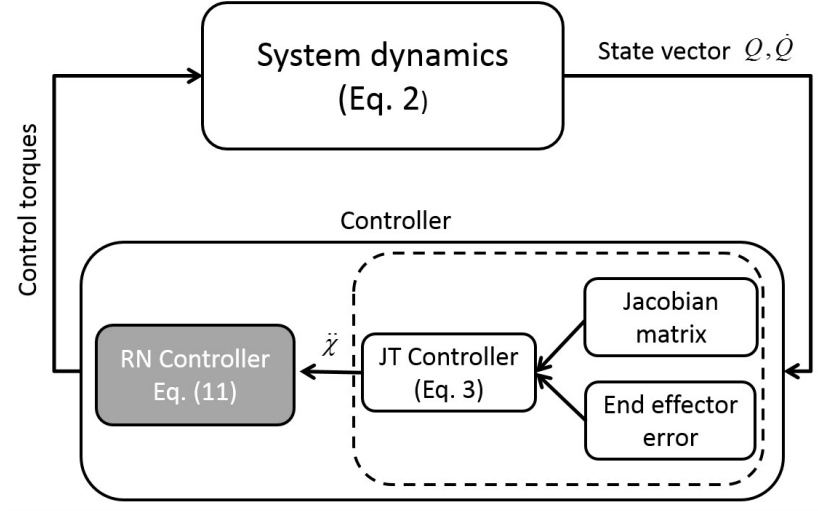
Figure 6.5: Control scheme of the RN controller.

6.3   Minimum reaction control

The limitations of the reaction-null approach call for new solutions where the constraint is relaxed, and control laws, which produce an acceptably low momentum exchange between the manipulator and the spacecraft, are considered. Specifically, the following optimal control problem is defined in order to obtain a control law for the joints torques τ_m such that:

- the error between the instantaneous joints acceleration vector and a joints reference acceleration vector is minimized;

- the instantaneous accelerations induced on the uncontrolled base are minimized.

To this end, a quadratic cost function is formulated and the proposed MR control law is derived by minimizing it:

$$\mathcal{H} = \frac{1}{2}\ddot{Q}_b{}^T\mathbf{W}_1{}^T\mathbf{W}_1\ddot{Q}_b + \frac{1}{2}\left(\ddot{Q}_m - \ddot{\chi}_m\right)^T\mathbf{W}_2{}^T\mathbf{W}_2\left(\ddot{Q}_m - \ddot{\chi}_m\right) \qquad (6.13)$$

where $\ddot{\chi}_m$ is the desired acceleration vector and the weight matrices $\mathbf{W}_1$ and $\mathbf{W}_2$ are introduced in order to obtain the desired balancing between the terms. As in the RN case, only the angular accelerations on the main platform $\ddot{Q}_{b,ang} = \left[\ddot{Q}_{b,\phi}\,,\,\ddot{Q}_{b,\theta}\,,\,\ddot{Q}_{b,\psi}\right]^T$

will be minimized, but the approach is reported for the general case. The main plat-
form of the system is left free-floating in order to avoid over-control problems, $\tau_b = 0$,
thus leading to the following expression for the platform accelerations:

$$\ddot{Q}_b = -\mathbf{H}_b^{-1} \left(\mathbf{H}_{bm}\, \ddot{Q}_m + \Sigma_b^* \right) \tag{6.14}$$

Substituting Eq. (6.14) back in the system's dynamics Eq. (6.2), yields:

$$\tau_m|_{MR} = \left(\mathbf{H}_m - \mathbf{H}_{mb}\, \mathbf{H}_b^{-1}\, \mathbf{H}_{bm} \right) \ddot{Q}_m - \mathbf{H}_{mb}\, \mathbf{H}_b^{-1}\, \Sigma_b^* + \Sigma_m^* \tag{6.15}$$

By substituting Eq. (6.14) into Eq. (6.3), cost function can be expressed as fol-
lows:

$$\begin{aligned}
\mathcal{H} =& \frac{1}{2} \left(\mathbf{H}_{bm}\, \ddot{Q}_m + \Sigma_b^* \right)^T \tilde{\mathbf{H}}_b^* \left(\mathbf{H}_{bm}\, \ddot{Q}_m + \Sigma_b^* \right) + \\
& \frac{1}{2} \left(\ddot{Q}_m - \ddot{\chi}_m \right)^T \tilde{\mathbf{W}}_2 \left(\ddot{Q}_m - \ddot{\chi}_m \right)
\end{aligned} \tag{6.16}$$

where $\tilde{\mathbf{H}}_b^* = (\mathbf{H}_b^{-1})^T \mathbf{W}_1^T \mathbf{W}_1 \mathbf{H}_b^{-1}$ and $\tilde{\mathbf{W}}_2 = \mathbf{W}_2^T \mathbf{W}_2$. The necessary and sufficient
optimality condition follows as:

$$\frac{\partial \mathcal{H}}{\partial \ddot{Q}_m} = \mathbf{H}_{bm}^T \tilde{\mathbf{H}}_b^* \left(\mathbf{H}_{bm}\, \ddot{Q}_m \right) + (\mathbf{H}_{bm})^T \tilde{\mathbf{H}}_b^* \Sigma_b^* + \tilde{\mathbf{W}}_2 \left(\ddot{Q}_m - \ddot{\chi}_m \right) = \mathbf{0} \tag{6.17}$$

Its solution leads to the optimal joints' acceleration as:

$$\ddot{Q}_m = - \left(\mathbf{H}_{bm}^T \tilde{\mathbf{H}}_b^* \mathbf{H}_{bm} + \tilde{\mathbf{W}}_2 \right)^{-1} \left(\mathbf{H}_{bm}^T \tilde{\mathbf{H}}_b^* \Sigma_b^* - \tilde{\mathbf{W}}_2\, \ddot{\chi}_m \right) \tag{6.18}$$

The expression of the control torques is finally obtained by substituting Eq. (6.3) into
Eq.(Eq16):

$$\begin{aligned}
\tau_m|_{MR} =& - \left(\mathbf{H}_m - \mathbf{H}_{mb}\, \mathbf{H}_b^{-1}\, \mathbf{H}_{bm} \right) \left(\mathbf{H}_{bm}^T \tilde{\mathbf{H}}_b^* \mathbf{H}_{bm}^T + \tilde{\mathbf{W}}_2 \right)^{-1} \cdot \\
& \cdot \left(\mathbf{H}_{bm}^T \tilde{\mathbf{H}}_b^* \Sigma_b^* - \tilde{\mathbf{W}}_2\, \ddot{\chi}_m \right) - \mathbf{H}_{mb}\, \mathbf{H}_b^{-1}\, \Sigma_b^* + \Sigma_m^*
\end{aligned} \tag{6.19}$$

6.3.1   Design of the reference acceleration vector

The derivation of the optimal control law in Eq. (6.3) requires the design of the in-
stantaneous reference acceleration vector $\ddot{\chi}_m = \ddot{\chi}_m(t)$. Since a closed-loop controller
is desired because of its inherent capability of compensating for external disturbances
and modelling inaccuracies, $\ddot{\chi}_m$ can be used to introduce a feedback. To this end, it
is possible to note that the joint accelerations generated by the JT control explicitly
depend on the end-effector error at each time instant. Therefore, the reference acceler-
ations are derived calculating the JT torque $\tau_m|_{JT}$ in Eq. (6.3) and back substituting

it into Eq. (6.2). Since the base is uncontrolled, Eq. (6.14) holds, and the reference trajectory can be written as:

$$\ddot{\chi}_m = \ddot{Q}_m(\tau_m|_{JT}) = \left(\mathbf{H}_m - \mathbf{H}_{mb}\,\mathbf{H}_b^{-1}\,\mathbf{H}_{bm}\right)^{-1}\left(\tau_m|_{JT} + \mathbf{H}_{mb}\,\mathbf{H}_b^{-1}\,\Sigma_b^* - \Sigma_m^*\right) \quad (6.20)$$

It is worth to note that this design solution lets the output torque of the MR controller be exactly the JT torque, when the weight matrix $\mathbf{W}_1$ is set to zero:

$$\tau_m|_{MR} \equiv \tau_m|_{JT} \quad : \quad \mathbf{W}_1 = \mathbf{0} \qquad (6.21)$$

In fact, by definition, $\mathbf{W}_1 = 0$ implies that $\tilde{\mathbf{H}}_b^* = 0$, therefore from Eq. (6.3) it follows that:

$$\tau_m|_{MR} = -\left(\mathbf{H}_m - \mathbf{H}_{mb}\,\mathbf{H}_b^{-1}\,\mathbf{H}_{bm}\right)\,\tilde{\mathbf{W}}_2^{-1}\,\tilde{\mathbf{W}}_2\,\ddot{\chi}_m - \mathbf{H}_{mb}\,\mathbf{H}_b^{-1}\,\Sigma_b^* + \Sigma_m^* \qquad (6.22)$$

By substituting the desired acceleration $\ddot{\chi}_m$ in Eq. (6.13), the relation $\tau_m|_{MR} \equiv \tau_m|_{JT}$ is obtained. On the other hand, for increasing values of the matrix $\mathbf{W}_1$, it will tend to the behaviour of the RN case. The overall control scheme of the MR reaction controller is shown in Fig.6.6. Table 6.1 outlines the main advantages and disadvantages of the
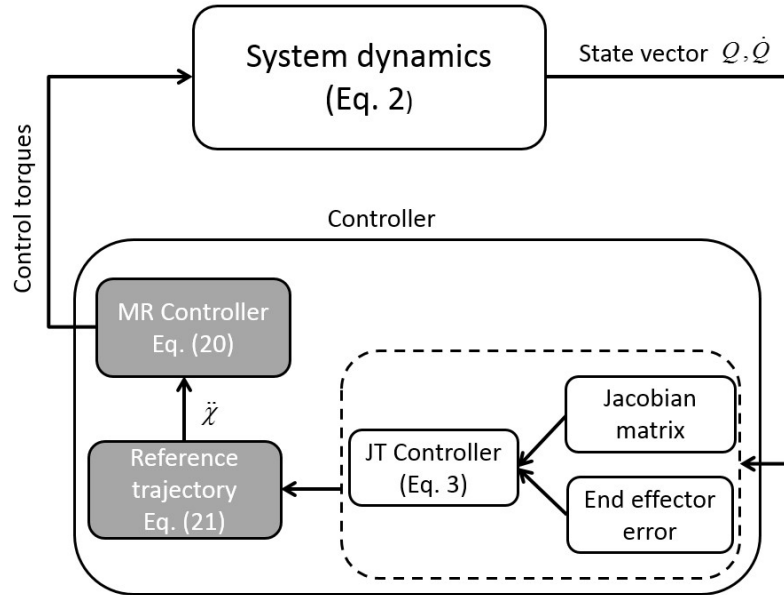
Figure 6.6: Control scheme of the MR controller.

JT, RN and MR techniques. With respect to the JT, the MR controller addresses the dynamic coupling issues; with respect to the RN controller, the MR does not suffer from singularity problems. On the other hand, the final formulation of the control law, Eq. (6.3), is more complex compared to Eq. (6.3) and Eq. (6.11), and it depends on a larger number of parameters to be tuned.

Controller	Pros	Cons
JT	Simple, direct position and velocity feedback	Dynamic coupling not addressed
RN	Dynamic coupling resolved	Reduced workspace
MR	Dynamic coupling reduced, Unlimited workspace	Complex formulation

Table 6.1: Main advantages and disadvantages of the JT, RN and MR controllers.

6.4   Case study1: Ideal rigid multibody

A case study has been selected in order to compare the MR control method, as it has been derived in the previous section, with the standard JT control and the RN control. A space multibody system, made by an asymmetric main spacecraft - i.e. a cubic bus of $2m$ side and a single solar array ($12m$ length and $2.50m$ wide) - plus a robotic arm, has been selected as the testing platform and it is represented in Fig.6.1. In this first test case, all the bodies (including the solar panel) are considered rigid and the joints are ideal revolute joints. The inertial properties and geometrical characteristics of the system are shown in Table 6.2 and Table 6.3.

	Mass(kg)	**L**(m)	**r**(m)
Base platform b	1500.0		
Solar panel σ	71.9		
Link 1	17.0	0.30	0.10
Link 2	45.1	0.80	0.10
Link 3	45.1	0.80	0.10
Link 4	45.1	0.80	0.10
Link 5	22.5	0.40	0.10
Link 6	22.5	0.40	0.10

Table 6.2: Mass properties and dimensions of the parts of the multibody

The initial configuration of the manipulator is represented in Fig.6.2, and the initial joint angles of such configuration are listed in Table 6.4. In the test case manoeuver, the end-effector has to reach a target position, fixed in the inertial reference frame. A number of different target positions have been tested, showing the same qualitative behavior. In this chapter, an exemplary one is reported. Its spherical coordinates, expressed in the main platform reference frame at the initial time, are shown in Table 6.5. The simulation time is set to 60s, however the end-effector has to reach its reference

	I_{xx} $(kg\ m^2)$	I_{yy} $(kg\ m^2)$	I_{zz} $(kg\ m^2)$
Base platform b	1000.0	1000.0	1000.0
Solar panel σ	3972.02	109.3	3931.50
Link 1	0.58	0.58	0.15
Link 2	9.83	9.83	0.41
Link 3	9.83	9.83	0.41
Link 4	9.83	9.83	0.41
Link 5	1.31	1.31	0.20
Link 6	1.31	0.20	1.31

Table 6.3: Moments of inertia of the multibody system

	Q_{mi} (deg)
Joint 1	90
Joint 2	-30
Joint 3	60
Joint 4	90
Joint 5	30
Joint 6	0

Table 6.4: Joints' coordinates representing the initial configuration of the manipulator.

position in 15 s.

Coordinates of Target Point		
Radius	r (m)	2.5
Polar angle	θ (rad)	$b/3$
Azimuth angle	ϕ (rad)	0.0

Table 6.5: Spherical coordinates of the target, defined relatively to the base reference frame at the initial time.

6.4.1 Controllers gains tuning

In order to have a fair comparison between the three controllers, an optimal tuning of the gains and parameters is performed. In particular, for the JT the aim is to determine the proportional and derivative gains that minimize the overall angular acceleration, under the constraint that the position error Δ_{EE} (i.e. the distance between end-effector and target, at the final time) does not exceed 1cm, with a relative velocity equal or less than $1\,mm/s$. By defining the gain matrices of the JT control as $\mathbf{K}_p^{ee} = k_p\,\mathbf{E}_{3\times3}$ and $\mathbf{K}_d^m = k_d\,\mathbf{E}_{N_m\times N_m}$, the following problem is defined as the minimization of the cost

function C :

$$\min_{k_p, k_d} C = \min_{k_p, k_d} \int_{t=0}^{t_f} \|\ddot{Q}_{b,ang}(t)\| \, dt$$

subject to:

$$\Delta_{EE} \leq 1 \, cm \quad \text{and} \quad \dot{\Delta}_{EE} \leq 1 \, mm/s$$

(6.23)

These cost functions have been selected in order to consider a global behavior during the maneuver. The Matlab® `fmincon` optimization algorithm has been used and the results are listed in Table 6.6. The reference acceleration $\ddot{\chi}_m$ of the RN controller (see Eq. (6.12)) will be computed relying on the same optimized values found for the JT control.

Control Method	k_p	k_d	Δ_{EE} (cm)	C (rad/s)
JT	65	140	0.33	0.5521

Table 6.6: Optimal gains and end-effector position error at the final manoeuvre time for the JT controller.

Concerning the MR control, the same optimal gains of the JT method are used to produce the instantaneous reference acceleration $\ddot{\chi}_m$, however a second optimization problem must be posed, since the MR controller depends on the additional weight matrices $\mathbf{W}_1$ and $\mathbf{W}_2$. In particular, in order to simplify the problem, the weight matrices are considered as dependent only on two scalar parameters, w_{1t} and w_{1r}:

$$\mathbf{W}_1 = w_{1t} \begin{bmatrix} \mathbf{E}_{3\times3} & \mathbf{0} \\ \mathbf{0} & \mathbf{0} \end{bmatrix} + \begin{bmatrix} \mathbf{0} & \mathbf{0} \\ \mathbf{0} & \mathbf{E}_{3\times3} \end{bmatrix}$$

$$\mathbf{W}_2 = \mathbf{E}_{N_m \times N_m}$$

(6.24)

where the subscripts of $\mathbf{E}$ represent the dimensions of the identity matrices. With this choice a distinction is made between angular and linear induced accelerations. The problem is defined as:

$$\min_{w_{1t}, w_{1r}} C = \min_{w_{1t}, w_{1r}} \int_{t=0}^{t_f} \|\ddot{Q}_{b,ang}(t)\| \, dt$$

subject to:

$$\Delta_{EE} \leq 1 \, cm \quad \text{and} \quad \dot{\Delta}_{EE} \leq 1 \, mm/s$$

(6.25)

The resulting optimal weights are listed in Table 6.7.

Control Method	w_{1t}^{opt}	w_{1r}^{opt}	Δ_{EE} (cm)	C (rad/s)
MR	1.99	57.92	0.30	0.2800

Table 6.7: Optimal weights for the MR controller and the relative manoeuvre end-effector position error at the final time.

6.4.2   Numerical Results

Fig.6.7 reports the distance between the end-effector and its desired position for the three maneuvers performed by means of the JT, RN and MR controllers. It is evident that only the JT and MR controllers satisfy the requirements of the mission. In fact, the reference point to be reached is inside the manipulator workspace, but outside the reaction null space, and the RN controller cannot successfully accomplish the mission.
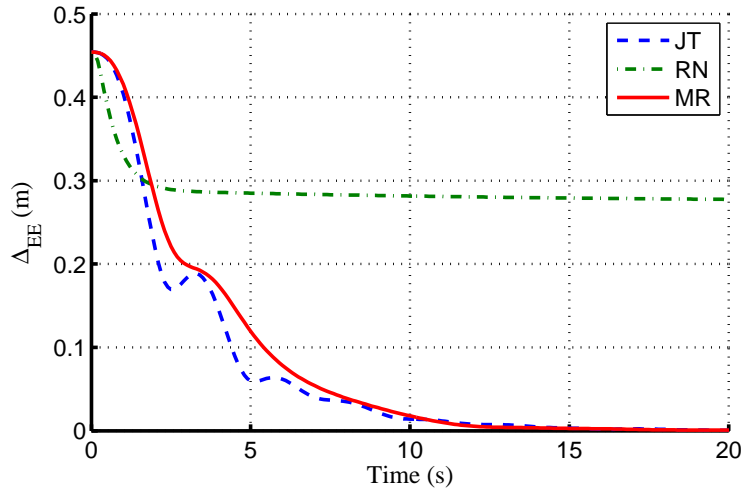
Figure 6.7: Distance between the end-effector and its desired position.

Fig. 6.8, Fig. 6.9 and Fig. 6.10 show the effects of the three different controllers on the angular accelerations induced at the base body. As expected, the RN does not affect at all the motion of the base. Angular accelerations are instead induced by the JT controller. These accelerations are sensibly reduced by the application of the MR controller, with no remarkable change in the torque requirements[3], as it can be seen in Fig.6.11 (where only the three largest torques are shown). Magnitude and frequency of the oscillations and the overall integral value of the torques required by the JT and RN are nearly the same.

Fig.6.12 shows the angular displacement of the main platform for the pitch axis, whose magnitude order is of 10^{-1} radians, i.e. a few degrees, while the yaw and roll angular deviations are not shown as negligible. This large angular displacement occurred as the MR controller has been designed with the aim of minimizing the accelerations

---

[3]Note that torques are all reduced.
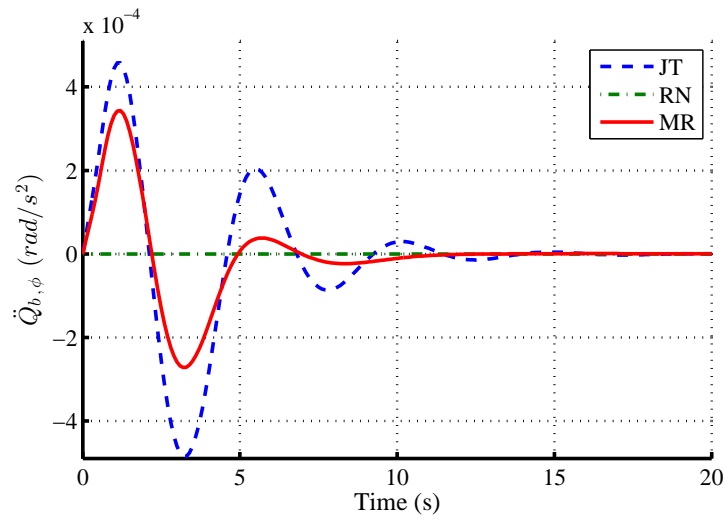
Figure 6.8: Comparison of the JT, MR and RN control effect on the base angular acceleration $\ddot{Q}_{b\,\phi}$.
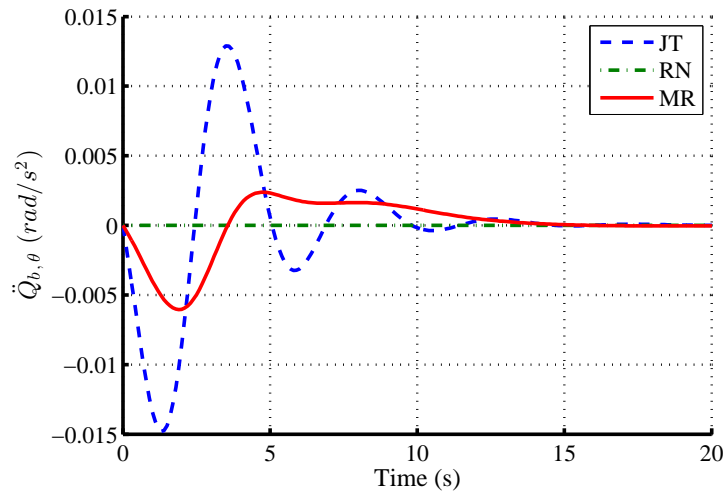
Figure 6.9: Comparison of the JT, MR and RN control effect on the base angular acceleration $\ddot{Q}_{b\,\theta}$.
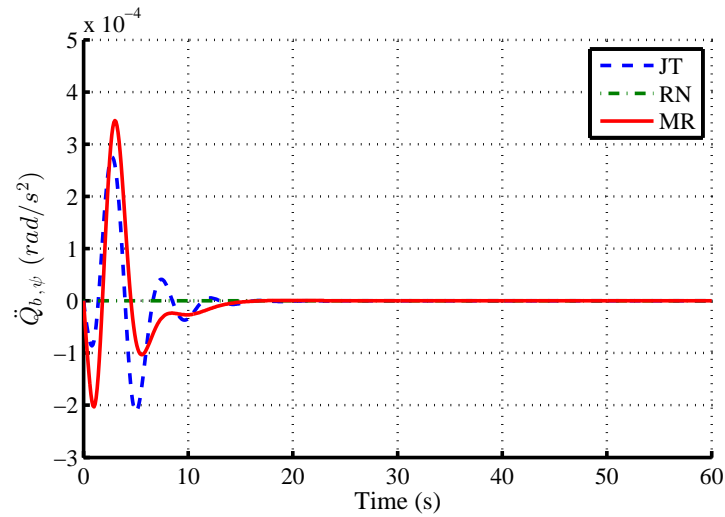
Figure 6.10: Comparison of the JT, MR and RN control effect on the base angular acceleration $\ddot{Q}_{b\,\psi}$.

induced to the spacecraft and not its displacements. Consequently, an effect on the base configuration is expected. It should be noted that the test case shown here considers a highly asymmetric body (due to the presence of the panel and of only one manipulator); additionally, the manipulator has a relatively low number of degrees of freedom, thus it has a limited workspace. Both these elements contribute to explain the magnitude of the effects of the controller on the spacecraft attitude.
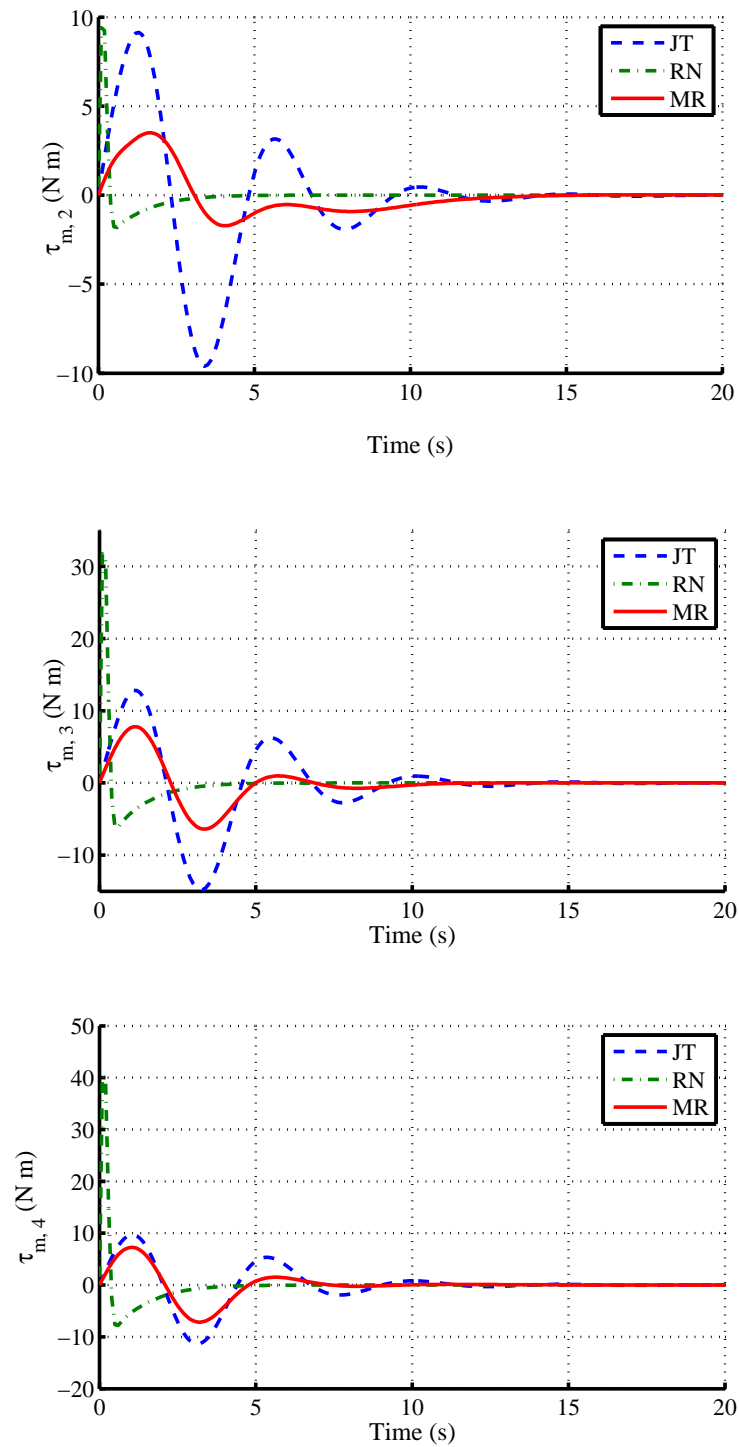
Figure 6.11: Comparison of the joints' control torques between the MR and the JT controllers.
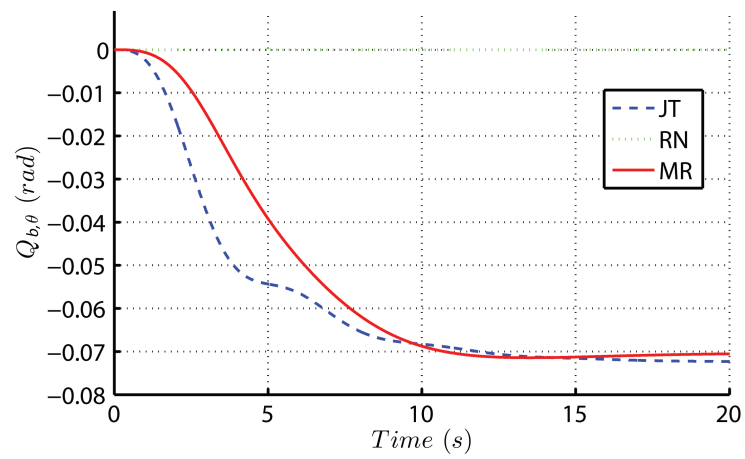
Figure 6.12: Comparison of the JT, MR and RN control effect on the base angular displacement. The figure shows the Euler angle $Q_{b,\theta}$

6.4.3   Further investigation on the MR behavior

In order to better understand the behavior of the MR controller, a parametric study is performed by varying the weight matrices. The results are summarized in Fig.6.13, where the cost function C (which represents the overall angular acceleration exerted on the platform) and the final error on the position of the end-effector are reported for different weight matrices, defined as functions of the optimal value:

$$w_{1r} = w_{1r}^{opt}\ 10^{\epsilon} \qquad ; \qquad w_{1t} = w_{1t}^{opt}\ 10^{\epsilon} \tag{6.26}$$

In the condition $\mathbf{W}_1 = \mathbf{0}$ (i.e. $\epsilon \to -\infty$), the MR controller behaves exactly as the
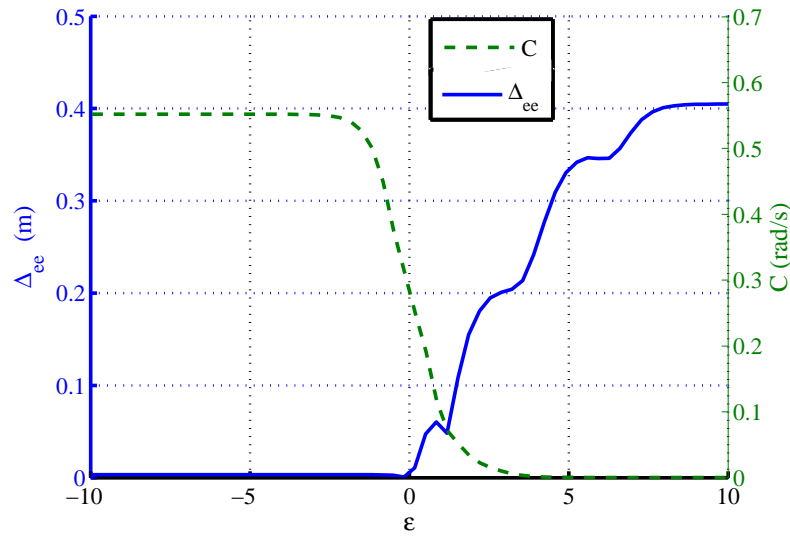
Figure 6.13: Cost function and final error on end-effector position for different orders of magnitude of the weight matrices.

JT controller, as expected from Eq. (6.3.1). Increasing the weight value, accelerations are reduced with the effect of increasing the final distance from the target; for $\mathbf{W}_1 \to \infty$ (i.e. $\epsilon \to +\infty$) the MR controller behaves just like the RN controller. In this sense, the proposed MR algorithm manages to achieve a balanced trade-off between the JT advantages (ability to reach the desired position for the end-effector) and the RN advantages (possibility to decrease the accelerations suffered by the platform). When the optimal weight parameters are used (i.e. $\epsilon = 0$) a low value of the base accelerations is obtained, without increasing the end-effector error. In this rigid and ideal case the presence of larger angular accelerations at the base does not seriously affect the mission requirements fulfilment. However, when flexibility is introduced in the dynamic model, as it will be shown in following Section 5, elastic oscillations are excited by these accelerations, thus resulting in an increase of the control torques, and even in the risk of structural damages.

6.5 Case study 2: Inclusion of flexible dynamics

In this section, some of the elements of the main platform b are considered as flexible bodies rather than rigid bodies. In particular, the solar panel is modeled as a highly flexible body locked at the central platform. The geometric and inertial characteristics of the panel are equal to the ones considered in the rigid case; the elastic characteristics are introduced by including in the system dynamics (but not in the controllers) the first five modes of vibration, whose characteristics and relevant natural frequencies are reported in Table 6.8 and qualitatively represented in Fig. 6.14.

	Frequency (10^{-1} Hz)	Modal Shape
1	1.98	Flexural
2	4.65	Torsional
3	4.95	Flexural
4	9.41	Flexural
5	9.83	Torsional

Table 6.8: Modal shapes and natural frequencies of the solar panel.
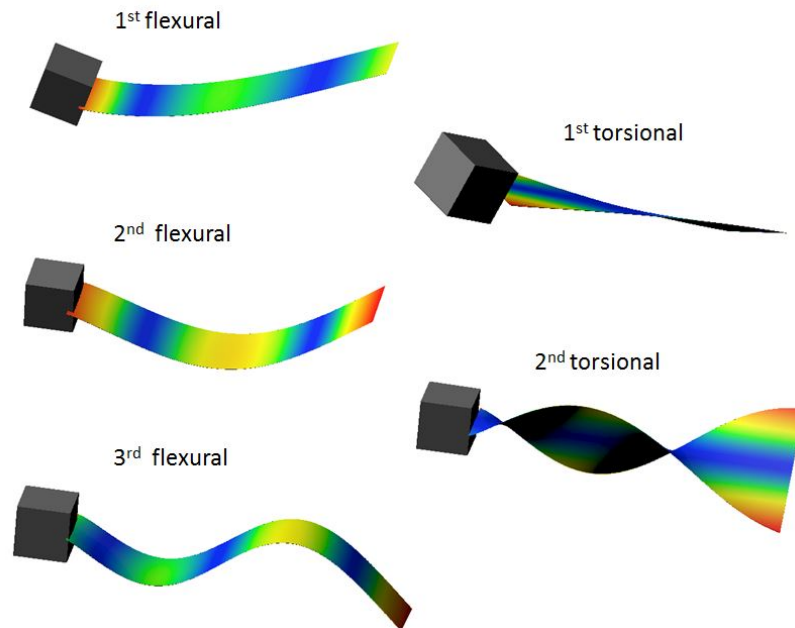
Figure 6.14: First five modal shapes of the solar panel.

In this second case study, the same manoeuvre is repeated with the same controllers of Section 4. Furthermore, the system matrices used for the evaluation of the JT, RN and MR controllers do not take the flexible effects into account. From the controller design point of view, these effects are equivalent to a disturbance, and the same gains and weight matrices of the rigid case are used in the simulations. The results, in terms of distance of the end-effector with respect to its desired position (Fig.6.15), and base

angular displacement, roughly $0.06rad$ in this case, are qualitatively not much affected by the introduction of the flexible dynamics.
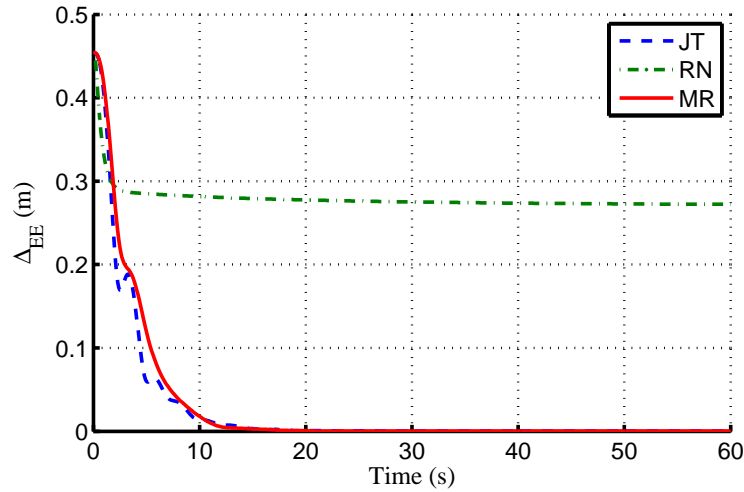
Figure 6.15: End-effector distance from the target during the fast manoeuvre (flexible solar panel).

On the other hand, it is clear that the ability of the RN control to completely cancel the angular accelerations at the base is heavily affected, as it is possible to see in Fig.6.16, Fig.6.17 and in particular in Fig.6.18. In fact, the null space of the system, modelled as a rigid multibody, does not coincide with the null space of the actual flexible multibody, hence the platform suffers from angular accelerations induced both in the JT, RN, and MR cases. Moreover, it can be noticed that, similarly to the rigid case, the MR control improves the JT performance in terms of smaller platform accelerations, and, on the other hand, improves the RN performance in terms of ability to reach the desired end-effector position. The presence of the accelerations induced on the platform by the movement of the manipulator produces an excitation on the flexible panel. Fig.6.19 reports the first five modes of vibration. Interestingly, the most solicited ones are different if RN is considered rather than JT and MR. In fact, the RN control produces very low (zero in the ideal rigid case) angular accelerations, with the result that elastic torsion of the panel is not highly affected. On the other hand, RN does not take linear accelerations into account, with the result that the flexural vibrations modes are sensibly excited, much more than in the case of the other controllers. Conversely, in the JT and MR case the first torsional mode (second subplot) is by far the most solicited, because of the particular manoeuvre of the manipulator, which causes high accelerations around the y-axis, i.e. the panel longitudinal axis. The application of the MR control has an evident advantage in the decrease of the oscillations, with maximum values of the oscillation reduced by 75.11% on the 2nd modal shape and by 72.81% on the 5th modal shape (torsional ones). This is achieved with a qualitatively equivalent behavior of the control torques obtained in the rigid cases.
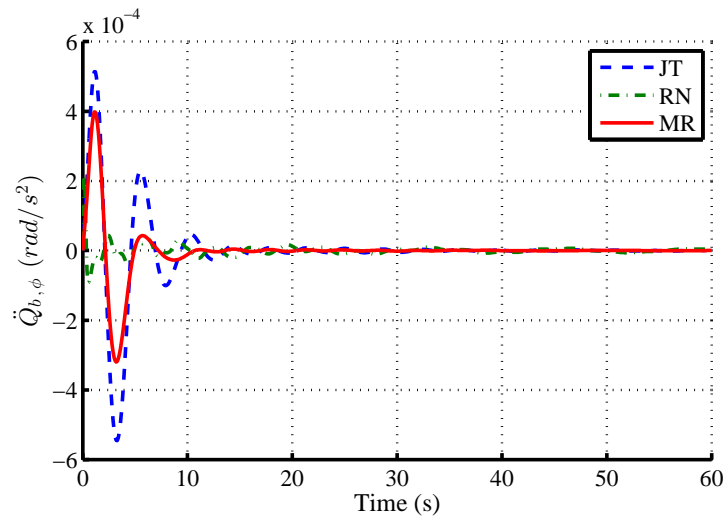
Figure 6.16: Comparison of the JT, MR and RN control effect on the base angular acceleration, $\ddot{Q}_{b\,\phi}$ (flexible solar panel).
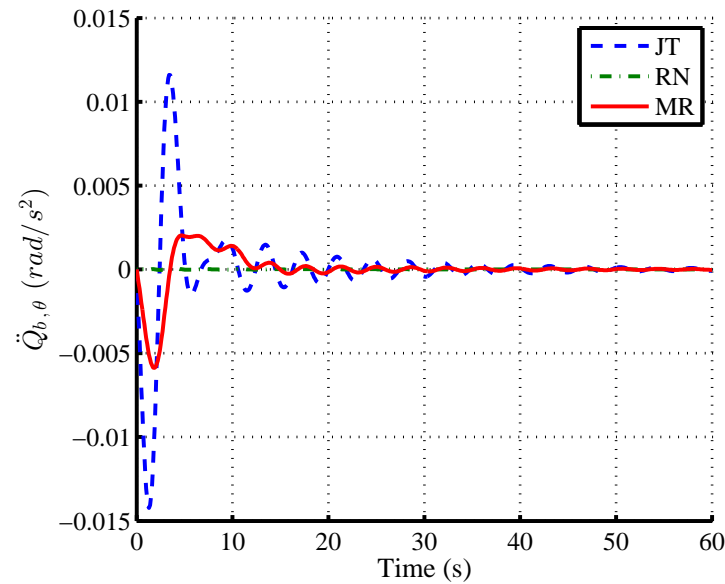
Figure 6.17: Comparison of the JT, MR and RN control effect on the base angular acceleration, $\ddot{Q}_{b\,\theta}$ (flexible solar panel).
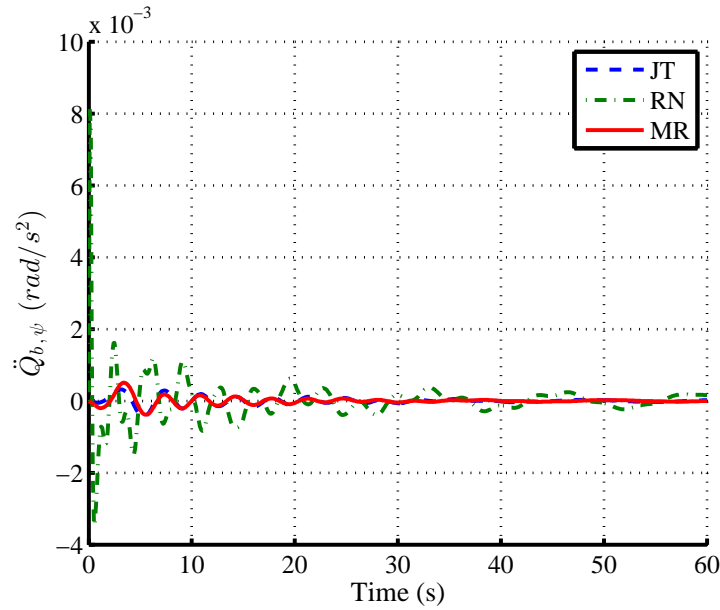
Figure 6.18: Comparison of the JT, MR and RN control effect on the base angular acceleration, $\ddot{Q}_{b\,\psi}$ (flexible solar panel).

6.6 Conclusions

This chapter has studied a generic 3D N-body system focussing on the problem of reducing the dynamic coupling between one of the bodies and the rest of the system. In particular, minimization of the reactions has been addressed as a control problem, a solution advantageous for autonomous systems. To this end, first, an optimal problem has been formulated and solved analytically using a quadratic cost function. Weight matrices have been introduced in the controller to obtain the desired balance between the reduction of the reaction forces on the main body and the limitation of the error over the system's desired configuration. In order to obtain a feedback controller, the JT control torque has been used as input. The derived controller has been tested on a system formed by an asymmetric spacecraft endowed with a six degrees of freedom manipulator, and, furthermore, compared with the standard JT controller and the RN controller for a reasonable mission scenario. A target position for the end-effector was set as fixed in the inertial reference frame and a mission manoeuvre time of $15s$ chosen. Results have shown that a RN controller cannot complete the mission and it ends far from the target. The JT controller can accomplish the mission with relatively small control torques. A MR controller can accomplish the mission with qualitatively equivalent control torques, the same accuracy and greatly reducing the accelerations suffered from the spacecraft during the manipulator's motion. A parametric study has shown how the weight matrices affect the behavior of the controller. When weights are set such that importance is given only to the tracking error, the MR controller behaves exactly as a JT controller. Conversely, if the weights are set such that only
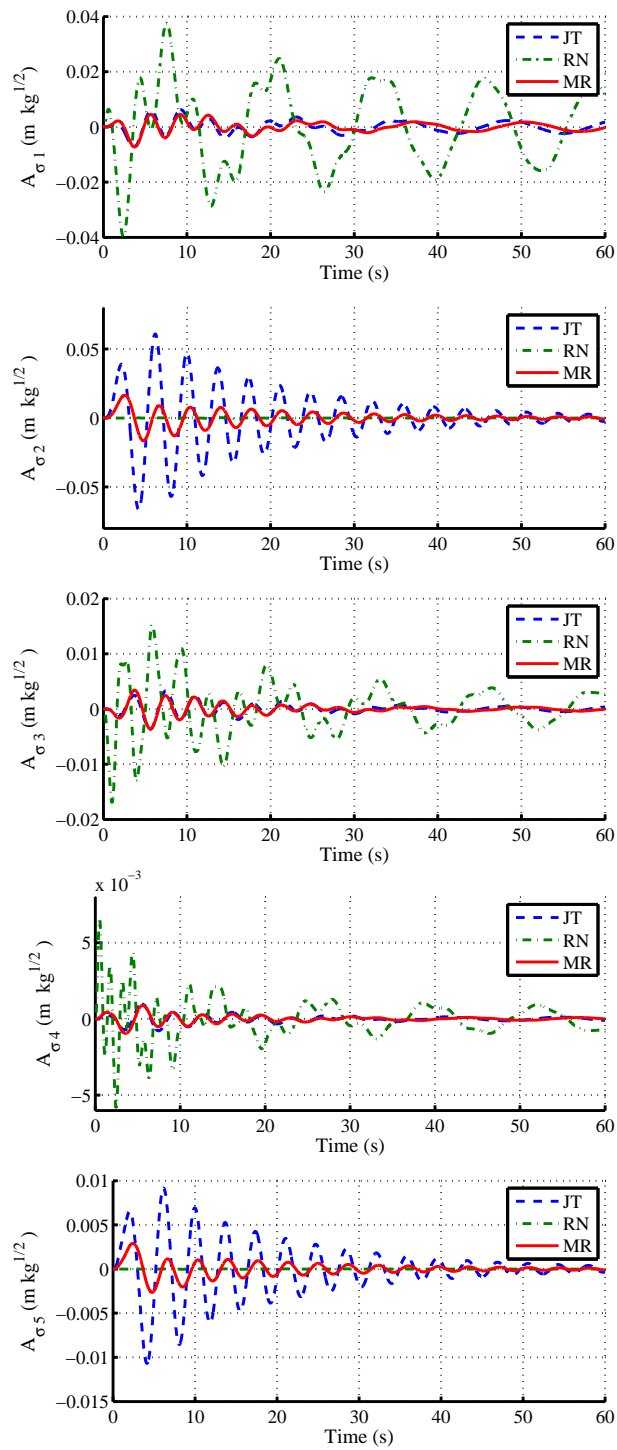
Figure 6.19: Modal amplitudes of the solar panel during the fast manoeuvre.

the minimization of the reactions is considered, the MR behavior gets closer to a RN controller. The three controllers have also been tested in a non-nominal case, in which the multibody includes a flexible panel, such as a solar array. In this case as well, the MR performance in terms of base acceleration reduction is confirmed, with the important consequence that also the amplitude of the flexible displacement of the panel decreases. This involves clear benefits in terms of structural solicitations and accuracy of the control. This performance is promising for a number of practical applications of the controller when very low (but not necessary zero) reactions are desired.

Conclusions and Future Research

7.1 Conclusions

The main aim of this thesis was to investigate the attitude dynamics of spacecraft described as rigid-body systems and, in particular, to analyse their natural motions, to evaluate the usefulness of mathematical tools to inform system and control design and, finally, to research efficient control techniques based on natural motions.

Results indicate the Hamiltonian and Lagrangian formalisms as the most appropriate for systems with a reduced number of bodies, providing a deep insight into the heavily nonlinear behaviour of the system, revealing the structure of the system's dynamics using a minimum-variables analytical form. Conversely, it is shown that Newton-Euler approach is the most appropriate to the study of many-bodies problem, as it provides a compact form, faster to derive than the Euler-Lagrange equations and enabling a more intuitive access to the physical understanding of the problem.

The single spacecraft

The study of multi-body spacecraft attitude dynamics has been undertaken starting from the single asymmetric rigid body, which describes the case where all mechanical joints are locked. Specifically, focus was placed on the integrable problem of a free spacecraft. The closed-form solution was revised and expressed both in quaternions form and rotation matrix form, as more useful for aerospace applications than the classical solutions. Main advantages of the derived solutions are in that they provide a

kinematical description of the system's natural evolution with no need of any numerical integration and, in addition, free of singularities. This, makes them convenient for a number of applications. In this thesis, it was suggested to employ them to design an open-loop control for efficient "bang-bang" large attitude manoeuvres.

Given a reasonable scenario, the reference derived from the closed form solution has been tracked using a simple open loop control strategy. Controlled motions, used to start and stop the motion, with a coasting phase. Despite the action of air drag and gravity gradient torques, included in the numerical simulation, the spacecraft could be reconfigured to the desired final configuration. The numerical test highlighted two limitations of the closed form solutions as derived in this thesis. First concerned the use of the incomplete elliptic integral of the third kind, whose evaluation might burden low-computational processors. The second, the presence of jump discontinuities in the quaternions form due to the non-uniqueness of the quaternions to represent a rotational motion.

The two-spacecraft system

Proceeding to study multi-body systems incrementally starts with a two-body system. The problem was restricted to the planar case and the action of a central gravitational field included. Hamilton's equations showed that attitude dynamics and orbital dynamics are coupled, however, could be decoupled by accepting a negligible error of approximation on the orbital motions. Concerning the attitude dynamics, it was shown that there are four relative equilibria, which exist only for circular orbits, defined by the bodies' relative position. Of those sets, two are nonlinearly unstable and one nonlinearly stable. On the contrary, the stability of the fourth set is parameter dependent. The stability condition could be condensed into a single equation and a bifurcation diagram, constructed varying length and hinge position of a spacecraft, was provided.

Globally, the behaviour of the system far from the equilibria consists of three different types: regular, quasi-regular and chaotic. Regions of periodic motion surround the stable equilibria; equivalently, regions of chaotic motion surround the unstable equilibria and, finally, quasi-periodic motions characterise the remaining domain. Lyapunov exponents analysis indicated that regular motions regions have an ellipsoidal shape, with the main axis parallel to the bisectrix of the first and third quadrant of the (q_{30}, q_{40}) plane. Furthermore, zero velocity maps reveal that the structure of the iso-energy manifolds is parameter dependent and that connections between stable equilibria could be naturally created.

The time scale of the natural attitude dynamics is of the same order of magnitude as

the orbital dynamics. The action of air drag does not alter this time scale and its effect is to displace equilibria without affecting their stability.

Given a reasonable mission scenario, the dynamical analysis was used to inform system and control design for a large reconfiguration manoeuvre. Results showed that natural motions could be practically exploited to improve efficiency. The proposed strategy integrated the spacecraft attitude control, designed to guarantee monotone convergence of the system to the global minimum, with the control of a system's parameter, i.e. the distance of the hinge in one of the spacecraft. Comparison with a PD controller, used as a standard reference, highlighted a significantly better performance of the tailored solution both in terms of control torques and energy consumption, both almost one order of magnitude smaller.

The three-body spacecraft

The thesis, then, extended the analysis to the three-body system. Six classes of relative equilibria were identified for a total number of 35 equilibria over the three attitude angles' domain. For every class each body is either aligned with the $X|_{ORF}$ or with the $Y|_{ORF}$, that is, parallel or perpendicular to the position vector of the overall center of mass with respect to the main inertial reference frame. Analysis of the stability determined that all the equilibria where the bodies are perpendicular to $X|_{ORF}$ are unstable and that all the configurations where the bodies' chain is fully open and bodies are aligned with $X|_{ORF}$ are stable, and that all the others are conditionally stable. Bifurcation diagrams highlighting the parametric dependency were provided. Furthermore, investigation showed a very complex structure of the underlying natural dynamics, and, even in this case, connections between equilibria were found using energy maps. Global behaviour was shown to be characterised by chaotic motions in most of the domain and stable manifolds surrounding the stable equilibria were found to be relatively much smaller than the two-body case. Despite the complex nature of the system it was demonstrated that the use of a simple PD controller is able to control the system maintaining an unstable equilibrium configuration even in presence of the disturbance of air drag, using little torque.

A comparison of the results in the first three chapter outlined important characteristics of orbiting multi-body systems. Increasing the number of bodies incrementally, the mathematical structure of the problem did not change and the equations remained, in the same form. However, this increased the complexity of the equations in terms of number of parameters involved and non-linearity. In addition, together with the number of bodies, the number of equilibria increased, with the majority of their stability being parameter dependent. Furthermore, the relative size of the regular motion domain decreased.

The N-body spacecraft control

Based on the results obtained, the research on rigid-body spacecraft was extended to consider a generic N-body system. The study concentrated on the dynamic coupling problem, a topic particularly relevant for articulated spacecraft, such as space manipulators. Using the Newton-Euler approach the problem was considered in the three dimensional space. Reduction of dynamical coupling between connected rigid bodies was addressed as a control problem. The controller combined the design method of the Reaction Null (RN) controller with the typical feedback form of a Jacobian Transposed (JT) controller. The resulting controller, called a Minimum Reaction controller, was tested in a typical mission scenario and compared both with the RN controller and the JT controller. Results showed that with no increase in control torques magnitude and equal manoeuvre accuracy there was a significant reduction of the dynamical coupling between manipulator and the spacecraft main bus. As further benefit of the MR controller action, vibrations of flexible appendages attached to the spacecraft were shown to be significantly dumped with respect to the JT control case. Main controller limitations were identified in the complex form of the controller, which depends on a number of parameters to be tuned, and in the lack of direct control on the spacecraft attitude.

The use of dynamical systems tools

The complex dynamics of multi-body systems and their non-integrability, except for the free single rigid body case, make the use of numerical dynamical tools critical to gain an insight into the system's behaviour. Phase plots and Poincaré sections are very simple and computationally fast tools, however they only provide a local behaviour description as based on the analysis of a single trajectory. This implies that, to understand the global behaviour, they have to be used a number of times and a methodology to select the initial conditions has to be formulated. In order to gain a wider description of the dynamics, more complex tools have to be used such as Poincaré maps and Lyapunov Exponents maps which, unfortunately, involve a non negligible cost in terms of required computational time (in the order of magnitude of days - Section 4.5.3). Information disclosed by Poincaré maps and LCE maps are complementary. The firsts provide a visual indication of the evolution of the system over the domain providing elements to understand the configuration manifold structure. LCE maps give a precise description of the system's behaviour over the domain as it is possible to directly map each initial condition studied with a real number containing the desired information. Finally, Hamiltonian maps have been used. These aid the understanding of the morphology of the gravitational potential over the domain which, ultimately, provided information about the evolution of the natural motions.

In conclusion, as each tool enriches the dynamical analysis providing a different "point of view" to the dynamics, these numerical tools are complementary and each of them is essential in order to gain a global portrait of the system behaviour. The main drawbacks are are related to the data collection and data processing. Increasing the number of bodies, the dimension of the configuration space increases and so the number of projections (e.g. Poincaré maps) required to inspect the configuration manifold increases. This results in a difficulty to provide a large quantity of information in a limited number of plots. For few-body systems these numerical techniques have proved invaluable but the computational expense and the quantity of data make them infeasible for many-body systems.

Control of multi-body systems

The design of reduced control strategies based on natural motion was one of the main research objectives of this thesis. The concept was a novelty in spacecraft attitude dynamics, although already efficaciously introduced in other fields such as astrodynamics. Results showed that only for single asymmetric rigid body an analytical description of the natural motions could be derived. This was effectively used to produce energy and torque efficient motions based on the exploitation of the natural motions. For more complex cases, the analysis was limited to a qualitative description of the behaviour over the domain. Nevertheless, control strategies base on the systems nonlinear dynamics could be designed and, in particular, the spacecraft ability to vary one or more of the parameters was used. Using simple PD controllers as a term of reference, numerical tests showed that significative performance improvements could be obtained. These results indicate that reduced control strategies which improve manoeuvreing efficiency by exploiting natural motions have the potential to extend spacecraft operational capabilities and pave the way to new multi-spacecraft missions. In addition, systems parameters, such as the hinge position, play a critical role and are identified as key control variables that could be exploited in future missions.

Similarly to few-body problems, dynamical analysis of the N-body problem was used as a starting point to design the minimum reaction controller. In particular, the investigation of the reaction null configuration space lead to the definition of the minimum reaction functional and it is identified as a key point to the addressing of the dynamical coupling problem.

7.2 Future Research

Chapter 2 presented a motion planner for asymmetric rigid spacecraft based on the use of natural motions as references for reconfiguration manoeuvres. The selection of

the required reference track was obtained using an optimisation of the desired initial angular velocities, however, no particular constraints on the trajectory path have been taken into account; for instance, some of the attitude domain may be forbidden in order to protect specific instruments from the sun light. A reference constructed using only a single natural motion, i.e. a single coasting phase, may not be able to solve these problems. Therefore, future work will have to address the design of more complex references constituted by sequences of natural motions. Furthermore, the main limitations of the references designed concern their on-board implementation. In particular, issues related to the evaluation of the elliptic integral of the third kind have to be addressed in order to increase the motion planner feasibility.

The investigation of the two-body and three-body systems were restricted to the planar case. In addition the shape of the bodies was assumed to be one dimensional. Future work will have to extend both these elements. In particular, modelling spacecraft as rigid asymmetric bodies can potentially introduce new equilibria and modify the stability of the known ones. The extension of the planar problem to 3D space will be a necessary step to consider more realistic scenarios. In addition, the investigation of tailored control solutions based on the results provided has to be further addressed as the presence of connections between equilibria in the Hamiltonian maps is identified as a potential element to design large reconfiguration manoeuvres using natural motions. Furthermore, the chaotic nature of the three-body problem in the vast majority of the domain suggest that chaotic controllers, such as the OGY method, [92], or the time-delayed Pyragas method, [93], could be useful.

The N-body chapter addressed the design of a minimum reaction controller to reduce the dynamical coupling of the multi-body system on one of the bodies, e.g. the space-craft main bus. Also in this case, a number of practical issues have to be tackled for a feasible employment of the MR controller on board. Concerning this problem, future work will first provide a deeper insight into the gains tuning process. This will aim to verify if the optimization process can indirectly solve undesired bus angular displacements and if a single gains optimization suffices to reach all the targets in the workspace with the required precision. Furthermore, robustness with respect to system inaccuracies or stronger external disturbances shall be examined.

Bibliography

[1] A. A. Shabana, *Dynamics of Multibody Systems, third edition*. Cambridge, 2005.

[2] NASA. (2014) National space science, data center. [Online]. Available: http://nssdc.gsfc.nasa.gov/nmc/masterCatalog.do?sc=1968-055A

[3] ——. (2014) National space science, data center. [Online]. Available: http://nssdc.gsfc.nasa.gov/nmc/masterCatalog.do?sc=1973-039A

[4] D. Akin, M. Misnky, E. Thiel, and C. Kurtzman, "Space applications of automation, robotics and machine intelligence system (aramis) - phase ii," NASA Contractor Report, Tech. Rep. 3734, 1983.

[5] J. Erickson, "Manned spacecraft automation and robotics," in *Proceedings of the IEEE*, vol. 75, no. 3, March 1989, pp. 417–426.

[6] E. Papadopoulos, "On the dynamics and control of space manipulators," Ph.D. dissertation, Department of Mechanical Engineering, Massachussetts Intitute of Technology, 1990.

[7] K. Yoshida, "Achievements in space robotics," *The International Journal of Robotics Research*, vol. 22, no. 5, pp. 321 – 335, May 2003.

[8] I. Tethers Unlimited. (2014) micropet: Propellantless electrodynamic tether propulsion for microsatellites. [Online]. Available: http://www.tethers.com/microPET.html

[9] R. Hoyt and R. Forward, "The terminator tether: autonomous deorbit of leo spacecraft for space debris mitigation," in *Proceeding of the 38th Aerospace Sciences Meeting & Exhibit*, Reno, Nevada, 2000.

[10] C. S. Agency. (2014) Canadian space agency official website - dextre. [Online]. Available: http://www.asc-csa.gc.ca/eng/iss/dextre/profile.asp

[11] E. Coleshilla, L. Oshinowoa, R. Rembalaa, B. Binaa, D. Reyb, and S. Sindelarb, "Dextre: Improving maintenance operations on the international space station," *Acta Astronautica*, 2009.

[12] B. Sicialiano and O. Khatib, *Springer Handbook of Robotics.* Springer, 2008.

[13] D. Reintsema, J. Thaeter, A. Rathke, W. Naumann, P. Rank, and J. Sommer, "Deos the german robotics approach to secure and de-orbit malfunctioned satellites from low earth orbits," in *Proceeding of the Robotics and Automation in Space (i-SAIRAS)*, Sapporo, Japan, 2010.

[14] T. Wolf, D. Reintsema, B. Sommer, P. Rank, and J. Sommer, "Mission deosproofing the capabilities of germans space robotic technologies," in *Proceeding of the International Symposium on Artificial Intelligence, Robotics and Automation in Spacei-SAIRAS*, 2012.

[15] C. I. o. T. Prof. S. Pellegrino. (2014) Aarest overview. [Online]. Available: http://pellegrino.caltech.edu/aarest.html

[16] J. P. Shoer, "Dynamics of reconfigurable multibody space systems connected by magnetic flux pinning," Ph.D. dissertation, Cornell University, 2011.

[17] J. Guo, D. Maessen, and E. Gill, "Fractionated spacecraft: the new sprout in distributed space systems," in *Proceeding of the International Astronautical Congress 2009, IAC-09-D1.1.4*, 2009.

[18] M. Macdonald (Editor), *Advances in Solar Sailing.* Springer Praxis Books / Astronautical Engineering, 2014.

[19] P. C. Hughes, *Spacecraft Attitude Dynamics.* Dover publications, inc, 2004.

[20] A. Guerman, "Spatial equilibria of multibody chain in a circular orbit," *Acta Astronautica*, vol. 58, no. 1, 2006.

[21] N. Sreenath, Y. Oh, P. Krishnaprasad, and J. Marsden, "The dynamics of coupled planar rigid bodies. part i reduction, equilibria and stability," *Dynamics and Stability of Systems*, vol. 3, no. 1 & 2, 1998.

[22] A. Sanyal and A. Bloch, "Two connected bodies in a central gravitational field," in *Proceeding of the IEEE Conference on Decision and Control. CDC. 43rd*, December 2004, p. 3968.

[23] A. Sanyal, "Dynamics and control of multibody systems in central gravity," Ph.D. dissertation, Department of Aerospace Engineering, University of Michigan, Ann Arbor, 2004.

[24] G. Patrick, "Two axially symmetric coupled rigid bodies: relative equilibria, stability, bifurcations, and a momentum preserving symplectic integrator," Ph.D. dissertation, Department of Mathematics, University of California, Berkeley, 1995.

[25] N. Sreenath, Y. Oh, P. Krishnaprasad, and J. Marsden, "The dynamics of coupled planar rigid bodies. part ii bifurcations, periodic solutions, and chaos," *Journal of Dynamics and Differential Equations*, vol. 1, no. 3, 1989.

[26] S. A. A. Moosavian and E. Papadopoulos, "Free-flying robots in space: an overview of dynamics modeling, planning and control," *Robotica*, 2007.

[27] D. King, "On-orbit satellite servicing and active debris removal," in *Proceeding of the Secure World Foundation Conference*, February 20th, 2013.

[28] S. V. Shah, I. Sharf, and A. K. Misra, "Reactionless path planning strategies for capture of tumbling objects in space using a dual-arm robotic system," in *AIAA Guidance, Navigation, and Control Conference*, Boston, 2013.

[29] G. B. Palmerini, M. Sabatini, P. Gasbarri, R. Monti, and L. Felicetti, "Design of debris removal missions performed by robotic graspers," in *Proceeding of the International Astronautical Congress 2012*, IAC-12-C2.2.11, 2012.

[30] E. Papadopoulos and S. Dubowsky, "On the dynamic singularities in the control of free-floating space manipulators," in *Proceedings of the 1989 ASME Winter Annual Meeting: Dynamics and Control of Multibody/Robotic Systems with Space Applications*, San Francisco, CA, December 1989.

[31] Z. Vafa and S. Dubowsky, "The kinematics and dynamics of space manipulators: The virtual manipulator approach," *The International Journal of Robotics Research*, vol. 9, no. 3, 1990.

[32] J. Marsden and T. Ratiu, *Introduction to Mechanics and Symmetry.* New York : Springer - Verlag, 1999.

[33] A. Bloch, *Nonholonomic Mechanics and Control.* Springer New York, 2003.

[34] W. S. Koon, M. W. Lo, J. E. Marsden, and S. D. Ross, *Dynamical Systems, the Three-Body Problem and Space Mission Design.* CalTech, 2011.

[35] M. Vetrisano, W. Van der Weg, and M. Vasile, "Navigating to the moon along low-energy transfers," *Celestial Mechanics and Dynamical Astronomy*, vol. 114, no. 1-2, pp. 25–53, 2012.

[36] A. Moore, S. Ober-Blobaum, and J. Marsden, "Trajectory design combining invariant manifolds with discrete mechanics and optimal control," *Journal of Guidance, Control, and Dynamics*, vol. 35, p. 1507, 2012.

[37] K. Flakamp, J. Timmermann, S. Ober-Blbaum, and A. Trchtler, "Control strategies on stable manifolds for energy-efficient swing-ups of double pendula," *International Journal of Control*, vol. 87, no. 9, p. 18861905, 2014.

[38] G. Rekleitis and E. Papadopoulos, "On on-orbit passive object handling by co-operating space robotic servicers," in *IEEE/RSJ International Conference on Intelligent Robots and Systems*, San Francisco, CA, USA, September 2011.

[39] J. Blanton and J. Junkins, "Dynamical constrains in satellite photogrammetry," *AIAA Journal*, vol. 15, no. 4, p. 488, April 1977.

[40] M. Meshcheryakov, "The integration of the equations for geodesies of left-invariant metrics on simple lie groups using special functions." *Mat. Sb.*, vol. 117, no. 159, p. 481, November 1982.

[41] E. T. Whittaker, *A treatise on the analytical dynamics of particles and rigid bodies*. Cambridge Mathematical Library, Cambridge University Press, 1999.

[42] F. F. Larry Bates, "The conjugate locus for the euler top i. the axisymmetric case," in *International Mathematical Forum, 2, no. 43*, 2007, pp. 2109 – 2139.

[43] F. Fassò, "The euler-poinsot top: a non-commutatively integrable system without global action-angle coordinates," *Z. Angew. Math. Phys.*, vol. 47, pp. 953–976, 1996.

[44] F. Olver, D. Lozier, R. Boisvert, and C. Clark, *NIST Handbook of Mathematical Functions*. Cambridge, 2010.

[45] Wolfram. (2012) Elliptic functions and elliptic integrals. [Online]. Available: http://functions.wolfram.com/EllipticFunctions/$\hskip2em\relax$http://functions.wolfram.com/EllipticIntegrals/

[46] J. Biggs, C. D. Maclean, and A. Caubet, "Heteroclinic optimal control solutions for attitude motion planning," in *Proceeding of the Australian Control Conference, ACC 2013*, 2013.

[47] C. Maclean, D. Pagnozzi, and J. Biggs, "Planning natural repointing manoeuvres for nano-spacecraft," *IEEE Transactions on Aerospace and Electronic Systems*, vol. 50, no. 3, p. 2129, 2014.

[48] C. D. Maclean, D. Pagnozzi, and J. Biggs, "Computationally light attitude controls for resource limited nano-spacecraft," in *Proceeding of the 62nd International Astronautical Congress 2011*, Cape Town, South Africa, 2011.

[49] W. W. Hooker and G. Margulies, "The dynamical attitude equations for an n-body satellite," *Journal of the Astronautical Sciences*, vol. 12, no. 4, pp. 123 – 128, 1965.

[50] W. W. Hooker, "Equations of motion for interconnected rigid and elastic bodies: a derivation independent of angular momentum," *Celestial Mechanics*, vol. 11, pp. 337 – 359, 1975.

[51] A. Pisculli and P. Gasbarri, "A minimum state multibody/fem approach for modeling flexible orbiting space systems," *Acta Astronautica*, vol. In Press, November 2014.

[52] P. Santini and P. Gasbarri, "General background and approach to multibody dynamics for space applications," *Acta Astronautica*, vol. 64, p. 1224, 2009.

[53] A. Sanyal, A. Bloch, and N. H. McClamroch, "Dynamics of multibody systems in planar motion in a central gravitational field," *Journal of Dynamicsal Sytems*, vol. 19, no. 4, pp. 303–343, 2004.

[54] B. Wie, *Space Vehicle Dynamics and Control*. AIAA Education Series, 2nd addition, 2008.

[55] O. I. Bogoyavlenskil, "Integrable problems of the dynamics of coupled rigid bodies," *Russian Acad. Sci. Izv. Math.*, vol. 41, no. 3, 1993, http://iopscience.iop.org/1468-4810/41/3/A01.

[56] P. Gasbarri, "A two-dimensional approach to multibody free dynamics in space environmnet," *Acta Astronautica*, vol. 51, no. 15, p. 831, 2002.

[57] P. Santini and P. Gasbarri, "Dynamics of multibody systems in space environment; lagrangian vs. eulerian approach," *Acta Astronautica*, vol. 54, p. 1, 2003.

[58] V. Jurdjevic, *Geometric Control Theory*. Advanced Studies in Mathematics, Cambridge University Press 52, 2008.

[59] N. A. Chaturvedi, A. K. Sanyal, and N. McClamroch, "Rigid-body attitude control using rotation matrices for continuous, singluarity-free control laws," *IEEE Control Systems Magazine*, vol. 30, June 2011.

[60] M. Shuster, "A survey of attitude representations," *Journal of Astronautical Sciences*, vol. 41, no. 4, 1993.

[61] J. Stuelpnagel, "On the parametrization of the three-dimensional rotation group," *SIAM Rev.*, vol. 6, no. 4, 1964.

[62] H. P.C., *Spacecraft Attitude Dynamics*. Wiley New York, 1986.

[63] J. D. Biggs, "Singularities of optimal attitude motions," in *18th IFAC conference on automatic control in aerospace*, Nara, Japan, 2010.

[64] P. E. Crouch, "Spacecraft attitude control and stabilization: Applications of geometric control theory to rigid body models," *IEEE. Transactions on automatic control*, vol. 29, no. 4, 1984.

[65] B. Wie and P. Barba, "Quaternion feedback for spacecraft large angle manoeuvers," *AIAA Journal of Guidance, Dynamics and Control*, vol. 8, no. 3, 1985.

[66] K. F., *The Mathematical Theory of the Top, in Congruence of Sets and other Monographs.* Chelsea Publishing Company, New York, Lectures delivered in Princeton in 1896, 1896.

[67] B. A. Springborn, "The toy top, an integrable system of rigid body dynamics," *Journal of Nonlinear Mathematical Physics*, vol. 7, no. 3, p. 386, 2000.

[68] H. N. Biggs, J. D., "Optimal geometric motion planning for a spin-stabilized spacecraft," *Systems and Control letters*, vol. 61, no. 4, p. 609, 2012.

[69] M. Audin, *Spinning Tops: A course on integrable systems.* Cambridge studies in Advanced Mathematics, Cambridge University Press, 51, 1996.

[70] B. Dubrovin, I. Krichever, and S. Novikov, *Integrable Systems I, in Dynamical Systems IV, Editors V.I. Arnold and S.P. Novikov.* in Encyclopaedia of Mathematical Sciences, no. 4,Springer, Berlin, 1990.

[71] P. D. Lax, "Integrals of nonlinear equations of evolution and solitary waves," *Communications on pure and applied mathematics*, vol. 21, p. 467, 1968.

[72] D. F. Lawden, *Elliptic Functions and Applications.* Berlin etc. Springer-Verlag 1989. XIV, Applied Mathematical Sciences 80, 1989.

[73] S. Rawashdeh and J. J. Lumpp, "Aerodynamic stability for cubesats at iss orbit," *Journal of Small Satellites*, vol. 2, no. 1, p. 85, 2013.

[74] C. Bonnal, J.-M. Ruault, and M.-C. Desjean, "Active debris removal: Recent progress and current trends," *Acta Astronautica*, vol. 85, pp. 51 – 60, 2013.

[75] NASA, "On-orbit satellite servicing study, project report," National Aeronautics and Space Administration Goddard Space Flight Center, Tech. Rep., 2010.

[76] A. Ogilvie and et al., "Autonomous satellite servicing using the orbital express demonstration manipulator system," in *Proc. of the 9th International Symposium on Artificial Intelligence, Robotics and Automation in Space (i-SAIRAS'08)*, 2008.

[77] R. B. Friend, "Orbital express program summary and mission overview," in *Proc. SPIE 6958, Sensors and Systems for Space Applications II*, April 2008.

[78] A. Guerman, "Equilibria of multibody chain in orbit plane," *Journal of Guidance, Control and Dynamics*, vol. 26, no. 6, November-December 2003.

[79] B. Rink and T. Tuwankotta, "Stability in hamiltonian systems: Applications to the restricted three-body problem," Mathematisch Instituut, Utrecht University, Tech. Rep., September 2003.

[80] J. Thompson and H. Stewart, *Nonlinear Dynamics and Chaos.* John Wiley and Sons, 1986.

[81] R. C. Hilborn, *Chaos and nonlinear dynamics : an introduction for scientists and engineers.* New York, Oxford University Press, 1994.

[82] M. Hénon and C. Heiles, "The applicability of the third integral of motion: Some numerical experiments," *The Astronomical Journal*, vol. 69, no. 1, February 1964.

[83] G. Benettin, L. Galgani, A. Giorgilli, and J.-M. Strelcyn, "Lyapunov characteristic exponents for smooth dynamical systems and for hamiltonian systems; a method for computing all of them'. part i: Theory." *Meccanica*, vol. 15, March 1980.

[84] ——, "Lyapunov characteristic exponents for smooth dynamical systems and for hamiltonian systems; a method for computing all of them'. part ii: Numerical application." *Meccanica*, vol. 15, March 1980.

[85] A. Wolf, *Quantifying chaos with Lyapunov exponents.* Chaos, Princeton University Press, 1986.

[86] G. Baker and J. Gollub, *Chaotic Dynamics: An Introduction.* Cambridge University Press, 1990.

[87] E. Gawlik, J. E. Marsden, P. Du Toit, and S. Campagnola, "Lagrangian coherent structures in the planar elliptic restricted three-body problem," *Celestial Mechanics and Dynamical Astronomy*, vol. 103, no. 3, p. 227, 2009.

[88] D. Perez, G. Gomez, and J. Masdemont, "Detecting invariant manifolds using hyperbolic lagrangian coherent structures," in *IAA Conference on Dynamics and Control of Space Systems*, 2012, conference Paper ID: IAA-AAS-DyCoSS1-08-06.

[89] T. Peacock and G. Haller, "Lagrangian coherent structures, the hidden skeleton of fluyd flows," *Physics Today*, February 2013.

[90] C. Senatore and S. Ross, "Detection and characterization of transport barriers in complex flows via ridge extraction of the finite time lyapunov exponent field," *International Journal for Numerical Methods in Engineering*, vol. 86, no. 9, p. 1163, June 2011.

[91] F. Christiansen and H. Rugh, "Computing lyapunov spectra with continuous gram-schmidt orthonormalization," *Nonlinearity*, vol. 10, p. 1063, 1997.

[92] A. L. Fradkov and A. Y. Pogromsky, *Introduction to Control of Oscillations and Chaos.* World Scientific Series on Nonlinear Science Series A: Vol. 35, 1998.

[93] K. Pyragas, "Delayed feedback control of chaos," *Philosophical transactions of the royal society A*, July 2006.

[94] J. G. del Amo and G. Saccoccia, "Electric propulsion activities at esa," in *Proceeding of the 31st International Electric Propulsion Conference, University of Michigan, Ann Arbor, Michigan, USA September 20 24, 2009*.

[95] Y. Umetani and K. Yoshida, "Resolved motion rate control of space manipulators with generalized jacobian matrix," *IEEE Transactions on Robotics and Automation*, vol. 5, no. 3, pp. 303 – 314, 1989, doi : 10.1109/70.34766.

[96] Y. Taira, S. Sagara, and R. Katoh, "Digital adaptive control of space robot manipulators using transpose of generalized jacobian matrix," in *Proceedings of the 2000 IEEE/RSJ International Conference on Intelligent Robots and Systems, IROS 2000*, vol. 2, 2000, p. 1553.

[97] K. Yoshida and D. Nenchev, "Space robot impact analysis and satellite base impulse minimization using reaction null space," in *Proceedings of the IEEE International Conference on Robotic and Automation.*, 1995, p. 1271.

[98] D. Dimitrov and K. Yoshida, "Momentum distribution in a space manipulator for facilitating the post-impact control," in *IEEE/RSJ International Conference on Intelligent Robots and Systems, IROS 2004*, 2004, p. 3345.

[99] G. Palmerini, M. Sabatini, P. Gasbarri, R. Monti, and L. Felicetti, "Design of debris removal missions performed by robotic graspers," in *63rd International Astronautical Congress, IAC-12-C2.2.11*, Naples, Italy, 2012.

[100] M. M. Castronuovo, "Active space debris removal - a preliminary mission analysis and design," *Acta Astronautica*, vol. 69, pp. 848 – 859, 2011.

[101] A. Flores-Abad and et al, "A review of space robotics technologies for on-orbit servicing," *Progress in Aerospace Sciences*, vol. 68, pp. 1–26, July 2014.

[102] W. Xu, B. Liang, and Y. Xu, "Survey of modeling, planning and ground verification of space robotic systems," *Acta Astronautica*, 2011.

[103] C. L. Chung, S. Desa, and C. W. deSilva, "Base reaction optimization of redundant manipulators for space applications," The Robotic Institute CMU-RI-TR, Tech. Rep., 1988.

[104] S. A. A. Moosavian and E. Papadopoulos, "Control of space free-flyers using the modified transpose jacobian algorithm," in *Proceedings of the 1997 IEEE/RSJ International Conference on Intelligent Robots and Systems, IROS '97*, vol. 3, 1997, p. 1500.

[105] T. Oki, H. Nakanishi, and K. Yoshida, "Time-optimal manipulator control of a free-floating space robot with constraint on reaction torque," in *IEEE/RSJ International Conference on Intelligent Robots and Systems, IROS 2008*, 2008, p. 2828.

[106] C. L. Chung and S. Desa, "A global approach for using kinematic redundancy to minimize base reactions of manipulators," Robotics Institute, Carnegie Mellon University, Tech. Rep., 1989, tech. report CMU-RI-TR-89-09.

[107] R. Lampariello, S. Agrawal, and G. Hirzinger, "Optimal motion planning for free-flying robots," in *IEEE International Conference on Robotics and Automation,. ICRA '03.*, vol. 3, 2003, p. 3029.

[108] P. Huang, K. Chen, and Y. Xu, "Optimal path planning for minimizing disturbance of space robot," in *9th International Conference on Control, Automation, Robotics and Vision ICARCV '06*, 2006, p. 1.

[109] H. Okubo, N. Nagano, N. Komatsu, and T. Tsumura, "Path planning for space manipulators to reduce attitude disturbances," *Journal of Guidance, Control and Dynamics*, vol. 20, no. 3, p. 609, 2014.

[110] S. Cocuzza, I. Pretto, and S. Debei, "Least-squares-based reaction control of space manipulators," *Journal of Guidance, Control, and Dynamics*, vol. 35, no. 3, 2012.

[111] R. Krenn and G. Hirzinger, "Modular, generic inverse kinematics algorithm applied to kinematically redundant space manipulators," in *8th ESAWorkshop on Advanced Space Technologies for Robotics and Automation, ESA WPP-236, ESA Publications Division, Noordwijk, The Netherlands*, 2004.

[112] Z. Vafa and S. Dubowsky, "On the dynamics of manipulators in space using the virtual manipulator approach," in *Proceedings of the 1987 IEEE International Conference on Robotics and Automation*, Raleigh, NC, March 1987.

[113] M. Marchesi and F. Angrilli, "Control strategy for a free-flying space manipulator," in *Proceedings of the 8th International Conference on Advanced Robotics, ICAR '97*, 1997, p. 665.

[114] B. Siciliano, "Closed-loop inverse kinematics algorithms for redundant spacecraft/manipulator systems," in *IEEE International Conference on Robotics and Automation*, vol. 3, 1993, p. 95.

[115] F. Caccavale and B. Siciliano, "Quaternion-based kinematic control of redundant spacecraft/manipulator systems," in *IEEE International Conference on Robotics and Automation, ICRA*, vol. 1, 2001, p. 435.

[116] A. Pisculli, L. Felicetti, P. Gasbarri, G. Palmerini, and M. Sabatini, "A reaction-null/jacobian transpose control strategy with gravity gradient compensation for on-orbit space manipulators," *Aerospace Science and Technology*, vol. 38, p. 30, 2014.

[117] ——, "Deployment analysis and control strategies of flexible space manipulators," in *64th International Astronautical Congress, IAC 2013*, Beijing, China, 2013, iAC-13-C2.2.6.

[118] T. Kane and D. Levinson, *Dynamics: Theory and Applications*. McGraw Hill book company, 1985.

[119] T. Kane, "Dynamics of nonholomic systems," *J. Appl. Mech.*, vol. 28, pp. 575–578, 1961.

[120] S. A. A. Moosavian and E. Papadopoulos, "Modified transpose jacobian control of robotic systems," *Automatica*, vol. 43, no. 7, 2007.

[121] C. Sunada, D. Argaez, S. Dubowsky, and C. Mavroidis, "A coordinated jacobian transpose control for mobile multi-limbed robotic systems," in *1994 IEEE International Conference on Robotics and Automation*, 1994.

[122] D. Nenchev, K. Yoshida, and M. Uchiyama, "Reaction null-space based control of flexible structure mounted manipulator systems," in *Proceeding of the 35th Conference on Decision and Control*, Kobe, Japan, December 1996.

[123] J. R. Wertz, *Spacecraft Attitude Determination and Control*. Kluwer Academic Publishers, 2002.

[124] W. J. Larson and J. Wertz, *Space Mission Analysis and Design, Third Edition*. Space Technology Library, Kluwer Academic Publishers, 1999.

[125] A. R. C. Mission Design Division Staff, "Small spacecraft technology state of the art," National Aeronautics and Space Administration (NASA), Tech. Rep., 2014, nASA/TP-2014-216648/REV1.

[126] A. Weiss, X. Yangy, I. Kolmanovskyz, and D. S. Bernsteinx, "Inertia-free spacecraft attitude control with reaction-wheel actuation," in *AIAA Guidance, Navigation, and Control Conference, 2 - 5 August*, Toronto, Ontario Canada, 2010.

Kinematics and dynamics

A.1 Kinematics

A.1.1 Reduction of the system configuration variables

Using the constraint equations together with eq. (2.1), each BRF_i position can be formulated as function of the joint vectors as :

$$\vec{r}_{iO} = \sum_{j=1}^{i-1} \left[L_j \left(\sum_{k=1}^{j} \frac{m_k}{m} \right) \right] - \sum_{j=i}^{N} \left[L_j \left(\sum_{k=j+1}^{N} \frac{m_k}{m} \right) \right] \tag{A.1}$$

By describing vectors $\vec{l}_{Li}$ and $\vec{r}_{Li}$ in each respective body reference frame as $\vec{l}_i$ and $\vec{r}_i$, i.e. $\vec{l}_{Li} = \mathbf{T}_{OI}\,\mathbf{T}_{iO}\,\vec{l}_i$ and $\vec{r}_{Li} = \mathbf{T}_{OI}\,\mathbf{T}_{i+1O}\,\vec{r}_i$, eq. (A.1) is equivalent to

$$\vec{r}_{iO} = \mathbf{T}_{OI} \left\{ \sum_{j=1}^{N-1} \left[\left(\mathbf{T}_{jO}\,\vec{l}_j + \mathbf{T}_{j+1O}\,\vec{r}_j \right) \Psi_{ij} \right] \right\} \tag{A.2}$$

with

$$\Psi_{ij} = \begin{cases} \sum_{k=1}^{j} \frac{m_k}{m} & \text{if } j < i \\ -\sum_{k=j+1}^{N} \frac{m_k}{m} & \text{if } j \geq i \end{cases}$$

A.1.2 Acceleration of the Orbital Reference Frame in spherical coordinates

Following from the description of the ORF position in spherical coordinates, the acceleration of the orbital reference frame is derived as:

$$\dot{\vec{v}}_{OI} = \dot{\Omega}_{OI}\mathbf{T}_{OI}\vec{r}_0 + \Omega_{OI}^2\mathbf{T}_{OI}\vec{r}_0 + 2\Omega_{OI}\mathbf{T}_{OI}\dot{\vec{r}}_0 + \mathbf{T}_{OI}\ddot{\vec{r}}_0 \tag{A.3}$$

with $\ddot{\vec{r}}_0 = \{\ddot{r}_0, 0, 0\}$.

A.2 Dynamics - Lagrangian Formulation

A.2.1 Derivation of the Kinetic Energy

$$\mathcal{T}_i = \frac{1}{2}\int_{\mathcal{B}_i} <\vec{v}_{\delta m_i\, I}\,,\,\vec{v}_{\delta m_i\, I}> \, dm_i \tag{A.4}$$

Considering that $\vec{v}_{\delta m_i\, I} = \vec{v}_{i\, I} + \vec{v}_{\delta m_i\, i} = \vec{v}_{i\, I} + \Omega_{i\, I}\vec{r}_{\delta m_i\, i}$, the kinetic energy is split in three terms

$$\mathcal{T}_i = \mathcal{T}_{i\natural} + \mathcal{T}_{i\flat} + \mathcal{T}_{i\sharp} \tag{A.5}$$

In detail:

$$\mathcal{T}_{i\natural} = \frac{1}{2}\int_{\mathcal{B}_i} <\vec{v}_{i\, I}\,,\,\vec{v}_{i\, I}> \, dm_i = \frac{1}{2}m_i <\vec{v}_{i\, I}\,,\,\vec{v}_{i\, I}> \tag{A.6}$$

$$\mathcal{T}_{i\flat} = \int_{\mathcal{B}_i} <\vec{v}_{i\, I}\,,\,\Omega_{i\, I}\,\vec{r}_{\delta m_i\, i}> \, dm_i = 0 \tag{A.7}$$

As having chosen the origin of BRF_i as the center of mass of the body it follows $\int_{\mathcal{B}_i} \vec{r}_{\delta m_i\, i}\, dm_i = 0$

$$\begin{aligned}
\mathcal{T}_{i\sharp} = &\frac{1}{2}\int_{\mathcal{B}_i} <\Omega_{i\, M}\,\mathbf{T}_{i\, M}\vec{r}_{\delta m_i}\,,\,\Omega_{i\, I}\,\mathbf{T}_{i\, I}\vec{r}_{\delta m_i}> \, dm_i = \\
&\frac{1}{2}\int_{\mathcal{B}_i} <-\mathbf{T}_{i\, I}\,\hat{\vec{r}}_{\delta m_i}\,\mathbf{T}_{i\, I}^T\,\omega_{i\, I}\,,\,-\mathbf{T}_{i\, I}\,\hat{\vec{r}}_{\delta m_i}\,\mathbf{T}_{i\, I}^T\,\omega_{i\, I}> \, dm_i = \\
&\frac{1}{2}\,\omega_{i\, I}^T\int_{\mathcal{B}_i}\mathbf{T}_{i\, I}\,\hat{\vec{r}}_{\delta m_i}^T\,\mathbf{T}_{i\, I}^T\,\mathbf{T}_{i\, I}\,\hat{\vec{r}}_{\delta m_i}\,\mathbf{T}_{i\, I}^T\, dm_i\;\omega_{i\, I} = \\
&\frac{1}{2}\,\omega_{i\, I}^T\,\mathbf{T}_{i\, I}\,\mathbf{I}_i\,\mathbf{T}_{i\, I}^T\,\omega_{i\, I}
\end{aligned} \tag{A.8}$$

where it has been introduced the inertia tensor $\mathbf{I}_i$ expressed in the BRF_i:

$$
\mathbf{I}_i = \begin{bmatrix}
\int_{\mathcal{B}_i} (r_{\delta m_i\,y}^2 + r_{\delta m_i\,z}^2)\, dm_i & 0 & 0 \\
0 & \int_{\mathcal{B}_i} (r_{\delta m_i\,x}^2 + r_{\delta m_i\,z}^2)\, dm_i & 0 \\
0 & 0 & \int_{\mathcal{B}_i} (r_{\delta m_i\,x}^2 + r_{\delta m_i\,y}^2)\, dm_i
\end{bmatrix}
$$

with $\vec{r}_{\delta m_i} = \{r_{\delta m_i\,x}, r_{\delta m_i\,y}, r_{\delta m_i\,z}\}$. Note that $\mathbf{I}_i$ is diagonal as expressed in BRF_i coordinates and the orientation of BRF_i has been set according to the body principal axes of inertia. When referred to the IRF, the matrix transforms in $\mathbf{I}_i^I$ such that $\mathbf{I}_i^I = \mathbf{T}_{i\,I}\,\mathbf{I}_i\,\mathbf{T}_{i\,I}^T$, with the further property that:

$$
\mathbf{I}_i^I = \begin{bmatrix}
\int_{\mathcal{B}_i} (r_{\delta m_i\,i\,y}^2 + r_{\delta m_i\,i\,z}^2)\, dm_i & -\int_{\mathcal{B}_i} r_{\delta m_i\,i\,y} r_{\delta m_i\,i\,x}\, dm_i & -\int_{\mathcal{B}_i} r_{\delta m_i\,i\,x} r_{\delta m_i\,i\,z}\, dm_i \\
-\int_{\mathcal{B}_i} r_{\delta m_i\,i\,x} r_{\delta m_i\,i\,y}\, dm_i & \int_{\mathcal{B}_i} (r_{\delta m_i\,i\,x}^2 + r_{\delta m_i\,i\,z}^2)\, dm_i & -\int_{\mathcal{B}_i} r_{\delta m_i\,i\,y} r_{\delta m_i\,i\,z}\, dm_i \\
-\int_{\mathcal{B}_i} r_{\delta m_i\,i\,x} r_{\delta m_i\,i\,z}\, dm_i & -\int_{\mathcal{B}_i} r_{\delta m_i\,i\,y} r_{\delta m_i\,i\,z}\, dm_i & \int_{\mathcal{B}_i} (r_{\delta m_i\,i\,x}^2 + r_{\delta m_i\,i\,y}^2)\, dm_i
\end{bmatrix}
$$

with $\vec{r}_{\delta m_i\,i} = \{r_{\delta m_i\,i\,x}, r_{\delta m_i\,i\,y}, r_{\delta m_i\,i\,z}\}$.

A.2.2 Potential Energy

Series expansion

For a particle δm_i, part of a body orbiting around the Earth, the gravitational potential is:

$$
\delta \mathcal{U} = -\frac{G\, m_\oplus}{\|\vec{r}_{\delta m_i\,I}\|}\delta m_i = -\frac{\mu}{\|\vec{r}_{\delta m_i\,i}\|}\delta m_i \tag{A.9}
$$

Where:

- G is the universal gravitational constant

- $m_\oplus$ is the mass of the Earth

- $\mu = G\, m_\oplus$

For the Lagrangian approach it is a convenient choice to center the Taylor polynomial over the center of mass position of the overall system, $\vec{r}_{O\,I}$, such that: $\vec{r}_{\delta m_i\,I} = \vec{r}_{O\,I} + \vec{r}_{\delta m_i\,O}$. It is assumed that the magnitude order of the vectors is significantly different $\|\vec{r}_{O\,I}\| \gg \|\vec{r}_{\delta m_i\,O}\|$. It is convenient to consider the ORF position in spherical coordinates in order to have: $r_0 = \|\vec{r}_{O\,I}\|$. Furthermore, it is introduced the $\vec{r}_{O\,I}$ unit vector: $\vec{\gamma}_0 = \frac{\vec{r}_{O\,I}}{r_0}$. The norm of $\vec{r}_{\delta m_i\,I}$ is then expanded as:

$$
\|\vec{r}_{\delta m_i\,I}\| = r_0 (1 + \frac{2}{r_0} <\vec{\gamma}_0\,,\,\vec{r}_{\delta m_i\,O}> + \frac{1}{r_0^2} <\vec{r}_{\delta m_i\,O}\,,\,\vec{r}_{\delta m_i\,O}>)^{\frac{1}{2}}
$$

Hence, the term $\frac{1}{\|\vec{r}_{\delta m_i\,I}\|}$ is expanded in series around the ORF position. To this end, the term is considered equivalently to the function $f(x)$ such that $f(x) = \frac{1}{k\sqrt{1+x}}$. This

expands in a Taylor polynomial series as

$$f(x) \approx \frac{1}{k} - \frac{x}{2k} + \frac{3}{8}\frac{x^2}{k} + o[x^3]$$

Therefore, the term $\frac{1}{\|\vec{r}_{\delta m_i I}\|}$ can be, similarly, approximated as:

$$\frac{1}{\|\vec{r}_{\delta m_i I}\|} \approx \frac{1}{r_0} - \frac{1}{2r_0}\left(\frac{2}{r_0} < \vec{\gamma}_0 , \vec{r}_{\delta m_i O} > + \frac{1}{r_0^2} < \vec{r}_{\delta m_i O} , \vec{r}_{\delta m_i O} >\right) +$$

$$+ \frac{3}{8}\frac{1}{r_0}\left(\frac{2}{r_0} < \vec{\gamma}_0 , \vec{r}_{\delta m_i O} > + \frac{1}{r_0^2} < \vec{r}_{\delta m_i O} , \vec{r}_{\delta m_i O} >\right)^2$$

$$= \frac{1}{r_0} - \frac{1}{r_0^2} < \vec{\gamma}_0 , \vec{r}_{\delta m_i O} > - \frac{1}{2}\frac{1}{r_0^3} < \vec{r}_{\delta m_i O} , \vec{r}_{\delta m_i O} >) +$$

$$+ \frac{3}{8}\frac{1}{r_0}\left(\frac{4}{r_0^2} < \vec{\gamma}_0 , \vec{r}_{\delta m_i O} >^2 + \frac{1}{r_0^4} < \vec{r}_{\delta m_i O} , \vec{r}_{\delta m_i O} >^2 +\right.$$

$$\left.+ \frac{4}{r_0^3} < \vec{r}_{\delta m_i O} , \vec{r}_{\delta m_i O} >< \vec{\gamma}_0 , \vec{r}_{\delta m_i O} >\right)$$

$$= \frac{1}{r_0} - \frac{1}{r_0^2} < \vec{\gamma}_0 , \vec{r}_{\delta m_i O} > + \frac{1}{r_0^3}\left(\frac{3}{2} < \vec{\gamma}_0 , \vec{r}_{\delta m_i O} >^2 +\right.$$

$$\left.- \frac{1}{2} < \vec{r}_{\delta m_i O} , \vec{r}_{\delta m_i O} >\right) + o[\frac{1}{r_0^4}]$$

As convenient for the integration over the body mass, the previous equation is further expanded considering the identity $\vec{r}_{\delta m_i O} = \vec{r}_{i O} + \vec{r}_{\delta m_i i}$:

$$\frac{1}{\|\vec{r}_{\delta m_i I}\|} \approx \frac{1}{r_0} - \frac{1}{r_0^2} < \vec{\gamma}_0 , \vec{r}_{\delta m_i O} > + \frac{1}{r_0^3}\left(\frac{3}{2} < \vec{\gamma}_0 , \vec{r}_{\delta m_i O} >^2 +\right.$$

$$\left.- \frac{1}{2} < \vec{r}_{\delta m_i O} , \vec{r}_{\delta m_i O} >\right) + o\left[\frac{1}{r_0^4}\right]$$

$$= \frac{1}{r_0} - \frac{1}{r_0^2}\left(< \vec{\gamma}_0 , \vec{r}_{i O} > + < \vec{\gamma}_0 , \vec{r}_{\delta m_i i} >\right) +$$

$$+ \frac{1}{r_0^3}\left[\frac{3}{2}\left(< \vec{\gamma}_0 , \vec{r}_{i O} >^2 + < \vec{\gamma}_0 , \vec{r}_{\delta m_i i} >^2\right) +\right.$$

$$+ 3 < \vec{\gamma}_0 , \vec{r}_{i O} >< \vec{\gamma}_0 , \vec{r}_{\delta m_i i} > - \frac{1}{2}\left(< \vec{r}_{i O} , \vec{r}_{i O} > + < \vec{r}_{\delta m_i i} , \vec{r}_{\delta m_i i} >\right) +$$

$$\left.- 2 < \vec{r}_{i O} , \vec{r}_{\delta m_i i} >\right] + o\left[\frac{1}{r_0^4}\right]$$

$$(A.10)$$

Integration

During the integration, the following terms will vanish due to the choice of placing the origin of the body reference frames over the body centers of mass:

$$\int_{\mathcal{B}_i} < \vec{\gamma}_0 \,,\, \vec{r}_{\delta m_i\, i} > dm_i = 0$$

$$\int_{\mathcal{B}_i} < \vec{\gamma}_0 \,,\, \vec{r}_{i\, O} > < \vec{\gamma}_0 \,,\, \vec{r}_{\delta m_i\, i} > dm_i = 0$$

$$\int_{\mathcal{B}_i} < \vec{r}_{i\, O} \,,\, \vec{r}_{\delta m_i\, i} > dm_i = 0$$

Then, the potential function for each body will follow as:

$$\mathcal{U}_i = - \mu \left\{ \frac{1}{r_0} \int_{\mathcal{B}_i} dm_i - \int_{\mathcal{B}_i} \frac{< \vec{\gamma}_0 \,,\, \vec{r}_{i\, O} >}{r_0^2} dm_i + \frac{1}{r_0^3} \int_{\mathcal{B}_i} \left[\frac{3}{2} \left(< \vec{\gamma}_0 \,,\, \vec{r}_{i\, O} >^2 + \right. \right. \right.$$
$$\left. \left. \left. + < \vec{\gamma}_0 \,,\, \vec{r}_{\delta m_i\, i} >^2 \right) - \frac{1}{2} \left(< \vec{r}_{i\, O} \,,\, \vec{r}_{i\, O} > + < \vec{r}_{\delta m_i\, i} \,,\, \vec{r}_{\delta m_i\, i} > \right) \right] dm_i \right\}$$

Note that the body mass integral can be transformed to an integral over the body's volume as the elementary mass dm_i is equivalent to $\rho(\delta m_i) d\mathcal{V}_i$ with $\rho(\delta m_i) = \rho(\vec{r}_{\delta m_i\, i})$ being the body density function and $\mathcal{V}_i$ the infinitesimal volume containing dm_i.

Some of the integrals of the function are trivial and can immediately be solved:

$$\mathcal{U}_i = - \mu \frac{m_i}{r_0} \left[1 - \frac{< \vec{\gamma}_0 \,,\, \vec{r}_{i\, O} >}{r_0} + \frac{1}{2\, r_0^2} \left(3 < \vec{\gamma}_0 \,,\, \vec{r}_{i\, O} >^2 - < \vec{r}_{i\, O} \,,\, \vec{r}_{i\, O} > \right) \right] +$$
$$- \frac{\mu}{2\, r_0^3} \int_{\mathcal{B}_i} \left(3 < \vec{\gamma}_0 \,,\, \vec{r}_{\delta m_i\, i} >^2 - < \vec{r}_{\delta m_i\, i} \,,\, \vec{r}_{\delta m_i\, i} > \right) dm_i$$

Moreover, it should be noted that the inner product $< \vec{\gamma}_0 \,,\, \vec{r}_{\delta m_i\, i} >^2$ can be calculated as follows:

$$< \vec{\gamma}_0 \,,\, \vec{r}_{\delta m_i\, i} >^2 = < \mathbf{T}_{OI}\, \vec{\gamma} \,,\, \mathbf{T}_{OI}\, \mathbf{T}_{iO}\, \vec{r}_{\delta m_i} >^2 = (\vec{\gamma}\, \mathbf{T}_{iO}\, \vec{r}_{\delta m_i})^2 =$$
$$= < \vec{r}_{\delta m_i}\, (< \vec{r}_{\delta m_i} \,,\, \mathbf{T}_{iO}^T\, \vec{\gamma} >)\,,\, \mathbf{T}_{iO}^T\, \vec{\gamma} >$$

with $\vec{\gamma} = \{1, 0, 0\}$ such that $\vec{\gamma}_0 = \mathbf{T}_{OI}\vec{\gamma}$. It follows that:

$$\int_{\mathcal{B}_i} < \vec{r}_{\delta m_i}(< \vec{r}_{\delta m_i} \,,\, \mathbf{T}_{iO}^T\vec{\gamma} >)\,,\, \mathbf{T}_{iO}^T\vec{\gamma} > dm_i =$$
$$= \int_{\mathcal{B}_i} < \|\vec{r}_{\delta m_i}\|^2\, I_d\, \mathbf{T}_{iO}^T\, \vec{\gamma}\,,\, \mathbf{T}_{iO}^T\, \vec{\gamma} > dm_i - < \mathbf{I}_i\, \mathbf{T}_{iO}^T\, \vec{\gamma}\,,\, \mathbf{T}_{iO}^T\, \vec{\gamma} >=$$
$$= < \int_{\mathcal{B}_i} \|\vec{r}_{\delta m_i}\|^2\, dm_i - < \mathbf{I}_i\, \mathbf{T}_{iO}^T\, \vec{\gamma}\,,\, \mathbf{T}_{iO}^T\, \vec{\gamma} >$$

with I_d being the 3 by 3 identity matrix. Noting that $\int_{\mathcal{B}_i} <\vec{r}_{\delta m_i i}, \vec{r}_{\delta m_i i}> dm_i = \int_{\mathcal{B}_i} \|\vec{r}_{\delta m_i}\|^2 dm_i$, the final form of the potential energy is then:

$$
\mathcal{U}_i = -\mu \frac{m_i}{r_0}\left[1 - \frac{<\vec{\gamma}_0, \vec{r}_{iO}>}{r_0} + \frac{1}{2 r_0^2}\left(3 <\vec{\gamma}_0, \vec{r}_{iO}>^2 - <\vec{r}_{iO}, \vec{r}_{iO}>\right)\right] +
$$
$$
+ \frac{\mu}{r_0^3}\left(-\int_{\mathcal{B}_i} \|\vec{r}_{\delta m_i}\|^2 dm_i + \frac{3}{2} <\mathbf{I}_i \mathbf{T}_{iO}^T \vec{\gamma}, \mathbf{T}_{iO}^T \vec{\gamma}>\right)
\tag{A.11}
$$

Lagrangian Function

From previous results, each body contribution, $\mathcal{L}_i$, to the Lagrangian function, $\mathcal{L} = \sum_{i=1}^N \mathcal{L}_i$, is obtained as:

$$
\mathcal{L}_i = \frac{1}{2} m_i <\vec{v}_{iI}, \vec{v}_{iI}> + \frac{1}{2} \omega_{iI}^T \mathbf{T}_{iI} \mathbf{I}_i \mathbf{T}_{iI}^T \omega_{iI} +
$$
$$
+ \mu \frac{m_i}{r_0}\left[1 - \frac{<\vec{\gamma}_0, \vec{r}_{iO}>}{r_0} + \frac{1}{2 r_0^2}\left(3 <\vec{\gamma}_0, \vec{r}_{iO}>^2 - <\vec{r}_{iO}, \vec{r}_{iO}>\right)\right] + \tag{A.12}
$$
$$
+ \frac{\mu}{r_0^3}\left(\int_{\mathcal{B}_i} \|\vec{r}_{\delta m_i}\|^2 dm_i - \frac{3}{2} <\mathbf{I}_i \mathbf{T}_{iO}^T \vec{\gamma}, \mathbf{T}_{iO}^T \vec{\gamma}>\right)
$$

The system Lagrangian can be simplified remembering that the origin of the ORF is the center of mass of the whole system, i.e. $\sum_{i=1}^N m_i \vec{r}_{iO} = \vec{0}$ and $\sum_{i=1}^N m_i \vec{v}_{iO} = \vec{0}$, with $\vec{0}$ the null vector.

$$
\sum_{i=1}^N \frac{1}{2} m_i <\vec{v}_{iI}, \vec{v}_{iI}> = \sum_{i=1}^N \frac{1}{2} m_i <\vec{v}_{OI} + \vec{v}_{iO}, \vec{v}_{OI} + \vec{v}_{iO}> =
$$
$$
= \frac{1}{2} m <\vec{v}_{OI}, \vec{v}_{OI}> + \sum_{i=1}^N \frac{1}{2} m_i <\vec{v}_{iO}, \vec{v}_{iO}>
$$

$$
\sum_{i=1}^N m_i <\vec{\gamma}_0, \vec{r}_{iO}> = 0
$$

Additionally, the function can be further transformed introducing the constraint equations to reduce the system. By using eq.s (2.4) and (2.5), yields:

$$
\sum_{i=1}^N m_i <\vec{v}_{iO}, \vec{v}_{iO}> = \sum_{i=1}^N m_i <\Omega_{OI} \vec{r}_{iO} + \vec{v}_{iO}^*, \Omega_{OI} \vec{r}_{iO} + \vec{v}_{iO}^*> =
$$
$$
\sum_{i=1}^N m_i <\Omega_{OI} \vec{r}_{iO}, \Omega_{OI} \vec{r}_{iO}> + \sum_{i=1}^N m_i <\vec{v}_{iO}^*, \vec{v}_{iO}^*>
$$

where it has been introduced the variable

$$\vec{v}_{iO}^{*} = \mathbf{T}_{OI} \left\{ \sum_{j=1}^{N} \left[\left(\Omega_{jO}\, \mathbf{T}_{jO}\, \vec{l}_j + \Omega_{j+1\,O}\, \mathbf{T}_{j+1\,O}\, \vec{r}_j \right) \Psi_{ij} \right] \right\}$$

obtaining the Lagrangian as:

$$
\begin{aligned}
\mathcal{L} =& \frac{1}{2}m <\vec{v}_{O\,I}\,,\,\vec{v}_{O\,I}> + \sum_{i=1}^{N} \frac{1}{2} \Big(m_i <\Omega_{OI}\,\vec{r}_{iO}\,,\,\Omega_{OI}\,\vec{r}_{iO}> + \\
& + m_i <\vec{v}_{iO}^{*}\,,\,\vec{v}_{iO}^{*}> \ + \omega_{iI}^{T}\,\mathbf{T}_{iI}\,\mathbf{I}_i\,\mathbf{T}_{iI}^{T}\,\omega_{iI} \Big) + \\
& + \frac{\mu\,m}{r_0} + \sum_{i=1}^{N} \frac{\mu\,m_i}{2\,r_0^3} \Big(3 <\vec{\gamma}_0\,,\,\vec{r}_{iO}>^2 - <\vec{r}_{iO}\,,\,\vec{r}_{iO}> \Big) + \\
& + \sum_{i=1}^{N} \frac{\mu}{r_0^3} \left(\int_{\mathcal{B}_i} \|\vec{r}_{\delta m_i}\|^2 \, dm_i \ - \frac{3}{2} <\mathbf{I}_i\,\mathbf{T}_{iO}^{T}\,\vec{\gamma}\,,\,\mathbf{T}_{iO}^{T}\,\vec{\gamma}> \right)
\end{aligned}
\tag{A.13}
$$

where the explicit expression of $\vec{r}_{iO}$ is given by eq.(2.4), which is recalled here:

$$\vec{r}_{iO} = \mathbf{T}_{OI} \left\{ \sum_{j=1}^{N} \left[\left(\mathbf{T}_{jO}\, \vec{l}_j + \mathbf{T}_{j+1\,O}\, \vec{r}_j \right) \Psi_{ij} \right] \right\} \tag{A.14}$$

A.3 The Newton-Euler formulation

Solving method

In order to integrate the Newton-Euler differential equations of motion, the reaction forces at the joints must be known at every time. To this end, the constraint equations can be used. Together with the definition of the ORF position, given by eq.(2.1), these are a set of N vectorial equations. By differentiating the set twice in time, this becomes a set of N vectorial equations containing the accelerations, which can hence introduced in the Newton-Euler differential equations in order to obtain the originally unknown reaction forces at the joints. Here eq. (2.18) is differentiated in time:

$$\vec{v}_{iO} + \Omega_{i\,I}\vec{l}_{Li} = \vec{v}_{i+1\,O} + \Omega_{i+1\,I}\vec{r}_{Li} \qquad \text{for} \quad i = 1, ..., N-1 \tag{A.15}$$

$$\vec{a}_{iO} + (\dot{\Omega}_{i\,I} + \Omega_{i\,I}^2)\vec{l}_{Li} = \vec{a}_{i+1\,O} + (\dot{\Omega}_{i+1\,I} + \Omega_{i+1\,I}^2)\vec{r}_{Li} \qquad \text{for} \quad i = 1, ..., N-1 \tag{A.16}$$

which can be conveniently arranged as:

$$\vec{a}_{i\,O} - \vec{a}_{i+1\,O} = \hat{\vec{l}}_{L\,i}\vec{\omega}_{i\,I} + \hat{\vec{r}}_{L\,i}\vec{\omega}_{i+1\,I} + \Omega^2_{i+1\,I}\vec{r}_{L\,i} - \Omega^2_{i\,I}\vec{l}_{L\,i} \qquad \text{for} \quad i = 1, ..., N-1 \quad \text{(A.17)}$$

Matrix Form

The Newton equation of motion of the body centers of mass relatively to the ORF is described as:

$$\mathbf{M}_a \vec{X}_a = \vec{G}_a + \vec{E}_a + \mathbf{F}_a \vec{L} \tag{A.18}$$

$\mathbf{M}_a$ is a $3(N)$ *by* $3(N)$ block diagonal matrix, with N sub-matrices on the diagonal:

$$\mathbf{M}_a = \begin{bmatrix} \mathbf{M}_1 & \mathbf{0} & \cdots & \mathbf{0} \\ \ddots & \mathbf{M}_2 & \ddots & \vdots \\ \ddots & \ddots & \ddots & \mathbf{0} \\ \mathbf{0} & \cdots & \mathbf{0} & \mathbf{M}_N \end{bmatrix} \quad ; \quad \mathbf{M}_i = \begin{bmatrix} m_i & 0 & 0 \\ 0 & m_i & 0 \\ 0 & 0 & m_i \end{bmatrix}$$

where $\mathbf{0}$ is the null matrix. $\mathbf{F}_a$ is a $3(N)$ *by* $3(N-1)$ matrix:

$$\mathbf{F}_a = \begin{bmatrix} I_d & \mathbf{0} & \cdots & \cdots & \mathbf{0} \\ -I_d & I_d & \mathbf{0} & \cdots & \vdots \\ \vdots & \ddots & \ddots & \ddots & \mathbf{0} \\ \vdots & \ddots & \ddots & -I_d & Id \\ \mathbf{0} & \cdots & \cdots & \mathbf{0} & -I_d \end{bmatrix}$$

where I_d is the 3 *by* 3 identity matrix. Furthermore, the Euler equations of motion can be described in matrix form as:

$$\mathbf{M}_\omega \vec{X}_\omega = \vec{G}_\omega + \vec{E}_\omega + \mathbf{F}_\omega \vec{L} \tag{A.19}$$

with

$$\vec{G}_\omega = \begin{pmatrix} \vec{t}_{g\,1} \\ \vec{t}_{g\,2} \\ \vdots \\ \vec{t}_{g\,N} \end{pmatrix} \qquad \vec{E}_\omega = \begin{pmatrix} \vec{t}_{ext\,1} \\ \vec{t}_{ext\,2} \\ \vdots \\ \vec{t}_{ext\,N} \end{pmatrix}$$

$\mathbf{M}_\omega$ is a $3(N)$ *by* $3(N)$ block diagonal matrix, with N sub-matrices on the diagonal

derived from the attitude dynamics equations:

$$\mathbf{M}_\omega = \begin{bmatrix} \mathbf{I}_1^I & \mathbf{0} & \cdots & \mathbf{0} \\ \mathbf{0} & \ddots & \ddots & \vdots \\ \vdots & \ddots & \ddots & \mathbf{0} \\ \mathbf{0} & \cdots & \mathbf{0} & \mathbf{I}_N^I \end{bmatrix}$$

with $\mathbf{F}_\omega$ a $3(N)$ *by* $3(N-1)$ matrix:

$$\mathbf{F}_\omega = \begin{bmatrix} \hat{\vec{l}}_{L\,1} & \mathbf{0} & \cdots & & \mathbf{0} \\ -\hat{\vec{r}}_{L\,1} & \hat{\vec{l}}_{L\,2} & \cdots & & \vdots \\ \mathbf{0} & \ddots & \ddots & & \mathbf{0} \\ \vdots & \ddots & -\hat{\vec{r}}_{L\,N-2} & \hat{\vec{l}}_{L\,N-2} \\ \mathbf{0} & \cdots & \mathbf{0} & -\hat{\vec{r}}_{L\,N-1} \end{bmatrix}$$

Combining together eq.(A.18) and eq.(A.19), yields:

$$\mathbf{M}\vec{X} = \vec{G} + \vec{E} + \mathbf{F}\vec{L} \tag{A.20}$$

where

$$\vec{X} = \begin{pmatrix} \vec{X}_a \\ \vec{X}_\omega \end{pmatrix} \qquad \vec{G} = \begin{pmatrix} \vec{G}_a \\ \vec{G}_\omega \end{pmatrix} \qquad \vec{E} = \begin{pmatrix} \vec{E}_a \\ \vec{E}_\omega \end{pmatrix}$$

$\mathbf{M}$ is a $3(2N)$ *by* $3(2N)$ block diagonal matrix, with $2N$ sub-matrices on the diagonal:

$$\mathbf{M} = \begin{bmatrix} \mathbf{M}_a & \mathbf{0}_N \\ \mathbf{0}_N & \mathbf{M}_\omega \end{bmatrix}$$

where $\mathbf{0}_N$ is an $3(N)$ *by* $3(N)$ null matrix and $\mathbf{F}$ is a $3(2N)$ *by* $3(N-1)$ matrix:

$$\mathbf{F} = \begin{bmatrix} \mathbf{F}_a \\ \mathbf{F}_\omega \end{bmatrix}$$

Constraint equations

Constraint equations together with the ORF acceleration equation can be formulated in Matrix form as:

$$\mathbf{A}_a\vec{X}_a - \mathbf{A}_\omega\vec{X}_\omega = \vec{\Lambda} \tag{A.21}$$

with $\mathbf{A}_a$ a $3(N)$ *by* $3(N)$ matrix:

$$\mathbf{A}_a = \begin{bmatrix} I_d & I_d & \cdots & \cdots & I_d \\ I_d & -I_d & \mathbf{0} & \cdots & \mathbf{0} \\ \mathbf{0} & \ddots & \ddots & \ddots & \vdots \\ \vdots & \ddots & \ddots & \ddots & \mathbf{0} \\ \mathbf{0} & \cdots & \cdots & I_d & -I_d \end{bmatrix}$$

$\mathbf{A}_\omega$ is a $3(N-1)$ *by* $3(N)$ matrix:

$$\mathbf{A}_\omega = \begin{bmatrix} \mathbf{0} & \mathbf{0} & \cdots & \cdots & \mathbf{0} \\ \hat{\vec{l}}_{L\,1} & -\hat{\vec{r}}_{L\,1} & \mathbf{0} & \cdots & \mathbf{0} \\ \mathbf{0} & \hat{\vec{l}}_{L\,2} & -\hat{\vec{r}}_{L\,2} & \ddots & \vdots \\ \vdots & \ddots & \ddots & \ddots & \mathbf{0} \\ \mathbf{0} & \cdots & \mathbf{0} & \hat{\vec{l}}_{L\,N-1} & -\hat{\vec{r}}_{L\,N-1} \end{bmatrix}$$

and $\vec{\Lambda}$, a $3(N-1)$ vector:

$$\vec{\Lambda} = \begin{pmatrix} \Omega_2^2 \,_I\vec{r}_{L\,1} - \Omega_1^2 \,_I\vec{l}_{L\,1} \\ \Omega_3^2 \,_I\vec{r}_{L\,2} - \Omega_2^2 \,_I\vec{l}_{L\,2} \\ \vdots \\ \Omega_N^2 \,_I\vec{r}_{L\,N-1} - \Omega_{N-1}^2 \,_I\vec{l}_{L\,N-1} \end{pmatrix}$$

Eq.(A.21) can be arranged in the form:

$$\mathbf{A}\vec{X} = \vec{\Lambda} \tag{A.22}$$

with

$$\mathbf{A} = [\mathbf{A}_a \; \mathbf{A}_\omega]$$

Reaction Forces

Combining equations (2.20) and (2.21), reaction forces are solved as follows:

$$\vec{X} = \mathbf{M}^{-1}\left(\vec{G} + \vec{E} + \mathbf{F}\vec{L}\right) \tag{A.23}$$

$$\mathbf{A}\mathbf{M}^{-1}\left(\vec{G} + \vec{E} + \mathbf{F}\vec{L}\right) = \vec{\Lambda} \tag{A.24}$$

$$\vec{L} = \left(\mathbf{A\,M^{-1}\,F}\right)^{-1}\left[\vec{\Lambda} - \mathbf{A\,M^{-1}}\left(\vec{G} + \vec{E}\right)\right] \tag{A.25}$$

Final form of the system

Eq.(2.24) is obtained from eq.(2.23) as follows:

$$\mathbf{K} = I_{d_{2N\times2N}} - \mathbf{F}\left(\mathbf{A\,M^{-1}\,F}\right)^{-1}\left(\mathbf{A\,M^{-1}}\right)$$
$$\mathbf{K^{-1}\,M}\vec{X} = \vec{G} + \vec{E} + \mathbf{K^{-1}\,F}\left(\mathbf{A\,M^{-1}\,F}\right)^{-1}\vec{\Lambda} \tag{A.26}$$

with $I_{d_{2N\times2N}}$ identity matrix of dimensions $2N$ by $2N$. By redefining the vectors $\vec{X}, \vec{G}, \vec{E}$ as follows:

$$\vec{X} = \begin{pmatrix} \vec{X}_a \\ \vec{X}_\omega \\ \vec{a}_{O\,I} \end{pmatrix} \qquad \vec{G} = \begin{pmatrix} \vec{G}_a \\ \vec{G}_\omega \\ \vec{g} \end{pmatrix} \qquad \vec{E} = \begin{pmatrix} \vec{E}_a \\ \vec{E}_\omega \\ \vec{e} \end{pmatrix}$$

The following identity

$$\tilde{\mathbf{M}}\vec{X} = \vec{G} + \vec{E} + \tilde{\vec{\Lambda}}$$

is obtained with $\tilde{\mathbf{M}}$ a $3(2N+1)$ *by* $3(2N+1)$ block diagonal matrix:

$$\mathbf{M} = \begin{bmatrix} \mathbf{K^{-1}\,M} & \mathbf{0} \\ \mathbf{0} & m\,I_d \end{bmatrix}$$

and with $\tilde{\vec{\Lambda}}$ a $3(2N+1)$ vector containing the nonlinear terms defined as:

$$\tilde{\vec{\Lambda}} = \begin{bmatrix} \mathbf{K^{-1}\,F}\left(\mathbf{A\,M^{-1}\,F}\right)^{-1}\vec{\Lambda} \\ \vec{0} \end{bmatrix}$$

Single Spacecraft Simulation

B.1   Mathematical model of a single rigid body in orbit

The mathematical description of a single rigid body in orbit is very well known. Here, for the sake of clarity, the equations of the dynamics are derived using the results of the previous chapter in order to show the mathematical background of the computer simulations shown. In particular, for this case the Euler-Lagrange approach is used.

B.1.1   Orbital Dynamics

The orbital dynamics used is that of the classical two-body keplerian problem.

$$\ddot{\vec{r}}_{CM} = -\frac{\mu}{|\vec{r}|^3}\vec{r} \tag{B.1}$$

B.1.2   Attitude Dynamics

The Euler's equations:

$$\dot{\vec{\omega}}_{bI} = \mathbf{I}^{-1}\left(-\vec{\omega}_{bI} \times \mathbf{I}\,\vec{\omega}_{bI} + \mathbf{T}_{Ext} + \mathbf{T}_{Ctrl}\right) \tag{B.2}$$

$\vec{\omega}_{bI}$ is the angular velocity of the body reference frame, BRF, with respect to the inertial reference frame. The vector is composed by the sum of the orbital angular velocity and that of the body spinning rate with respect to the orbital reference frame: $\vec{\omega}_{bI} = \vec{\omega}_{OI} + \vec{\omega}_{bO}$, $\vec{\omega}_{OI} = \frac{\vec{r}_{CM} \times \vec{v}_{CM}}{|\vec{r}_{CM}|^2}$. $\mathbf{I}$ is the spacecraft tensor of inertia. This has to include all subsystems of the spacecraft, included, for instance, thrusters or reaction wheels. All quantities are expressed with their BRF representation.

In the external torques, due to the orbit altitude chosen, only gravity gradient and air drag are considered.

Gravity Gradient Torque

$$\mathbf{T}_{GG} = 3\frac{\mu}{|\vec{r}_{CM}|^3}\hat{r}_{CM} \times \mathbf{I}\,\hat{r}_{CM} \tag{B.3}$$

with $\hat{r}_{CM}$ unit vector of the center of mass position. Gravity gradient torque can be derived from eq. (1.14) in previous chapter. For further details see [54] for instance.

Air Drag Torque

The following references have been used to derive the air drag torque equation: [123], [124].

$$\mathbf{T}_{AD} = \frac{1}{2}\,\rho\,|\vec{v}_{CM}|^2\,C_d\,A\,\hat{v}_{CM} \times \vec{S}_{cp} \tag{B.4}$$

with $\hat{v}_{CM}$ unit vector of the center of mass velocity, ρ density of the air at the orbital altitude, C_d drag coefficient of the spacecraft (assumed $C_d = 2$), A area of the spacecraft exposed to the wind and $\vec{S}_{cp}$ position of the center of gravity with respect to the center of pressure.

Control Torques - Reaction Wheels model

Reaction wheels are the most used actuator for attitude control of very small scale satellites, [125]. The actuators dynamics is well known, [126], and it has been described as follows:

$$\mathbf{T}_{Ctrl} = \sum_{i=1}^{3} \left\{ \mathbf{I}_{w\,i}\,\vec{\nu}_i \times \vec{\omega}_{bI} + [\mathbf{I}_{w\,i}\,(\vec{\nu}_i \times \vec{\omega}_{bI}) - \vec{\nu}_i \times \mathbf{I}_{w\,i}\,\vec{\omega}_{bI}] - \mathbf{I}_{w\,i}\vec{u}_i \right\}$$

$$\frac{d}{dt}\nu_i = u_i$$

(B.5)

where $\mathbf{I}_{w\,i}$ is the inertia matrix of the wheel, $\vec{\nu}_i$ is the spinning rate of the wheel and $\vec{u}_i$ is the angular acceleration of the wheel, which, in this case, is considered the control variable of the system. Note that, in the wheel reference frame, it is: $\vec{\nu}_i = \{0, 0, \nu_i\}^T$, $\mathbf{I}_{w\,i}\,\vec{\nu}_i = \{0, 0, I_{w\,i}\,\nu_i\}^T$ and $\vec{u}_i = \{0, 0, u_i\}^T$. Furthermore, saturation occurs when u_i reaches the maximum allowed acceleration as well as ν_i reaches the maximum allowed speed:

$$\begin{aligned} u_i &= 0 && \text{if} && \|\nu_i\| = \nu_{max} \text{ and } \nu_i\,u_i > 0 \\ u_i &= u_{max} && \text{if} && \|u_{idl}\| > u_{max} \end{aligned}$$

(B.6)

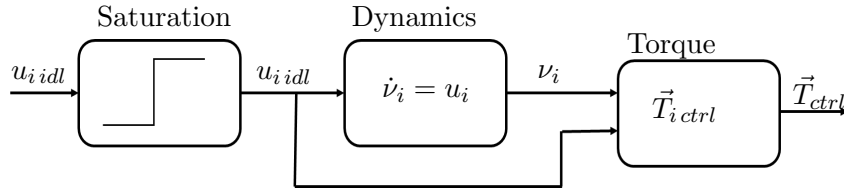where u_{idl} is the input from the controller.

Figure B.1: Schematics description of the reaction wheels dynamics used.

Control Torques - Controller

The attitude control for the test case simulation has been designed using an open loop control for the nominal duration of the manoeuver $(t_i\,,\,t_f)$ and, then, using a velocity feedback control in the following seconds to completely halt the motion. In particular, two rectangular pulses have been applied for Δt_i and Δt_f seconds to start and stop the slew manoeuvre, based on the reference angular velocity profile derived from the free motion planner. No action is taken during the coasting phase between torque's pulses. After the nominal duration of the manoeuvre, a velocity feedback control is used in order to correct non-zero residual angular velocity.

Pulses Design

Calculate the times required to start and stop the body's motion:

$$\Delta t_i = \max\left(\mathbf{I}\,\vec{\omega}_{ref}(0)\,/\,T_{max}\right)$$

$$\Delta t_f = \max\left(\mathbf{I}\,\vec{\omega}_{ref}(tf)\,/\,T_{max}\right)$$

where $T_{max} \in \mathbb{R}^+$ is the maximum torque available by a single reaction wheel.

Open Loop Control

$$
\begin{aligned}
&\text{for } t < \Delta t_i && T_{ctrl}|_{idl} = (\mathbf{I}\,\vec{\omega}_{ref}(0)/\Delta t_i) \\
&\text{for } (tf - \epsilon\Delta t_f) > t > \Delta t_i && T_{ctrl}|_{idl} = 0 \\
&\text{for } [tf + (1-\epsilon)\Delta t_f] > t > (tf - \epsilon\Delta t_f) && T_{ctrl}|_{idl} = (\mathbf{I}\,\vec{\omega}_{ref}(tf)/\Delta t_f) \\
&\text{with } \epsilon \in (0,1)
\end{aligned}
\tag{B.7}
$$

Closed Loop Control

$$
\begin{aligned}
&\text{for } t > [tf + (1-\epsilon)\Delta t_f] && T_{ctrl}|_{idl} = -\mathbf{C}\,\vec{\omega}_{bI} \\
&\text{with } \epsilon \in (0,1) && \mathbf{C} = k\,\mathbf{I}\,,\; k \in \mathbb{R}^+
\end{aligned}
\tag{B.8}
$$

The ϵ parameter has been introduced to adjust the final pulse time distribution and set as $\epsilon = \frac{1}{10}$. The following figure show schematically the controller logic. As a consequence the open loop controller is used during the first $t_f + (1-\epsilon)\Delta t_f$ seconds of the manoeuvre and the closed loop controller is used for the last ten seconds of manoeuvre.
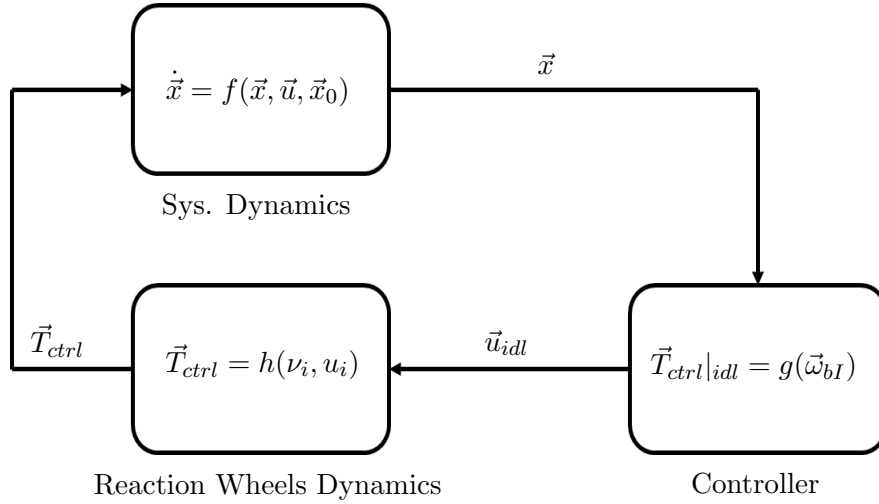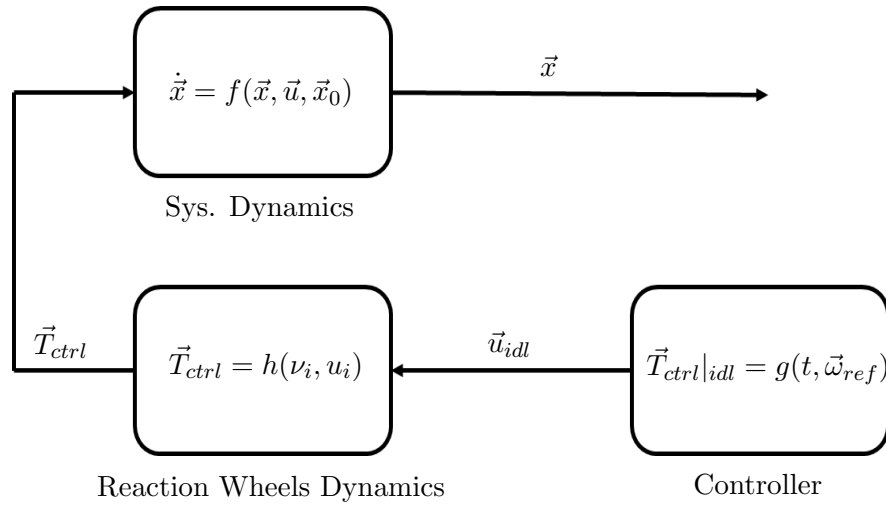

Figure B.2: Open loop controller.

Figure B.3: Closed loop controller.

B.1.3 Attitude Kinematics

Quaternions are used to the kinematical description of the BRF with respect to the orbital reference frame.

$$\dot{\vec{q}}_{bO}(t) = \mathbf{Q}_d(t)\,\vec{\omega}_{bO}(t) \tag{B.9}$$

with

$$\mathbf{Q}_d = \frac{1}{2}\begin{bmatrix} -q_1(t) & -q_2(t) & -q_3(t) \\ q_0(t) & -q_3(t) & q_2(t) \\ q_3(t) & q_0(t) & -q_1(t) \\ -q_2(t) & q_1(t) & q_0(t) \end{bmatrix} \tag{B.10}$$